Lattice Dynamical Studies of Select MAX Phases

A Thesis

Submitted to the Faculty

of

Drexel University

by

Nina J. Lane

in partial fulfillment of the

requirements for the degree

of

Doctor of Philosophy

April 2013

Dedications

This is dedicated to the beautiful young minds of future science, technology, art, and humanities. May your imagination and creativity bring about brilliant ideas that will carry the world forward in an uplifting way.

Acknowledgments

It gives me great pleasure to be able to thank all the people to whom I owe this work. There are *so* many of you to thank and I am excited at this opportunity to be able to express my gratitude.

First and foremost, a gigantic thank you to my primary thesis advisor, Prof. Michel Barsoum. Your invaluable support means the world to me. The endless flow of ideas constantly manifesting into successful projects is inspiring in itself, but beyond that you truly want your students to live up to their full potential and succeed as scientists and you offer tireless support to that end. I know I have been fortunate with the opportunities that have opened up to me during my PhD studies, all of which were made possible by you. Most importantly, your confidence in me made me constantly strive to be deserving of it. I am incredibly thankful for your encouragement, guidance, constructive suggestions, stimulating and enthusiastic discussions, and complete dedication to whatever project is at hand. There are no words to fully express my gratitude so I can simply count my lucky stars that I found a place in your research group and offer a humble thank you.

I am also indebted to several other people who have all taken on the role of a mentor for me during this research. Thanks to Prof. James Rondinelli. Not only did you guide my work as a co-advisor, but you inspired me in your way of carrying research projects forward in such an organized, streamlined, and succinct fashion that makes the most involved projects look effortless. You help me focus on both the smallest details of physics and the broader implications of my work, and your advice is always exactly on point. A special thank you to Dr. Sven Vogel from Los Alamos National Laboratory. You initiated me into my first research project, steered me away from mouse-clicking, and introduced me to the world of bash. You have taught me so

many valuable research skills and always offer the most thoughtful input on any project. You constantly push me to go above and beyond in exploring all facets of physics and you never let me get away with sloppy assumptions, which is something I will carry with me throughout my scientific career. Dr. El'ad Caspi, I am thankful I got to work with you during the end of my PhD and I only wish to reach a fraction of your expertise in Rietveld refinement and crystallography. In addition to our research collaboration, your insight on my PhD thesis has been truly priceless and it helped me realize the significance of my work while I was getting lost in the small details. You have been extremely generous with your knowledge, time, and guidance, and working with you has been an absolute privilege.

A huge thank you to my collaborators at Linköping University. Professor Igor Abriksov and Dr. Sergei Simak, you introduced me to first-principles calculations with your *ab initio* short course and you have ever since served as powerful mentors. A thank you to Prof. Lars Hultman – you have supported me in many ways, and you have been a role model in your patience and thoroughness in the midst of your incredibly full and busy schedule. You made my visits to Sweden not only productive, but enjoyable.

Thanks to Dr. Gilles Hug for hosting me at the French Aerospace Lab, along with Dr. Laurent Chaput and Dr. Atsushi Togo for your guidance and programming help with some major modeling aspects of my work. All the MAX phase phonon work that is a central part of my PhD thesis would certainly not have been possible without you, and it has been both a learning experience and an absolute pleasure to work on.

A special thank you to IPAM at UCLA, including directors Prof. Christain Ratsch and Prof. Russel Caflisch, all the organizers, and the lovely staff, especially my former colleagues in the finance department. Thank you for hosting me on a three-month mathematical journey to learn about different computational techniques. I couldn't have asked for a more productive,

stimulating, and well-organized program. It not only gave me insight on considering defects in materials modeling, but it allowed me to build invaluable connections with scientists and mathematicians.

I would also like to thank the rest of my committee members. Professor Steven May, our discussions always fuel my enthusiasm for science and your encouragement makes me aim high in my scientific career. Professor Som Tyagi, having you on my committee has been immensely beneficial to my work and your input has not only made my thesis stronger, but it has led me to be more deliberate and thoughtful in how I present and communicate my research.

I owe everything to all the brilliant, talented, gracious, and wonderfully productive members of the MAX phase research group. I couldn't ask for a better group of people to work with. The sense of camaraderie is incredible! I have never seen a trace of hesitation or resentment in our group – on the contrary, everyone is overflowing with sincerity and enthusiasm to happily help take on another person's problem and consider it theirs too. Every person in the group has the type of character made of gold that one seldom comes across in a lifetime, and there has never been an exception as the group has evolved. Many thanks from the bottom of my heart to all current and past researchers whom I've had the pleasure of sharing time with in the MAX phase group: Grady Bentzel, Justin Griggs, Joseph Halim, Mohamed Shamma, Dr. Ivy Yang, Ismail Albayrak, Charles B. Spencer Jr., Dr. Youngsoo Chung, Dr. Shahram Amini, Dr. Ted Scabarozi, Prof. Aaron Sakulich, and Prof. Alexander Moseson. An extra special thank you to Babak Anasori, Michael Naguib, and Darin Tallman – you have saved my life (or at least my research projects) countless times. I will always cherish the help, support, humor, encouragement, and above all friendship from everyone.

The members of the Prof. Rondinelli's Materials Theory and Design group have also been my second research family during the last year of my PhD. Joshua Young, Dr. Antonios Cammarata,

Dr. Danilo Puggioni, and the other MTDG members – thank you for taking me into your group as an orphan MAX phase experimentalist-modeler. Collaborating with you has made the computational aspects of my work so much less isolated, and I appreciate all your insight and advice on my scientific problems.

Thanks to the stellar faculty in the department of Materials Science and Engineering at Drexel. Notably, I am grateful for the support, advice, and guidance of Prof. Yury Gogotsi, Prof. Antonios Zavaliangos, Prof. Jonathan Spanier, Prof. Caroline Schauer, and Prof. Richard Knight. A special thank you to the MSE staff – especially Keiko Nakazawa, Dorilona Rose, Yenneeka Long, Sarit Kunz, Leslie Anastasio, Danielle Tadros, and Andrew Marx – for making such a great environment within our department. I would also like to give a big enthusiastic thank you to the Drexel graduate students, both within the Materials department and those in other STEM fields whom I've gotten to know and work with. There are far too many great people to name, but you know who you are – the past four years would not have been the same without the company, moral support, encouragement, hilarious entertainment, and friendship of my incredible peers at Drexel. I would also like to thank the Materials faculty at UCLA, and the small MSE class of 2008, for giving me the best undergraduate education that I could have asked for.

I am grateful for funding support from the National Science Foundation (especially the IGERT fellowship), the Swedish Research Council, and the Department of Energy, which have allowed me to travel, learn, and freely explore the scientific problems that excite me the most without limitation.

A heartfelt thank you to my fantastic friends who have always been so supportive and loving. No matter where our paths are moving, we always intersect at just the right time.

I owe my whole existence to my family. My enlightened mom, your way of thinking has permeated all the work that I do. You miraculously understand my research better than anyone

I know and any strength and integrity in character that I have is all yours. My loving dad, you taught me how to write, build, program, and you always fed my scientific curiosity and insisted that I stay in engineering whenever I strayed. My amazing sister, I am infinitely lucky to have you as an extension of me. You moved all the way across the country to keep me grounded and centered in Philadelphia and carry out extraordinary work of your own. I am constantly inspired by your righteousness and I am forever grateful for your unconditional love.

I would also like to thank *you*, the reader, for looking at this thesis, hopefully skimming it and perhaps reading some of it. And last but certainly not least, thank you to the divine world that exists in everything and works through everyone.

Nina Jeong-Mi Lane

April 2013

Table of Contents

List of Tables

List of Figures

Abstract

Lattice Dynamical Studies of Select MAX Phases

Nina J. Lane

Michel W. Barsoum, PhD

James M. Rondinelli, PhD

Atomic vibrations weave into the fabric of the materials properties landscape in a diverse multitude of ways. They play a major role in specific heat and thermodynamic properties, they affect electronic transport as electron scatterers, they are central to thermal expansion and high-temperature thermal stability, and they alter the intensity of scattered data in probing the crystal structure of a material. While there are cases where the static lattice model gives a reasonable description of materials in the solid state, there are other situations where the assumption of immobile atoms locked into fixed sites fails dramatically. For this work, the role of atomic motion is investigated for a group of materials known as $M_{n+1}AX_n$ ("MAX") phases. They are made up of M (a metal), A (an A-group element), and X (carbon or nitrogen) and exhibit a unique set of properties, combining some of the most desirable attributes of ceramics and metals. Because of their high thermal conductivity and high-temperature stability, their most promising applications are at elevated temperatures, including nuclear reactor cladding and heating elements. Atomic motion is central to understanding and predicting materials properties at high temperatures, especially high-temperature damping and thermal conductivity.

The aim of this work is to investigate the lattice dynamics of select MAX phases through first-principles phonon calculations in order to provide a foundation for modeling their high-temperature properties. The phonon dispersions and density of states are computed. Based on the phonon properties, the theoretical temperature-dependent atomic displacement parameters and Raman-active modes are determined and compared to those determined experimentally

from Raman spectroscopy and high-temperature neutron diffraction. The bond length behavior in one of the MAX phases, Ti_3GeC_2, suggests correlation between the thermal motion of the Ti and Ge atoms. A model is proposed for the effect of correlated motion on temperature-dependent bond lengths, which serves to explain the unusual bond expansion observed through Rietveld analysis of neutron time-of-flight data. Anharmonic effects are explore through first principles calculations of the mode-dependent Grüneisen parameters, which suggest localization and anharmonicity of the low-frequency phonon modes.

Out of the 20 MAX phases studied in this thesis, the Al-containing phases show the best agreement between theory and experiment for their lattice dynamical properties. The Al-containing phases are also some of the most promising MAX phases for industrialization because of their high oxidation resistance and the low cost of their starting materials. This therefore suggests that the MAX phases that are most desirable commercially may also be the most reasonable to model at high temperatures.

This work provides a basis for understanding important phenomena associated with phonons, interatomic bonding, and thermal vibrations in periodic systems, which is not only relevant to the fundamental properties of MAX phases but can be extended to other crystals in the solid state.

Chapter 1: Introduction

This chapter introduces the main topics covered in this thesis and provides a summary of the scope of this work, along with an outline of how the chapters are structured.

1.1 Overview

One interesting aspect of matter is that it can never be completely motionless. Although objects that surround us may appear to be standing still, all matter is made of atoms that are bonded together with interatomic forces and are constantly deviating from their equilibrium positions. Thus, all atoms that make up materials are always vibrating.

The motion of atoms within materials as they move about their equilibrium positions is a largely intuitive phenomenon. Atoms vibrate with higher amplitudes as temperature rises, and atomic vibrations vary in frequency, direction, and amplitude among different materials depending on the nature of their bonds. While atomic displacements can be characterized by average amplitudes and normal mode frequencies, it is also not surprising that the motion of atoms is often not completely random but related to the movement of their neighbors.

The dynamical behavior of atoms in a material is readily apparent in any scattering experiment. Analyzing data scattered from a vibrating atom is much like photographing a fidgeting subject – it would be convenient if the atoms would sit still! However, an understanding of atomic vibrations and their contribution to diffraction data can go far in obtaining meaningful results from a diffraction data set. Atomic vibrations therefore play a major role in all scattering experiments – *e.g.* neutron and x-ray diffraction – regardless of what parameters are sought from a given study. The Debye-Waller factor, which factors into the intensity as a decrease due to

the "blurriness" of a moving atom, is essential to all diffraction data-fitting. In theory, this term represents the mean-squared atomic displacement of an atom from its equilibrium position, but it does not always agree with the theoretical displacement of an atom. Thus, the discrepancies can reveal a great deal about how much a sample deviates from an "ideal" system, and/or other experimental factors that may affect scattering.

This thesis is a materials science journey that involves experimental and theoretical techniques for investigating the lattice dynamics of a unique and interesting class of nanolaminate materials called MAX phases. These materials exhibit extraordinary – and in many cases, unique – combinations of properties that include some of the favorable properties of ceramics and metals. Atomic motion behavior in these phases is especially significant in considering their damping, thermal, and electrical conductivities. Since atomic vibrations are largely governed by interatomic forces, the study of atomic vibrations sheds light onto bonding, which is important in these solids because their unique properties are largely due to the covalent-ionic-metallic bonds [1].

Identifying the nature of vibrational lattice behavior can be nontrivial, but a wide range of experimental and computational tools is currently available for probing materials at the atomic level. In addition to diffraction experiments that yield Debye-Waller factors, inelastic scattering measures the vibrational frequencies of certain modes that are activated by radiation. From a modeling standpoint, first-principles calculations based on density functional theory serve as a powerful tool in computational materials science, with the ability to theoretically investigate materials based only on fundamental laws governing interactions between particles without the need for empirical data. Forces within a periodic crystal can be computed through first-principles calculations, and by analyzing the forces induced by small displacements within a system, the lattice dynamics of a material can be described.

In this thesis, these useful experimental and computational tools are invoked to explore the vibrational behavior of atoms in the intriguing MAX phases as a starting point for modeling their high-temperature properties.

1.2 SCOPE

First-principles phonon calculations provide the backbone for investigating the lattice dynamics of MAX phases. The phonon dispersion is computed using density functional theory for approximately 20 MAX phases, and then experimental studies – mostly Raman spectroscopy and neutron time-of-flight experiments – are used to assess the agreement of the parameters that can be measured with those that are based on the fundamental atomic physics of a perfect, pure, single-phase crystal. This combination of theoretical and experimental tools provides both a physics-based model for explaining the experimentally-determined parameters, as well as a set of physical data to show how real systems behave.

In addition to phonon calculations and comparisons of vibrational frequencies and mean-squared displacements, a model for correlated atomic motion is proposed to explain unexpected bond length behavior observed in high-temperature neutron diffraction. Anharmonic effects are also computationally investigated through the mode-dependent Grüneisen parameters.

This thesis provides a number of insights into various different aspects that relate to the lattice dynamics of MAX phases including bonding, thermal properties, thermodynamics, damping, phonon conductivity, and defects. It is shown that the displacements of the *A* atoms (*e.g.* Si, Ge, Sn, or Al) are strong functions of their atomic mass and the valence electron structures of all the atoms in the materials. The quality of agreement between calculated and measured displacements serves as an indicator of defects and anharmonicity in the interatomic potentials. It is also postulated that the atomic motions of the *A* and *M* atoms are correlated to avoid

collision, and a correlated motion model is invoked to explain unexpected bond length behavior determined from Rietveld analysis of neutron diffraction data.

Of course, like any useful scientific study, this work also opens up just as many questions as it answers. It is highly likely, and hopeful, that at least some of these questions will be eventually answered as more tools become available and materials research progresses. An effort is made to be critical of everything that strays from elegant physics – and of everything that doesn't stray and agrees too perfectly, for that matter – and it is encouraged that readers will do the same so that materials mysteries continue to unfold.

1.3 OUTLINE

This thesis is divided into two main parts, plus additional sections in the appendices:

- **Part I** (Chapters 2 - 8) includes relevant background in materials science and condensed matter physics, an overview of previous literature on select MAX phases, and the basic underlying theory for the computational and experimental techniques presented including important concepts behind lattice dynamics, density functional theory, neutron scattering, and Raman spectroscopy. In addition, the experimental procedures are described, which include sample synthesis, experimental set-up, and data analysis.

- **Part II** (Chapters 9 - 16) presents and discusses the results obtained by me and my collaborators, most of which have been published in Refs [2–6]:

  - ◇ Chapter 9 presents the predicted vibrational properties from first-principles calculations, including the phonon dispersion and phonon density of states.

  - ◇ Chapter 10 focuses on Raman scattering experiments, including Raman spectra, calculations of Raman-active modes and Raman frequencies from first-principles calculations, and their relationship to bonding, mass, and elastic properties.

- In Chapter 11, the calculated atomic displacement parameters are presented for a large number of MAX phases, and in Chapter 12 experimental values from high-temperature neutron time-of-flight experiments are compared with the predictions in Chapter 11.
- Chapter 13 focuses on the temperature-dependent crystal structures, emphasizing the bond expansions in the "conventional" (*i.e.*, not higher-order) MAX phases, mostly based on experimental results.
- Chapter 14 presents results on the temperature-dependent crystal structures and atomic displacements for a higher-order "523" MAX phase, $Ti_5Al_2C_3$, from HTND, along with results for other MAX phases in the Ti–Al–C system.
- In Chapter 15, correlated motion and anharmonicity are discussed, invoking a model to explain unexpected behavior in bond expansion observed from high-temperature neutron diffraction.
- Finally, Chapter 16 summarizes the most important findings of this work and discusses future directions for building upon the research in this thesis.

- **Appendices A and B** provide additional information that is slightly outside of the scope of this thesis:
  - Appendix A provides details on the texture, composition, and diffraction statistics for the high-temperature neutron diffraction experiments. Additional characterization of samples used for Raman spectroscopy is also presented.
  - Appendix B includes other studies that are not directly related to lattice dynamics, but are mentioned throughout this thesis and offer insight on the behavior of MAX phases and MAX-related materials through combinations of first-principles calculations and

experimental techniques. Five papers, Refs. [7–11], are included in this section. The papers include research on low-dimensional MXenes, structure determination of higher-order MAX phases, a first-principles study on deformation of hexagonal close-packed metals through kink band formation, and polymorphism in the 413 phases.

Part I

Background, theory and methods

Chapter 2: Materials science and engineering

This chapter introduces materials science and engineering and discusses its importance in a general sense. In addition, some introductory concepts related to materials are presented.

2.1 The basics of materials science and engineering

Everything that exists in the universe is made out of something – more specifically, some material, or matter. The field of materials science is, in short, the **study of matter**. The matter that makes up any object drives its properties, its usefulness to humans, and its performance in applications. The interactions of human beings with the world have been largely driven by the materials that we have used. Since the earliest ages of mankind – appropriately named the stone age – we have evolved from the use of stones and natural materials to the smelting and casting of metals to glass and stone-paste ceramics. Today, modern materials science includes metallurgy, advanced ceramic materials, polymers, soft matter, nanomaterials, and an incredibly abundant landscape of manmade materials with diverse sets of properties that allow humans to carry smartphones and fly halfway across the world in under a day.

All objects are made of atoms, which are composed of neutrons, protons, and electrons. The properties of matter are determined by the types of elements that make up the material and the way in which they are arranged. Most materials that we deal with fit into a few categories based on their chemistry, bonding, and properties. As a basic guide, the main categories are:

- **Metals**: The majority of elements that are solid at room temperature are metals, (see periodic table in Fig. 2.1), and there are also many alloys and intermetallics that consist of a number of metal elements. The atoms in metals are held together by metallic bonds,

where a sea of electrons binds the positive cores to one another. As a result of their bonding, they are generally ductile, good conductors of heat and electricity, and shiny.

  - ◇ *Examples:* tin, gold, silver.

- **Semiconductors**: These are covalently bonded solids that are hard, brittle, and have electrical conductivities between those of conductors and insulators. Their electrical conductivity increases with increasing temperature, unlike metals, and impurities can often be added to make them conduct electricity. Most modern technology – computer chips, DVD players, phones – depends on semiconductors.

  - ◇ *Examples:* gallium arsenide (GaAs), silicon, germanium.

- **Polymers**: Polymers consist of long carbon-based chains that are covalently bonded within the chains, with weak bonding between the chains. They tend to melt at low temperatures and have relatively low stiffnesses. Synthetic polymers are commonly known as plastics.

  - ◇ *Examples:* polyvinyl chloride (PVC), nylon, silly putty.

- **Ceramics**: Nearly everything that is not a polymer, a metal, or a semiconductor is a ceramic. With the addition of oxygen or nitrogen, metals can become ceramics. Ceramics can be loosely defined as compounds that comprise of two or more elements, with at least one of them being a nonmetal or a nonmetallic elemental solid. Ceramics are generally hard and brittle, and often thermal insulators.

  - ◇ *Examples:* glass (SiO_2), table salt (NaCl).

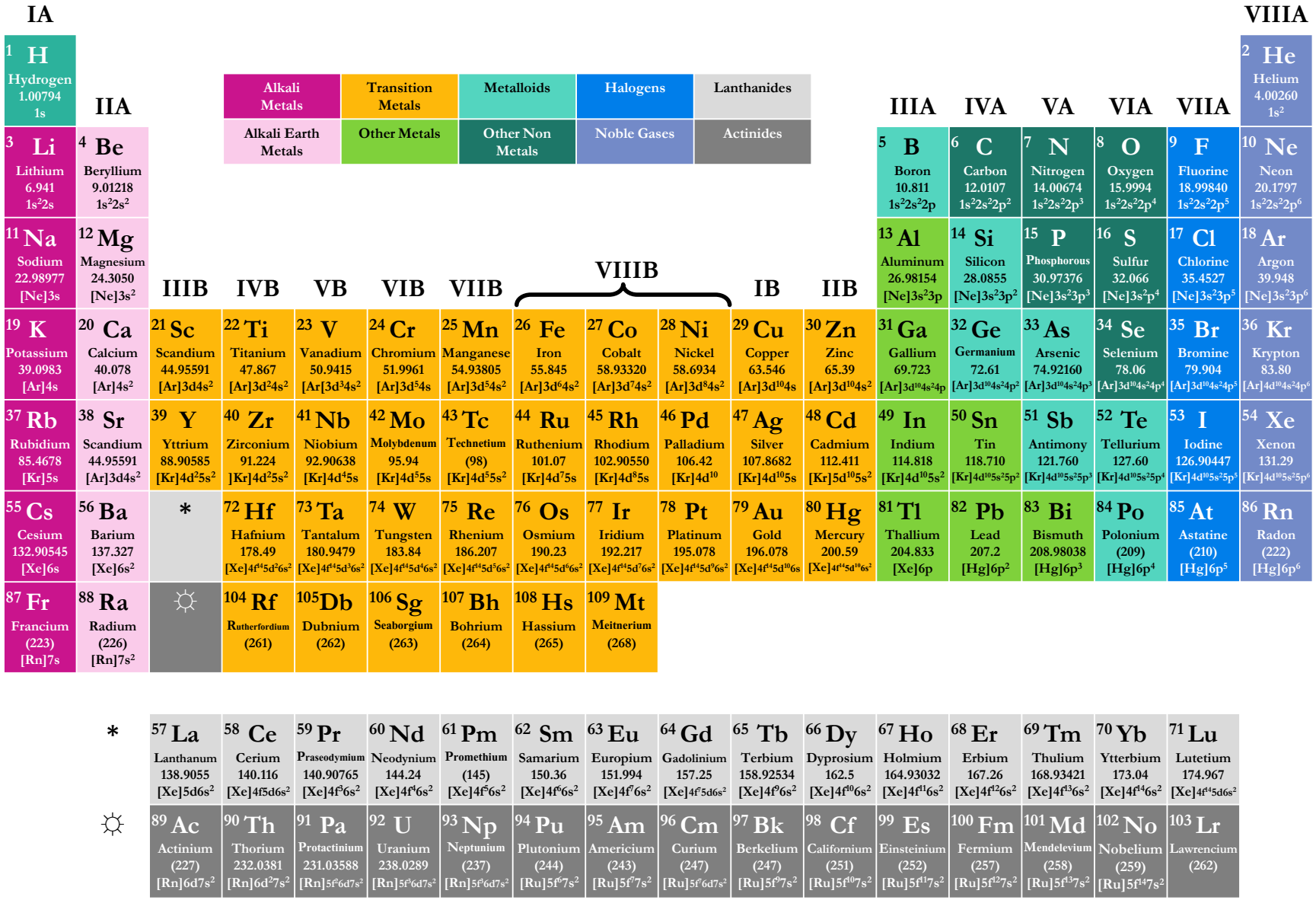

Figure 2.1: The periodic table of elements. In each box, from top to bottom, is the atomic number, atomic symbol, name, atomic weight, and electron configuration. An atomic weight in parentheses indicates the mass number of the most stable isotope.

Materials classification can get much more complicated than the classes summarized above, especially in dealing with the advanced materials of modern materials science such as low-dimensional materials, composites, and biomaterials. The systems and definitions that are used to classify materials are constantly evolving.

By now we have a wide range of experimental tools to help us characterize the materials that already exist, but these days we must go further to optimize and develop new materials. While materials *science* is essentially the study of matter, materials *engineering* is the use of atoms as building blocks to create new materials and alter the properties of old ones. As technology advances, the need to optimize materials becomes ever more central. When it comes to the engineering aspect of materials, the trial and error cycle of synthesis and characterization can be too slow to meet growing needs. Computational materials science thus can play a major role in guiding materials design, in both understanding the science behind different phenomena and predicting the outcome of materials experiments.

All in all, understanding the atomic-level physics of materials is key to advancing materials science, and experimental and theoretical techniques are both important tools in gaining insight.

2.2 IMPORTANT PHYSICAL CONCEPTS IN MATERIALS SCIENCE AND ENGINEERING

2.2.1 Physical properties of materials

Each type of material has a unique set of properties that governs its response to stimuli and surrounding environments, its interactions with other matter and radiation, and, ultimately, its suitability for various applications.

Here, some of the different types of properties, or systems for characterizing materials, are summarized to give a condensed picture of the materials properties landscape.

Response of a material to stress

The way materials respond to stress is a crucial aspect in essentially any application. When stress is applied to a material, the material responds through either reversible (elastic) deformation or irreversible deformation, which includes fracture and plastic strain. Mechanical properties of materials are very much related to the vibrational behavior of atoms, as the forces between atoms are what hold them together, dictating their dynamical behavior and their response to external forces.

Thermal expansion

When a material is heated, its volume changes. In solids, atoms vibrate around their equilibrium positions and, as temperature increases, energy increases, leading to a rise in amplitude of atomic vibrations. For an anharmonic potential, this corresponds to changes in the equilibrium spacing between atoms. In most cases, materials expand upon heating.

The rate of change in dimension of a crystal along a linear direction (l) with temperature is called the coefficient of thermal expansion, CTE, and is denoted by α:

$$\alpha = \frac{1}{l}\frac{dl}{dT}. \tag{2.1}$$

The average CTE, α, over a range of temperatures is determined by the slope of $[l(T)-l_0]/l_0$ vs. T, where l_0 is the original length (*i.e.* the length at some reference temperature) and $l(T)$ is the length at another temperature, T.

Depending on crystal structure symmetry, the rate of expansion may be different in different directions. For a hexagonal structure, α is different in the a and in the c direction, and the CTE in each direction, α_a and α_c, can be determined by measuring a and c as a function of temperature. In many cases – for example, with polycrystals and multiphase samples – this is not

possible by dilatometry (simply measuring the bulk dimensions of a sample) and thus diffraction techniques are useful for measuring the anisotropic thermal expansion in certain materials.

Electronic properties and thermal conductivity

Other important materials concepts include their response to an electric field and their ability to transport heat. Some materials conduct electricity (metals), some do not (insulators), and others behave somewhere in between (semiconductors). The electronic properties depend on the energy distribution of free elections in a material and is important in determining how, or whether, a material will transport electric current. The MAX phases studied in this thesis (see Chapter 3) conduct both heat and electricity, which is not the case with many ceramic materials which often behave as insulators - both thermal and electronic.

2.2.2 Crystal structures

In materials, atoms are the building blocks for engineering. The atoms that come together to make up solids are not simply jumbled in a random configuration. Nature tends to be more elegant, and atoms in most solids are arranged in an ordered way that periodically repeats throughout a material.

The volume of space that repeats itself is known as the unit cell. In a primitive unit cell, this volume is the smallest repeatable unit, but in so-called "conventional" unit cells such as face-centered and body-centered lattices, this is not necessarily the case. The crystal structure of a material, which defines the arrangement of atoms, can be classified by shape and symmetry. The lattice parameters a, b, and c define the dimensions of a unit cell, and angles α, β, and γ define the angles. There are seven lattice types (or symmetries for a, b, c, α, β, and γ) which can be divided into 14 Bravais lattices (further classification by lattice points), and then into 230 space groups, which describe the symmetry operations for the atoms that repeat inside a unit

cell.

There are several notations for defining these 230 space groups. The space groups can be defined by a number, where each space group has a unique number from 1 to 230, as assigned and published in tables by the International Union of Crystallography [12]. Another notation is the Hermann-Mauguin notation, which describes the lattice and symmetry operators for points on the lattice. A detailed description of these crystal structures and their formalism can be found in a number of textbooks [13–15].

The symmetry of the arrangement of atoms is crucial to keep in mind in any structural investigation of solids. In neutron scattering, the ordered atomic arrangement is what leads to diffraction peaks, and the symmetry of the atoms is what defines the unique atomic sites – that is, which atoms have the same environment in a crystal. The dynamical behavior of individual atoms, the thermal expansion of the unit cell, and the atomic positions (among many other factors) are all constrained and influenced by the crystal structure symmetry.

Chapter 3: MAX phases

The materials that are the focus of the research in this thesis are ternary carbides and nitrides known as MAX phases. This chapter introduces the crystal structure of the MAX phases, an overview of their general properties as a class, and a review of literature to date on select phases that are significant to this thesis.

3.1 Introduction to MAX phases

The MAX phases are a group of >60 nanolaminate ternary carbides and nitrides. They have received considerable attention since it was discovered that, as a class, they possess a unique and remarkable combination of properties [16–19]. Their general formula is $M_{n+1}AX_n$, where n = 1, 2, or 3, M is an early transition metal, A is an A-group element – mostly from groups IIA and IVA – and X is carbon and/or nitrogen [see Fig. 3.1(a)]. They can be further classified by their values of n as "211" ($n = 1$), "312" ($n = 2$), and "413" ($n = 3$) phases. The MAX phases crystallize in the hexagonal space group D^4_{6h}, with Hermann-Mauguin notation $P6_3/mmc$, No. 194 in the International Tables. The meaning of this nomenclature is as follows:

- P - "Primitive" Bravais lattice, which means there is no additional translational symmetry for the lattice points, and the lattice points are on the cell corners only, *i.e.*, there are no other face-, base-, or body-centered positions. All hexagonal space groups have a primitive lattice.

- 6_3 - This is the screw-axis (rotational and translational) symmetry, where the "6" refers to 6-fold symmetry and the "3" subscript refers to the distance for translation along the

primary axis.* The notation n_r describes a symmetry with a rotation by $2\pi/n$ followed by a translation of a fraction r/n of the unit cell length along the rotation axis [0001] (*i.e.* the c lattice parameter). For 6_3, this is rotation by $\pi/3$ (60°) around the c axis and translation halfway along c.

- *mmc* - The part after the slash refers to mirror and glide plane symmetry perpendicular to the primary, secondary, and tertiary axes.* The "*mm*" represents mirror symmetry across the (0001) and $(10\bar{1}0)$ planes. The "*c*" denotes axial glide plane symmetry perpendicular to the $(11\bar{2}0)$ plane, with glide vector $c/2$. †

The atoms in MAX phases are arranged in alternate nanolaminate layers consisting of close-packed layers of M and X atoms – where the X atoms fill the octahedral sites between M layers – interleaved with layers of pure A elements [Fig. 3.1(b)]. The Wyckoff positions for the atom sites in 211, 312, and 413 structures are listed 3.1.

The structure and chemistry of these phases lead to an unusual – yet attractive and often unique – set of properties that bring together some of the best attributes of ceramics and metals [16, 17, 19]. Like metals, they are excellent electric and thermal conductors, with exceptional thermal shock resistance and damage tolerance [16, 17, 20]. Moreover, they are elastically quite stiff and can maintain their strengths at high temperatures like ceramics, yet they are readily machinable [21]. In some cases, they are creep [22–25], oxidation [18, 26], and fatigue [27] resistant.

*For hexagonal systems, the primary direction is [0001] (along the c axis), secondary is $[10\bar{1}0]$ (along the a axis) and the tertiary is $[11\bar{2}0]$ (the bisector of the a and b axes).

†Although the full notation is $P6_3/m\ \ 2/m\ \ 2/c$, the number 2 may be omitted due to the fact that a 2-fold symmetry is trivial. Therefore, the shortened symbol is typically used.

Table 3.1: Positions of atom sites in the 211, 312, 413 (α and β polymorphs), and 523 MAX phases.

Phase	Space group	Atom	Wyckoff	x	y	z
$\mathbf{M_2AX}$, **211**	P_{63}/mmc	M	$4f$	1/3	2/3	$z_M \simeq 0.08$
		A	$2d$	1/3	2/3	3/4
		X	$2a$	0	0	0
$\mathbf{M_3AX_2}$, **312**	P_{63}/mmc	M_{I}	$4f$	2/3	1/3	$z_{M_{\mathrm{I}}} \simeq 0.14$
		M_{II}	$2a$	0	0	0
		A	$2b$	0	0	1/4
		X	$4f$	1/3	2/3	$z_X \simeq 0.07$
α-$\mathbf{M_4AX_3}$, **413**	P_{63}/mmc	M_{I}	$4e$	0	0	$z_{M_{\mathrm{I}}} \simeq 0.16$
		M_{II}	$4f$	1/3	2/3	$z_{M_{\mathrm{II}}} \simeq 0.05$
		A	$2c$	1/3	2/3	1/4
		X_{I}	$4f$	2/3	1/3	$z_{X_{\mathrm{I}}} \simeq 0.10$
		X_{II}	$2a$	0	0	0
β-$\mathbf{M_4AX_3}$, **413**	P_{63}/mmc	M_{I}	$4f$	1/3	2/3	$z_{M_{\mathrm{I}}} \simeq 0.66$
		M_{II}	$4f$	1/3	2/3	$z_{M_{\mathrm{II}} \simeq 0.05}$
		A	$2c$	1/3	2/3	1/4
		X_{I}	$4e$	0	0	$z_{X_{\mathrm{I}}} \simeq 0.10$
		X_{II}	$2a$	0	0	0
$\mathbf{M_5A_2X_3}$, **523**	$R\bar{3}m$	M_{I}	$6c$	0	0	$z_{M_{\mathrm{I}}} \simeq 0.72$
		M_{II}	$3a$	0	0	0
		M_{III}	$6c$	0	0	$z_{M_{\mathrm{III}}} \simeq 0.81$
		A	$6c$	0	0	$z_A \simeq 0.10$
		X_{I}	$6c$	0	0	$z_{X_{\mathrm{I}}} \simeq 0.36$
		X_{II}	$3b$	0	0	1/2

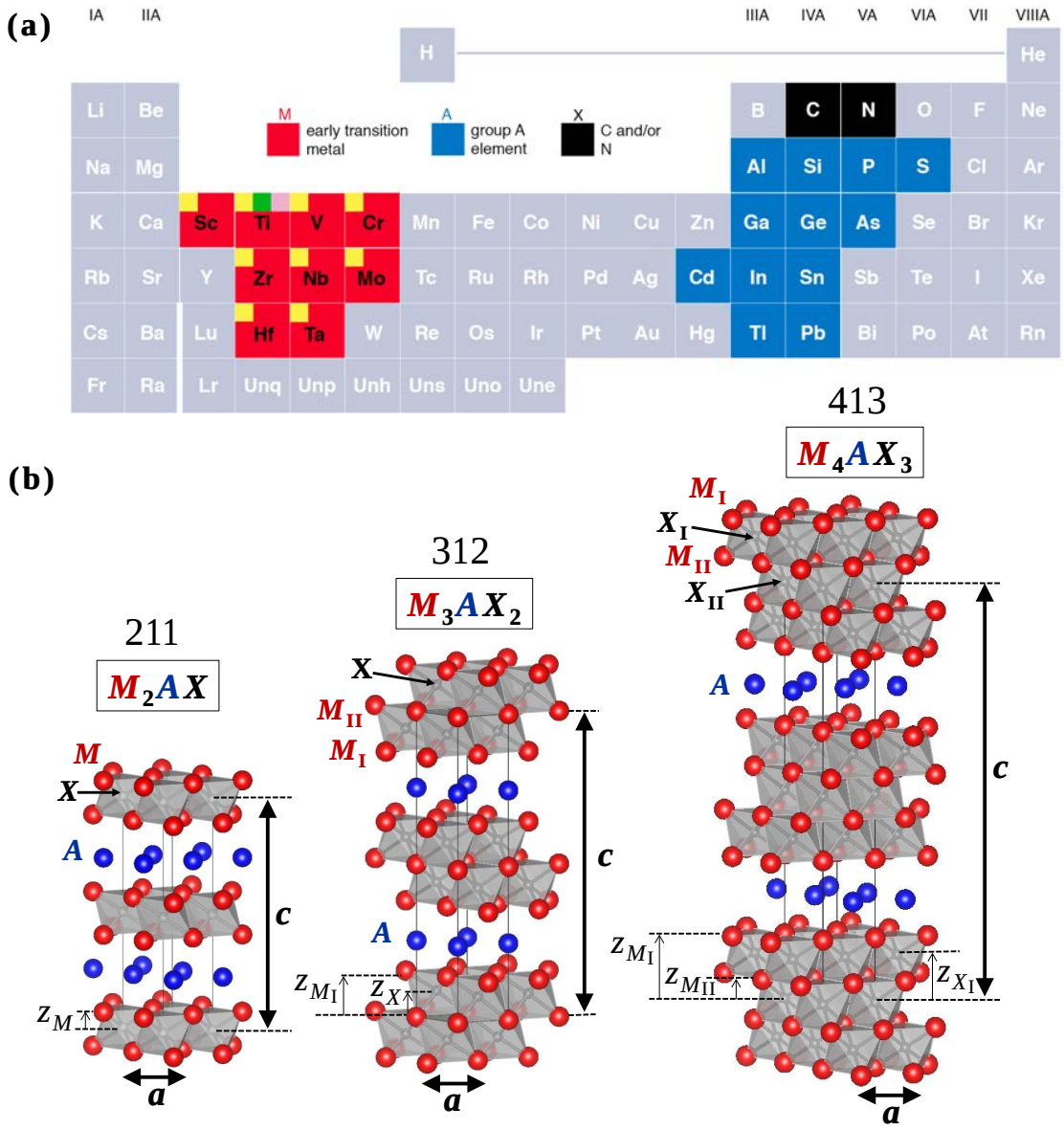

Figure 3.1: (a) Elements in the periodic table that react together to form the MAX phases, and (b) the crystal structures and stoichiometry of 211, 312, and 413 MAX phases showing internal z coordinates, atomic sites and a and c lattice parameters. For the periodic table squares in (a) and the atoms in (b), red represents the M elements, blue represents the A elements, and the black represents the X elements, which are carbon and/or nitrogen atoms that sit inside the gray octahedra in (b).

3.2 LITERATURE REVIEW OF SELECT MAX PHASES

This section provides a condensed literature review of relevant properties and previous work on some of the MAX phases studied in this thesis. This is meant to give an overview of some of the phenomena and properties associated with the phases that will be discussed throughout this thesis. Also, one of the main purposes of this section is to set the stage for the results that will be presented in Part II by giving an idea of what literature was previously available on the phases studied in this work prior to the work carried out through my research.

3.2.1 211 phases: Ti_2AlN, Cr_2GeC, and Ti_2SnC

Three of the 211 phases that are investigated through HTND and/or Raman spectroscopy in this work are Ti_2AlN, Cr_2GeC, and Ti_2SnC. All three phases were first discovered in the 1960s by Jeitschko *et al* [28, 29].

Ti_2AlN was confirmed at 1273 K in 1984 by Schuster and Bauer in their investigation of the ternary Ti–Al–N system [30]. Later, Pietzka and Schuster determined the N content using Dumas chromatography assuming the Ti:Al ratio to be 2:1 and found that the stoichiometry of their phase was actually $Ti_2AlN_{0.82}$ [31]. In 1997, Barsoum *et al.* reported on the fabrication and characterization of fully dense, predominantly single-phase bulk Ti_2AlN samples [32]. In a high-pressure XRD study, Ti_2AlN was found to be more compressible along both directions than Ti_4AlN_3, which has a larger fraction of Ti–N bonds [33]. This shows that that the Ti–N bonds are less compressible than the Ti–Al bonds in $Ti_{n+1}AlN_n$, at least when hydrostatically compressed. Furthermore, the anisotropic compressibilities and lattice parameters of Ti_2AlN compared to Ti_2AlC suggest that the higher compressibility of Ti_2AlN in the a direction may be due to N vacancies [33].

In a study of the electronic and thermal properties of Ti_2AlN compared with Ti_2AlC and their

solid solutions, wet chemical analysis and EDS showed that the two different Ti_2AlN samples in that study were also nonstochiometric, with chemistries of $Ti_2Al_{1.04}N_{0.98}$[‡] and $Ti_2AlN_{0.95}$ with an uncertainty of ±0.03 in the stoichiometric values [34]. The latter sample had a higher electrical resistivity and lower phonon and thermal conductivities, which was attributed to the higher concentration of N-vacancies [34]. A study of the Ar^{2+} irradiation effects on nitrogen-deficient Ti_2AlN_x suggested that nitrogen vacancies may be responsible for its high nuclear damage recovery [35]. In another study of the phonon conductivities of Ti_2AlN and Ti_2AlC and their solid solutions, it was proposed that vacancies on the N sites were responsible for the low shear sound velocity in Ti_2AlN as well [36]. In that study, the Ti_2AlN samples were also found to be nonstochiometric, with chemistries determined from EDS and wet chemical analysis to be $Ti_2AlN_{0.996}$ and $Ti_{1.93}AlN_{0.975}$. At 8.1(±0.2) $\times 10^{-6}$ K^{-1}, the average expansion of Ti_2AlN determined from HTXRD is similar to that of Ti_2AlC [37]; for the direction-dependent lattice expansions, however, the CTE of Ti_2AlN determined from HTXRD is greater in the a- than c-direction, while the opposite is true for Ti_2AlC [33, 38]. This may be attributed to the stronger Ti–N and Ti–Al bonds in Ti_2AlN that have been shown in first-principles studies of bonding [39, 40].

The ternary Cr_2GeC phase was re-discovered a decade later than Ti_2AlN in 2007, when the fabrication and characterization of fully dense, predominantly single-phase Cr_2GeC was achieved [38, 41–43]. Like Ti_2AlN and other MAX phases, Cr_2GeC is a kinking nonlinear elastic solid [43]. Also like Ti_2AlN and other MAX phases it is stable up to quasi-hydrostatic pressures of the order of 50 GPa, with a bulk modulus of 182±2 GPa [42]. The CTEs determined through HTXRD in the 298 – 1073 K temperature range were some of the highest of the MAX phases studied to date, $\alpha_a = 12.9(\pm 0.1) \times 10^{-6}$ K^{-1} and $\alpha_c = 17.6(\pm 0.1) \times 10^{-6}$ K^{-1} [38].

[‡]Where the excess Al was situated in the this sample was not understood.

Ti_2SnC is known for its high electric conductivity among the MAX phases, which has suggested its use as reinforcement for copper and enhancing its mechanical performance without much loss in conductivity [44–46]. Ti_2SnC was also studied as a binder in diamond composites for cutting tools [47].

Compared to the 312 MAX phases, the 211 MAX phases have not been as thoroughly characterized, and even less information is available on Ti_2AlN, Ti_2SnC, and Cr_2GeC compared to the more widely investigated 211 phase Ti_2AlC. HTND experiments are important in understanding the bulk thermal properties of materials and the unit cell expansion. Anisotropic thermal displacement can also shed light on the bonding in these solids. These two 211 phases are studied in later chapters through both first-principles calculations, HTND, and Raman spectroscopy in order to investigate their thermal atomic vibrations and their temperature-dependent crystal structures.

3.2.2 312 phases: Ti_3SiC_2, Ti_3GeC_2, Ti_3AlC_2, and Ti_3SnC_2

Four other phases that are studied in this thesis are the 312 phases Ti_3SiC_2, Ti_3GeC_2, Ti_3AlC_2, and Ti_3SnC_2. Ti_3SiC_2 and Ti_3GeC_2 were first synthesized in powder form in the 1960s [48, 49]. It was not until recently, however, that they ere fabricated and fully characterized in bulk form as fully dense, single-phase solids [19, 20, 32].

The structure of Ti_3SiC_2 has since been confirmed using convergent beam electron diffraction by Arunajatesan and Carim, who obtained lattice parameters of $a = 3.06$ Å and $c = 17.66$ Å [50]. The chemical bonding and thermal properties of Ti_3SiC_2 have been extensively investigated. Following its discovery and structure verification, a neutron diffraction, ND, study was conducted to confirm the original structure and report bond lengths and bond angles, with lattice parameters $a = 3.0575$ and $c = 17.6235$ Å [51]. In that study, it was found that the Ti–C

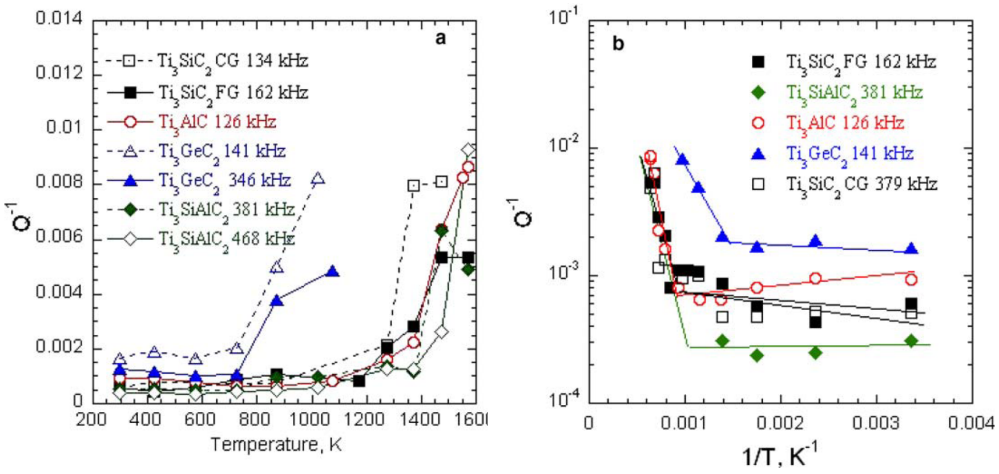

Figure 3.2: (a) Q^{-1} vs. temperature and (b) Arrhenius plots of $\ln Q^{-1}$ for 312 MAX phases Ti_3SiC_2, Ti_3AlC_2, Ti_3GeC_2, and $Ti_3(SiAl)C_2$ for select frequencies, taken from Ref. [52].

distances were comparable to normal covalent distances in TiC, whereas the Ti–Si distance was slightly larger than in a normal covalent bond and closer to the sum of metallic Ti and covalent Si radii. Furthermore, a slight distortion of the CTi_6 octahedra, indicated by the distinctly different bond lengths for Ti_I–C and Ti_{II}–C, was noted. Effectively the C atoms relax in the direction of the Si layers. This results in slightly smaller and more distorted octahedra than in TiC [51].

Another ND study of Ti_3SiC_2 was conducted soon after in the 298 – 1273 K temperature range to determine its thermal properties [53]. The CTEs were determined in the a and c direction to be 8.6(±0.1) $\times 10^{-6}$ K^{-1} and 9.7(±0.1) $\times 10^{-6}$ K^{-1}, respectively, for an average volume expansion of 8.9(±0.1) $\times 10^{-6}$ K^{-1}. The latter is in fairly good agreement with the values determined from dilatometry, 10(±1) $\times 10^{-6}$ K^{-1} [16], 9.2 $\times 10^{-6}$ K^{-1} [19], and 9.1(±0.2) $\times 10^{-6}$ K^{-1} [53].

Like Ti_3SiC_2, Ti_3AlC_2 has been relatively well studied. Ti_3AlC_2 was discovered in 1994 [31]. Of the > 60 MAX phases known to date, Ti_3AlC_2 – along with another MAX phase in the Ti–Al–C system, Ti_2AlC_2 – is particularly attractive in terms of high temperature applications.

The $Ti_{n+1}AlC_n$ phases are two of the most lightweight and oxidation resistant MAX phases [54, 55], and the accessibility and relative low cost of their raw materials render them the most promising for up-scaling and industrialization.

Much less information is available for Ti_3GeC_2. A number of papers have been published on $Ti_3Si_xGe_{1-x}C_2$ solid solutions [20, 56–59] in which it was shown that both low (4–300 K) temperature transport [58] and mechanical properties [20] are fairly insensitive to x. The average of the expansions along the a and c directions, 8.1(±0.2) × 10^{-6} K^{-1} and 9.7(±0.2) × 10^{-6} K^{-1}, respectively, were slightly higher than the dilatometric CTE of Ti_3GeC_2, 7.8 × 10^{-6} K^{-1}[38].

Studies on Ti_3SnC_2 are also scarce. It was first reported much more recently than the other 312 MAX phases in a study on thin films by Högberg *et al.* [60]. Bulk Ti_3SnC_2 was discovered coincidently by Dubois *et al.* in 2007 [61] during the synthesis of Ti_2SnC by introducing Fe from the steel container, starting with a Ti:Sn:C ratio of 2:1:1 at.% and applying a two-step heat treatment (1123 K for 1 h, then 1588 K for 4 h). The starting amount of Fe was not known at that point. In a following study by the same group, a more controlled amount of Fe was used, with a starting ratio of 3:1:0.6:2 at.% for Ti:Sn:Fe:C. After mixing, the powders were hot isostatically pressed at 1423 K for 10 h using pressure of 500MPa [62]. In another study, less Fe was used (Ti:Sn:Fe:C of 3:1:0.1:2 at.%) but the powders were heated to a higher temperature (1723 K for 2 h) [63]. In all those studies, iron intermetallics were observed in the resultant materials.

While the 312 phases are closely related structurally and exhibit similar properties, there are also a number of differences in their thermal and mechanical properties that are not fully understood. For example, the mechanical damping – or internal friction, Q^{-1}, determined over the 300 – 1573 K temperature range – of Ti_3GeC_2, Ti_3SiC_2, Ti_3AlC_2, and $Ti_3(SiAl)C_2$

was investigated by resonant ultrasound spectroscopy [52] (see Fig. 3.2). Up to a critical temperature, Q^{-1} was nearly constant, after which it increased dramatically. This critical temperature was ~1273 K for Ti_3SiC_2, Ti_3AlC_2, and $Ti_3(SiAl)C_2$, but only ~623 K for Ti_3GeC_2. Given the otherwise similar properties of Ti_3SiC_2 and Ti_3GeC_2, this was a surprising result. A number of possibilities for explaining this behavior, including increases in the mobility of dislocations and/or other defects such as vacancies in the *A* planes, as well as an order-disorder transition – most probably in the *A* planes – were postulated [52].

One of the aims of the HTND work on the four 312 phases (presented in Chapters 12, 13, and 15) is to shed some light on this unexpected mystery by investigating the changes in the crystal structure as a function of temperature.

3.2.3 413 phases: Ta_4AlC_3 and Ti_4AlN_3

Although some of the numerous 211 phases (there are over 50) and 312 phases have been extensively investigated and characterized, the 413 MAX phases are relatively new. Initially, it was believed that Ti_4AlN_3 was the only 413 MAX phase [64]. In 2004, several new 413 phases were discovered, beginning with the synthesis of Ti_4SiC_3 and Ti_4GeC_3 thin films [65, 66]. Since then, the phases Ta_4AlC_3 [67–71], V_4AlC_3 [72, 73], Nb_4AlC_3 [74], and Ti_4GaC_3 [75] have been synthesized in bulk form.

For most of the 413 phases, the M_I and M_{II} atoms occupy Wyckoff position $4f$ and $4e$, respectively, the *A* atoms occupy $2c$, and the X_I and X_{II} atoms are on the $2a$ and $4f$ positions, respectively (Table 3.1). Ta_4AlC_3 stands out as the only 413 MAX phase known today that exists as two different polymorphs [67, 76**?**]. The two polymorphs are referred to as α-Ta_4AlC_3, which has the same stacking sequence as all the other 413 MAX phases, and β-Ta_4AlC_3, in which the Ta_I shifts from Wyckoff position $4e$ to $4f$, and C_I shifts from $4f$ to $4e$ (Table 3.1). While it is

most likely that the polymorphism in Ta_4AlC_3 is thermodynamically driven, the reasons for the polymorphism and mechanism of any polymorphic phase transformation remain elusive. For more information on polymorphism in Ta_4AlC_3, refer to the paper in Appendix B.4.

The Raman spectrum of Ti_4AlN_3 has been previously reported [77]. However, the vibrational behavior associated with the Raman-active modes was not definitively identified. Also, as far as I am aware, before the work in this thesis, the Raman spectra had not been reported for Ta_4AlC_3. In Chapter 10 the Raman-active modes in both Ta_4AlC_3 and Ti_4AlN_3 from both theory and experiment are presented, along with the calculated Raman frequencies for Nb_4AlC_3 for the sake of exploring the dependence of the vibrational frequencies on reduced mass. The study of the Raman modes in this work provide the first analysis of the displacements associated with the Raman-active modes in the 413 phases, and shed light on the role of mass and chemistry in the vibrational character of these phases.

3.2.4 A 523 phase: $Ti_5Al_2C_3$

Another MAX phase that is studied in this thesis is a so-called "higher-order" MAX phase. Later, in Chapter 14, I will present important results on the temperature-dependent crystal structure of this phase that have to do with the role of octahedral stacking in bonding and atomic vibrations. Therefore, a more in-depth description of its stacking, bonding, and symmetry will be presented in that chapter. In addition, more detailed information on its stacking sequence and structure determination may be found in the two papers in Appendix B.2. This section serves as an introductory summary of background information on this phase.

The previous sections have summarized literature on select 211, 312, and 413 MAX phases that all have the general formula $M_{n+1}AX_n$. In addition to these "conventional" MAX phases, there is also a category of higher-order MAX phases, which have been observed in MAX phase

thin films in several studies. They were first reported in 2004 in the Ti–Si–C system (*i.e.* $Ti_5Si_2C_3$ and $Ti_7Si_2C_5$) by Palmquist *et al.* through transmission electron microscopy, TEM, micrographs and additional peaks in X-ray diffraction, XRD, patterns [66]. Ti_7SiC_2 has since been reported as a minority phase [78] and as epitaxial predominantly single-phase thin films [79]. To date, higher-order phases have been observed in thin films for a number of different MAX phase systems including $Ti_5Ge_2C_3$ and Ti_7GeC_2 [65], $(Ti,V)_5Ge_2C_3$ and $(Ti,V)_7Ge_2C_5$ [80], and $Ti_5Al_2C_3$ [81]. A review of the higher-order phases in thin films can be found in by Eklund *et. al.* [82].

Of interest to this thesis is the "523" phase $Ti_5Al_2C_3$. Outside of thin film growth, $Ti_5Al_2C_3$ was recently reported in bulk in two studies, where it was characterized using XRD studies [8, 83]. In our study [8], the characterized sample contained 43(±2) wt.% $Ti_5Al_2C_3$. In another study [83], only a small amount of $Ti_5Al_2C_3$ was observed and neither weight nor volume fractions were reported. We note in passing that the first structure proposed by Wang *et al.* in Ref. [83] is totally wrong and unsubstantiated by the results shown in that paper (see Ref. [9]). It is also crucial to note that our paper was submitted a few weeks before that of Ref. [83]. After our paper was published, the same group reproduced and confirmed our correct description of the structure, working with a composition that was only 19.7 wt% $Ti_5Al_2C_3$. They confirmed the structure through convergent beam electron diffraction, and they further added that the structure could also be described by another space group, $R\bar{3}m$, which is identical in atomic positions to our structure but has higher symmetry [84] (see Table 3.1).

For the 211 and 312 MAX phases in the Ti–Al–C system (and like all other conventional MAX phases), Ti–C layers (Ti_2C for Ti_2AlC and Ti_3C_2 for Ti_3AlC_2) are interleaved between layers of Al. The $Ti_5Al_2C_3$ phase, on the other hand, consists of alternating Ti_2C ("211-like") and Ti_3C_2 ("312-like") layers interleaved between Al layers. Due to the shift in stacking sequence, three formula

units need to be included in a unit cell. The lattice parameters are thus a=3.064(±0.002) Å and c=48.23(±0.02) Å (see B.2.1).

While we had previously used XRD and TEM to characterize the room temperature lattice parameters of $Ti_5Al_2C_3$ and verify its stoichiometry and stacking sequence, a complete structure refinement to determine bond lengths had not been performed until the work in this thesis. Furthermore, its TECs had not been measured previously. So far, neither our research group nor our colleagues have been able to synthesize phase-pure $Ti_5Al_2C_3$, and the highest composition that has been reported is 47%. This is an important phase that tends to evolve during high-temperature processing for reasons that are unclear and difficult to anticipate. Therefore, a comparison of its structure and properties – starting with its crystal structure – to the other MAX phases is important for determining the effects of this secondary phase on a MAX phase sample.

The work that will be presented in Chapter 14 thus serves as the first high-temperature study of this phase, and helps us understand its other MAX phase relatives and the role of stacking and symmetry in their high-temperature properties.

Chapter 4: Lattice dynamics

In the preceding chapters, elementary materials-related concepts have been summarized in brief. The materials of interest to this thesis – MAX phases – have been introduced and some of the previous work on these phases has been summarized. Now I will make a turn in a more theoretical direction to provide important background on lattice dynamics theory in order to introduce the scientific concepts behind the experimental and theoretical studies within this thesis.

So far, crystal structures have been discussed at a basic level, with the positions of atoms in a solid to be fixed at their positions. While materials in the solid state may be considered to be made up of a static arrangement of atoms as a first approximation, in reality atoms are not infinitely massive or held together by infinite forces; consequently they have a thermal energy that causes a certain amount of motion in the vicinity of their equilibrium positions. Since atoms in crystals experience thermal vibrations, it is important to consider dynamic effects in order to understand finite temperature behavior. This chapter outlines the basic concepts related to lattice dynamics, beginning with a few simple models. The theory behind phonon calculations and their dispersion curves is discussed, along with the equations relevant to computing temperature-dependent ADPs. Most of the information from this section can be found in various textbooks [13–15, 85–87]. For complete derivations and further reading on lattice dynamics, refer to those references.

4.1 CLASSICAL THEORY OF MOLECULAR VIBRATIONS

Before introducing examples of simple periodic systems and deriving their dynamical behavior, some basic concepts in classical harmonic theory will be introduced, including the equation of motion and solutions for the simple harmonic oscillator, the contribution of atomic displacements to the Hamiltonian, the harmonic approximation, and a definition of interatomic forces.

4.1.1 The simple harmonic oscillator

A good starting point for moving from static to dynamical systems is the harmonic oscillator, which provides a simple example of how to move from the classical to the quantum model and a good basis for understanding vibrating bodies. The simplest model that comes to mind is a body of mass M attached to a spring with elastic constant k, which is a one-dimensional harmonic oscillator with motion in the x direction. For this system, the classical Hamiltonian – which describes the total energy of a system in quantum mechanics – is:

$$\mathcal{H} = \mathcal{T} + \mathcal{V} = \frac{p^2}{2M} + \frac{M\omega^2 u^2}{2} \tag{4.1}$$

where $\mathcal{T}$ and $\mathcal{V}$ are the kinetic and potential energies, respectively, p is the momentum in the x direction, and $u = x - x_{\text{eq}}$ is the displacement of the oscillating body from its equilibrium position x_{eq}. The frequency of oscillations, ω, is

$$\omega = \sqrt{\frac{k}{M}}. \tag{4.2}$$

The Hamiltonian contains both the kinetic and potential energy. Here, the potential energy is the elastic energy stored in the deformed spring. Classically, the equation of motion can be

derived from the Hamiltonian:

$$\dot{x} = \frac{\partial \mathcal{H}}{\partial p} = \frac{p}{M} \quad \text{and} \quad \dot{p} = -\frac{\partial \mathcal{H}}{\partial p} = -M\omega^2 u \tag{4.3}$$

where p is momentum, and $\dot{p}$ and $\dot{x}$ are the derivatives of momentum and position, respectively, with respect to time. Taken together, the equations in Eq. 4.3 lead to

$$M\ddot{x} = -M\omega^2 u = -ku = F. \tag{4.4}$$

This is just Newton's second law, $F = ma$, where the force F is the elastic force. The solution to the differential equation, Eq. 4.4, has the general form:

$$\begin{aligned} u(t) &= a_1 \sin(\omega t) + a_2 \cos(\omega) t \\ &= b_1 e^{i\omega t} + b_2 e^{-i\omega t} \\ &= A\cos(\omega t + \phi). \end{aligned} \tag{4.5}$$

The equation forms above are equivalent, each depending on two unknown constants (a_1 and a_2, b_1 and b_2, or A and ϕ), which are found from initial conditions for x and p. This introduces the general form of an isolated harmonic oscillator. Now I will move onto oscillations for atoms that are part of a lattice, wherein the general form $u(t) = A\cos(\omega T + \phi)$ will be used.

4.1.2 Atomic displacements

To consider atoms as non-stationary bodies vibrating around their equilibrium positions, we may begin with a single atom at lattice site R, whose position is denoted by $\vec{r}(R)$. Its mean position is $\vec{R}$, which would be equal to $\vec{r}(R)$ if the ion was stationary in its lattice site. However, if it is

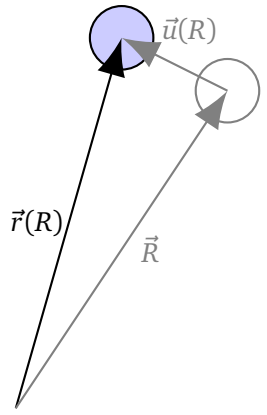

Figure 4.1: Model of the atomic displacement of atom site R with equilibrium position vector $\vec{R}$, displacement $\vec{u}(R)$, and displaced position vector $\vec{r}(R)$.

actually deviating from its average position, then its position at a given time is

$$\vec{r}(R) = \vec{R} + \vec{u}(R), \tag{4.6}$$

where $\vec{u}(R)$ is the deviation of this ion from its equilibrium position on lattice site R (Fig. 4.1.

Now, considering the potential energy of a crystal, $\mathcal{V}$, as the sum of the contribution from all distinct pairs on lattice sites R and R', $\mathcal{V}$ would be:

$$\mathcal{V} = \frac{1}{2}\sum_{RR'} \mathcal{U}(R - R') \tag{4.7}$$

where $\mathcal{U}(R - R')$ is the potential between R and R'. Taking into account the fact that the atoms are not necessarily found at their equilibrium positions [*i.e.*, $\vec{r}(R) \neq \vec{R}$], and the potential is a

function of their separation, then Eq.4.7 may be replaced by:

$$\begin{aligned}\mathcal{V} &= \frac{1}{2}\sum_{RR'} \mathcal{U}(\vec{r}(R) - \vec{r}(R')) \\ &= \frac{1}{2}\sum_{RR'} \mathcal{U}(\vec{R} - \vec{R}' + \vec{u}(R) - \vec{u}(R')).\end{aligned} \tag{4.8}$$

The potential energy therefore depends on the dynamical variables $\vec{u}(R)$. This shows how the dynamical problem is governed by the Hamiltonian:

$$\begin{aligned}\mathcal{H} &= \mathcal{T} + \mathcal{V} \\ &= \sum_{R} \frac{p(R)}{2M} + \frac{1}{2}\sum_{RR'} \mathcal{U}(\vec{R} - \vec{R}' + \vec{u}(R) - \vec{u}(R'))\end{aligned} \tag{4.9}$$

where $\mathcal{T}$ is the kinetic energy term, $p(R)$ is the momentum of the ion at equilibrium position R, and M is the atomic mass.

4.1.3 The harmonic approximation

Pair potentials often have forms that make it hopelessly difficult to extract an exact solution. It is therefore necessary to resort to an approximation that relies on the fact that the atoms do not deviate substantially from their equilibrium positions. If $|\vec{u}(R) - \vec{u}(R')| \ll |\vec{R} - \vec{R}'|$, then $\mathcal{U}(\vec{R} - \vec{R}' + \vec{u}(R) - \vec{u}(R'))$ can be expanded about its equilibrium position using Taylor's theorem:

$$\begin{aligned}f(x+a) &= \sum_{n=0}^{\infty} \frac{f^{(n)}(x)}{n!} a^n \\ &= f(x) + f'(x)a + \frac{f''(x)}{2!}a^2 + \frac{f'''(x)}{3!}a^3 \cdots\end{aligned} \tag{4.10}$$

Applying this to $\mathcal{U}(\vec{R}-\vec{R}'+\vec{u}(R)-\vec{u}(R'))$ in Eq. 4.8, taking x as $\vec{R}-\vec{R}'$ and a as $\vec{u}(R)-\vec{u}(R')$ gives

$$\begin{aligned}\mathcal{U}(\vec{R}-\vec{R}'+\vec{u}(R)-\vec{u}(R')) = \mathcal{U}(\vec{R}-\vec{R}') + \mathcal{U}'(\vec{R}-\vec{R}')\cdot(\vec{u}(R)-\vec{u}(R')) \\ + \frac{1}{2}\mathcal{U}''(\vec{R}-\vec{R}')\cdot(\vec{u}(R)-\vec{u}(R'))^2 + O(\vec{u}^3)\end{aligned} \tag{4.11}$$

and, neglecting higher-order ($n > 3$) terms, Eq. 4.8 becomes:

$$\begin{aligned}\mathcal{V} = &\frac{1}{2}\sum_{RR'}\mathcal{U}(\vec{R}-\vec{R}') + \frac{1}{2}\sum_{RR'}\mathcal{U}'(\vec{R}-\vec{R}')\cdot(\vec{u}(R)-\vec{u}(R')) \\ &+ \frac{1}{4}\sum_{RR'}\mathcal{U}''(\vec{R}-\vec{R}')\cdot(\vec{u}(R)-\vec{u}(R'))^2.\end{aligned} \tag{4.12}$$

The coefficient of the linear term, $\vec{u}(R)$, is $\mathcal{U}'(\vec{R}-\vec{R}')$, which equals zero because the potential energy is a minimum when particles are at their equilibrium positions. This also implies that there is no net force on any atom at equilibrium. Since the linear term vanishes, and the potential energy of the equilibrium configuration is

$$\mathcal{V}_0 = \frac{1}{2}\sum_{RR'}\mathcal{U}(\vec{R}-\vec{R}'), \tag{4.13}$$

then the nonvanishing correction to the equilibrium potential energy is given by the quadratic term. In the so-called **harmonic approximation**, the potential energy is:

$$\begin{aligned}\mathcal{V} &= \mathcal{V}_0 + \frac{1}{4}\sum_{RR'}\sum_{\alpha,\beta=x,y,z}[u_\alpha(R)-u_\alpha(R')]\cdot\Phi_{\alpha\beta}(R,R')\cdot[u_\beta(R)-u_\beta(R')] \\ &= \mathcal{V}_0 + \mathcal{V}_{\text{harm}}\end{aligned} \tag{4.14}$$

where u now has a scalar form since α and β are now introduced as the Cartesian components –

that is, the x, y, or z direction – and the $\Phi_{\alpha\beta}(R,R')$ components are second-order tensors,

$$\Phi_{\alpha\beta}(R,R') = \frac{\partial^2 \mathcal{U}(R-R')}{\partial u_\alpha(R)\partial u_\beta(R')}, \tag{4.15}$$

which are the second derivatives of the energy with respect to displacements of atoms from their equilibrium positions. The harmonic part of $\mathcal{V}$, $\mathcal{V}_{\text{harm}}$, is the starting point for essentially all lattice dynamics studies. The higher-order corrections to $\mathcal{V}$ are known as anharmonic terms and can play a major role in understanding many physical phenomena outside of the harmonic approximation. Most of the work in this thesis is in the harmonic approximation, but anharmonic effects will be discussed in Chapter 15.

4.1.4 Interatomic forces

As we can see from Eq. 4.15, the interactions between particles are related to the forces on atoms with atomic displacements. Assuming the validity of the harmonic approximation above, the forces are linear functions of the displacements and do not involve higher-order terms (second, third, or above). The force on an atom R due to the displacement of another atom R' may be represented by

$$F_\alpha(R) = -\Phi_{\alpha\beta}(R,R')u_\beta(R'), \tag{4.16}$$

which represents the concept that a force exerted on atom R in some direction is proportional to the displacement of atom R' in some other direction. Equation 4.16 represents a set of three

linear equations, and the quantity $\mathbf{\Phi}(R,R')$ is a 3×3 matrix:

$$\mathbf{\Phi}(R,R') = \begin{pmatrix} \Phi_{11} & \Phi_{12} & \Phi_{13} \\ \Phi_{21} & \Phi_{22} & \Phi_{23} \\ \Phi_{31} & \Phi_{32} & \Phi_{33} \end{pmatrix}. \tag{4.17}$$

This is known as the **force constant matrix**, where the $\Phi_{\alpha\beta}$ terms represent α and β combinations for $\Phi_{\alpha\beta}(R,R')$ (see Eq. 4.15). The $\alpha\beta$ subscripts refer to axis directions – for instance, $\Phi_{12}(R,R')$ is the negative of the force on atom R in the x ("1") direction when atom R' is displaced in the y ("2") direction.

4.2 THE DISPERSION RELATION IN PERIODIC SYSTEMS

Having introduced some concepts associated with atomic displacements, interatomic forces, and their contributions to the Hamiltonian, the next section applies these ideas to periodic systems. Section 4.2.1 uses an example of a linear chain of particles, which is simpler than a three-dimensional system and instructive for obtaining a physical understanding while avoiding many mathematical complexities. A three-dimensional lattice is considered in Sections 4.2.2 and 4.2.3, where it will be apparent that the vibrational properties of three-dimensional crystals are also possessed – at least qualitatively – by a one-dimensional chain.

4.2.1 Lattice vibrations in a monoatomic one-dimensional chain

To consider periodic systems, let us begin with a chain of identical particles with mass M, equally spaced a distance a apart and held together by elastic forces (Fig. 4.2). Taking two particles – the n^{th} and $(n+m)^{\text{th}}$ particles – and assuming that the forces obey Hooke's law, then the energy between them would simply be a function of their separation, $\mathcal{U}(r) = \mathcal{U}(|x_{n+m} - x_n|)$, where x is a scalar that represents the particle's position along the chain. Since $u \ll a$ – *i.e.* the atomic

displacements are much smaller than the distances between the atoms – then $\mathcal{U}(x_{n+m} - x_n)$ can be expanded in a Taylor series about the point $x = ma$ (Eq. 4.10). Again neglecting terms of higher order than 2 (the harmonic approximation), and given that the coefficient of the linear term is zero, the expression for potential energy is

$$\mathcal{V} = \mathcal{V}_0 + \frac{1}{2}\sum_n \sum_{m>0} (u_{n+m} - u_n)^2 \mathcal{U}''(ma), \tag{4.18}$$

where

$$\mathcal{V}_0 = \sum_n \sum_{m>0} \mathcal{U}(ma). \tag{4.19}$$

This takes into account all pairs, without counting any twice (*i.e.* $m > 0$ only). Assuming only nearest-neighbor interaction (that is, $m = 1$ in Eq. 4.18), the expression for the potential energy becomes:

$$\mathcal{V} = \mathcal{V}_0 + \frac{1}{2}\Phi \sum_n (u_{n+1} - u_n)^2. \tag{4.20}$$

Now, $\mathcal{V}_0 = N \cdot \mathcal{U}(a)$ (where N is the number of atoms and $\mathcal{U}(a)$ is the potential energy for one near-neighbor bond), and Φ is the second derivative of $\mathcal{U}$, or the force constant (see Eq. 4.15), evaluated at interatomic distance a.

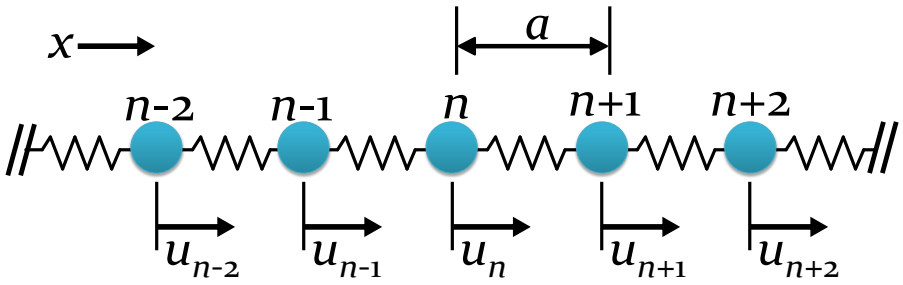

Figure 4.2: A linear chain consisting of identical particles equally spaced a distance a apart and held together by elastic forces. The interactions are represented as springs, and displacements are represented by u.

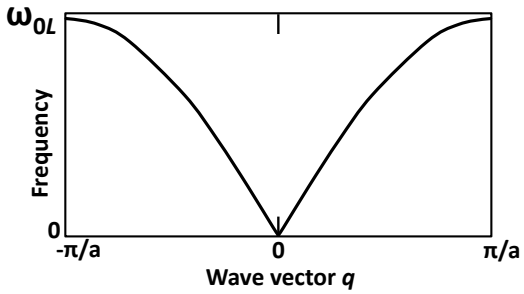

Figure 4.3: Dependence of frequency on the wave vector for longitudinal vibrations in a one-dimensional chain.

The equation of motion (see Eq. 4.4) for a particle n can be written as:

$$M\frac{d^2u_n}{dt^2} = \mathcal{U}''(a)[u_{n+1} - 2u_n + u_{n-1}] \tag{4.21}$$

To solve this equation of motion, we assume the atomic displacement has the general form:

$$u = A_L \exp[-i(\omega t - qna)] \tag{4.22}$$

where A_L is the amplitude of the longitudinal wave. Substituting this into Eq. 4.21, the solution is

$$\omega = \sqrt{\frac{4\mathcal{U}''(a)}{M}}\left|\sin\frac{qa}{2}\right| = \omega_{0L}\left|\sin\frac{qa}{2}\right|, \tag{4.23}$$

where

$$\omega_{0L} = \sqrt{\frac{4\mathcal{U}''(a)}{M}}. \tag{4.24}$$

This gives the angular frequency ω as a function of wave vector q, which is known as the **dispersion relation** for this simple case (Fig. 4.3).

4.2.2 Lattice vibrations in a simple Bravais lattice

In this section, I will discuss the motion of particles in a three-dimensional simple Bravais lattice, which is a simple case of a periodic system where atoms sit on the corners of a unit cell and repeat throughout a material.

Equations of motion

Let the primitive vectors of the lattice be $\vec{a}_1$, $\vec{a}_2$, and $\vec{a}_3$. If the three-dimensional lattice is perfect and infinite, any atom can be chosen as a reference and, choosing an arbitrary atom as a reference, the equilibrium position of any other atom is:

$$r(R) = R_1\vec{a}_1 + R_2\vec{a}_2 + R_3\vec{a}_3 \tag{4.25}$$

where R_1, R_2, and R_3 are integers representing the position of that atom, and may be referred to as R. As the atoms exhibit small oscillations about their lattice sites, the instantaneous displacement of the R^{th} atom from its equilibrium position is denoted by $\vec{u}(R)$. Its components are $u_\alpha(R)$ where α is 1, 2, or 3, which correspond to the x-, y-, and z-directions. The kinetic energy of an atom with mass M is given by

$$\frac{1}{2}M(\dot{u_1}^2 + \dot{u_2}^2 + \dot{u_3}^2) = \frac{1}{2}M\sum_\alpha \dot{u}_\alpha^2(R). \tag{4.26}$$

The kinetic energy, $\mathcal{T}$, of the lattice is thus

$$\mathcal{T} = \frac{1}{2}M\sum_R\sum_\alpha \dot{u}_\alpha^2(R). \tag{4.27}$$

For the potential energy of the lattice, the harmonic approximation can be applied through a Taylor expansion of $\mathcal{V}$ in powers of the atomic displacement and neglecting terms of orders

higher than 2. The expression for $\mathcal{V}$ simplifies to:

$$\mathcal{V} = \mathcal{V}_0 + \sum_{\substack{R,\alpha \\ R',\beta}} \mathcal{U}_{\alpha\beta}(RR')u_\alpha(R)u_\beta(R') \tag{4.28}$$

where $\mathcal{V}_0$ is the potential of the equilibrium configuration of atoms.

In this approximation, the Hamiltonian $\mathcal{H}$ of the system can be written as:

$$\mathcal{H} = \mathcal{T} + \mathcal{V} = \frac{1}{2}M\sum_{R,\alpha} p_\alpha^2(R) + \frac{1}{2}\sum_{\substack{R,\alpha \\ R',\beta}} \mathcal{U}_{\alpha\beta}(RR')u_\alpha(R)u_\beta(R') \tag{4.29}$$

where

$$p_\alpha(R) = M\dot{u}_\alpha(R). \tag{4.30}$$

From the equation of motion, you can obtain

$$M\ddot{u}_\alpha(R) = \sum_{R'} F_\alpha(R'), \tag{4.31}$$

where

$$F_\alpha(R') = -\sum_{\beta=1,2,3} \mathcal{U}''_{\alpha\beta}(RR')u_{\alpha\beta}(R'), \tag{4.32}$$

which means that, for example, $F_1(R')$ is the x component of force acting on the R^{th} atom arising from the displacement of atom R' atom, summed along β, the displacement directions for atom R'. Note that the reference to the R^{th} atom is implied.

Since the restoring force between two atoms will depend only on their relative separation rather than their absolute positions, then we can write

$$\mathcal{U}_{\alpha\beta}(RR') = \mathcal{U}_{\alpha\beta}(R-R') = \mathcal{U}_{\alpha\beta}(R'R). \tag{4.33}$$

Because of periodicity, the general form of the displacements can be written as:

$$u_\alpha(R) = A_\alpha \exp[-i(\omega t - q \cdot r(R))] \tag{4.34}$$

where A_α is the amplitude of the wave, independent of R. This is the same form as for the one-dimensional chain, Eq. 4.22.

Substituting this into equation 4.31 then we get

$$\omega^2 A_\alpha = \sum_{\beta=1,2,3} \boldsymbol{D}_{\alpha\beta}(q) A_\beta \tag{4.35}$$

where $\boldsymbol{D}_{\alpha\beta}(q)$ is the **dynamical matrix**:

$$\boldsymbol{D}_{\alpha\beta}(q) = \frac{1}{m} \sum_{R'} \mathcal{U}''_{\alpha\beta}(R - R') e^{-iq\cdot[r(R')-r(R)]}. \tag{4.36}$$

Since this is summed over all values of R', D should be independent of R and can therefore be rewritten as (for a perfect periodic crystal):

$$\boldsymbol{D}_{\alpha\beta}(q) = \frac{1}{m} \sum_{R'} \mathcal{U}''_{\alpha\beta}(R') e^{-iq\cdot r(R')}. \tag{4.37}$$

Because of the periodicity of the system, the problem has been drastically simplified from a set of differential equations (Eq. 4.31) to a set of three linear homogeneous equations with three unknowns (Eq. 4.35).

Solving the equations of motion

Equation 4.35 can be re-arranged and re-written as:

$$\sum_{\beta=1,2,3} [\boldsymbol{D}_{\alpha\beta}(q) - \omega^2 \delta_{\alpha\beta}] A_\beta = 0 \tag{4.38}$$

where $\delta_{\alpha\beta}$ is the Kronecker delta function (zero if $\alpha \neq \beta$; and equal to 1 if $\alpha = \beta$).

For nontrivial solutions, the determinant of the coefficients must vanish and thus

$$\left| \boldsymbol{D}_{\alpha\beta}(q) - \omega^2 \delta_{\alpha\beta} \right| = 0. \tag{4.39}$$

For the case of a primitive Bravais lattice with one atom per unit cell, this is a 3×3 determinant. When expanded, it gives a cubic equation in ω^2 with three solutions – corresponding to three acoustical branches – for a given value of q. This can be reduced to an eigenvalue problem where the eigenfunction corresponding to the eigenvalue $\omega_p^2(q)$ (where p is the vibrational branch, or "band" index [*]), is denoted by $\mathbf{e}_p(q)$ and is defined by:

$$\boldsymbol{D}(q)\mathbf{e}_p(q) = \omega_p^2(q)\mathbf{e}_p(q) \tag{4.40}$$

where $\boldsymbol{D}(q)$ is a 3×3 matrix of $D_{\alpha\beta}$ (Eq. 4.37):

$$\boldsymbol{D}(q) = \begin{pmatrix} D_{xx} & D_{xy} & D_{xz} \\ D_{yx} & D_{yy} & D_{yz} \\ D_{zx} & D_{zy} & D_{zz} \end{pmatrix} \tag{4.41}$$

[*] for the simple Bravais lattice with three solutions, $p = 1, 2$, or 3.

4.2.3 *Lattice vibrations in a lattice with a basis: generalized solutions*

The previous section was for a system with just one atom per unit cell. For a lattice with a basis, and more than one atom per unit cell, the potential energy is no longer a function of only the distance between atoms. The Hamiltonian now includes a summation over (RR') interactions:

$$\mathcal{H} = \mathcal{T} + \frac{1}{2}\sum_{RR'}\sum \alpha,\beta\,\Phi_{\alpha\beta}(RR')\mathcal{U}_{\alpha}(R)\mathcal{U}_{\beta}(R'). \tag{4.42}$$

Here we generalize the methodology in the examples of the linear chain and the simple Bravais lattice for lattices with more than one atom per unit cell.

The dynamical matrix

For the dynamical Hamiltonian of a lattice with a basis (Eq. 4.42), the eigenvalue problem is now:

$$D_{\alpha\beta}(q) = \frac{1}{N\sqrt{M_R M_{R'}}}\sum_{RR'}\Phi_{\alpha\beta}(R,R')e^{iq[r(R)-r(R')]} \tag{4.43}$$

where $\Phi_{\alpha\beta}(R,R')$ is the force constant matrix (Eq. 4.15), N is the number of atoms, M_R and $\mathrm{M}_{R'}$ are the masses of atoms R and R', respectively, and $r(R)-r(R')$ is their separation. In this case, $D_{\alpha\beta}(q)$ also includes (RR') atom pairs, so the 3×3 dynamical matrix of Eq. 4.41 is now a $3N\times 3N$ matrix. For two atoms per unit cell, for example:

$$\boldsymbol{D}(q) = \begin{pmatrix} D_{xx}(11) & D_{xy}(11) & D_{xz}(11) & D_{xx}(12) & D_{xy}(12) & D_{xz}(12) \\ D_{yx}(11) & D_{yy}(11) & D_{yz}(11) & D_{yx}(12) & D_{yy}(12) & D_{yz}(12) \\ D_{zx}(11) & D_{zy}(11) & D_{zz}(11) & D_{zx}(12) & D_{zy}(12) & D_{zz}(12) \\ D_{xx}(21) & D_{xy}(21) & D_{xz}(21) & D_{xx}(22) & D_{xy}(22) & D_{xz}(22) \\ D_{yx}(21) & D_{yy}(21) & D_{yz}(21) & D_{yx}(22) & D_{yy}(22) & D_{yz}(22) \\ D_{zx}(21) & D_{zy}(21) & D_{zz}(21) & D_{zx}(22) & D_{zy}(22) & D_{zz}(22) \end{pmatrix} \tag{4.44}$$

and for a more general case where R and R' go from atom indices $1 \ldots N$:

$$\boldsymbol{D}(q) = \begin{pmatrix} D_{xx}(11) & D_{xy}(11) & D_{xz}(11) & D_{xx}(12) & D_{xy}(12) & D_{xz}(12) & \cdots & D_{xx}(1N) & D_{xy}(1N) & D_{xz}(1N) \\ D_{yx}(11) & D_{yy}(11) & D_{yz}(11) & D_{yx}(12) & D_{yy}(12) & D_{yz}(12) & \cdots & D_{yx}(1N) & D_{yy}(1N) & D_{yz}(1N) \\ D_{zx}(11) & D_{zy}(11) & D_{zz}(11) & D_{zx}(12) & D_{zy}(12) & D_{zz}(12) & \cdots & D_{zx}(1N) & D_{zy}(1N) & D_{zz}(1N) \\ \\ D_{xx}(21) & D_{xy}(21) & D_{xz}(21) & D_{xx}(22) & D_{xy}(22) & D_{xz}(22) & \cdots & D_{xx}(2N) & D_{xy}(2N) & D_{xz}(2N) \\ D_{yx}(21) & D_{yy}(21) & D_{yz}(21) & D_{yx}(22) & D_{yy}(22) & D_{yz}(22) & \cdots & D_{yx}(2N) & D_{yy}(2N) & D_{yz}(2N) \\ D_{zx}(21) & D_{zy}(21) & D_{zz}(21) & D_{zx}(22) & D_{zy}(22) & D_{zz}(22) & \cdots & D_{zx}(2N) & D_{zy}(2N) & D_{zz}(2N) \\ \vdots & \vdots & \vdots & \vdots & \vdots & \vdots & \ddots & \vdots & \vdots & \vdots \\ D_{xx}(N1) & D_{xy}(N1) & D_{xz}(N1) & D_{xx}(N2) & D_{xy}(N2) & D_{xz}(N2) & \cdots & D_{xx}(NN) & D_{xy}(NN) & D_{xz}(NN) \\ D_{yx}(N1) & D_{yy}(N1) & D_{yz}(N1) & D_{yx}(N2) & D_{yy}(N2) & D_{yz}(N2) & \cdots & D_{yx}(NN) & D_{yy}(NN) & D_{yz}(NN) \\ D_{zx}(N1) & D_{zy}(N1) & D_{zz}(N1) & D_{zx}(N2) & D_{zy}(N2) & D_{zz}(N2) & \cdots & D_{zx}(NN) & D_{zy}(NN) & D_{zz}(NN) \end{pmatrix} \tag{4.45}$$

Eigenvectors of the dynamical matrix

The eigenvector problem of Eq. 4.40 can be solved numerically by diagonalization of the dynamical matrix. The solution will give $\omega_p(q)$, the dispersion relations for each band p, and the eigenvectors, $\mathbf{e}_p(q)$, which are normalized such that

$$\sum_R |\mathrm{e}_p(R)|^2 = 1, \tag{4.46}$$

where $R = 1 \ldots N$. These contain the information about the relative displacements of the atoms due to wave q, which come into the equations for the mean-squared displacement in subsequent sections.

4.3 THE QUANTIZATION OF LATTICE VIBRATIONS

By now it is apparent that in real materials, where an atomic configuration repeats throughout the material, atoms cannot be considered as individual harmonic oscillators because vibrations in crystals depend on the arrangement of atoms in a periodic lattice and the forces between them that govern their interactions. In this section, the ideas introduced in the preceding sections

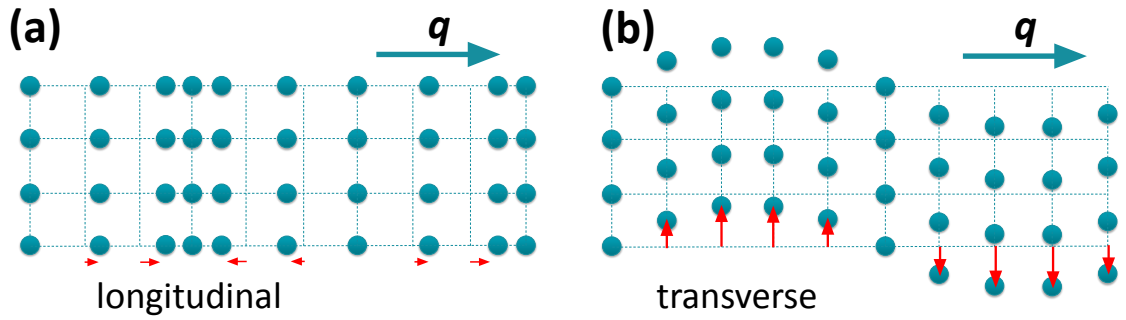

Figure 4.4: Schematics of atomic displacements (red arrows) caused (a) a longitudinal wave and (b) a transverse wave (b) with wave vector q propagating through a simple Bravais lattice.

of this chapter are brought together to discuss topics related to quantum theory of atomic vibrations in crystals, including the quantization of normal modes, phonon density of states, and mean-squared atomic displacements.

4.3.1 Collective oscillations: phonons

An important concept is the idea of vibrational modes where each part of a lattice oscillates with the same frequency. In classical mechanics, these special types of vibrational modes are called "normal modes" and in quantum mechanics, they are quantized as "phonons." These normal modes are of great importance in lattice dynamics because any arbitrary vibrational motion in a lattice can be represented as a superposition of normal modes with various frequencies. In essence, phonons are the elementary quanta in lattice vibrations.

In sections 4.1 and 4.2, the dynamical theory of crystals and methodology for computing the frequency dispersion of a wave by solving the equations of motion were presented. It has been shown that a wave passing through a periodic arrangement of atoms leads to the atoms being displaced from their equilibrium positions. Figure 4.4 illustrates the atomic displacements in a simple Bravais lattice induced by the propagation of a longitudinal wave, where the displacements are parallel to q, and a transverse wave, where the displacements are

perpendicular to q. The three solutions to the equations of motion give three phonon modes for a wave vector q: one longitudinal [Fig. 4.4(a)] and two transverse – an "up-and-down" mode [Fig. 4.4(b)] and a "side-to-side" wave. Note that this is a system where all the atoms are identical and periodically spaced throughout the material, so for a given wave vector, the time-averaged displacement of each atom is equal. This is not the case for a lattice containing N unique atoms per unit cell, where the atoms differ in potential and mass and will have different dynamical properties, resulting in $3N$ bands.

4.3.2 Phonon density of states

Another useful way to represent the lattice dynamics of a crystal is through a frequency distribution of the number of phonon vibrations, which is known as the phonon **density of states** (DOS), $g(\omega)$. The total and partial (only including specific atom sites) DOS are computed numerically by choosing a q sampling mesh and solving the eigenvalue problem (Eq. 4.40). Instead of computing $\omega_p(q)$ along a q-point path, the phonon properties are computed for q-points in the reciprocal space mesh. The density of states is a way of organizing all the frequencies for the vibrational states and counting the number of vibrational states around ω. The phonon density of states is then determined numerically with a form of $g(\omega) = \sum_q \delta(\omega - \omega(q))$, where δ is some delta function or an effective algorithm that selects the states near ω.

4.3.3 Atomic displacements

In lattice dynamics, the eigenvectors of the dynamical matrix give the relative displacements of the atoms in a crystal. The Cartesian components of the overall displacement of an atom can be derived from the phonon dispersion using these eigenvectors. An eigenvector $\vec{\mathbf{e}}_p(q)$ represents the relative displacement for a specific vibrational mode, or band p, due to a given wave with wave vector q. The eigenvectors are normalized and they do not take into account

temperature, at least when working within the harmonic approximation. Of course, one would expect the displacement amplitude to depend on temperature. This is where the normal mode coordinate, $Q_p(q)$, comes in, which subsumes the time and temperature dependence of a wave. Furthermore, the mass of the atoms must also be accounted for in the atomic displacement equation. Therefore, for atom site R in the unit cell l, the displacement caused by wave vector q for normal mode p is a function of the eigenvectors that give the relative displacement, the normal mode coordinate that accounts for temperature, the number of atoms N and the mass of the atom M_R:

$$\vec{u}(Rl) = \frac{1}{\sqrt{NM_R}} \vec{\mathbf{e}}_{R,p}(q) \exp\left[iq \cdot r(Rl)\right] Q(q,p). \tag{4.47}$$

Summing the contribution of all normal modes and taking a Cartesian component, α, the total displacement in a direction α (which can be x,y,or z) is expressed as:

$$u_\alpha(Rl) = \frac{1}{\sqrt{NM_R}} \sum_{q,p} \mathbf{e}_{\alpha,R,p}(q) \exp\left[iq \cdot r(Rl)\right] Q(q,p). \tag{4.48}$$

From this, the velocity is $\dot{u}(Rl)$ and the kinetic energy of the crystal can be calculated by summing $\frac{1}{2}M_R|\dot{u}(Rl)|^2$ for all atoms Rl. After simplifying, the kinetic energy of the crystal becomes:

$$\frac{1}{2}\sum_{R,l} M_R|\dot{u}(Rl)|^2 = \frac{1}{2}\sum_{q,p} \omega_p^2(q)|Q_p(q)|^2. \tag{4.49}$$

Knowing that, for a harmonic oscillation, the average vibrational potential energy is equal to the average kinetic energy, the total energy is obtained by multiplying the above by a factor of two. Further, this equation can be solved by setting it equal to the total energy obtained based on the ground state energy of harmonic vibrations, which is $E_0 = \frac{1}{2}\hbar\omega$. This energy can be changed by integral units of the phonon energy, $\hbar\omega$, such that the mean energy of each vibrational mode

becomes

$$E = \hbar\omega \left[\frac{1}{2} + n(\omega, T)\right], \tag{4.50}$$

where $n(\omega, T)$ is the phonon distribution (see below, Eq. 4.56).

Summing this over p and q and setting this total energy of the crystal equal to the righthand side of Eq. 4.49 multiplied by two gives

$$\frac{\hbar}{2}\sum_{q,p}\omega_p(q)\left[1 + 2n(\omega, T)\right] = \sum_{q,p}\omega_p^2(q)|Q_p(q)|^2 \tag{4.51}$$

and, solving for $|Q_p(q)|$ we get:

$$|Q_p(q)| = \sqrt{\frac{\hbar}{2}}\sum_{q,p}[\omega_p(q)]^{-1/2}\left[1 + 2n(\omega, T)\right]^{1/2}. \tag{4.52}$$

Plugging this back into equation 4.48, $u_\alpha(Rl)$ is

$$u_\alpha(Rl) = \sqrt{\frac{\hbar}{2NM_R}}\sum_{q,p}\mathbf{e}_{\alpha,R,p}(q)[\omega_p(q)]^{-1/2}\exp[iq\cdot r(Rl)]\left[1 + 2n(\omega, T)\right]^{1/2} \tag{4.53}$$

To handle the exponential portion of this equation, it can be written in terms of creation and annihilation operators, $a_p^\dagger(q)$ and $a_p(q)$ with thermodynamic properties

$$u_\alpha(Rl) = \frac{\hbar}{2NM_R}\sum_{q,p}[\omega_p(q)]^{-1/2}[a_p(q)\exp(-i\omega_p(q)t + a_p^\dagger(-q)\exp(i\omega_p(q)t]\exp(iq\cdot r(Rl))\mathbf{e}_{\alpha,p,R}(q) \tag{4.54}$$

and the mean-squared atomic displacement is calculated as an "expectation value" (essentially, the weighted average) of $u_\alpha(Rl)\cdot u_\alpha(Rl)$ by making use of creation and annihilation operators (see Ref. [87]). Using the commutation relation of creation and annihilation operators and expectation values of combinations of operations (e.g: $[a_p(q), a_{p'}^\dagger(q')] = \delta(q - q')\delta_{pp'}$,

$[a_p(q), a_{p'}(q')] = 0$), the mean-squared displacement is:

$$\langle u_\alpha(Rl) \cdot u_\alpha(Rl) \rangle = \langle |u_\alpha(R)|^2 \rangle = \frac{\hbar}{2NM_R} \sum_{q,p} \omega_p(q)^{-1}(1 + 2n_p(q,T))|\mathbf{e}_{\alpha,R,p}(q)|^2. \tag{4.55}$$

Here, the mean squared displacement is a function of the phonon dispersion $\omega_p(q)$ and eigenvectors $\mathbf{e}_p(q)$. The temperature dependence factors in through $n(\omega, T)$, the phonon distribution, which is given by the Bose-Einstein relation as:

$$n(\omega, T) = \frac{1}{\exp(\hbar\omega/k_B T) - 1}. \tag{4.56}$$

Here we can see that the temperature dependence of the average displacements of atoms from their equilibrium positions can be estimated by summing all the contributions from wave vectors and normal modes. This will be useful for comparison to experimental values from diffraction techniques.

4.4 ANHARMONIC EFFECTS

While the average displacements are described quite well in many cases from the phonon spectrum within the harmonic approximation, there are limitations that cannot be overcome without taking into account anharmonic effects. Another model called the **quasi-harmonic approximation** allows phonon frequencies to be volume dependent, which includes some anharmonic effects. This model is the same as the harmonic approximation, but taking the volume into account [88]. This model provides a relatively simple method to calculate the thermal expansion, which is a phenomenon that caused by the anharmonicity of the atomic potential.

The **mode-dependent Grüneisen parameters** can also be evaluated from first-principles

phonon calculations at three different volumes to explore anharmonic contributions. For each phonon (wave vector q and band p), the Grüneisen parameter, γ, which expresses the volume dependence of the mode frequency, is calculated using the following approximation:

$$\begin{aligned} \gamma_p(q) &= -\frac{V}{\omega_p(q)}\frac{d\omega(q)}{dV} \\ &\simeq -\frac{V}{2(\omega_p(q))^2}\left\langle e_p(q)\left|\frac{\Delta D(q)}{\Delta V}\right|e_p(q)\right\rangle, \end{aligned} \tag{4.57}$$

where V is the periodic cell volume and $\omega_p(q)$ is the phonon frequency of the mode.

4.5 CALCULATING PHONON DISPERSIONS

It has been shown that the properties of phonons can be described in the harmonic approximation based on one fundamental quantity, the force constant matrix (Eq. 4.15), which relates the displacement of an atom to the force on another. Once the force constant matrix is determined, evaluating the eigenvalues and eigenvectors of the dynamical matrix is relatively straightforward and can be done numerically.

Since the physical meaning of the force constant matrix is the relation of the displacement of an atom with the force on another atom, computing the phonon properties of a material requires access to forces. One useful tool for calculating forces is first-principles calculations based on density functional theory, which require no experimental parameters in the numeric model and provide a reasonable description of bonding interactions for uncorrelated electron systems. Some relevant background, theory, and details of these calculations will be provided next in Chapter 5.

Chapter 5: First-principles calculations based on density functional theory

Various computational methods are available for materials modeling. One important tool is the use of calculations based on first principles, which are especially useful for materials in the solid state and phenomena that are controlled by properties of materials on the atomic length scale. These calculations are known as "first-principles," or "*ab initio*", calculations, which refer to the fact that they are derived from the first principles of quantum mechanics, with no experimental parameters used in the numerical model. While the central equations of quantum mechanics are virtually impossible to solve explicitly, approximations and reformulations can be used to obtain a result that converges to the solution of the Schrödinger equation. One important first-principles method for quantum mechanical modeling that uses functionals of the electron density is known as density functional thoery (DFT).

As outlined in Chapter 4, theoretical investigation of the dynamical properties of crystals requires calculations of the atomic forces. First-principles calculations provide a powerful and versatile means of accessing forces in an atomic configuration for a wide range of materials. All the phonon calculations in this thesis rely on DFT calculations to determine the force constant matrix, from which the phonon dispersion, phonon density of states, mean-squared atomic displacements, Raman frequencies, and thermal expansions can be calculated. In addition, DFT calculations have been used in this body of work* to predict ground state crystal structures, elastic constants, relative polymorph stability, electronic density of states, dislocation boundary energies, and magnetic ordering in two-dimensional materials. This chapter will summarize relevant concepts behind these calculations.

*Some of this work is out the scope of this thesis and is presented in the appendix.

5.1 BASIC QUANTUM MECHANICS

The field of quantum mechanics makes it possible to describe a physical system at the atomic level based only on its electronic structure and atomic arrangement, without the need to input any empirical parameters. Here we walk through important topics in quantum mechanics to set the stage for what equations must be solved to describe materials.

5.1.1 Schrödinger's equation

The central equation of quantum mechanics is that of Erwin Schrödinger [89], who came up with his famous equation in 1926:

$$\hat{\mathcal{H}}\Psi = \hat{E}\Psi, \tag{5.1}$$

where $\hat{\mathcal{H}}$ is the Hamiltonian, Ψ is the wave function, and $\hat{E}$ is the energy. For a system with N electrons (positions denoted by r) and M nuclei (positions R), the (time-independent) wavefunction Ψ depends on the positions of all the interacting bodies:

$$\Psi = \Psi(r_1, r_2, r_3, \ldots, r_N, R_1, R_2, R_3, \ldots, R_M) \tag{5.2}$$

The Hamiltonian, $\hat{\mathcal{H}}$, is the sum of the kinetic and potential energy operators, $\hat{\mathcal{T}}$ and $\hat{\mathcal{V}}$, respectively:

$$\hat{\mathcal{H}} = \hat{\mathcal{T}}_{\text{nuc}} + \hat{\mathcal{T}}_e + \hat{\mathcal{V}}_{\text{nuc}} + \hat{\mathcal{V}}_{ee} + \hat{\mathcal{V}}_{\text{ext}}. \tag{5.3}$$

$\mathcal{T}_{\text{nuc}}$ and $\hat{\mathcal{T}}_e$ are the kinetic energy operators of the nuclei (k) and the electrons (i):

$$\hat{\mathcal{T}}_{\text{nuc}} = -\frac{\hbar}{2M_k}\sum_k \nabla_k^2,\ \hat{\mathcal{T}}_e = -\frac{\hbar}{2m_e}\sum_i \nabla_i^2. \tag{5.4}$$

$\hat{\mathcal{V}}_{\text{nuc}}$ is the Coulomb interaction between the nuclei (k,l),

$$\hat{\mathcal{V}}_{\text{nuc}} = \frac{1}{2}\sum_{k\neq l}\frac{Z_k Z_l e^2}{|R_k - R_l|} \tag{5.5}$$

where $Z_k e$ is the charge of a nucleus at position k. $\hat{\mathcal{V}}_{ee}$ is the corresponding term for the electron-electron (i,j) interaction,

$$\hat{\mathcal{V}}_{ee} = \frac{1}{2}\sum_{i\neq j}\frac{e^2}{|r_i - r_j|}, \tag{5.6}$$

and $\hat{\mathcal{V}}_{\text{ext}}$ is the potential acting on the electrons (i) due to the nuclei (k),

$$\hat{\mathcal{V}}_{\text{ext}} = \sum_{i,k}\frac{Z_k e^2}{|r_i - R_k|}. \tag{5.7}$$

While there is an analytical solution for the hydrogen atom, the main problem with Schrödinger's equation for many-particle systems is that it is not possible, in general, to solve analytically. Approximations must therefore be made.

5.1.2 Born-Oppenheimer approximation

To begin with, protons and neutrons in the nuclei are more than three orders of magnitude more massive than the electrons, and thus their velocities must be much smaller. Based on this, the motion of the nuclei and electrons may be separated and the nuclei can be treated as "frozen". The nuclei have zero velocities and thus the $\mathcal{T}_{\text{nuc}}$ term in Eq. 5.3 can be set to zero. Furthermore, because the motion of the nuclei and electrons can be separated, the electronic and nuclear problems can be solved with independent wavefunctions. With the nuclei assumed as frozen then the Coulomb interaction between the nuclei is constant. Therefore, the $\mathcal{V}_{\text{nuc}}$ term can be omitted in solving the Schrödinger equation and added later as a constant to the total

energy. This separation of electronic and nuclear problems is known as the **Born-Oppenheimer approximation** [90].

Adopting Hartree atomic units $\hbar = m_e = e = 1$ and removing $\mathcal{T}_{\text{nuc}}$ and $\mathcal{V}_{\text{nuc}}$ in Eq. 5.3, the Hamiltonian can now be simplified to:

$$\begin{aligned} \mathcal{H} &= \mathcal{T}_e + \mathcal{V}_{ee} + \mathcal{V}_{\text{ext}} \\ &= -\tfrac{1}{2}\sum_i \nabla_i^2 + \tfrac{1}{2}\sum_{i\neq j}\frac{1}{|r_i - r_j|} + \sum_{i,k}\frac{Z_k}{|r_i - R_k|}. \end{aligned} \tag{5.8}$$

Still, this is too complex to solve, which is where DFT comes in.

5.2 DENSITY FUNCTIONAL THEORY

The approach for solving many-particle problems with pure quantum theory lies in DFT, which is a clever reformulation of the problem which replaces the many-particle problem (Eq. 5.8) by many one-body problems. This is accomplished by using equations for a system of non-interacting bodies that generate the same density as a given system of interacting bodies. Here, an overview of the general theory and relevant equations behind DFT will be presented.

5.2.1 The Hohenberg-Kohn theorems

In 1964, Pierre Hohenberg and Walter Kohn introduced the first formulations of DFT with two theorems, known as the Hohenberg-Kohn theorems [91]:

1. For a many-particle system, the ground state density, $n_0(r)$, uniquely determines the potential.

    - The theorem was proved by considering two systems of electrons, each trapped in potentials $v_1(r)$ and $v_2(r)$, that give rise to the same ground state density, $n_0(r)$. It can be shown by *reductio ad absurdum* that $v_1(r) - v_2(r) = \text{const}$.

2. For an external potential $\mathcal{V}_{\text{ext}}(r)$, a universal energy functional, F[n], can be defined in terms of the density.

   - Since the ground state density determines the potential and the ground state wave-functions, then all properties in a system are also determined.
   - The universal energy functional has the form: $F[n] = \mathcal{T}[n] + \mathcal{V}_{ee}[n]$.

The so-called Hohenberg-Kohn functional accounts for the aspects of the total energy that only depend on the density and includes the kinetic energy of the electrons and the electron-electon interactions. The total energy functional must also include a term for the external potential, and will have the form:

$$\begin{aligned} E[n] &= F[n] + \int dr\, \mathcal{V}_{\text{ext}}(r) n(r) \\ &= \mathcal{T}[n] + \mathcal{V}_{ee}[n] + \int dr\, \mathcal{V}_{\text{ext}}(r) n(r). \end{aligned} \tag{5.9}$$

While the Hohenberg-Kohn theorems rigorously prove the existence of a functional of the electron density that may be used to solve the Schrödinger equation, they do not provide a construction for this functional, which is where the Kohn-Sham ansatz comes in.

5.2.2 The Kohn-Sham ansatz

Walter Kohn and Lu Jeu Sham approached this problem in 1965, introducing the concept that the many-particle interacting system governed by the Hamiltonian (Eq. 5.8) could be replaced by an auxiliary system that can be more easily solved. Since there was no way to uniquely create this auxiliary system, an **ansatz** was made [92], resting upon two assumptions:

1. The ground state density of an auxiliary system of non-interacting particles can represent the exact ground state density.

2. The auxiliary Hamiltonian will have the usual kinetic energy operator and an effective local potential.[†]

This auxiliary system of non-interacting bodies is defined by the auxiliary Hamiltonian, $\hat{\mathcal{H}}_{\text{aux}}$:

$$\hat{\mathcal{H}}_{\text{aux}} = \hat{\mathcal{T}}_{\text{aux}} + \hat{\mathcal{V}}_{\text{aux}} = -\frac{1}{2}\nabla^2 + \mathcal{V}(r). \tag{5.10}$$

In order to define the density functionals, expressions must be applied for all potentials $\mathcal{V}(r)$ in some range and for the ground state with one electron in each orbital $\psi_i(r)$. The density of the auxiliary system is

$$n(r) = \sum_{i=1}^{N} f_i |\psi_i(r)|^2, \tag{5.11}$$

where f_i is the Fermi-Dirac distribution.

The classical Coulomb interaction energy of the electron density $n(r)$ interacting with itself is taken to be the Hartree energy:

$$E_{\text{Hartree}}[n] = \frac{1}{2}\iint dr dr' \frac{n(r)n(r')}{|r - r'|}, \tag{5.12}$$

where [n] denotes a functional of the density $n(r)$, which is position-dependent.

The energy due to the interaction between electrons and the nuclei, E_{ext}, is:

$$E_{\text{ext}}[n] = \int dr\ \mathcal{V}_{\text{ext}} n(r). \tag{5.13}$$

[†]This is a useful simplification that is not necessary, but is often taken as part of the Kohn-Sham approach. In their original paper, Kohn and Sham did propose an alternative approach with non-local operator for exchange, to which correlation effects are added.

The Kohn-Sham approach for reformulating the interacting many-particle problem involves rewriting the Hohenberg-Kohn total energy functional [91] (Eq. 5.9) as:

$$\begin{aligned} E_{\mathrm{KS}}[n] &= E_{\mathrm{Hartree}}[n] + E_{\mathrm{ext}} + \mathcal{T}_s[n] + E_{\mathrm{nuc}} + E_{\mathrm{xc}}[n] \\ &= \frac{1}{2}\iint dr\,dr'\frac{n(r)n(r')}{|r-r'|} + \int dr\ \mathcal{V}_{\mathrm{ext}}n(r) + \mathcal{T}_s[n] + E_{\mathrm{nuc}} + E_{\mathrm{xc}}[n], \end{aligned} \tag{5.14}$$

where $\mathcal{T}_s$ is the independent-particle kinetic energy, E_{nuc} is the energy that accounts for the Coulomb-interaction between the nuclei, and E_{xc} is the exchange-correlation energy, which contains the many-particle interactions but whose general form is unknown. E_{xc} represents the difference between the kinetic and internal interaction energies of the true many-particle system and the auxiliary system where the electron-electron interactions have been replaced by the Hartree energy (Eq. 5.12).

Determining the Kohn-Sham auxiliary system for the ground state can be viewed as a problem of energy minimization with respect to the density $n(r)$. For a system of N electrons, the density should integrate to exactly N:

$$N = \int dr\ n(r), \tag{5.15}$$

which is used as a constraint in the search for the variational minimum, along with the orthonormalization constraints

$$\int \psi_i^*(r)\psi_j'(r) = \delta_{i,j}. \tag{5.16}$$

The independent-particle kinetic energy, $\mathcal{T}_s$, is:

$$\mathcal{T}_s = \frac{1}{2}\sum_{i=1}^{N}|\nabla\psi_i|^2 \tag{5.17}$$

which is already given explicitly as a functional of $n(r)$ (Eq. 5.11). Applying the variational principle to derive the variational equation, $\frac{\delta E_{\mathrm{KS}}}{\delta \psi_i(0)} = 0$, to Eq. 5.14 gives:

$$\frac{\delta \mathcal{T}_s}{\delta \psi_i(r)} = \frac{1}{2}\nabla^2 \psi_i(r); \ \frac{\delta n(r)}{\delta \psi_i(r)} = \psi_i(r). \tag{5.18}$$

Applying the aforementioned constraints through the Lagrange multiplier method leads to the following Schrödinger-like equation for non-interacting particles:

$$\mathcal{H}_{\mathrm{eff}} \psi_i(r) = \varepsilon_i \psi_i(r) \tag{5.19}$$

where ε_i are the eigenvalues and the effective Hamiltonian is:

$$\mathcal{H}_{\mathrm{eff}}(r) = -\frac{1}{2}\nabla^2 + \mathcal{V}_{\mathrm{eff}}(r). \tag{5.20}$$

The potential for the non-interacting system is $\mathcal{V}_{\mathrm{eff}}(r)$, with the following condition:

$$\mathcal{V}_{\mathrm{eff}} = \mathcal{V}_{\mathrm{ext}}(r) + \mathcal{V}_{\mathrm{xc}}(r) + \int dr' \frac{n(r')}{|r - r'|}. \tag{5.21}$$

Equations 5.19–5.21 are known as the Kohn-Sham equations. They are solved self-consistently – that is, subject to the condition that the effective potential, $\mathcal{V}_{\mathrm{eff}}(r)$ and the density, $n(r)$, are consistent. Note that, for the sake of brevity, spin is not taken into account in any formulae so far. However, the inclusion of spin is accomplished through two separate densities for spin up and down, which are the solutions of the Kohn-Sham equation for the spin-dependent effective potential. The effective potential accounts for spin in the exchange-correlation potential.

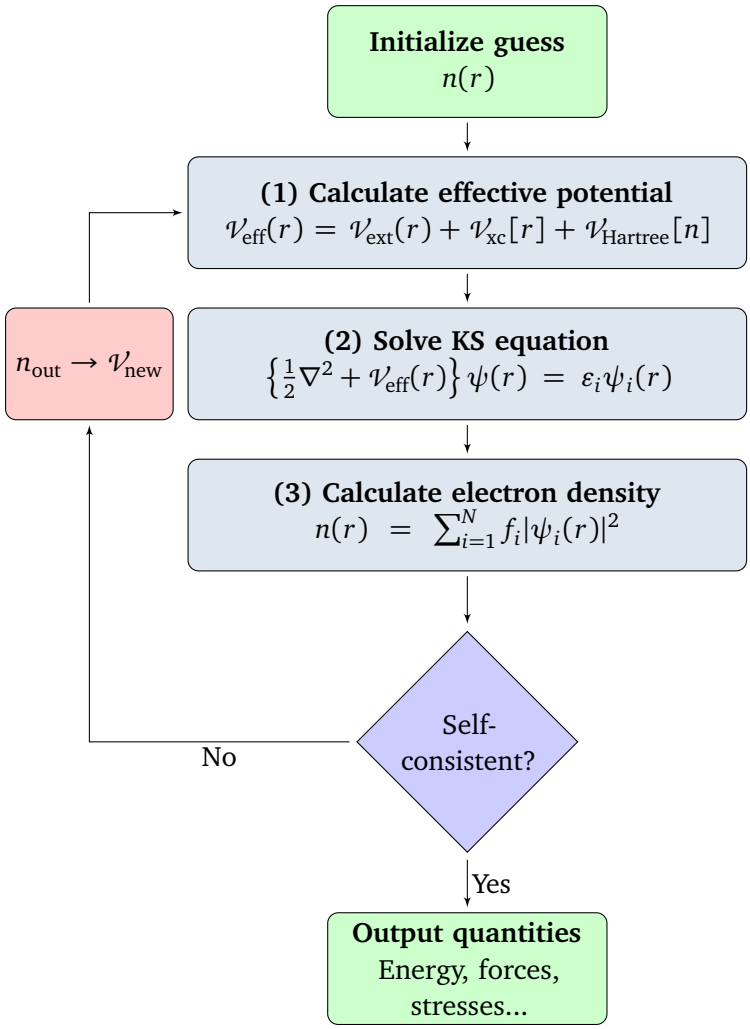

Figure 5.1: Schematic of the self-consistent loop for solving the Kohn-Sham equations.

The iteration scheme for the Kohn-Sham equations is summarized in the flow chart in Fig. 5.1. The most computationally intensive step is solving the Kohn-Sham equation for a given potential, step (2) in the loop. In this step, the equations are uniquely solved with a given $\mathcal{V}_{\text{in}}$ for an output density, n_{out}.

After achieving convergence in the self-consistent loop of Fig. 5.1, subsequent iteration schemes can be used to minimize the energy further – for instance, by moving the atomic positions or adjusting the cell volume. The Kohn-Sham equations are indeed much easier to

solve than the equations for many-particle interacting systems. However, the major caveat to this technique is that we do not know the form of the exchange-correlation functional. It turns out that this can be approximated reasonably well.

5.2.3 Exchange-correlation functionals

Since the true form of the exchange-correlation functional is unknown, an approximation must be made for a functional that will lead to reasonable results. The one simple case where this functional can be derived exactly is for a uniform electron gas. Kohn and Sham had already pointed out in their paper [92] that the properties of a homogeneous electron gas (HEG) may be useful for approximating real systems – atoms, molecules, solids, etc. – where the electron density is nonuniform. In the local density approximation (LDA), the exchange-correlation energy is calculated, at each position, as the exchange-correlation energy in a uniform electron gas with the electron density observed at that position. The exchange-correlation functional in the LDA is thus

$$E_{\mathrm{xc}}^{\mathrm{LDA}}[n] = \int \epsilon_{\mathrm{xc}}^{\mathrm{HEG}}[n(r)]. \tag{5.22}$$

The exchange part of $\epsilon_{\mathrm{xc}}^{\mathrm{HEG}}$ is known analytically [93],

$$\epsilon_{\mathrm{x}}^{\mathrm{HEG}}[n(r)] = -\frac{3(3\pi^2)^{1/3}}{4\pi} n^{4/3}, \tag{5.23}$$

and the exact exchange energy functional in the LDA can be obtained as

$$E_{\mathrm{x}}^{\mathrm{HEG}} = E_{x}^{\mathrm{LDA}} = -\frac{3(3\pi^2)^{1/3}}{4\pi} \int dr n(r)^{4/3}. \tag{5.24}$$

The functionals for correlation are not as simple, and analytical expressions are not known for the HEG, except in the high- and low-density limits. There are various approaches for

representing the correlation functional in the LDA, such as that of Perdew-Wang (PW92) [94].

Since electrons in a single atom will naturally be different from electrons in a uniform gas, the LDA approximation may appear to be a crude estimation of little value for real systems. However, LDA has been a widely used and extremely successful approximation that has been around for over 40 years [95–97].

In addition to the LDA, there are a number of other functionals that approximate the exchange and correlation and correct some of the problems with the LDA. Another popular class of functionals is the generalized gradient approximation (GGA), which takes into account the local gradient in the electron density. The general form is

$$E_{\mathrm{xc}}^{\mathrm{GGA}}[n] = \int f\left[n(r), \nabla(r)\right] n(r)\, dr. \tag{5.25}$$

Because there is no unique way to incorporate information from the gradient of the electron density into a functional, there are a number of distinct GGA functionals. One widely used functional for solids is that of Perdew, Berke, and Ernzerhof (PBE) [98], which is used for the majority of the calculations in this thesis. In addition to the PBE-GGA functional, there are dozens of other functionals out there, many of which are particularly useful for calculations on isolated molecules.

Even though the GGA includes more physical information than the LDA, it should not be assumed that it is more accurate. This is not always the case, and each functional has different strengths and weaknesses that should be taken into account when choosing an appropriate functional [99–102]. Each functional is appropriate for particular parameter regimes corresponding to different materials systems

5.3 FIRST-PRINCIPLES PHONON CALCULATIONS

As we saw from Chapter 4, dynamical properties of materials depend on the calculation of forces between atoms in a system. Phonon calculations are only one example out of many materials phenomena that rely on access to atomic forces. Structure optimization, for instance, can be carried out by minimizing the forces – that is, calculating the forces on an atomic configuration, moving the atoms by a small amount in the direction of the forces, re-evaluating the forces, and so forth until the forces are below a threshold. This optimization by allowing atoms to move toward their equilibrium positions is known as relaxing the atomic positions. In the next two subsections, force calculations from first-principles calculations are briefly described, followed by a discussion of the methods available for first-principles phonon calculations.

5.3.1 Forces in density functional theory

There are several ways in which forces can be evaluated through first-principles calculations. Generally, the force on an atom is described by the total energy change with respect to atomic displacement:

$$F_i = -\frac{\partial E}{\partial R_i}. \tag{5.26}$$

Since $E = \langle \Psi | \hat{\mathcal{H}} | \Psi \rangle$, the Hellman-Feynman theorem relates $\frac{\partial E}{\partial R_i}$ to the expectation of the derivative of the Hamiltonian with respect to R_i:

$$F_i = -\frac{\partial E}{\partial R_i} = -\left\langle \Psi \left| \frac{\partial \hat{\mathcal{H}}}{\partial R_i} \right| \Psi \right\rangle = -\int dr\ n(r) \frac{\partial \mathcal{V}_{\text{ext}}(r)}{\partial R_i} - \frac{\partial E_{\text{ion}}}{\partial R_i}. \tag{5.27}$$

where E_{ion} is the energy of the ion cores. Since the wavefunctions are solved for through the self-consistent loop for the Kohn-Shams equations (Fig. 5.1), this shows that the forces – and therefore the phonon properties – can be accessed through DFT calculations.

5.3.2 Methods for phonon calculations

There are two available methods for determining the force constants – and from that, the phonon spectrum – in plane-wave-based DFT calculations. They are known as the "supercell" method, and the "linear response" method.

The **supercell method** – also called the "small displacement" method, the "direct" method, or the "frozen phonon" method – is the most straightforward method for calculating the force constant matrix. The method involves shifting the atomic positions in a crystal by small amounts and then calculating the forces on the other atoms [103]. Since the physical meaning of the force constants is that they relate the displacement of an atom to the force on another atom (Eq. 4.15), the entire force constant matrix may be computed with an appropriate set of displacements. Since the forces on atoms extend beyond the nearest neighbor atoms in a unit cell, supercells are constructed to account for the full range of force constants outside the primitive cell. The choice of atomic displacements is important in obtaining meaningful results; the number of displacements should be minimized, and so should their magnitudes so that the system is in the harmonic regime, but they should be large enough that the numerical noise is not too high compared to the computed forces. The number of displacements required depends on the crystal structure and also the anharmonicity of the system. The main drawback of this method is the need for supercells, and therefore a large number of atoms. For instance, for the smallest MAX phase structure (the 211 structure with 12 atoms/unit cell), a $2 \times 2 \times 1$ supercell requires $2^2 \cdot 12 = 48$ atoms. Furthermore, the force constant range is truncated to the edge of the supercells. While convergence tests may be performed to converge the phonon properties to help overcome this, special attention is needed to minimize size effects in the system.

The other phonon calculation method is the more recently developed **linear response** method [104, 105], which is based on density functional perturbation theory (DFPT) . This one

is not as straightforward to grasp in terms of physical meaning compared to the direct calculation with the supercell method, and therefore the frozen phonon method is a nicer way to become acquainted with phonon calculations. DFPT provides a means of computing the second derivative of the total energy with respect to a given perturbation. Since all harmonic force constants (and elastic constants, etc.) only involve the second derivative of energy, this method calculates the dynamical matrix – or the reciprocal space force constant matrix (Eq. 4.45) – directly for a set of q vectors. Due to the variational principle of density functional theory (see Eq. 5.9), the second order change in energy depends on the first linear change in electron density. Unlike the frozen phonon method, there are no issues with converging the phonon properties to the size of the system. The phonon properties can be determined from the electronic wavefunctions and eigenvalues of the undistorted crystal. However, it is computationally more expensive and generally takes longer than the frozen phonon method. In this thesis, mainly DFPT calculations are used; however, frozen phonon calculations are performed where convenient or necessary, for example if there are computational limitations for DFPT.

Chapter 6: Neutron diffraction

So far, the dynamical behavior of periodically-ordered atoms has been considered from a purely theoretical point of view, along with a condensed discussion of other fundamental materials properties. The next two chapters are devoted to background, theory, and physical concepts relevant to two different types of experimental techniques, elastic scattering (this chapter on neutron diffraction) and inelastic scattering (the next chapter on Raman spectroscopy). These two types of scattering techniques give access to different pieces of information on physical properties and atomic-level physics of materials in the solid state. In this thesis, they are used to investigate the dynamical behavior of the atoms in MAX phases through parameters that will be directly compared with results from the computational modeling through first-principles phonon calculations, for which the underlying theory has been discussed in the previous chapters.

The focus of the present chapter is neutron diffraction. While this is only one of a number of diffraction techniques currently available for crystal structure investigation (e.g. X-ray diffraction and electron diffraction), neutron diffraction is the method that is most heavily used for the experimental work in this thesis. Although there are major differences in the way beams interact with atoms depending on the particles or waves that make up the beam, diffraction techniques also share common qualities in their theory and mathematical descriptors. Therefore some of the topics of this chapter will be a more broad discussion of diffraction that are applicable for other diffraction techniques; however, in later sections emphasis will be placed on neutron scattering, which is most relevant to the work carried out in this thesis.

6.1 DIFFRACTION BASICS

Diffraction techniques are extremely powerful and essential tools in probing the atomic ordering in materials. It was over 100 years ago, in 1912, that Max [von] Laue* and his colleagues, Walker Friedrich and Paul Knipping, decided to irradiate a copper sulfate crystal and became the first to observe diffraction from the crystal planes. They simultaneously demonstrated two important things in their experiment with a $CuSO_4$ crystal: (1) the existence of X-rays as a potentially useful form of electromagnetic radiation for probing atoms in solids, and (2) the fact that solids have a periodic form. The discovery immediately gained widespread attention, and soon after was exploited by William Henry Bragg and his son William Lawrence Bragg to develop an alternative method that gave birth to X-ray diffraction and X-ray crystallography (see Bragg's law, Section 6.1.2). Both von Laue and the Braggs swiftly received Nobel prizes in 1914 and 1915, respectively, and to this day, X-ray diffraction – along with neutron and electron diffraction – has been a widely used tool among chemists, materials scientists, and physicists. It is routinely employed and considered essential if one wants to gain some understanding of the crystal structure of a material.

This section introduces the fundamentals concepts of diffraction, with general considerations for the relationship between the geometry of a coherent beam and the periodic structure of a crystal. The last part of this section discusses the different types of radiation beams typically used for diffraction before moving onto neutron diffraction, which is the main focus of Section 6.2 and onwards.

*At the time of the 1912 experiment, he was known as Laue; later, he went by von Laue.

6.1.1 *Diffraction fundamentals*

Diffraction, by definition, is elastic, coherent scattering from a crystal with long-range order (*i.e.* periodicity). **Elastic** scattering refers to a process where the incident and scattered radiation have the same wavelength – that is, the beam does not change in wavelength through the scattering process. This definition of elastic can be somewhat contradictory to other uses of the word. In elementary physics courses, an elastic collision is taken to mean a collision in which the total energy is conserved, but the individual bodies transfer energy through the collision. In elastic scattering, "elastic" has a completely different meaning, and no energy is transferred to the crystal when the beam is scattered.

6.1.2 *Bragg's law*

When a beam interacts with atoms in a crystal, most combinations of wavelengths and angles lead to destructive interference of the reflected beam, where the scattering from the atoms causes phase shifts that interfere and cancel out. When the normal to the reflecting plane is aligned in a certain way, however, the reflected beams are in phase and thus interfere constructively to form a diffraction peak. The equation that governs this is known as **Bragg's law**:

$$\lambda = 2d_{hkl} \sin \theta_{hkl}. \tag{6.1}$$

This can be visualized through Fig. 6.1, where a wave reflecting on a given plane travels an extra distance, $2d_{hkl} \sin \theta_{hkl}$ (twice the distance $d \sin \theta$ labeled in blue), before it joins the waves reflecting from the other planes. In order to be in phase with these other waves, this extra distance must be equal to integer multiples of λ (labeled in green).

Bragg's law is important because it relates the scattering angle, θ, and the wavelength, λ, to

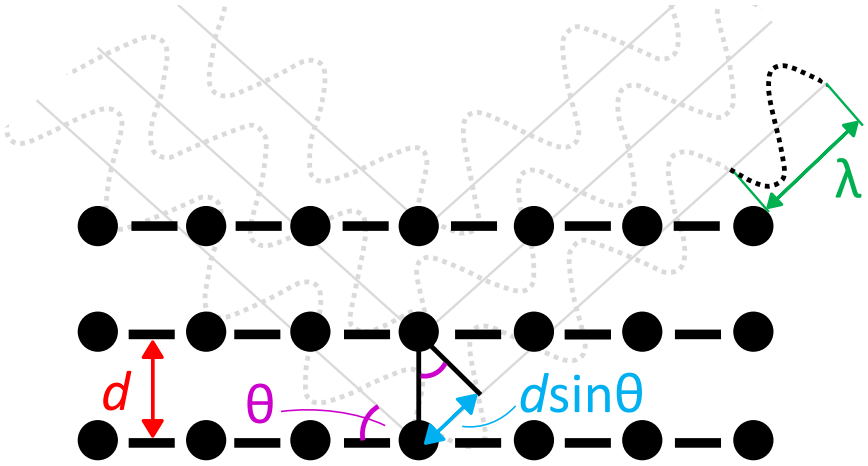

Figure 6.1: Bragg's law.

a dimension within the crystal. The d-spacing, d_{hkl}, is the distance between planes (hkl)[†] in a crystal. Since only certain wavelengths and angles lead to constructive interference, one can access d_{hkl} within a crystal by measuring either the angles (for a coherent beam of constant λ) or the wavelengths (for a constant angle) that form a peak in scattered light/neutrons/electrons.

6.1.3 Types of diffraction

Crystal structure investigation through diffraction requires the use of beams of radiation. Moreover, the wavelength of radiation should be on the order of the typical distances between atoms in a crystal in order to obtain useful, high-resolution information on the atomic arrangement. This is also a fundamental condition for Bragg's law, where λ cannot be larger than the distance $d \sin\theta$ (Fig. 6.1), since n must be an integer – which is usually equal to 1 for the length scales of the beams typically used.

The main candidates for beams are neutrons, electrons, and electromagnetic radiation in the X-ray spectrum. While the former two are particles with a mass, the fundamental notion of wave-particle duality allows all to be treated as waves according to the relationship between

[†]In hexagonal materials, planes can also be indexed by $(hkil)$, where i indexes the direction that bisects the vectors corresponding to the $-h$ and $-k$ indices. By symmetry, $i = -(h+k)$.

momentum, $\vec{p}$, and wave vector $\vec{k}$, which is given by the expression for the de Broglie wavelength:

$$\vec{p} = \hbar\vec{k}, \tag{6.2}$$

where $\vec{p} = m\vec{v}$, and $|\vec{k}| = 2\pi/\lambda$.

Electron beams have wavelengths that are much smaller than those of X-rays and neutrons. In the case of transmission electron spectroscopy, electrons are much smaller than interatomic distances and pass through thin samples. However, it is not as useful for determining crystal structures because the relationship between the intensity of the diffracted data and the crystal structure is not as straightforward as with neutrons and X-rays and the data refinement processes cannot be as readily automated. Furthermore, the strong interaction of electrons with matter (due to the scattering by the positive potential inside the electron clouds) makes the scattering more influenced by dynamical effects. Therefore, electron diffraction is generally not as reliable for obtaining quantitative crystal structure information, and it is typically used to image long-range atomic ordering to survey scattering in reciprocal space.

X-ray diffraction and neutron diffraction are the most common and powerful tools for probing crystal structures. Most laboratory X-ray diffraction experiments are performed with constant-wavelength copper K_α radiation ($\lambda = 1.54$ Å), using the scattering angle as a variable. A range of angles is scanned – where the incident beam and detectors are simultaneously varied to detect the elastically scattered X-rays – and the intensity of the scattered beam at each angle is measured with an electronic detector. Another X-ray diffraction method is the use of synchotron sources, which can produce a continuous distribution of X-ray wavelengths. This offers higher beam intensities and more versatility in wavelengths, however they are not as accessible as laboratory X-ray diffractometers and synchotron sources are limited so considerable advanced planning is needed for proposing and scheduling experiments.

Neutron diffraction is an alternative to X-ray diffraction. Neutron beams can be produced either with a nuclear reactor or with a spallation source. Unlike X-ray diffraction, there is no way to produce neutrons in a laboratory and so, like synchotron X-ray experiments, neutron diffraction experiments can only be performed at limited facilities and experimental planning must be done in order to apply for – and make good use of – neutron beam time. Neutron diffraction is similar to X-ray diffraction in formalism and experimental technique in terms of analogous experimental set-ups and data refinement, but there are some significant differences in how neutrons interact with atoms that make it more advantageous in many cases.

6.2 NEUTRON DIFFRACTION

Neutron diffraction experiments are an integral part of this thesis in measuring the temperature-dependent crystal structures and atomic displacements of atoms *in situ*. The rest of this chapter focuses on neutron diffraction, although many aspects may apply to general diffraction techniques. Background on the scattering of neutrons from a crystal, neutron scattering factors, experimental methods (primarily time-of-flight experiments, which are used for the work in this thesis), powder-profile refinement, and the Debye-Waller factor for atomic motion will be discussed. Finally, the useful applications of neutron scattering and its advantages over X-ray diffraction will be discussed

6.2.1 Neutron scattering from nuclei

There are two ways in which a neutron may be scattered by an atom: by interaction with the nucleus, or by interacting with unpaired electrons. Since magnetism is not studied through neutron diffraction in this thesis, only nuclear scattering will be considered in this section. Most of the theory can be found in a number of other works [13, 106–109]. For further details on the concepts introduced in this chapter, consult those books.

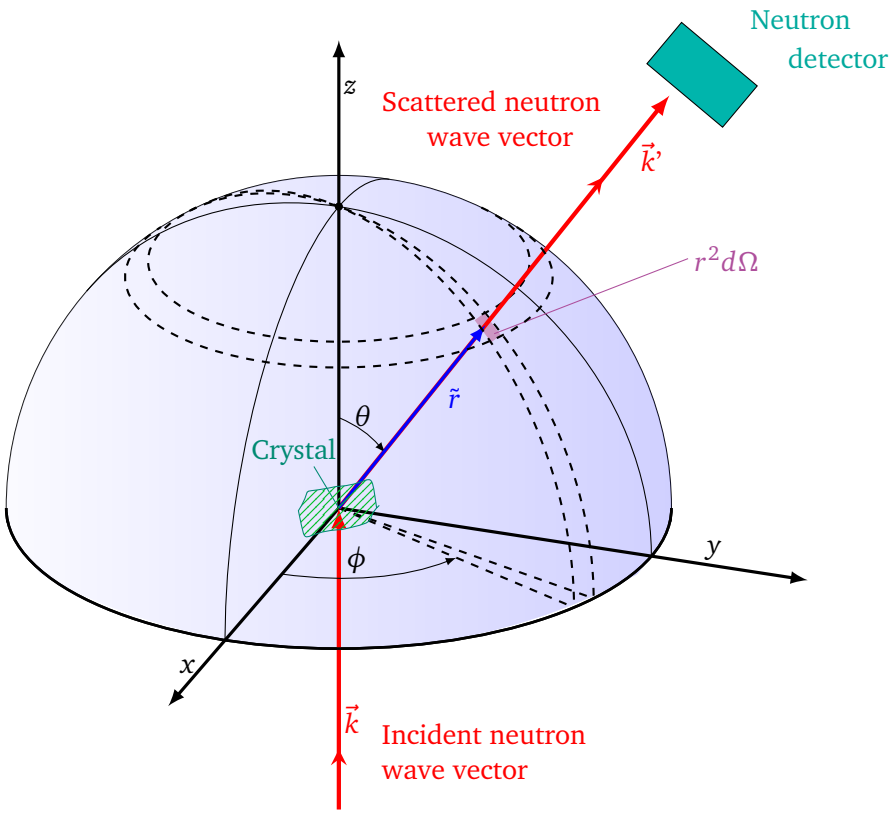

Figure 6.2: The geometry of neutron scattering. Schematic is based on Fig. 1.1 in [106]

Formally, the neutron scattering problem is described by the scattering of a neutron, with wave vector $\vec{k}$, into a state with wave vector $\vec{k}$' by a crystal (Fig. 6.2). The direction of propagation of the scattered neutron state is defined with respect to the incident state by the polar angle θ and the azimuthal angle ϕ (Fig. 6.2). For elastic scattering, where no energy is transferred to the crystal, the number of neutrons scattered per unit time into solid angle $d\Omega = \sin\theta d\phi$ is

$$\mathcal{N}\left(\frac{d\sigma}{d\Omega}\right) d\Omega, \tag{6.3}$$

where $\mathcal{N}$ is the neutron flux defined as the number of incident neutrons per unit area per unit time, and $d\sigma/d\Omega$ is the differential cross-section. The neutron cross-section, σ, is governed by

the atom's ability to scatter neutrons and has units of area. Since the scattering of a beam of neutrons from an atom's nucleus will depend on the interaction potential, $\mathcal{V}(\vec{r})$, between the neutron and the atomic nucleus, the probability (per unit time) of such a transition ($\vec{k} \to \vec{k}'$) is given by Fermi's Golden rule:

$$W_{k\to k'} = \frac{2\pi}{\hbar} \left| \int d\vec{r} \psi^*_{\vec{k}'}(\vec{r}) \mathcal{V}(\vec{r}) \psi_{\vec{k}}(\vec{r}) \right|^2 \rho_{\vec{k}'}(E), \tag{6.4}$$

where $\psi_{\vec{k}}(\vec{r})$ and $\psi_{\vec{k}'}(\vec{r})$ are the normalized wave functions of the incident and scattered states, respectively. Here $\rho_{\vec{k}'}(E)$ is the density of states for the scattered neutrons per unit energy range, which is

$$\rho_{\vec{k}'}(E) = \frac{L}{2\pi} \frac{mk}{\hbar^2} d\Omega \tag{6.5}$$

for a box of volume L^3. The velocity of the incident neutrons is $\vec{v} = \hbar\vec{k}/m$ and the incident flux of neutrons for this box is $\mathcal{N} = \vec{v}/L^3 = \hbar\vec{k}/(mL^3)$. The wave functions of the initial and scattered states, $\psi_{\vec{k}}(\vec{r})$ and $\psi_{\vec{k}'}(\vec{r})$ respectively, are normalized by $L^{-3/2}$ for confinement in the box. Since σ is the inverse of the incident flux multiplied by the number of neutrons scattered per second, it follows that:

$$d\sigma = \frac{W_{\vec{k}\to\vec{k}'}}{\mathcal{N}} = \left(\frac{m}{2\pi\hbar^2}\right)^2 \left| \int d\vec{r} \exp(-i\vec{k}' \cdot \vec{r}) \mathcal{V}(\vec{r}) \exp(i\vec{k} \cdot \vec{r}) \right|^2 d\Omega. \tag{6.6}$$

Now we consider the a single nucleus fixed at the origin of coordinates (*i.e.*, a bound nucleus with position $\vec{R} = 0$) and turn to the potential between the nucleus and the scattered neutron, which is a function of their separation $\vec{r}$. Its exact dependence on $\vec{r}$ is not known in practice but, from experimental results, we know it is a potential of extremely short range that falls rapidly to zero beyond the nuclear dimensions. Because the latter distance is much smaller than

the wavelength of the neutrons, the nucleus acts as a point scatterer – that is, the scattering is isotropic and can be characterized by a single parameter, b, known as the **scattering length** and is dependent on the isotope type. To represent $\mathcal{V}(\vec{r})$, a Fermi pseudo-potential given by a delta function (the only form that gives isotropic scattering) may be used, which is defined as:

$$\mathcal{V}(r) = \frac{2\pi\hbar^2}{m} b\delta(\vec{r}). \tag{6.7}$$

Substituting this into Eq. 6.6 and solving for $d\sigma/d\Omega$, we get:

$$\frac{d\sigma}{d\Omega} = \left(\frac{m}{2\pi\hbar^2}\right)^2 \left(\frac{2\pi\hbar^2}{m}\right)^2 |b|^2 \left| \int d\vec{r} \exp(-i\vec{k}' \cdot \vec{r}) \delta(\vec{r}) \exp(i\vec{k} \cdot \vec{r}) \right|^2 = |b|^2 \tag{6.8}$$

and thus the total cross-section for the rigid atom is

$$\sigma = \int |b|^2 d\Omega = 4\pi |b|^2. \tag{6.9}$$

6.2.2 Neutron scattering cross-sections

Now we consider the scattering from a rigid array of N nuclei. As mentioned earlier, the scattering is dependent on the atom isotope so we must now take into account the different isotopes. There are two different implications of the "isotope effect", and the total cross-section can be subdivided into different contributions for the two types of scattering, coherent and incoherent scattering:

$$\left(\frac{d\sigma}{d\Omega}\right)_{\text{tot}} = \left(\frac{d\sigma}{d\Omega}\right)_{\text{coh}} + \left(\frac{d\sigma}{d\Omega}\right)_{\text{incoh}}. \tag{6.10}$$

The cross-sections are given in units of barn=bn=10^{-24}cm^2 and account for two ways that the scattering from different isotopes come together. Now these two effects will be discussed

separately.

Coherent cross-section

The first contribution to the total cross-section is due to the combined scattering from different isotopes where there is strong interference between the waves scattered from each nucleus. For an element such as titanium, whose naturally-occurring state contains several different isotopes, the effective value of b, which can be distinguished now as $\bar{b}$, is the average b among the isotopes,

$$\bar{b} = \sum_j c_j b_j \tag{6.11}$$

where b_j is the scattering length for the j^{th} isotope and c_j is its fractional abundance. The contribution for **coherent scattering** comes from the average scattering potential and ends up being proportional to $\bar{b}$ of Eq. 6.11 as follows: we denote the position vector of the l^{th} nucleus as $\vec{R_l}$ and its scattering length as b_l such that the interaction potential of Eq. 6.7 becomes

$$\mathcal{V}(r) = \frac{2\pi\hbar^2}{m} \sum_l b_l \delta(\vec{r} - \vec{R_l}). \tag{6.12}$$

Plugging this into Eq. 6.6 gives us a term for the coherent scattering:

$$\left(\frac{d\sigma}{d\Omega}\right)_{\text{coh}} = \left| \sum_l b_l \exp(i\vec{\kappa} \cdot \vec{R_l}) \right|^2, \tag{6.13}$$

where $\vec{\kappa} = \vec{k} - \vec{k'}$. Since $\sum_l b_l$ is $\bar{b}$ of Eq. 6.11, then

$$\left(\frac{d\sigma}{d\Omega}\right)_{\text{coh}} = |\bar{b}|^2 \left| \exp(i\vec{k} \cdot \vec{R_l}) \right|^2. \tag{6.14}$$

This coherent scattering term accounts for the average scattering potential that gives inter-

ference effects, thereby determining the intensities of the diffraction peaks.

Incoherent cross-section

In addition to coherent scattering, there is also some disordered scattering that will result from the presence of different randomly-distributed isotopes and that contributes to the background of the pattern, which is **incoherent scattering**. The incoherent cross-section is:

$$\left(\frac{d\sigma}{d\Omega}\right)_{\text{incoh}} = N[\overline{|b|^2} - |\bar{b}|^2], \tag{6.15}$$

where $\bar{b}$ is the term in Eq. 6.11 and $\overline{|b|^2}$ is calculated as follows:

$$\overline{|b|^2} = \sum_j c_j |b_j|^2. \tag{6.16}$$

Physically, the incoherent scattering term can be seen as the aspect of the "isotope effect" that accounts for the deviations from the average potential, which are randomly distributed and therefore cannot give interference effects.

6.2.3 Elastic nuclear scattering

Now we will consider elastic scattering from an ordered crystal. Since it is the coherent scattering contribution that makes up the (hkl) peaks, we begin with Eq. 6.14 for the coherent scattering cross-section. As a starting point, a Bravais lattice with one atom per unit cell leads to:

$$\left(\frac{d\sigma}{d\Omega}\right)_{\text{coh}} = |\bar{b}|^2 \left|\exp(i\vec{k}\cdot\vec{l})\right|^2, \tag{6.17}$$

where $\vec{l}$ is the lattice vector of cell l, related to the basis vectors of the unit cell ($\vec{a_1}$, $\vec{a_2}$, and $\vec{a_3}$) through integer values l_1, l_2, and l_3 by:

$$\vec{l} = l_1\vec{a_1} + l_2\vec{a_2} + l_3\vec{a_3}. \tag{6.18}$$

For a large crystal, it can be shown that

$$\left(\frac{d\sigma}{d\Omega}\right)_{\text{coh}} = \frac{N(2\pi)^3}{V_0}|\bar{b}|^2 \sum_{\vec{\tau}} \delta(\vec{\kappa} - \vec{\tau}), \tag{6.19}$$

where $\vec{\tau}$ is the reciprocal lattice vector and V_0 is the volume of the unit cell, $V_0 = \vec{a_1} \cdot (\vec{a_2} \times \vec{a_3})$. This can be generalized to a material with more than one atom per unit cell as follows:

$$\left(\frac{d\sigma}{d\Omega}\right)_{\text{coh}} = \frac{N(2\pi)^3}{V_0} \sum_{\vec{\tau}} \delta(\vec{\kappa} - \vec{\tau})|F_N(\vec{\tau})|^2, \tag{6.20}$$

where the **structure factor**, $|F_N(\vec{\tau})|^2$, is defined as

$$F_N(\vec{\tau}) = \sum_d \exp(i\vec{\tau} \cdot \vec{d})\bar{b}_d, \tag{6.21}$$

where $\vec{d}$ denotes the position vector of atom d in the cell and is summed for all the unique sites in a unit cell. Keep in mind that this is assuming bound atoms with no atomic motion.

From Eq. 6.20 it is apparent that, in order for the coherent scattering term to be large, $\vec{\kappa}$ must be equal to a reciprocal lattice vector; otherwise the terms will be out of phase with each other and cancel out . Therefore, the following condition must be fulfilled in order for coherent scattering (*i.e.* **Bragg scattering**) to occur:

$$\vec{\kappa} = \vec{k} - \vec{k'} = \vec{\tau}. \tag{6.22}$$

This is another form of Bragg's law (Eq. 6.1), since $|\vec{\kappa}|$ is related to θ (where the angle between $\vec{k}$ and $\vec{k'}$ is given as 2θ) by $|\vec{\kappa}| = 2|\vec{k}|\sin\theta$, which must be equal to $|\vec{\tau}|$, so we get

$$|\vec{\tau}| = 2|\vec{k}|\sin\theta. \tag{6.23}$$

It can be shown that $|\vec{\tau}|$ and $|\vec{k}|$ are related to the wavelength and integer multiples (n) of d-spacing by:

$$|\vec{\tau}| = \frac{2\pi}{d}n \quad \text{and} \quad |\vec{k}| = \frac{2\pi}{\lambda}, \tag{6.24}$$

and Eq. 6.23 is simply Bragg's law, $n\lambda = 2d\sin\theta$.

Now let's break down the components of the coherent scattering cross-section. We have three main parts to Eq. 6.20:

(i) $N(2\pi)^2/V_0$ is simply a multiplier to account for the volume of the unit cell and the number of atoms,

(ii) $\delta(\vec{\kappa} - \vec{\tau})$ is the selection condition for Bragg scattering to occur by an (hkl) plane based on the reciprocal lattice vector $\vec{\tau}$, which is essentially the wave vector form of Bragg's law, and

(iii) $F_N(\vec{\tau})$ is the term that accounts for the peak intensities due to the scattering based on the properties of the atoms in the unit cell. In the static model (Eq. 6.21), this term is governed by the scattering length of the atoms in the unit cell and their positions.

Now that the basic ideas behind coherent neutron scattering from a static crystal have been introduced, we will introduce dynamical effects, which clearly comes into play in (iii), the structure factor term.

6.2.4 *The Debye-Waller factor*

In the dynamical model, the structure factor of Eq. 6.20 becomes:

$$F_N(\vec{\kappa}) = \sum_d \bar{b}_d \exp(i\vec{\kappa}\cdot\vec{d}) \exp(-W_d(\vec{\kappa})), \tag{6.25}$$

where the last exponential term, $\exp(W_d(\vec{\kappa}))$, is known as the **Debye-Waller factor** that accounts for the thermal motion correction of the structure factor (see section 4.3 of [106] for details). Therefore, we can see that the cross-section for coherent elastic scattering by a dynamical crystal is the static cross-section multiplied by a factor of $\exp(-2W(\vec{\kappa}))$. By definition,

$$2W_d(\vec{\kappa}) = \langle(\vec{\kappa}\cdot\vec{u_d})^2\rangle, \tag{6.26}$$

such that $2W_d$ is simply the mean-squared displacement of atom nucleus d multiplied by $\vec{\kappa}^2$ [86]. In structure refinement, the exponential term accounting for anisotropic thermal atomic motion is expressed as:

$$\begin{aligned} W_d = -2\pi^2(&\mathrm{U}_{11}h^2\tau_1^2 + \mathrm{U}_{22}k^2\tau_2^2 + \mathrm{U}_{33}l^2\tau_3^2 \\ &+ 2\mathrm{U}_{23}kl\tau_2\tau_3 + 2\mathrm{U}_{13}lh\tau_3 + 2\mathrm{U}_{12}hk\tau_1\tau_2) \end{aligned} \tag{6.27}$$

where τ_1, τ_2 and τ_3 are the edges of the unit cell in reciprocal space associated with the a, b, and c lattice parameters, respectively; h, k, and l are the indices for a given (hkl) plane [110]. The U_{ij} terms are components to the Gaussian mean-squared atomic displacement matrix, and they are known as **atomic displacement parameters** (ADPs). The diagonal terms U_{11}, U_{22} and U_{33} are the mean-squared displacements in the direction of the a, b, and c lattice vectors, respectively. The off-diagonal terms represent the orientation of the thermal motion ellipsoids.

For hexagonal structures, due to site symmetry U_{23} and U_{13} are both equal to 0 and the equation simplifies:

$$W_d = -2\pi^2(U_{11}h^2\tau_1^2 + U_{22}k^2\tau_2^2 + U_{33}l^2\tau_3^2 + 2U_{12}hk\tau_1\tau_2). \tag{6.28}$$

For the hexagonal crystal system, these anisotropic U_{ij}'s may be converted to an approximated isotropic temperature factor U_{eq} given by [111]

$$U_{eq} = \frac{1}{3}(U_{11} + U_{22} + U_{33}). \tag{6.29}$$

This shows that the displacements of atoms from their equilibrium positions can be extracted from the intensities of a neutron diffraction pattern depending on how much the intensity decreases compared to the static lattice model. The Debye-Waller factor is also determined in other types of diffraction experiments, but neutron diffraction has several advantages over X-rays that make it more favorable for certain materials systems. These are discussed in Section 6.2.7.

6.2.5 Neutron diffraction experiments

Among the many set-ups that exist for making experimental observations through neutron scattering, there are two main types that may be distinguished. The first type is concerned with measuring the distribution of neutrons in space for neutrons of a constant wavelength, often only in a single plane. The other type makes measurements of the wavelength at a fixed detector position for polychromatic neutrons by measuring their **time-of- flight** (TOF).

The TOF method was mostly developed for elastic scattering by Buras and his collaborators using the pulsed reactor at Dubna, Russia [112]. In this thesis, the neutron diffraction experiments are carried out on a neutron TOF diffractometer, but it also combines position-sensitive detectors [113]. The experimental set-up is described in more detail in Chapter 8.

Neutron diffraction experiments are generally used for materials problems that are structural (where knowledge on atomic positions is sought), while problems that are essentially dynamical, where the main focus is the atomic motion, turn to inelastic neutron scattering. However, for inelastic scattering, the information is most valuable and free of ambiguity when single crystals are used, since the directional correlations are preserved. Single crystals for many materials are extremely difficult to produce, especially in sizes adequate for neutron diffraction, and thus techniques that are applicable to powdered or polycrystalline materials are extremely valuable. Structural studies on powdered materials using profile refinement of neutron TOF data is thus an extremely powerful and versatile technique for probing the structure. Furthermore, as I outlined in the previous section, the Debye-Waller factors account for the atomic vibrations of the atoms in a material and provide information about their average atomic displacements.

The peak intensities, shapes, and positions from a neutron TOF diffraction pattern reveal a great deal of useful structural information about crystals, and the quality of results extracted from the data depends heavily on the profile refinement of the pattern. Structural studies require a comprehensive survey of the entire diffraction pattern rather than discrete measurements of (hkl) intensities, and it is advantageous to have high detector coverage and a wide range of wavelengths.

6.2.6 Profile refinement

The previous sections have outlined the relationship between the crystal structure of a material and the pattern of scattered neutrons – that is, the rules governing the wavelengths that interfere constructively to form a diffraction peak, and the factors that influence the peak intensities. It is clear that the diffraction pattern of scattered neutrons is directly related to the crystal structure of the material. In practice, in order to fit a structural model to this diffraction pattern, some

previous knowledge (or at least a reasonable guess) of the crystal is required to postulate a suitable initial structure based on a limited number of identifiable parameters including those that are structural and those that are related to the instrument. The "goodness" of the fit between the measured and calculated profile is then assessed through a least-squares analysis, using both the instrumental and structural parameters.

This refinement strategy is known as **Rietveld refinement**, after Rietveld who developed the method [114]. The method rests on the fact that the diffraction peaks in a neutron diffraction pattern are extremely close to Gaussian in shape. The profile function includes variables that are refined to fit the peak width and also ones that depend on the instrument to account for the instrument alignment – for example, in my work I refined σ_1 in the profile function and "DIFC" for the instrument alignment. Mathematical descriptions of refineable parameters can be found in Ref. [110].

The precision of an analysis can be expressed in a number of different ways. The **weighted profile R-factor**, R_{wp}, is the most straightforward expression of the discrepancy. It is simply the square root of the minimized quantity scaled by the weighted intensities [115]:

$$R_{wp}^2 = \frac{\sum_i w_i (y_{\text{calc},i} - y_{\text{obs},i})^2}{\sum_i w_i (y_{\text{obs},i})^2}, \tag{6.30}$$

where w_i is the weight, i refers to a data point at wavelength λ_i, and $y_{\text{calc},i}$ and $y_{\text{obs},i}$ are, respectively, the calculated and observed intensities. Another useful concept is the **expected R-factor**, R_{exp}, which represents the ideal model of the "best possible" R_{wp} that would be obtained if the average value of $(y_{\text{calc},i} - y_{\text{obs},i})^2$ was equal to the uncertainty estimate of the observed data, $\sigma^2[y_{\text{obs},i}]$. In this case, $w_i(y_{\text{calc},i} - y_{\text{obs},i})^2$ would equal one and the numerator of Eq. 6.30 would be equal to the number of degrees of freedom, $N + P + C$, where N is the number of data

points, P is the number of parameters, and C is the number of the constraints. This gives an R-factor of:

$$R_{\text{exp}}^2 = \frac{N}{\sum_i w_i (y_{\text{obs},i})^2}. \tag{6.31}$$

A related concept is "chi squared", or χ^2, which is a statistical term that represents the average ratio between $(y_{\text{calc},i} - y_{\text{obs},i})^2$ and $\sigma^2[y_{\text{obs},i}]$, which, again, would be equal to one for an ideal dataset. Note that it is also the ratio of Eqs. 6.30 and 6.31, given by

$$\chi^2 = \frac{1}{n} \sum_i \frac{(y_{\text{calc},i} - y_{\text{obs},i})^2}{\sigma^2[y_{\text{obs},i}]} = \frac{R_{wp}^2}{R_{\text{exp}}^2}. \tag{6.32}$$

During a refinement process, χ^2 starts out large – when the model is poor – and decreases as the model better fits the observed pattern. A good refinement strategy is of utmost importance for obtaining meaningful results from a dataset. However, even with good statistics and minimized differences between the observed and fitted profile, there can be more than one optimal solution, with local minima and correlated parameters so there will always be an amount of uncertainty in the a final profile fit. Throughout this thesis, error bars and standard deviations are used in figures and tables to estimate statistical error. Further details on the refinement strategies are described in Chapter 8, and the refinement statistics are presented in Appendix A.

6.2.7 Advantages over X-rays

Neutron diffraction can sometimes be considered an alternative to X-ray diffraction, where the two techniques have similar formalism; they both involve elastic scattering where the scattered radiation is related to the arrangement of atoms within the crystals through the spacing between the reflection planes. However, there are fundamental differences in the way that neutrons interact with atoms in a crystal, and consequentially there are a number of advantages of

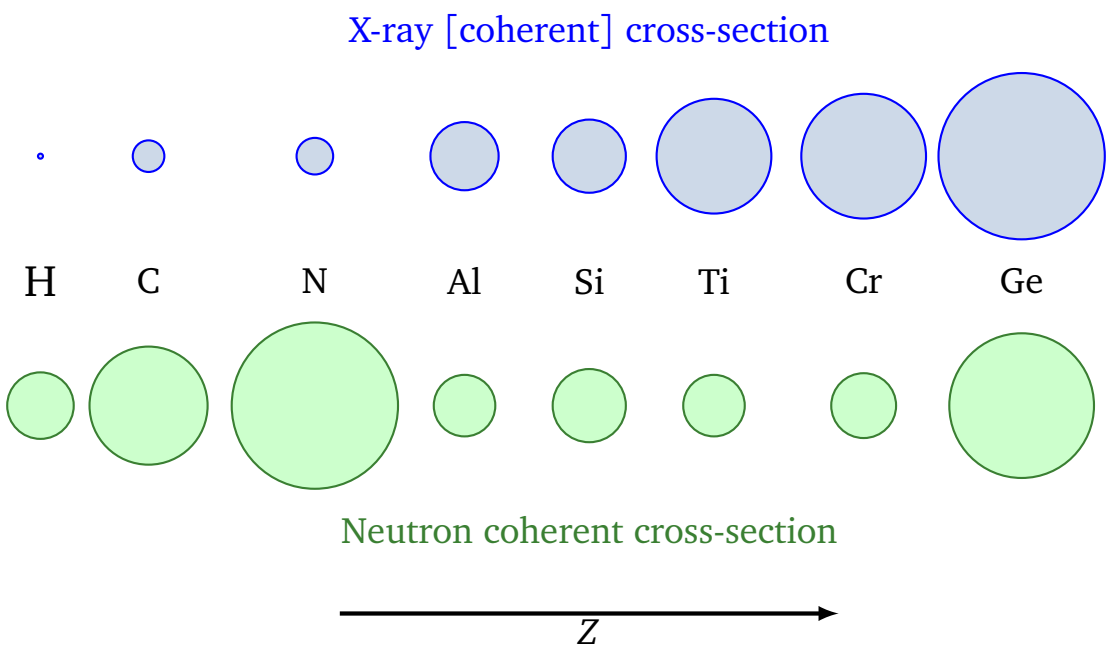

Figure 6.3: Schematic comparison of scattering cross-sections of select elements for x-rays and neutrons. Data for neutron cross-sections is from [116].

neutrons over X-rays:

- The most relevant advantage for work with the MAX phases is that the ability of an atom to scatter neutrons does not scale with the atomic number, Z. X-rays interact with the electron clouds of atoms, so the scattering power of X-rays scales directly with the number of electrons. On the other hand, neutrons interact with the nuclei of atoms, which are typically $\sim 10^{-5}$ times the size of the atom, and therefore the wavelengths of the neutrons are generally similar to the atomic size. As a result, there is no correlation between the neutron scattering length and the atomic number. Figure 6.3 shows a schematic of the relative effective X-ray scattering cross-sections (blue) and neutron coherent cross-sections (green) of various elements that are typically present in MAX phases. While the scattering power of X-rays scales with Z, the neutron scattering cross-section does not. This is especially useful for carbides and nitrides, since the light C and N atoms are difficult to resolve in X-ray diffraction because the scattering from the heavier M (*e.g.*, Ti and Cr) and

A (*e.g.*, Al, Si, and Ge) atoms dominate the diffraction pattern.

- Another important advantage of neutrons is their long penetration depth in matter due to the fact that they are uncharged particles. They are good for sampling large volumes and therefore probing bulk properties, whereas X-rays only probe the surface and sample small volumes.

- Neutron scattering also has no angular dependence on scattering. X-rays, on the other hand, decay in scattering factor with increasing angles, because the wavelength of X-ray radiation is of the order of the atom diameters and therefore most of the scattering is in the forward (low θ, Fig. 6.1) direction.

- Finally, other important applications of neutrons include their ability to investigate magnetism by interacting with unpaired electrons, and also their ability to get phonon properties away form the Γ-point; however, the latter is an advantage of inelastic neutron scattering, not diffraction, and a single crystal is required in order to measure the phonon distribution. Further, these two advantages are not exploited in this thesis.

All in all, neutron diffraction is a powerful and versatile technique for probing the crystal structure of materials and are especially useful for the MAX phases, with their light C and N atoms. Results from neutron diffraction are an integral part of this thesis. The temperature-dependent atomic displacements and crystal structures (including bond lengths and lattice parameters) determined through Rietveld analysis of HTND TOF data will be presented for a large number of MAX phases throughout the chapters in Part II. By supplementing the HTND results with first-principles phonon calculations, the combined studies are useful in shedding light on bonding, defects, atomic motion, and interatomic interactions in the MAX phases.

Chapter 7: Raman Spectroscopy

For the elastic scattering involved in diffraction discussed in Chapter 6, the reflected waves have the same energy as those in the incident beam. In contrast to elastic scattering, **inelastic** scattering involves an energy loss due to the interaction of the beams with atoms due to vibrational modes. This is the fundamental difference between diffraction and **spectroscopy**. So, while a diffraction pattern refers to a graph where collected data all have the same energy, a spectrum is the plot for a data set that is a function of energy.

One common inelastic scattering is **Raman scattering**, named after Sir Chandrasakara Raman for his discovery of inelastic photon scattering (the Raman effect) in 1928 [117]. This technique is used in this thesis to measure the frequencies of vibrational modes in the materials under study. This chapter outlines some fundamental concepts behind the technique.

7.1 The basics of Raman spectroscopy

Raman spectroscopy is a useful experimental tool for measuring vibrational and rotational modes in a system through the inelastic scattering of monochromatic light from a laser, usually in the visible light range or around it in the near-ultraviolet/near-infrared ranges.

The main idea in Raman spectroscopy is that a laser hits a material and it is scattered by phonons that change the wave vector and energy of the beam. Because the wave vector of light is small, the energy shifts are also small but can be measured to a reasonably high resolution with laser beams of high enough intensity and high-precision analysis of the collected light through interferometric techniques. From these small energy shifts, the contributions from a single phonon can be isolated to discrete values for $\omega_p(q)$ (see Chapter 4). Only certain modes are

"Raman-active", which are those that change the crystal polarizability (see discussion in sections below). The main disadvantage of Raman scattering over other forms of inelastic scattering with larger energy shifts (namely, inelastic neutron scattering) is that a small change in wave vector implies that the phonons must have wave vectors close to zero. The measurable phonons are severely limited in reciprocal space compared to the range of wave vectors in the Brillouin zone, the measurable phonons are effectively at $k = (0, 0, 0)$, the Γ-point. But despite this limitation, Raman spectroscopy provides an accessible and high-resolution means of measuring the frequencies of certain Γ-point vibrational modes.

7.2 THE RAMAN EFFECT

The theoretical basis for Raman spectroscopy is the inelastic scattering of photons, the Raman effect, whereby a photon is scattered with a different energy than before it was scattered. The energy difference corresponds to the energy required to excite a molecule to a higher vibrational mode. When photons from a laser beam are absorbed by molecules, the molecules are excited to a virtual state. If they come back to their original state, then they will re-emit a photon of the same energy as the incoming photons. This is known as Rayleigh scattering. On the other hand, if a molecule relaxes into a vibrational state with a different energy than its original state, the emitted photon will have a different energy than the original one.

For a vibrational state with a lower energy than the initial state [see Figs. 7.1(a) and (c)], the emitted photon will have a higher energy than the original photon, and a phonon – with vibrational frequency ω_p and energy $\hbar\omega_p$ corresponding to the energy difference between the initial and final state – is absorbed into the crystal. This is **anti-Stokes** Raman scattering. An upshift in energy between the initial and excited vibrational state [see Figs. 7.1(b) and (d)] leads to an emitted photon of lower energy and an emitted phonon, which is the **Stokes** component

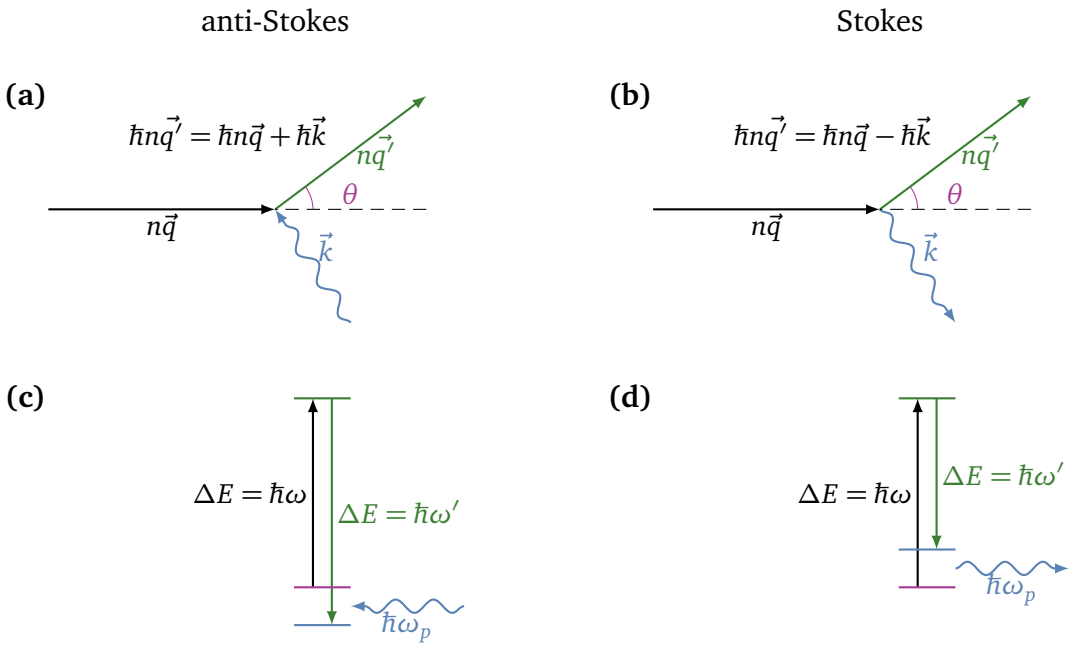

Figure 7.1: Feynman diagram for (a) anti-Stokes and (b) Stokes scattering, and schematics of energy levels for (c) anti-Stokes and (d) Stokes scattering. The wave vectors for a photon with initial free-space wave vector $\vec{q}$ and energy $\hbar\omega$ are scattered through an angle θ to a final free-space wave vector $\vec{q'}$ with energy $\hbar\omega'$. $n\vec{q}$ and $n\vec{q'}$ are the respective wave vectors in the crystal, where n is the index of refraction of the material. A phonon of wave vector $\vec{k}$ and energy $\hbar\omega_p$ is either absorbed [anti-Stokes, (a) and (c)] or emitted [Stokes, (b) and (d)].

of scattered radiation.

Conservation of energy and crystal moment in a one-phonon process leads to the following condition for the free-space (as opposed to within a crystal) wave vectors of incident and scattered photons, $\vec{q}$ and $\vec{q'}$, and their corresponding frequencies, ω and ω':

$$\hbar\omega' = \hbar\omega \pm \hbar\omega_p(\vec{k}). \tag{7.1}$$

$\omega_p(\vec{k})$ is the frequency of the absorbed/emitted photon, and the + and - signs correspond to anti-Stokes and Stokes scattering, respectively.

The Raman spectrum is typically represented as Raman shifts in wavenumbers with units of

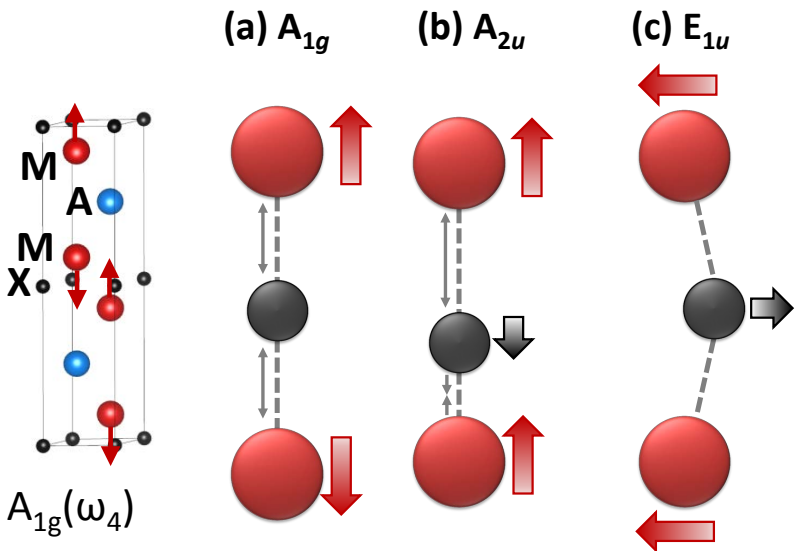

Figure 7.2: Schematic of three different normal modes, showing (a) A_{1g} (Raman-active), (b) A_{2u} (not Raman-active), and E_{1u} (not Raman-active).

inverse length (*e.g.* cm^{-1}). The wavenumber, Δw, is:

$$\Delta w = \left(\frac{1}{\lambda} - \frac{1}{\lambda'}\right), \tag{7.2}$$

where λ is the excitation wavelength, which corresponds to the energy $\hbar\omega$ in Fig. 7.1, and λ' is the wavelength of the photon emitted from Raman scattering. The wavenumber therefore corresponds to the vibrational mode of the absorbed/emitted phonon. The emitted photons will contain both Stokes and anti-Stokes scattering, which form a symmetric spectrum above and below $1/\lambda$.

7.3 RAMAN-ACTIVE MODES

Having established that phonon vibrational frequencies can be determined from the energy of photons that are emitted after a molecule relaxes to a vibrational state, we now move onto a discussion on what kind of excited states can be activated by Raman scattering.

In Raman scattering, light interacts with the electron clouds and bonds within a molecule, and the ability for a molecule to exhibit a Raman effect is determined by the amount of deformation of the electron cloud. Essentially, a vibrational mode is **Raman-active** if its displacements change the molecular polarization potential, and the Raman intensity depends on the polarizability change induced by a mode.

To take some examples, consider some vibrational modes of a 3-atom molecule, shown in Fig. 7.2. The symmetric A_{1g} mode [Fig. 7.2(a)] involves the simultaneous stretching and then simultaneous compression of bonds, which will lead to a distortion in the electron clouds. Indeed this mode is Raman-active in the MAX phases, and a schematic of this mode in the 211 phase is shown in the inset (left). The A_{2u} mode also involves bond stretching and compression [Fig. 7.2(b)], but in this case there is bond stretching and compression going on at the same time and the polarizability effects on each of the bonds end up canceling out. This mode is therefore not Raman-active. The E_{1u} mode involves stretching of the bonds as well, but because of the symmetry the bond stretching does not have a linear relationship with the displacements (it exhibits only second-order effects), and this mode would not be Raman-active either. Note that while the E_{1u} and and A_{2u} bonds are not Raman-active, they are in fact Infrared-(IR) active because IR spectroscopy is based on different selection rules. Since these two modes involve changes in dipole moment, absorption arises from the oscillations. On the other hand, the A_{1g} mode is not IR-active since it retains its center of symmetry.

The Raman-active modes in a crystal are a subset of the Γ-point normal modes. There are selection rules that govern which of the normal modes are Raman-active are controlled by symmetry. An analysis of the crystal symmetry with group theory can determine which modes are Raman-active for interpretation of a measured Raman spectrum.

Since phonon calculations give both the vibrational frequencies and the relative displace-

ments of phonon modes, an analysis of the phonon modes at $q = 0$ will also determine the frequencies of those activated by Raman spectroscopy. Taken together, much can be revealed about the dynamics of a crystal – not only the Γ-point vibrational character, but also the extent to which the chosen computational method for forces (ones based on first-principles, for example) can describe this character.

Chapter 8: Experimental and computational procedures

In this chapter, the procedures for carrying out the experimental and computational work in this thesis are summarized.

8.1 Experimental procedures

Here, a summary of the sample synthesis procedures is provided for the materials studied. The Raman spectroscopy and high-temperature neutron diffraction experiments are also described, along with the structure refinement strategies for the time-of-flight neutron diffraction data with MAUD and GSAS.

8.1.1 Sample synthesis

This section includes a brief description of the sample synthesis details for the bulk, polycrystalline samples of Ti_3SiC_2, Ti_3GeC_2, Ti_2AlN, Cr_2GeC, Ta_4AlC_3, Ta_2AlC, and Ti_4AlN_3 that were used for the experiments in this work. Since most of the samples used in the studies presented in this thesis were obtained from other sources and I did not fabricate most of them myself, references are provided for further details. For the studies on $Ti_5Al_2C_3$, one sample was used for the XRD and TEM, and another multi-phase ($Ti_5Al_2C_3$, Ti_2AlC, and Ti_3AlC_2) sample was used for the high-temperature neutron diffraction study.

Ti_3GeC_2: The Ti_3GeC_2 sample was fabricated by Dr. A. Ganguly [20], where stoichiometric mixtures of Ti, Ge, and C powders were ball milled and hot pressed in a two-step process (1173 K for 3 h, then 1873 K and $\sim$ 45 MPa for 6 h). The sample was then annealed for 48 h in an Ar

atmosphere at 1873 K to allow unreacted phases to react and to grow the grains. Details on the synthesis can be found in Ref. [20].

Ti_3SiC_2: The Ti_3SiC_2 samples was obtained from Dr. T. El-Raghy [118]. Ti, SiC and graphite were dry-mixed together in a V-blender for 2 h and cold pressed under 180 MPa into bars. The bars were then introduced in a graphite die and hot pressed at 1873 K for 4 h to produce coarse-grained microstructure. Further synthesis details can be found in Ref. [118].

Ti_3AlC_2: The Ti_3AlC_2 sample was also obtained from Dr. T. El-Raghy. The sample was prepared by hot pressing, HPing, pre-reacted Ti_2AlC (Kanthal, Hallstahammar, Sweden) and titanium carbide (Alfa Aesar,Ward Hill, MA) in a 1:1 ratio to make 3:1:2 stoichiometry of Ti:Al:C. Powders were ball milled for 24 h, placed in a graphite die, and heated in a graphite-heated hot press under a vacuum of 10^{-1} Torr at a rate of 500°C h^{-1} to 1400°C. It was held for 4 h under a pressure of $\sim$ 40 MPa before cooling.

Ti_2AlN: The Ti_2AlN sample was made by Dr. T. Scabarozi [34] by hot pressing Ti and AlN powders. The powders were stoichiometrically weighed, ball milled for 12 h, and dried in vacuum for 12 h at 423 K. The powder mixture was then poured and wrapped in graphite foil, placed in a graphite die, and heated under vacuum at 10 K/min in a graphite-heated hot press up to 1673 K and held for 8 h. During heating, $\sim$ 45 MPa was applied when the temperature reached 773 K and maintained throughout the run. A more detailed synthesis description can be found in Ref. [34].

Cr_2GeC: The Cr_2GeC sample was obtained from Dr. S. Amini, who fabricated the bulk, coarse-grained sample by hot pressing elemental powders. Powders of Cr, Ge, and C were stoichiometrically weighed and ball milled for 24 h, then dried under a mechanical vacuum for

24 h at 403 K. The powder mixture was poured and wrapped in graphite foil, then heated in a graphite die in a graphite-heated hot press under vacuum at 10 K/min up to 1623 K and held for 6 h. During heating, when the temperature reached 873 K, a pressure of $\sim$ 45 MPa was applied and maintained throughout the run. Further synthesis and characterization details on that sample can be found in Ref. [43]

Ta_4AlC_3 and Ta_2AlC: Samples of Ta_4AlC_3 and Ta_2AlC used in the Raman study were synthesized by M. Naguib by pressureless sintering [5]. Ta, Al, and C powders were mixed using ball milling for 12 h and then cold pressed under a pressure of 500 MPa. The cold pressed billets were then heated (10 K/min) to 1773 K for 1 h in an Ar atmosphere.

Ti_4AlN_3: The Ti_4AlN_3 sample used in the Raman study was made by hot isostatic pressing; for details see Ref. [119].

$Ti_5Al_2C_3$: To study the high-temperature structure and thermal motion of higher-order MAX phase $Ti_5Al_2C_3$, a 3-phase $Ti_5Al_2C_3$ –Ti_3AlC_2 – Ti_2AlC sample was used. The three-phase sample was prepared by cold-pressing pre-reacted Ti_2AlC powders that were commercially obtained (Kanthal, Hallstahammar, Sweden) and sintering at 2 h under a hydrogen atmosphere.

Binary carbides, TiC and WC: In addition to the MAX phases, binary carbides were also studied for benchmarking. Commercially obtained samples were used for TiC (Sigma Aldrich, $\leq$ 4 mu powder, $\geq$ 95% purity) and WC (Alfa Aesar, 99% purity, -100+270 mesh powder).

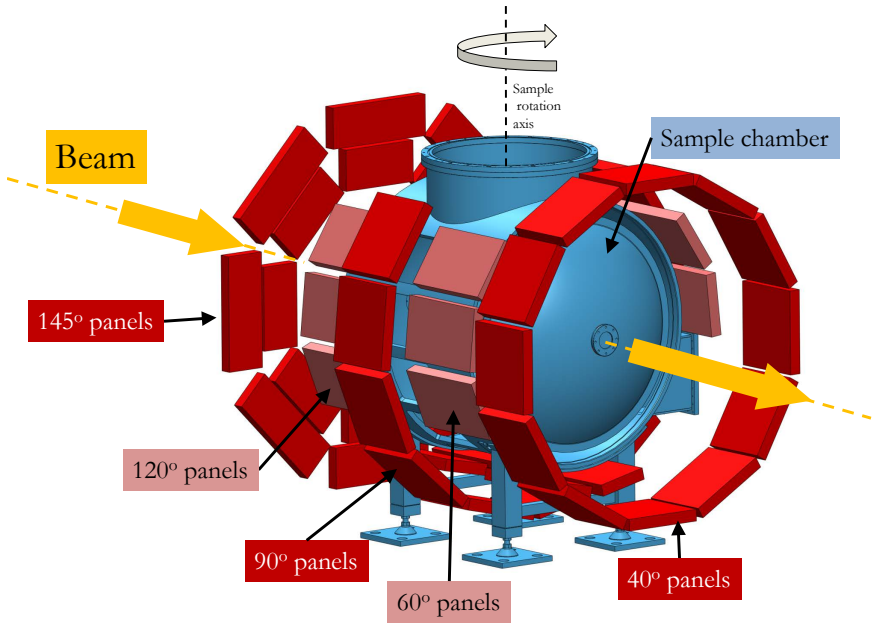

Figure 8.1: Experimental set-up for the High Pressure Preferred Orientation (HIPPO) diffractometer at the Lujan Center at Los Alamos National Laboratory, showing He^3 detector bank orientations, sample changer, and sample rotation axis.

8.1.2 High-temperature neutron diffraction

Experiments on the HIPPO

High temperature neutron diffraction (HTND) experiments were conducted on the High-Pressure Preferred Orientation Neutron diffractometer (HIPPO) [113, 120] at the Lujan Neutron Scattering Center, Los Alamos National Laboratory. For all phases studied, bulk samples were placed in a vanadium holder, mounted in an ILL-type high-temperature vacuum furnace with a vanadium setup (heating elements and heat shields), and heated at a rate of 200 K/min. TOF data were collected under vacuum at selected temperature points during heating and again during cooling to assess possible hysteresis. Temperature was measured by two type-K thermocouples inside the $\sim$ 15 cm high hot zone of the furnace about 5 cm above the beam center. At each chosen data collection temperature (see Table 8.1), neutrons were detected with 27 detector panels

Table 8.1: Summary of temperatures, detector bank diffraction angles, and sample rotation orientations around the vertical axes for each of the phases studied through high-temperature neutron diffraction. Unless otherwise indicated, data were collected during both heating and cooling for the temperatures listed. Further details on the instrument set-up can also be found in the references.

Phase [Ref.]	Collection temperatures (K)	Diffraction angles	Sample rotations
Ti_3SiC_2 [3]	573, 773, 973, 1373	40°, 90°, 144°	0°, 45°, 67.5°, 90°
Ti_3GeC_2 [3]	373, 575, 773, 873, 973, 1073, 1173, 1273	40°, 90°, 144°	0°, 45°, 67.5°, 90°
Ti_3AlC_2 [6]	373,† 473, 573,† 673, 773,† 873, 973,† 1073, 1173,† 1273	39°, 60°, 90°, 120°, 144°	0°, 22°, 45°
Ti_3SnC_2 [121]	473, 573,† 673, 773,† 873, 973,† 1073, 1173,† 1273	39°, 60°, 90°, 120°, 144°	0°, 22°, 45°
Cr_2GeC [2]	373,† 523,† 573,† 623,† 673† 774,† 873,† 973,† 1073,† 1173,† 1273†	40°, 90°, 144°	0°, 45°, 67.5°, 90°
Ti_2AlN [2]	373,⋆ 573, 773, 973, 1173, 1373	40°, 90°, 144°	0°, 45°, 67.5°, 90°
$Ti_5Al_2C_3$ [6]§	373,† 473, 573,† 673, 773,† 873, 973,† 1073, 1173,† 1273	39°, 60°, 90°, 120°, 144°	0°, 22°, 45°
TiC [4]	373,† 474, 573,† 673, 773,† 873, 973,† 1073, 1173,† 1273	39°, 60°, 90°, 120°, 144°	0°, 22°, 45°
WC [4]	373,† 474, 573,† 673, 773,† 873, 973,† 1073, 1173,† 1273	39°, 60°, 90°, 120°, 144°	0°

† Data collected during heating only.
⋆ Data collected during cooling only.
§ Multi-phase sample consisting of 38(±1) wt% $Ti_5Al_2C_3$, 32(±1) wt% Ti_2AlC, 18(±) wt% Ti_3AlC_2 and 12(±) wt% $(Ti_{0.5}Al_{0.5})Al$.

of ^{3}He detector tubes arranged on either three rings or five rings. The samples were measured at a series of rotation angles around the vertical axis to allow for full texture analysis at each temperature. Details about detector panel diffraction angles and rotation angles used for each phase are listed in table 8.1. The count time for each sample orientation and temperature was 15 minutes per orientation, during which the temperature and orientation were constant for data collection.

Structure refinement

The neutron data were analyzed with the Rietveld method using the General Structure Analysis System (GSAS) [110] and Material Analysis Using Diffraction (MAUD) [122] software packages. For the runs with Ti_3GeC_2, Ti_3SiC_2, Ti_2AlN, and Cr_2GeC, interference from the adjacent WNR facility was observed in the backscattered 144° bank at TOF between 15 and 18 ms; this region

was thus excluded from the refinements for those phases. Since hexagonal structures often exhibit preferred orientation [123], texture analysis was performed for selected data-sets using the entropy algorithm of Williams, Imhof, Matthies and Vinel (E-WIMV) [124] as implemented in MAUD. For the GSAS analysis, the data from detectors with the same nominal diffraction angle were integrated and subsequently the sample orientations (Table 8.1) were summed up, therefore randomizing preferred orientation effects. A script-controlled multi-histogram refinement against the data from the three or five detector banks was performed with GSAS. In all cases, the crystal structure parameters from the full texture model analyzed with MAUD agreed, within error bars, with the random texture assumed for the GSAS analysis. The weak texture observed (see Appendix A) was smeared out by integrating the individual detector panels of rings/banks with the same nominal detector angle and then integrating the data of each bank recorded for the different rotations. Therefore the data was analyzed using GSAS assuming a random texture. All additional phases found were refined in both GSAS and MAUD. See Appendix A for results on composition, texture, and diffraction statistics for each phase.

The GSAS script-controlled refinement with the *gsaslanguage* [125] ensures that identical refinement strategies were used on all compositions. The instrument alignment (DIFC parameter in GSAS) was fixed for the backscattered (144°) detector bank, which has the highest resolution, and refined for other banks in all the lowest-temperature runs. For subsequent runs, DIFC was fixed for all the banks. For the Ti_3GeC_2 and Ti_3SiC_2 samples, instrument calibration was performed using the room temperature lattice parameters determined previously from XRD for Ti_3SiC_2 ($a = 3.075$, $c = 17.7105$ [118]) and Ti_3GeC_2 ($a = 3.090$, $c = 17.764$ [20]). These parameters were extrapolated to the lowest temperatures, 573 K and 373 K, respectively, using the CTE values determined through the present HIPPO neutron diffraction study. With these lattice parameters as internal standards, DIFC was calibrated and fixed for the subsequent runs.

Table 8.2: Summary of secondary phases included in refinements and the refined parameters for each phase studied. Background refers to 16 background parameters of GSAS background function #1; DIFC is the instrument alignment parameter, which was calibrated to an internal standard only where noted (as described in the text); σ_1 is the peak width in the fitted profile; a and c are the lattice parameters; U_{ij} and U_{iso} are the anisotropic and isotropic thermal motion parameters, respectively; FRAC is the occupancy for a given atomic site. Phase fractions were refined for all samples with impurities listed. Refined parameters for secondary phases are followed by the phase(s) in brackets.

Phase [Ref.]	Impurities (wt%)	Refined parameters in GSAS
Ti_3SiC_2 [3]	None	Background, a, c, z_{TiI},z_{C}, DIFC†, σ_1, absporption, U_{ij}
Ti_3GeC_2 [3]	TiC (19.1±0.3), Ge (5.2±0.2)	Background, a, c, z_{TiI}, z_{C}, DIFC†, σ_1, absorption, U_{ij}, phase fractions, U_{iso}[TiC, Ge], a[TiC, Ge].
Ti_3AlC_2 [6]	TiC (18±1)	Background, a, c, z_{TiI}, z_{C}, absorption, U_{iso}, phase fractions, U_{iso}[TiC], a[TiC]
Ti_3SnC_2	Ti_2SnC, TiC, Fe	
Cr_2GeC	Cr_2O_3 (4.9±0.3), graphite (< 1)	Background, a, c, z_{Ti}, DIFC, σ_1, absorption, U_{ij}, phase fractions, U_{iso}[Cr_2O_3, graphite], a[Cr_2O_3, graphite].
Ti_2AlN	None	Background, a, c, z_{Ti}, DIFC, σ_1, absorption, U_{ij}, phase fractions, FRAC_{N}.
$Ti_5Al_2C_3$ [6]	Ti_2AlC (32±1) wt%), Ti_3AlC_2 (18±1), $Ti_{0.5}Al_{0.5}$)Al (12±1)	Background, a, c, z_{TiI}, z_{TiII}, z_{C}, absorption, U_{iso}, phase fractions, U_{iso}[Ti_3AlC_2, Ti_2AlC, $Ti_{0.5}Al_{0.5}$)Al], a[Ti_3AlC_2, Ti_2AlC, $Ti_{0.5}Al_{0.5}$)Al], c[Ti_3AlC_2, Ti_2AlC], FRAC_{Ti}[$Ti_{0.5}Al_{0.5}$)Al]
TiC [4]	None	Background, DIFC, U_{iso}, a, absorption.
WC [4]	None	Background, DIFC, U_{ij}, a,c absorption.

† Calibrated to an internal standard.

Refined parameters were generally 16 background parameters of GSAS background function #1, phase fraction of additional phases, lattice parameters, atom positions with symmetry constraints, instrument alignment (DIFC, only for the first run), peak width (σ_1 in the profile function), absorption, scale factor, and thermal motion parameters. The refined parameters are listed in Table 8.2 for each of the phases studied.

8.1.3 Raman spectroscopy

The Raman spectroscopy measurements reported in this thesis were carried out by M. Naguib. Raman spectra were collected from bulk samples at ambient temperatures using a Renishaw inVia spectrometer (Peltier-cooled CCD array detector). Argon ion laser radiation (514.5 nm) was focused to a spot size of ~1 mm with an incident power of 2.0±0.8 mW. The peak positions and full width at half maximum (FWHM) were obtained from Lorentzian peak fitting. The experimental resolution of the peak positions is ≤1 cm^{-1}.

8.2 COMPUTATIONAL DETAILS

In order to calculate the phonon spectrum, the force constant matrix must be computed. Earlier chapters address considerations for computing the phonon spectrum and atomic displacements (see Chapter 4) and relevant background on first-principles calculations (Chapter 5). This section summarizes the parameters used in the first-principles calculations, including details about the functionals, potentials, and *k*-point mesh.

8.2.1 First-principles phonon calculations on pure MAX phases

For phonon calculations, $2 \times 2 \times 1$ supercells were used, which consisted of 24, 32, and 48 atoms for the 211, 312, and 413 phases, respectively. For TaC and TiC, $2 \times 2 \times 2$ supercells consisting of 64 atoms were used. For WC, a $2 \times 2 \times 2$ supercell with 8 atoms was used. First-principles

calculations based on DFT were performed using the projector-augmented wave (PAW) method [126], as implemented in the VASP code [127–129]. The exchange-correlation function used was the Perdew-Burke-Ernzerhof (PBE) generalized gradient approximation (GGA) [98]. The plane-wave cutoff was set to 500 eV, and the total energy was converged to 10^{-8} eV with a Γ-centered k-point grid of $6 \times 6 \times 4$.

Real-space force constants in the supercells were calculated using density functional perturbation theory (DFPT) [104] implemented in the VASP code. The frequencies were calculated from the force constants using the Phonopy code [130, 131]. The displacements of atoms from their equilibrium positions, U_{ij}, are calculated according to Eq. 4.55 using the eigenvectors, $\mathbf{e}_{\alpha,R,p}(q)$ and phonon frequencies, $\omega_p(q)$, determined from the diagonalization of the force constant matrix.

8.2.2 Phonon calculations on vacancies

To explore the effect of vacancies on thermal motion, the ADPs are also calculated for a $2 \times 2 \times 1$ Ti_3GeC_2 supercell with one vacant Ge site, representing a material with 12.5% ordered vacancies. The break in symmetry results in 35 single displacements and the frozen phonon method was used to compute the forces induced by finite displacement through the Hellmann-Feynman theorem. The frequencies are calculated from the force constants using the phonopy code, and the temperature-dependent $\langle u^2 \rangle$ values are calculated from Eq. 4.55.

Part II

Results

Chapter 9: First-principles phonon calculations

Before presenting any experimental findings, a summary of the predicted lattice dynamics for select MAX phases will be presented. This chapter provides an overview of results from first-principles phonon calculations in the harmonic approximation. Table 9.1 shows a summary of the phases studied in this thesis through first- principles phonon calculations, including the methods that were employed for the theoretical and experimental results presented.

Table 9.1: Materials studied in this thesis through first principles phonon calculations. The theoretical and experimental studies performed are summarized for each phase, including phonon band structures, phonon partial density of states (PDOS), Raman frequencies, calculations of the atomic displacement parameters (ADPs), volume-dependent phonon calculations in the quasi-harmonic approximation (QHA), the Grüneisen parameter, high-temperature neutron diffraction (HTND), and x-ray diffraction (XRD).

		Theoretical studies						Experimental studies		
	Phase	band	PDOS	Raman	ADPs	QHA	Grün	HTND	XRD	Raman
523	$Ti_5Al_2C_3$				✓			✓	✓	
413	α-Ta_4AlC_3	✓	✓	✓					✓	✓
	β-Ta_4AlC_3		✓	✓						
	Ti_4AlN_3	✓	✓	✓	✓					✓
	Nb_4AlC_3			✓						
312	Ti_3SiC_2	✓	✓		✓		✓	✓		
	Ti_3GeC_2	✓	✓		✓		✓	✓		
	Ti_3SnC_2	✓		✓	✓	✓		✓	✓	✓
	Ti_3AlC_2	✓			✓			✓		
211	Ti_2SnC			✓	✓					✓
	Ti_2AlN	✓	✓	✓	✓			✓		
	Ti_2AlC	✓		✓	✓			✓		
	Cr_2GeC	✓	✓	✓	✓			✓		
	Ta_2AlC	✓		✓	✓					✓
	V_2GaC			✓	✓					
	V_2GeC			✓	✓					
	V_2AsC			✓	✓					
	V_2AlC			✓	✓					
	Cr_2AlC			✓	✓					
	Nb_2AlC			✓	✓			✓		

In all cases, first-principles phonon calculations were carried out for the phases summarized, but different representations of the phonon modes are presented – e.g. phonon density of states, Raman-active frequencies, mean-squared displacements – depending on the experimental comparison or trends sought. In this chapter, the phonon band structures and site-projected partial density of states are presented for select MAX phases. In subsequent chapters, the Raman frequencies (Chapter 10), atomic displacement parameters (Chapters 11 and 12), temperature-dependent volumes from the quasi-harmonic approximation (Chapter 13), and mode-dependent Grüneisen parameters (Chapter 15) will be presented, along with relevant experimental results.

9.1 PHONON BAND STRUCTURES AND VIBRATIONAL MODES

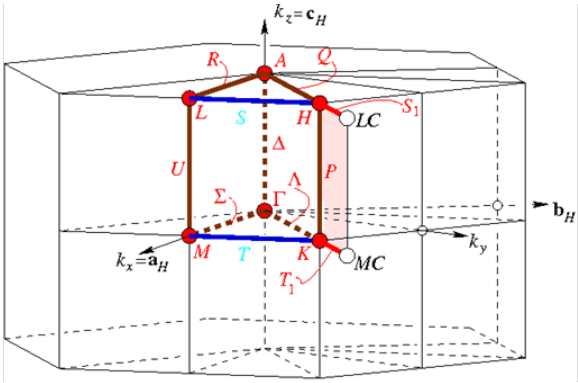

Figure 9.1: The brillouin zone for $P6_3/mmc$, labeling high-symmetry points and paths.

The phonon band structure is a useful way of representing the lattice dynamics of a periodic system because the phonon frequencies can be represented as a set of normal modes of a wave vector, k. In a three-dimensional periodic system of atoms, atomic vibrations cause wave propagations throughout the lattice. Therefore, wave vector coordinates (see Fig. 9.1) can often be more useful than real-space coordinates of the particles for investigating the nature of vibrations in a material. From the first-principles phonon calculations (see Section 4.2), the frequency dispersion of the normal modes can be computed along a k-point path as a phonon

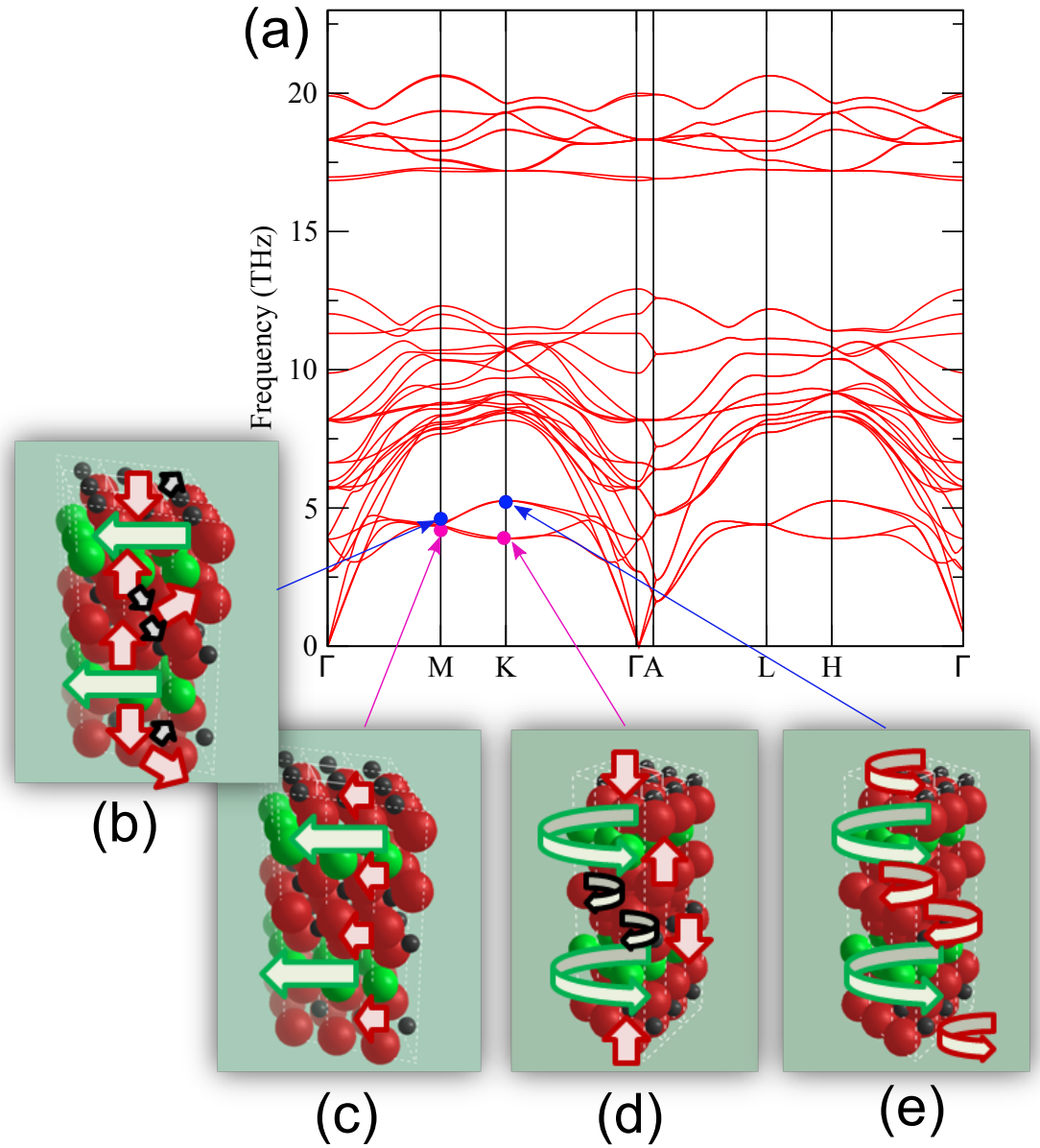

Figure 9.2: (a) Phonon band structure of Ti_3SiC_2 and schematics of vibrational modes associated with the eigenvectors for select q-points corresponding to k vectors M [(b) and (c)] and K [(d) and (e)] in the low-frequency bands. The red atoms and arrows represent Ti; green corresponds to Si, and black corresponds to C.

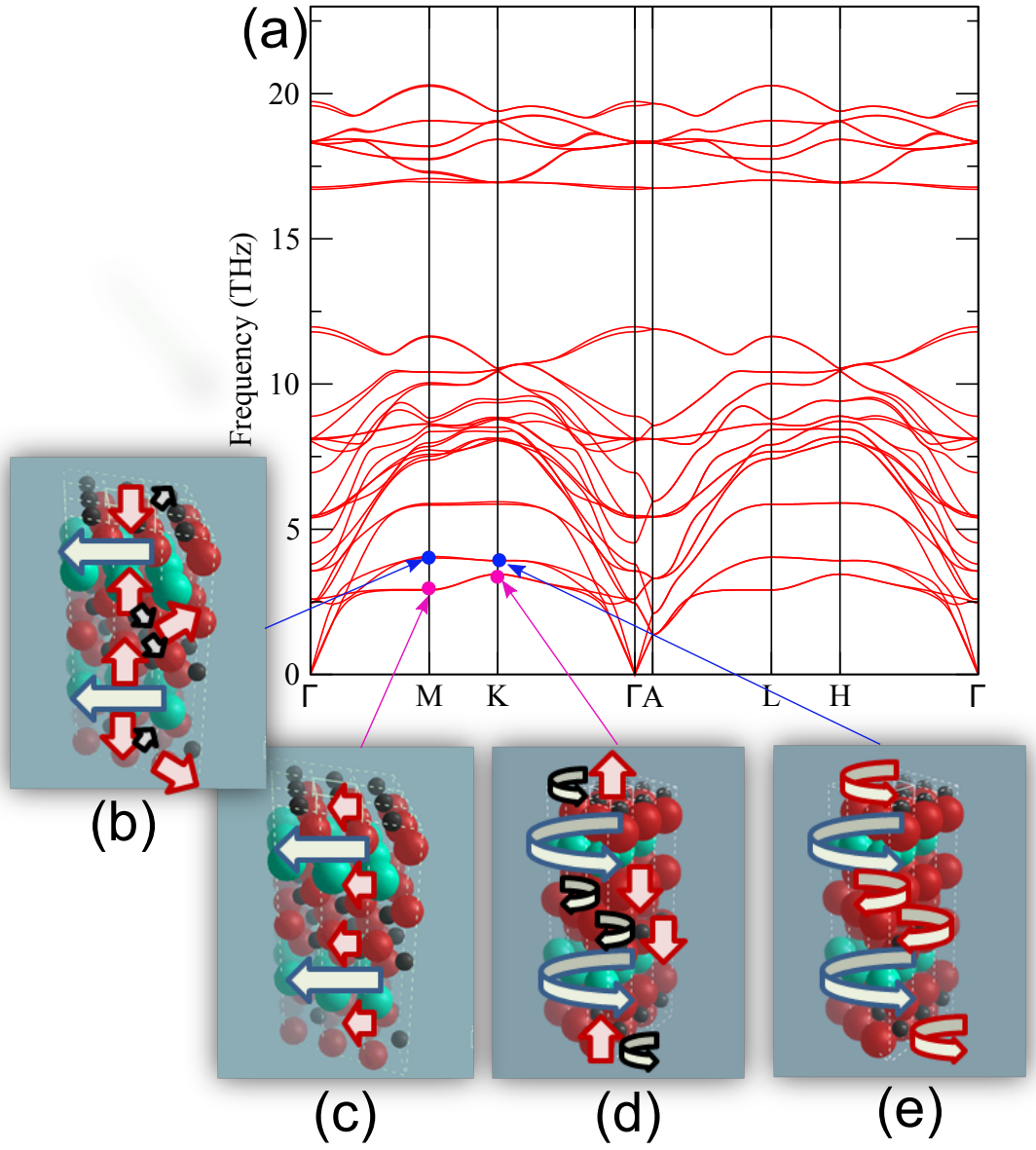

Figure 9.3: (a) Phonon band structure of Ti_3GeC_2 and schematics of vibrational modes associated with the eigenvectors for select q-points corresponding to k vectors M [(b) and (c)] and K [(d) and (e)] in the low-frequency bands. The red atoms and arrows represent Ti; blue corresponds to Ge, and black corresponds to C

band structure.

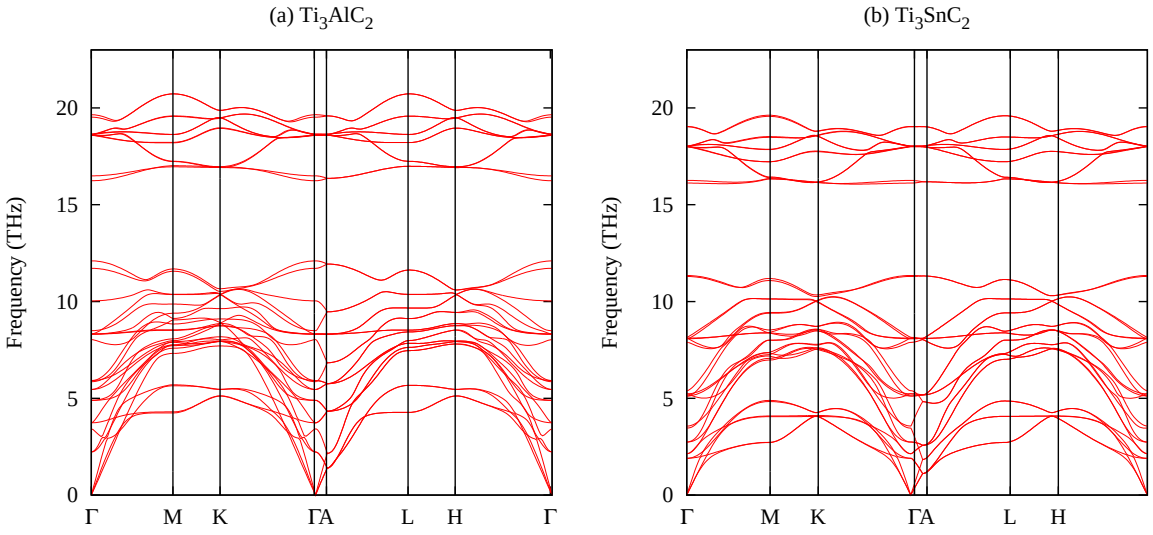

Figure 9.4: (a) Phonon band structures calculated from first-principles phonon calculations for select 312 MAX phases, (a) Ti_3AlC_2 and (b) Ti_3SnC_2

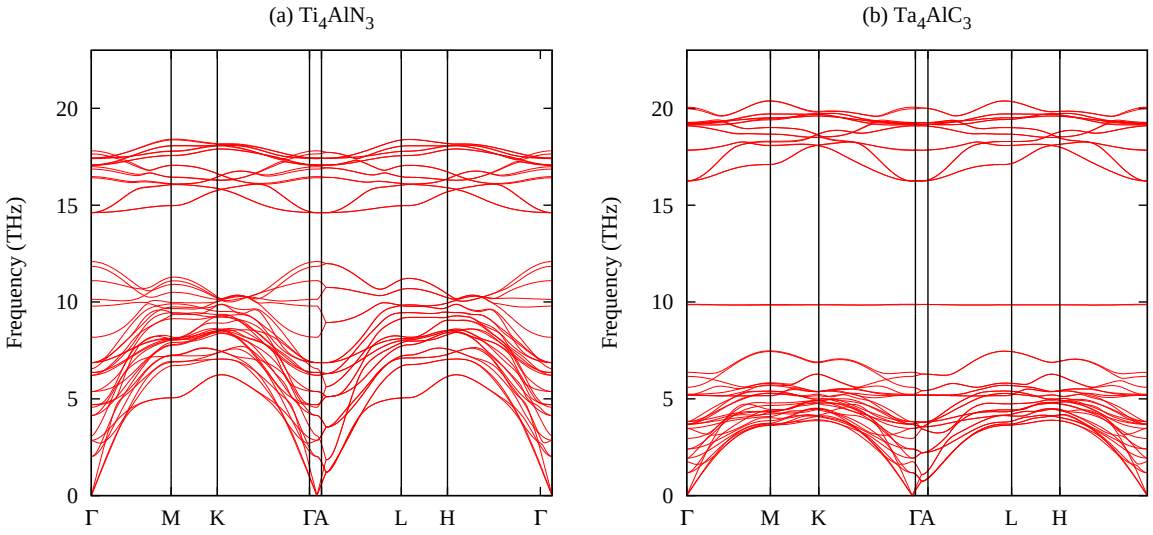

Figure 9.5: Phonon band structures calculated from first-principles phonon calculations for select 413 MAX phases, (a) Ti_4AlN_3 and (b) Ta_4AlC_3.

Figures 9.2(a) and 9.3(a) show the phonon band structure for Ti_3SiC_2 and Ti_3GeC_2, respectively, along the path $\Gamma(0,0,0) \rightarrow M(\frac{1}{2},0,0) \rightarrow K(\frac{1}{3},\frac{1}{3},0) \rightarrow \Gamma(0,0,0) \rightarrow A(0,0,\frac{1}{2}) \rightarrow L(\frac{1}{2},0,\frac{1}{2}) \rightarrow H(\frac{1}{3},\frac{1}{3},\frac{1}{2}) \rightarrow \Gamma(0,0,0)$. The band structure along $\Gamma \rightarrow M \rightarrow K \rightarrow \Gamma$ is similar to that along $\Gamma \rightarrow L \rightarrow H \rightarrow \Gamma$, indicating that the phonons are not very dispersive along the z

axis. Both structures exhibit similar features in their phonon band structures, especially for the higher-frequency optical bands above 17 eV. This is because those bands correspond to the vibrational modes of the carbon atom, which have the same environment in both materials (i.e. within Ti_3C_2 octahedra). The low-frequency bands, however, exhibit variations in their frequency dispersions, indicating differences in vibrational character of the *A* element, Si and Ge.

Figures 9.2(b)-(e) and 9.3(b)-(e) show the real-space displacements corresponding to the eigenvectors for select *q*-points on the low-frequency phonon bands, which are indeed governed primarily by the motion of the Ti (red) and Si (green) or Ge (blue) atoms. The carbon atoms participate in some of the modes, but the amplitudes are considerably lower than those of the Ti and Si/Ge atoms. Note that unlike the Raman-active modes, which will be discussed in Chapter 10, these are for wave vectors away from the Γ point that involve motion which is not constrained to one plane and may have imaginary components that lead to nonlinear motion, such as the orbiting motion at *K* [Figs. 9.2(d), 9.2(e), 9.3(d), and 9.3(e)].

The most prominent differences between the phonon band structures of Ti_3SiC_2 and Ti_3GeC_2 are in the low-frequency bands at the *M* and *K* points. The *M*-point low-frequency bands in Ti_3SiC_2 are degenerate at *M* [Figs 9.2(b) and (c)] whereas the corresponding modes in Ti_3GeC_2 [Figs 9.3(b) and (c)] split off into two distinct frequencies. On the other hand, at the *K* point the low-frequency bands in the Ti_3GeC_2 band structure [Figs. 9.3(d) and (e)] are closer together than those in the Ti_3SiC_2 band structure [Figs. 9.2(d) and (e)]. This suggests different interactions between the phonon bands for each of the two structures, which is in line with the correlated motion that will be presented in Chapter 15. These real-space displacements a high-symmetry points will serve as a useful tool for understanding correlation effects in atomic motion. Furthermore, in a general sense the real-space displacements such as the ones shown play a major role in predicting mean-squared atomic displacements of atoms in select

MAX phases (Chapter 12) because their sum enters the equation for $\langle|U|^2\rangle$ to account for the differences in interatomic forces.

Phonon band structures for two other 312 phases, Ti_3AlC_2 and Ti_3SnC_2, are shown in Figs. 9.4(a) and (b), respectively. Again, the high-frequency phonon modes are similar to those in Ti_3SiC_2 (Fig. 9.2) and Ti_3GeC_2 (Fig. 9.3), while the low-frequency modes vary between the four phases. The bands with the lowest frequencies correspond to those in Ti_3SnC_2, which includes a flattened band in addition to the two low-frequency bands typical of the other three 312 phases. This is likely associated with the higher mass of Sn that leads to lower-frequency *A* atom vibrations and causes the degenerate phonon states to split into different states.

Figures 9.5(a) and (b) show the phonon band structures for two of the 413 phases, Ti_4AlN_3 and Ta_4AlC_3, respectively. The high-frequency bands are slightly depressed in the nitride Ti_4AlN_3 compared to Ta_4AlC_3, while the low-frequency bands in Ta_4AlC_3 are significantly lower than those in Ti_4AlN_3. This is also observed in Ti_2AlN and Ta_2AlC [Figs. 9.6(a) and (c), respectively]. The high-frequency bands correspond to the C or N atom vibrations, and are lower in the nitrides. Since C and N are comparable in mass, this suggests that the *M*-N bonds should be stiffer than the *M*-C bonds, at least in defect-free materials. The decrease in frequency for the lower bands is a result of the heavier 5*d* Ta atom, whose vibrational frequency is lower than the frequency corresponding to the lighter Ti atom. The flat band at ∼10 THz in the Ta_4AlC_3 [Fig. 9.5(b)] and Ta_2AlC [Fig. 9.6(c)] band structures also result from the higher mass of Ta, since the modes dominated by the Ta vibrations split from the Al modes and lead to a localized Al band. This flattened band corresponds to modes involving Al vibrations along the *z* direction. On the other hand, for the vibrational modes in all the other phases shown in Figs. 9.4, 9.5, 9.6, which contain lighter 3*d* metals (i.e. Ti and Cr), the Ti/Cr atoms are similar in mass to the *A* atoms and thus overlap with the *A* vibrational modes. This leads to dispersive low-frequency bands

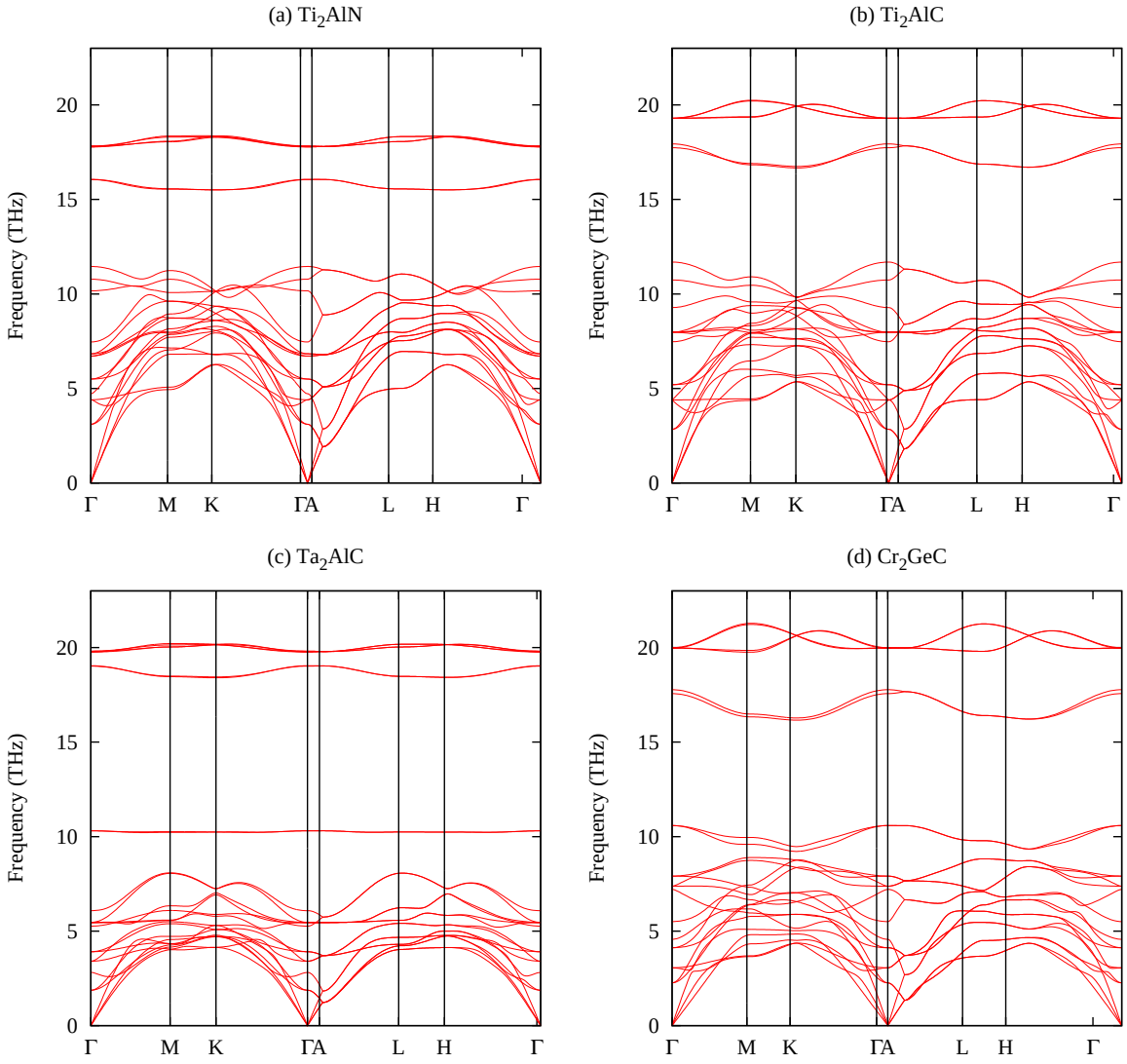

Figure 9.6: (a) Phonon band structures calculated from first-principles phonon calculations for select 211 MAX phases, (a) Ti_2AlN, (b) Ti_2AlC, (c) Ta_2AlC, and (d) Cr_2GeC.

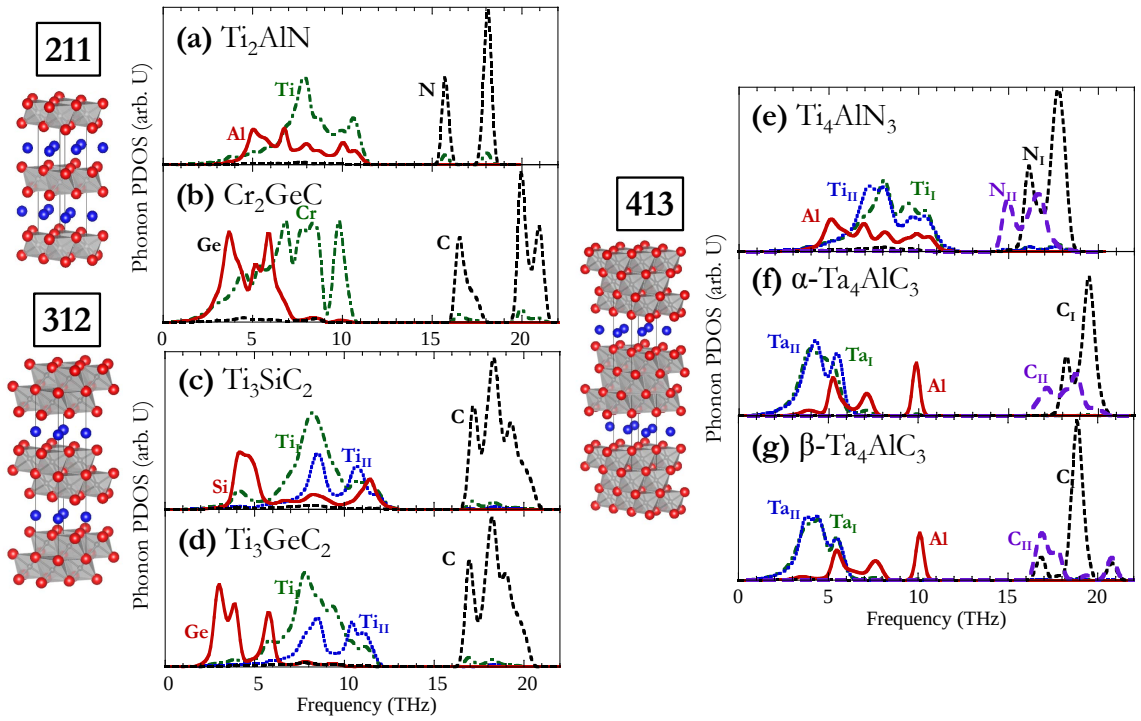

Figure 9.7: Partial phonon density of states of select $M_{n+1}AX_n$ phases: 211 phases (a) Ti_2AlN and (b) Cr_2GeC; 312 phases (c) Ti_3SiC_2 and (d) Ti_3GeC_2; and the 413 phases (e) Ti_4AlN_3, (f) α-Ta_4AlC_3 and β-Ta_4AlC_3.

that are shared by the M and A atoms – that is, the phonon modes involve the simultaneous vibrations of the M and A atoms.

The fact that the lack of overlap between the M and A vibrational frequencies in the Ta-containing MAX phases leads to such different dispersions for the lower bands in their phonon band structures [Figs. 9.5(b) and 9.6(c)] illustrates the importance of mass in the vibrational behavior of these phases. This is also evidenced by the experimental and calculated Raman frequencies in Ti_4AlN_3 and Ta_4AlC_3, which will be discussed in Chapter 10.

9.2 PHONON PARTIAL DENSITY OF STATES

The phonon behavior of atoms can also be projected onto a site-dependent phonon partial density of states (PDOS), which represents the number of vibrational modes for each site as a

function of frequency. Figures 9.7(c)-(d) show the phonon PDOS for the two 312 phases in Figs 9.2 and 9.3, respectively, along with two 211 MAX phases, Ti_2AlN and Cr2GeC [(a) and (b), respecitvely], and the 413 phases Ti_4AlN_3 (d) and α- and β-Ta_4AlC_3 [(e) and (f)]. See Appendix B.4 for further details on the differences between the α and β polymorphs of Ta_4AlC_3.

These phases were chosen because of the availability of materials for experimental studies – specifically high-temperature neutron diffraction – which will be presented and discussed in Chapter 12. For now, they serve as a useful tool for understanding thermal conductivity and bonding within the MAX phases, at least from a theoretical standpoint within the harmonic approximation and for pure, defect-free crystals.

From the phonon partial density of states, it can be seen that the phonon frequencies of the Ge states are lower than those of the Al and Si states since Ge is heavier. Furthermore, the spread of the Si and Al states [Figs. 9.7(b), (c) and (d)] indicates more decoupling of the $x-y$ and z vibrational states, since the eigenvectors of the dynamical matrix for the lower-frequency states correspond to atomic vibrations within the basal plane ($x-y$), while the higher-frequency states are vibrations perpendicular to the basal plane (z). In Ti_3SiC_2, the Si atom vibrating within the basal plane, represented by peak between 3 and 6 THz, is highly localized. Note that in Ref. [132], where a $4\times4\times1$ supercell was used, this band is even narrower. This localized peak manifests itself as a higher degree of anisotropy for Si thermal vibrations than for Ge as determined by first-principles calculations, which will be discussed in the following section.

As indicated by the spread of the phonon dispersions discussed in the previous section, in the MAX phases with the lighter 3d metals, Ti and Cr, the M and A phonon states show a broad overlap. In Figs. 9.7(a)-(e), the A atom vibrations (red PDOS curves) are generally lower in frequency than the M atom vibrations (green and blue PDOS curves). On the other hand, in the Ta_4AlC_3 polymorphs [Figs. 9.7(f) and (g)], the heavy Ta atoms are much lower in frequency

than the Al states. This leads to a localized Al state, which manifests in the band structures as a flattened band at around 10 THz [Fig. 9.5(b)].

There are a few interesting features in the set of phonon PDOS plots. First of all, the PDOS curve for the Al atom in Ti_2AlN is the same as that in Ti_4AlN_3, showing that the vibrational behavior of Al is not affected by the stacking of the Ti-N octahedra – a result that is not surprising. Similarly, the Ti PDOS plots for Ti_3SiC_2 and Ti_3GeC_2 are also similar, indicating that the chemistry of the *A* atom does not affect the Ti vibrations. On the other hand, the large difference in mass between Ti and Ta not only leads to a different PDOS curve for the Ta and Ti atoms themselves [Figs. 9.7(e) and (f), respectively], but also causes the Al PDOS curve to be dramatically different in shape. This is a strong indicator of correlation of the *M* and *A* vibrations, and also the importance of *M* atom mass in the vibrational behavior. To further explore these phenomena from an experimental standpoint, the Raman-active modes are studied in the next chapter for Ti_4AlN_3 and Ta_4AlC_3, among other relevant 211 and 312 phases.

9.3 SUMMARY

In this chapter, the theoretical results of the first-principles phonon calculations are presented, including phonon band structures and phonon PDOS plots. It was shown that the low-frequency bands correspond primarily to the *M* and *A* atom vibrations. The high-frequency bands are similar among all the carbides and all the nitrides because they are primarily controlled by C or N atom vibrations. Schematics of the displacements associated with the low-frequency modes at select *q*-points are shown for Ti_3SiC_2 and Ti_3GeC_2. The differences in their low-frequency bands suggest different vibrational character of the *M* and *A* atoms. It is also shown that changing the *A* atom element affects the phonon PDOS for the *M* element, and vice versa, especially when there are considerable differences in mass.

Chapter 10: Theory and experiment: Raman-active modes

Calculations of the phonon band structures provide useful theoretical tools for representing the dynamical behavior of materials. When it comes to actually measuring the phonon dispersion, however, the task is challenging, especially with materials systems such as the MAX phases where pure, single-crystal samples are not easily accessible. An experimental technique that gives a portion of the experimental phonon dispersion picture is Raman spectroscopy, which provides information about the vibrational frequencies of certain Γ-point modes (as discussed in Chapter 7). Even though this is far from capturing the entire dispersion of phonon bands, it provides a few data-points in the phonon frequency dispersion that may be compared with the phonon band structure calculated from first-principles calculations. This chapter focuses on calculated and measured Raman frequencies and their relationship to mass and bond stiffness in select MAX phases.

10.1 Raman-active mode calculations

Of all the vibrational phonon modes for a material, only some are Raman-active. The highest-symmetry modes are at the Γ point, and those are the only modes that can be Raman-active. There are $3N$ phonon bands, where N is the number of atoms in a unit cell. Even with some of them being degenerate at the Γ point, there are still only a few of the $3N$ Γ-point phonon modes that are Raman-active, which are governed by symmetry rules in group theory (see Chapter 7).

The Γ-point frequencies are computed through the first principles phonon calculations, as presented in chapter 9, and group theory rules are used to determined which of the modes are Raman-active. The eigenvectors of the phonon modes give the direction and relative

Table 10.1: Raman-active modes for 211, 312, and 413 MAX phases showing number of modes for each irreducible representation and the atoms involved in each vibrational mode, where the yellow ✓ represents allowed vibrations and a gray ✗ represents no vibrations in that mode.

			Irr. Rep: E_{2g}	E_{1g}	A_{1g}
211	Number of modes:		2	1	1
	Atoms involved (Wyckoff):	M $(4f)$	✓	✓	✓
		A $(2d)$	✓	✗	✗
		X $(2a)$	✗	✗	✗
312	Number of modes:		3	2	2
	Atoms involved (Wyckoff):	M_{I} $(4f)$	✓	✓	✓
		M_{II} $(2a)$	✗	✗	✗
		A $(2b)$	✓	✗	✗
		X $(4f)$	✓	✓	✓
413	Number of modes:		4	3	3
	Atoms involved (Wyckoff):	M_{I} $(4e)$	✓	✓	✓
		M_{II} $(4f)$	✓	✓	✓
		A $(2c)$	✓	✗	✗
		X_{I} $(4f)$	✓	✓	✓
		X_{II} $(2a)$	✗	✗	✗

displacement amplitudes associated with each of the normal modes. An example of the phonon band structure and Raman frequency selection is shown for the 413 phase Ti_4AlN_3 in Fig. 10.1, which has the highest number of bands and Raman-active modes (discussed below). Also shown on the right is the site-projected phonon DOS, which illustrates which atoms are involved in the range of vibrational frequencies. The circles mark the frequencies of the ten Raman-active modes, where three of them are in the high-wavenumber region corresponding to N atom vibrations (purple markers), and the other seven correspond to Ti and Al vibrations (red, blue, and green markers).

Table 10.1 lists the number of Raman-active modes for each irreducible representation and the atoms involved in the 211, 312, and 413 Raman modes. Note that the check marks and x marks only indicate whether the atoms are allowed to vibrate in that mode due to symmetry

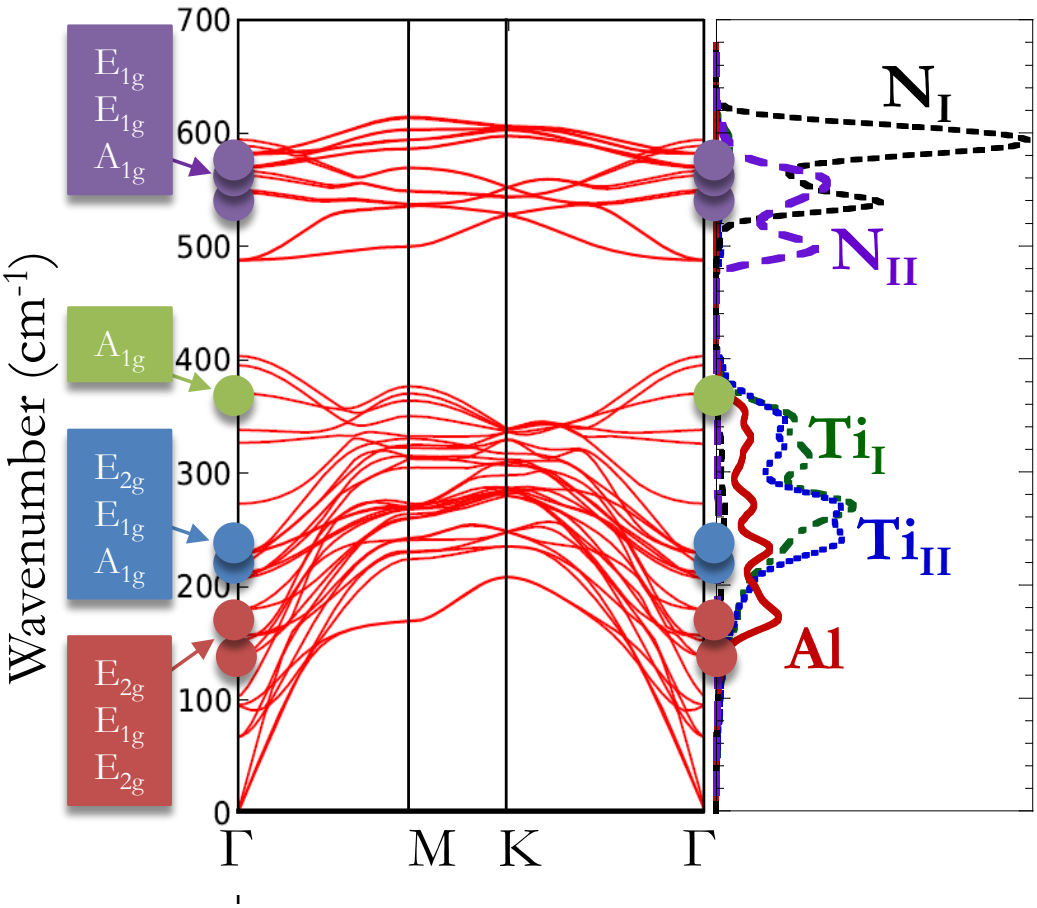

Figure 10.1: Phonon band structure of Ti_4AlN_3 with markers at the Γ-point Raman-active modes. Right panel shows the phonon site-projected density of states.

based on their Wyckoff positions and do not indicate their amplitudes of vibration, which vary from mode to mode. Schematics of the Raman-active modes in 211, 312, and 413 phases are shown in in Figs. 10.2, 10.3, and 10.4, respectively. Summaries of their modes and the atoms involved are presented in Table 10.1.

In the 211 phases, with 8 atoms/unit cell, there are a total of $3N = 24$ vibrational modes, out of which four are Raman active. Three are only Raman-active modes ($A_{1g} + 2E_{2g}$) and one is both Raman- and infrared-active (E_{1g}) [41, 77, 133]. Because of the symmetry of the Wyckoff positions, no first-order Raman-active modes in the 211 phases are associated with vibrations of

the X sublattice. The 312 phases, on the other hand, have a total of seven Raman-active modes ($2A_{1g} + 2E_{1g} + 3E_{2g}$), out of which six are observed experimentally [41, 77, 134]. There are ten Raman-active modes ($3A_{1g} + 3E_{1g} + 4E_{2g}$) in the 413 phases, where the A_{1g} and E_{1g} modes involve the M_{I}, M_{II}, and X_{II} layers and the E_{2g} modes involve the M_{I}, M_{II}, A, and X_{II} layers (Fig. 10.4). Note that the schematic in Fig. 10.4 is consistent with the phonon PDOS in Fig. 10.1, where the high-wavenumber bands correspond to $\mathrm{N_I}$ vibrations. Indeed, modes $\omega_1 - \omega_7$ involve the M and A atoms primarily, while modes $\omega_8 - \omega_{10}$ involve vibrations of the X atoms.

10.2 EXPERIMENTAL RAMAN SPECTRA COMPARED TO THEORY

The phases studied experimentally in this thesis are the 413 phases Ti_4AlN_3 and Ta_4AlC_3, the 312 phase Ti_3SnC_2, and the 211 phases Ti_2SnC and Ta_2AlC. These phases are of interest because the Ta-containing phases involve heavy M atoms (Ta), while the Sn-containing phases contain heavy A atoms (Sn). The 413 phase Ti_4AlN_3 is also studied mostly for benchmarking and validation of our methodology, even though the Raman spectrum for that phase had been previously reported.

The Raman spectra and comparisons between theory and experiment in the following subsections are divided into two groups:

- Section 10.2.1: The first of the two sections will focus on the 413 phases Ti_4AlN_3 and the Ta_4AlC_3 polymorphs, along with the related 211 phase Ta_2AlC.
- Section 10.2.2: The next section will focus on the Sn-containing phases Ti_3SnC_2 and Ti_2SnC.

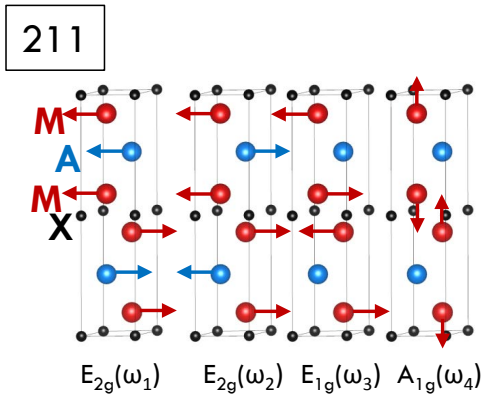

Figure 10.2: Schematics of the atomic displacements associated with the Raman-active modes in 211 M_2AX phases.

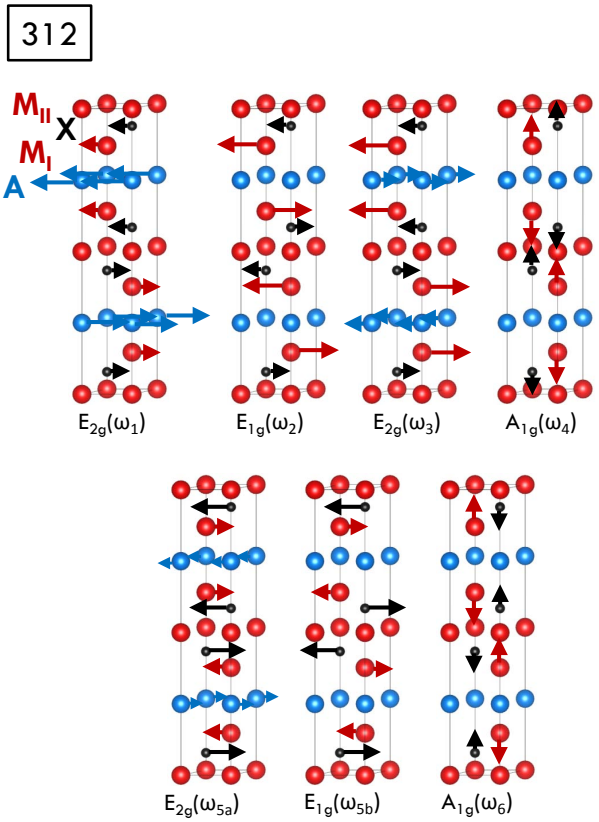

Figure 10.3: Schematics of the atomic displacements associated with the Raman-active modes in 312 M_3AX_2 phases.

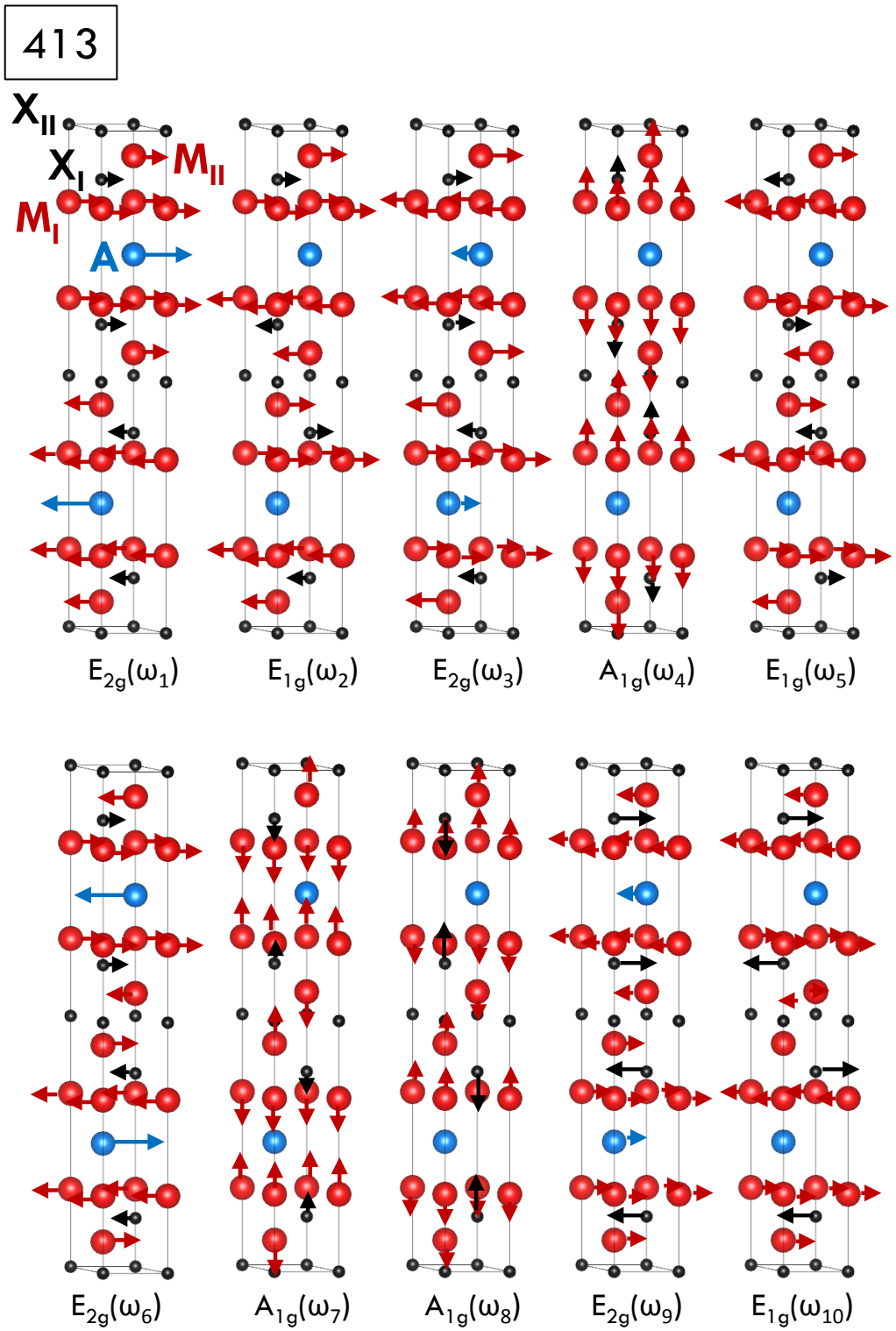

Figure 10.4: Schematics of the atomic displacements associated with the Raman-active modes in 413 M_4AX_3 phases.

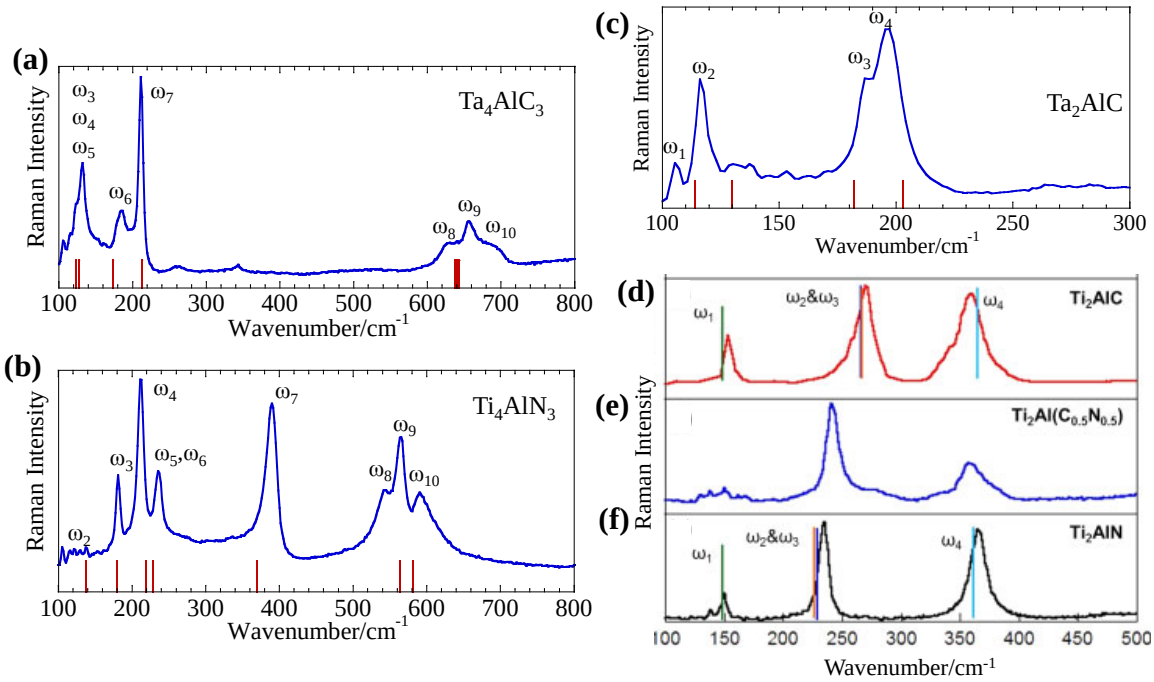

Figure 10.5: First-order Raman spectra of (a) Ta_4AlC_3, (b) Ti_4AlN_3, and (c) Ta_2AlC from this work, where the red markers below represent the calculated frequencies. Also shown for comparison are the Raman spectra of (d) Ti_2AlC, (e) $Ti_2Al(C_{0.5}N_{0.5})$, and (f) Ti_2AlN from Ref. [135].

10.2.1 First-order Raman scattering of Ti_4AlN_3, Ta_4AlC_3, and Ta_2AlC

In this section, the results for two 413 MAX phases, Ta_4AlC_3 and Ti_4AlN_3, are reported and the displacements associated with their modes are investigated. The 211 phase Ta_2AlC is also studied for benchmarking. The main purpose of this study was to analyze the symmetry of each of the observed Raman modes in the 413 MAX phases – which had never been previously reported – and to present the Raman spectrum of α-Ta_4AlC_3 for the first time. Furthermore, I performed DFT calculations on both α-Ta_4AlC_3 and β-Ta_4AlC_3 to compare the vibrational behavior of the two polymorphs, even though β-Ta_4AlC_3 was not available for experimental investigation. Details on sample synthesis and experimental procedures for Raman scattering are summarized Sections 8.1.1 and 8.1.3, respectively. Further sample characterization through

Table 10.2: Experimental and theoretical wavenumbers, ω, in cm^{-1}, symmetry assignment, and FWHM of the Raman modes of the 413 phases. Values in parentheses are from Ref. [77].

		Ti_4AlN_3			Nb_4AlC_3	α-Ta_4AlC_3			β-Ta_4AlC_3
Mode	Irr. Rep.	ω_{expt}	$FWHM_{expt}$	ω_{calc}	ω_{calc}	ω_{expt}	$FWHM_{expt}$	ω_{calc}	ω_{calc}
ω_1	E_{2g}	-	-	95	82	-	-	65	44
ω_2	E_{1g}	132 (132)	8.4 (9.7)	138	106	-	-	80	68
ω_3	E_{2g}	181 (181)	7.3 (7.6)	179	158	115	2.3	123	120
ω_4	A_{1g}	211 (208)	13.3 (5.5)	219	169	123	4.8	127	125
ω_5	E_{1g}	236 (235)	13.3 (9.4)	229	176	132	9.5	128	123
ω_6	E_{2g}	-	-	229	182	188	19.0	173	179
ω_7	A_{1g}	387 (386)	18.9 (11.2)	370	291	211	6.5	212	201
ω_8	A_{1g}	546 (539)	46.8 (9.3)	563	626	629	21.5	637	637
ω_9	E_{2g}	563 (563)	9.5 (7.9)	582	610	657	19.3	641	627
ω_{10}	E_{1g}	596 (592)	42.4 (10.6)	581	612	685	27.8	643	627

XRD can be found in Appendix A.2, and HRTEM of the stacking sequence can also be found in the paper in Appendix B.4.

I will also present the calculated Raman-active modes of two other MAX phases relevant to this work, Nb_4AlC_3, Ti_4AlN_3. The calculated phonon energies for the ten Raman-active modes in Ti_4AlN_3, α-Ta_4AlC_3 and β-Ta_4AlC_3 are listed in Table 10.2, along with the experimental fitted positions for the Raman modes of Ti_4AlN_3 and α-Ta_4AlC_3. Table 10.3 lists the calculated and measured wavenumbers of the Raman bands for Ta_2AlC, along with those from Ref. [41]. Also listed for comparison are the Raman frequencies for Ti_2AlC calculated in this thesis, along with experimental and calculated values from Refs [135]. Good agreement is found between the experimental and calculated values, with differences in wavenumber between experimental and calculated band positions of less than 10%. For Ti_4AlN_3, there is good agreement between the experimental Raman peak positions determined herein and those reported in Ref. [77] with wavenumber differences below 2%. It should be noted that some of the calculated frequencies and the assignment of the modes for Ti_4AlN_3 are different in Ref. [77]; the updated values are listed herein.

Table 10.3: Experimental and theoretical wavenumbers, ω, in cm^{-1}, symmetry assignment, and FWHM of the Raman modes of Ta_2AlC and Ti_2AlC. Values in parentheses are from Ref. [41]; values in brackets are from Ref. [77].

		Ta_2AlC			Ti_2AlC		
Mode	Irr. Rep.	ω_{expt}	$FWHM_{expt}$	ω_{calc}	ω_{expt}	$FWHM_{expt}$	ω_{calc}
ω_1	E_{2g}	117 (118)	4.37	114 (115)	[150]	[13]	146 (151) [149]
ω_2	E_{2g}	186 (188)	7.45	182 (185)	[268]	[10]	266 (256) [262]
ω_3	E_{1g}	131 (130)	15.05	130 (132)	[262]	[6]	266 (270) [248]
ω_4	A_{1g}	197 (199)	11.95	203 (199)	[365]	[12]	360 (366) [387]

Assuming a FWHM of $\sim$10 cm^{-1}, and considering the instrumental resolution, Raman modes less than $\sim$10 cm^{-1} apart from each other may appear as one broad band. On the basis of these assumptions, first principles calculations predict four distinct modes for Ta_4AlC_3, and seven for Ti_4AlN_3 in the 100-800 cm^{-1} range. For Ta_2AlC, there are four calculated Raman-active modes.

This is generally consistent with the measured data. From the Raman spectra of the two 413 phases [Figs. 10.5(a) and (b)], it is clear that Ti_4AlN_3 and Ta_4AlC_3 differ largely in band positions.In Ti_4AlN_3, there is a band at 546 cm^{-1} (reported at 539 cm^{-1} in [77]) that is lower than the calculated value for the predicted A_{1g} mode ($\omega_{8,calc} = 563 cm^{-1}$), which involves primarily the longitudinal antiparallel displacements of the N_I atoms. In Ta_4AlC_3, the three high-wavenumber Raman bands assigned to ω_8, ω_9, and ω_{10} are wider spread and located at higher wavenumbers. In both cases, the middle band in the group of three [labeled ω_9 in Figs. 10.5(a) and (b)] has the highest intensity. A possible explanation is defects such as N or C vacancies, leading to a local decrease in molecular symmetry resulting in peak splitting, broadening of the Raman signature, or higher-order scattering. This is consistent with the assignment of the modes, where $\omega_8 - \omega_{10}$ correspond primarily to the vibration of the C or N atoms (Fig. 10.4).

The wavenumbers of all four Raman bands in Ta_2AlC [41] are all significantly lower than those of Ti_2AlC [77, 135] [compare Figs. 10.5(c) and (d)], which differs only in the M element

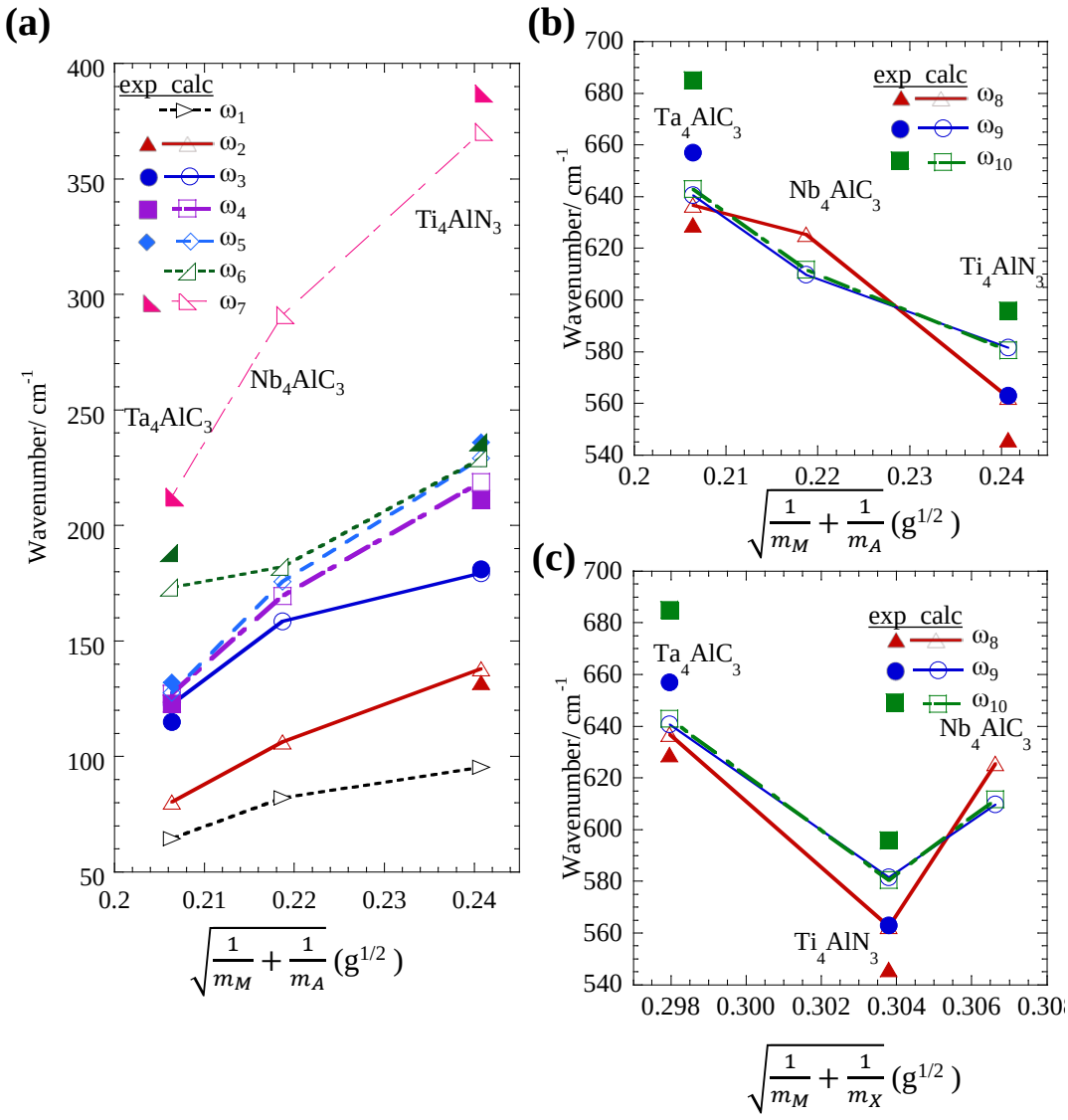

Figure 10.6: Plots of ω vs. $\sqrt{1/m_{\text{red}}}$ for the 413 phases, where m_{red} is the reduced mass: (a) shows modes $\omega_1 - \omega_7$ using the reduced mass for M and A atoms. Modes $\omega_8 - \omega_{10}$ are shown using the reduced mass of (b) M and A atoms and (c) M and X atoms. Open symbols and the lines correspond to calculated values; solid symbols represent experimental values.

(*i.e.* Ta is replaced by Ti). Note that in Ta_2AlC the frequency of ω_3 is so depressed that it falls below that of ω_2, which is because the $1g$ modes (ω_3 and ω_4) only involve the M atoms and are therefore severely affected by the mass of M (*i.e.* the heavy mass of Ta). On the other hand, the $2g$ modes (ω_1 and ω_2) involve both M and A (see Table 10.1), so the common Al element between Ti_2AlC and Ta_2 AlC cause their frequencies to be similar.

Like the 211 phases, the low-wavenumber Raman bands in the 413 phases (ω_1 through ω_7) are lower in Ta_4AlC_3 than in Ti_4AlN_3. Again, at least some of this difference can be attributed to the larger atomic mass of Ta compared with Ti (as discussed below). On the other hand, modes ω_8, ω_9, and ω_{10} are at higher wavenumbers in Ta_4AlC_3 than in Ti_4AlN_3, which implies, as discussed below, that other factors other than mass alone contribute to the differences.

To further explore this aspect, the frequencies of the Raman-active modes in Nb_4AlC_3 are calculated, for which the mass of the M element, Nb, is between that of Ti and Ta. The values obtained from *ab initio* phonon calculations are shown in Table 10.2. To understand the effects of mass and bonding and distinguish between the two factors,we begin with the basic equation for the frequency of a bond, assuming harmonic oscillation given by $\omega = \sqrt{k/m}$, where k is the bond stiffness and m is the mass. For a two-body system, m can be represented by the reduced mass:

$$m_{\text{red}} = \frac{1}{\frac{1}{m_1} + \frac{1}{m_2}} \tag{10.1}$$

and, therefore,

$$\omega = \sqrt{\frac{k}{m_{\text{red}}}} = \sqrt{k\left(\frac{1}{m_1} + \frac{1}{m_2}\right)} \tag{10.2}$$

In Figs 10.6(a) and (b), the vibrational frequency of each mode is plotted as a function

of $\sqrt{1/m_{red}}$. The reduced mass, corresponding to the M and A atoms, is used as a first approximation, because the low wavenumber Raman-active modes involve these two atoms (see Fig. 10.4). According to Eqn. 10.2, if the bond stiffness does not change with mass, then the dependence would be linear with a slope of k. For $\omega_1 - \omega_7$, the plots are close to linear with positive slopes, indicating that mass differences are responsible for at least some of the differences in frequencies.

The same plot for $\omega_8 - \omega_{10}$ [Fig. 10.6(b)] shows a different trend, with a negative slope for ω versus $\sqrt{\frac{1}{m_{red}}}$ in all cases. It is thus clear that the nature of the features associated with these Raman-active modes cannot be represented by the harmonic oscillation governed by the M-A bonds with a constant bond stiffness. Taking into account that these vibrational modes involve primarily the X atoms (Fig. 10.4), this result is not surprising. However, using the same model, a plot of ω versus $\sqrt{\frac{1}{m_{red}}}$, where now the masses considered are those of the M and X atoms, is also nonlinear [Fig. 10.6(c)]. More importantly, the overall slope is again negative, which implies that in this case, bond stiffness is much more a function of chemistry than mass. Furthermore, the results imply the following order for the bond stiffness values: Ta–C>Nb–C>Ti–N. This is consistent with what is known about the M–X bonds. For example, TaC has the highest melting point of these compound, with the melting points of TaC, NbC, and TiN at 3983, 3600, and 2949 °C, respectively [136].

In addition to the measured Raman spectrum and calculated Raman bands for α-Ta_4AlC_3, I also carried out first principles calculations on β-Ta_4AlC_3 to predict its Raman-active modes. The atomic displacements associated with the ten Raman-active modes are shown in Fig. 10.4 for α-Ta_4AlC_3 and the calculated wavenumbers are listed in Table 10.2 for both polymorphs. The calculated displacements associated with the Raman-active modes in β-Ta_4AlC_3 (not shown) were found to be essentially the same as α-Ta_4AlC_3, except for slight differences in the M_{II} atom

displacement at ω_1. The only major differences in wavenumber are in the modes at ω_9 (E_{2g}) and ω_{10} (E_{1g}), which occur at lower wavenumbers for β-Ta_4AlC_3. Both these modes primarily involve the shear vibrations of the X_I atoms within the basal plane. Because ω_9 and ω_{10} are predicted to occur at lower wavenumbers in β-Ta_4AlC_3, the wavenumber of these modes relative to the longitudinal mode at ω_8 (A_{1g}) would also be reversed, where ω_8 is predicted to be higher than ω_9 and ω_{10} in β-Ta_4AlC_3. This could be indicated experimentally by a difference in shape, relative intensity, or frequency for the three high-wavenumber bands in β-Ta_4AlC_3 compared with α-Ta_4AlC_3.

10.2.2 First-order Raman scattering of Ti_3SnC_2 and Ti_2SnC

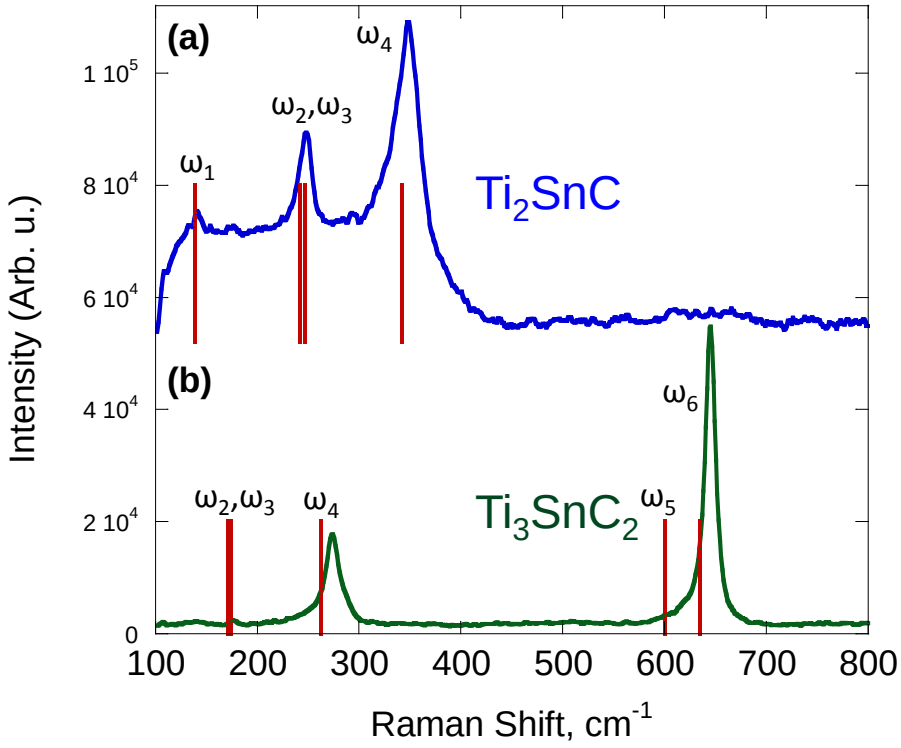

Figure 10.7: First order Raman spectra of (a) Ti_2SnC, and (b) Ti_3SnC_2. The red vertical lines represent the calculated frequencies of the Raman-active moods for each phase.

Along with the 211 and 413 Ta-containing MAX phases, the 211 and 312 Sn-containing phases are studied. Whereas the former contain heavy M elements, the latter have heavy A

Table 10.4: Experimental and theoretical wavenumbers, ω, in cm^1, symmetry assignment, and FWHM of the Raman modes of Ti_2SnC.

Mode	Irr. Rep.	ω_{expt}	$FWHM_{expt}$	ω_{calc}
ω_1	E_{2g}	140.4	7.4	139
ω_2	E_{2g}	247.0	22.3	242
ω_3	E_{1g}			247
ω_4	A_{1g}	347.4	27.2	342

Table 10.5: Experimental and theoretical wavenumbers, ω, in cm^1, symmetry assignment, and FWHM of the Raman modes of Ti_3SnC_2 and Ti_3SiC_2. Values in parentheses are from Ref. [77];values in brackets are from Ref. [135];all other values are from this work.

		Ti_3SnC_2			Ti_3SiC_2		
Mode	Irr. Rep.	ω_{expt}	$FWHM_{expt}$	ω_{calc}	ω_{expt}	$FWHM_{expt}$	ω_{calc}
ω_1	E_{2g}	-	-	63	(159)	(10.5)	129 (145) [129]
ω_2	E_{1g}	176.3	4.0	174	(226)	(5.0)	190 (217) [190]
ω_3	E_{2g}			171	(279)	(5.6)	221 (253) [222]
ω_4	A_{1g}	273.8	16.8	263	(301)	(N/A)	274 (301) [273]
ω_{5a} †	E_{2g}	-	-	601	(625)	(5.5)	611 (590) [610]
ω_{5b} †	E_{1g}	-	-	601	-	(5.5)	611 (622) [611]
ω_6	A_{1g}	645.0	10.9	635	(673)	(4.7)	667 (657) [666]

† There are two modes at ω_5; nomenclature of modes is chosen to be consistent with that used in previous literature [77, 135].

elements. Table 10.4 lists the measured and calculated Raman frequencies of Ti_2SnC. The Raman spectrum is shown in Fig. 10.7(a), where the red markers represent the calculated frequencies. The agreement between the calculated and measured frequencies is excellent. Since the Sn atoms are heavier than Al, the frequencies for Ti_2SnC are lower than for Ti_2AlC (see Table 10.3). Although the *A* atoms only participate in modes with frequencies of ω_1 and ω_2 (see Fig. 10.2), this applies to all four of the modes – even the ones that involve only the *M* atoms, ω_3 and ω_4 – which demonstrates that the *M* vibrational behavior is affected by the *A* atom mass and that the *M* and *A* vibrational behavior is coupled.

The effect of mass is also apparent from the 312 phase Ti_3SnC_2 compared to other 312 phases. Table 10.5 lists the calculated and experimental Raman frequencies for Ti_3SnC_2, along

with the experimental and calculated frequencies for Ti_3SiC_2 from previous work [77, 135] and calculated frequencies from this work for comparison with Ti_3SnC_2. The Raman spectrum for Ti_3SnC_2 is also shown in Fig. 10.7(b). In Ti_3SnC_2, the frequencies of ω_1 and ω_3 are significantly depressed compared to Ti_3SiC_2 while the differences between the two phases for ω_4-ω_6 are not as severe. Note that ω_2 in Ti_3SiC_2 is lower than ω_3, which is also the case with most of the other 312 phases [135]; however, in Ti_3SnC_2 $\omega_3 < \omega_2$. This is because for the 312 phases, the A atoms do not participate in the $1g$ vibrational modes (see Table 10.1), so the effect of the A-atom mass on ω_2 (with irreducible representation E_{1g}) is not as drastic as the effect on the E_{2g} modes, ω_1 and ω_3, which involve heavy Sn vibrations (blue atoms in Fig. 10.3).

Another interesting observation regarding the theoretical A and M interaction is that there is a greater difference between Ti_3SiC_2 and Ti_3SnC_2 for calculated ω_6 (667 vs. 635 cm^{-1}) than for ω_5 (611 vs. 601 cm^{-1}). This is a subtle distinction, but it is in line with the directions of the displacements associated with the modes and the atoms involved. Since the $E_{1g}$and A_{1g} modes in the 312 phases only involve the M_I and X atoms (see Table 10.1), this implies that the A_{1g} mode, ω_6, is more affected by the A atom than the E_{1g} mode, ω_5. Since the difference between the two modes is that the A_{1g} mode involves vibrations along the c axis while the E_{1g} involves vibrations within the basal planes (see Fig. 10.2), this demonstrates that the vibrations of Ti_I – the Ti atom adjacent to A – along the c axis are constrained by the A atom vibrations. Experimentally, there is no peak corresponding to the calculated frequency of the E_{1g} mode in Ti_3SnC_2 (Fig. 10.7), which may be because the mode actually occurs at higher frequencies and merges with ω_6. This idea is further supported by the fact that the ω_{5a} peak in Ti_3SiC_2 occurs at a higher frequency than that predicted.

10.3 SUMMARY

In this chapter, an overview of the number of Raman modes, their irreducible representations, and the atoms involved was first presented for 211, 312, and 413 MAX phases. The Raman frequencies measured through Raman spectroscopy lend credibility to theoretical phonon frequencies, serving as reference points for the frequencies of select Γ-point modes to validate the DFT calculations. The calculated and experimental Raman frequencies were presented for Ta_2AlC, Ti_2SnC, Ti_3SnC_2, Ta_4AlC_3, Ti_4AlN_3. It was shown that the low-frequency modes in both the Sn- and Ta-containing phases are much lower when compared to the Si- and Ti-containing phases, respectively, because of the increase in mass. The effects of mass and bond stiffness are discussed based on the relationship between the Raman frequencies and the reduce masses for atom pairs. In the 413 phases, it is shown that mass plays a large role in the differences in vibrational frequencies between the different chemistries, while the high-frequency modes – which are governed primarily by the motion of the C or N atoms – include stiffness effects that must account for the observed Raman frequency differences.

Chapter 11: Predicted mean-squared atomic displacement parameters

Raman spectroscopy provides information about the vibrational frequencies for the normal modes that are activated by light around the visible spectrum, but it does not describe the equilibrium thermal vibrations for atoms, nor does it give information about the vibrational amplitudes of the atoms. Indeed first-principles phonon calculations can be supplemented with experimental frequencies to provide information about the atomic vibrations involved – as shown in Chapter 10 – but the Raman spectrum itself does not provide any direct experimental measurements of the atomic displacements. Furthermore, while the phonon partial density of states serves to decompose the phonon modes into site-dependent representations of the number of phonon states and their distribution with energy, it does not give any information about the actual real-space motion of the atoms. Because the position of an atom and its average displacement is information that is readily accessible through diffraction techniques – *i.e.*, from the Debye-Waller factor – it is instructive to compute the average amplitude of each atom as well. From the first principles phonon calculations, each mode – that is, each frequency and q-point, $\omega(q)$ – has an eigenvector that can be represented as real-space vibrational behavior, such as the schematics shown at the bottom of Figs. 9.2 and 9.3.

In this chapter, the predicted equivalent isotropic and anisotropic temperature-dependent ADPs are presented for select 312 M_3AX_2 and 211 M_2AX phases. The dependences of the thermal motion parameters on the mass and valence electron configuration for both the M and A elements are also explored. This chapter is purely theoretical and discusses only the calculated mean-squared displacements for ideal, defect-free, single-phase, stoichiometric crystals. This theoretical study sets the stage for discussing the experimentally observed atomic motion, which

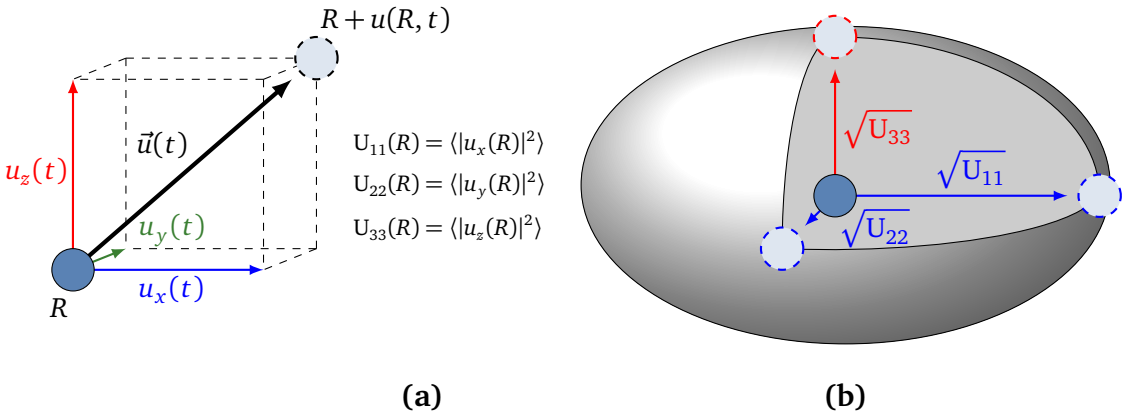

Figure 11.1: (a) Model of the atomic displacement of atom site R at time t, $\vec{u}(R)$, and its Cartesian components, u_x, u_y and u_z. (b) Schematic of the mean-squared atomic displacement parameters of atom site R, which are the time-averaged squared Cartesian components of $\vec{u}(t)$.

will be introduced in later chapters.

11.1 NOTATIONS FOR ADPS

In Chapter 4, the theory behind the computation of the mean-squared displacement parameters was summarized. An equation was derived for computing the the mean-squared atomic displacement from phonon calculations (Eq. 4.55), which gave $\langle |u_\alpha(R)|^2 \rangle$ in terms of the phonon frequencies and eigenvectors. The Cartesian component, α, is the projection of the vector $\vec{u}$ onto the x,y, or z axis. A schematic is shown in Fig. 11.1(a) and for an instantaneous displacement $\vec{u}(t)$ for atom R.

From neutron diffraction, the anisotropic Debye-Waller factor is given by a tensor **U** whose diagonal terms, U_{11}, U_{22}, and U_{33}, give the mean-squared displacements along the a, b and c axes, respectively [Fig. 11.1(b)]. Since a=b for hexagonal crystals, the displacement is equivalent in any direction within the basal plans, so $U_{11} = U_{22} = \langle |u_x|^2 \rangle = \langle |u_y|^2 \rangle$. Also, the displacement along the c axis is equal to the z component of $\vec{u}$ so $U_{33} = \langle |u_z|^2 \rangle$. Note that a

lower case U denotes a displacement in units of length, while an upper case U is a mean-squared value in units of length squared (*e.g.* Å^2).

In the remainder of this thesis, the notation U_{ij} is used for consistency. The values of U_{11} and U_{33} presented in this chapter are therefore $\langle|u_\alpha|^2\rangle$ calculated from Eq. 4.55 for $\alpha = x$ and z, respectively. In addition, U_{eq} is calculated from U_{11} and U_{33} with equation 6.29. It is computed in this way (rather by the averaging of $\vec{u}$ in all directions, for example) for comparison with the Debye-Waller factor.

11.2 PREDICTED TEMPERATURE-DEPENDENT ATOMIC DISPLACEMENT PARAMETERS

Although atomic displacements in the hexagonal MAX phases occur at different amplitudes in different directions, a good starting point is the equivalent **isotropic** mean-squared atomic displacements, U_{eq}, which represent the square of the average displacement of a given atom site from its equilibrium position, $U_{eq} = \langle|\vec{u}|^2\rangle$. The temperature dependences of the calculated equivalent isotropic thermal motion parameters are shown in Fig. 11.2 for the four 312 carbides, Ti_3AlC_2, Ti_3SiC_2, Ti_3GeC_2, and Ti_3SnC_2. To date, there are only five known MAX phases with 312 stoichiometry, the missing one being Ta_3AlC_2. The four Ti-containing 312 phases are chosen for this theoretical investigation to in order to work with a set of phases that differ only in the *A* atoms. Note that all four of these phases are also measured experimentally through high-temperature neutron diffraction, which will be discussed in Chapter 12. All these phases differ only in their *A* element, where Si, Ge, and Sn have the same valence election configurations but significantly different masses. Al is next to Si in the periodic table with one fewer electron than the other elements.

For the two Ti atoms and the C atom, the mean-squared atomic displacements are similar. Given that the four phases have common elements in all three of those sites, this is not entirely

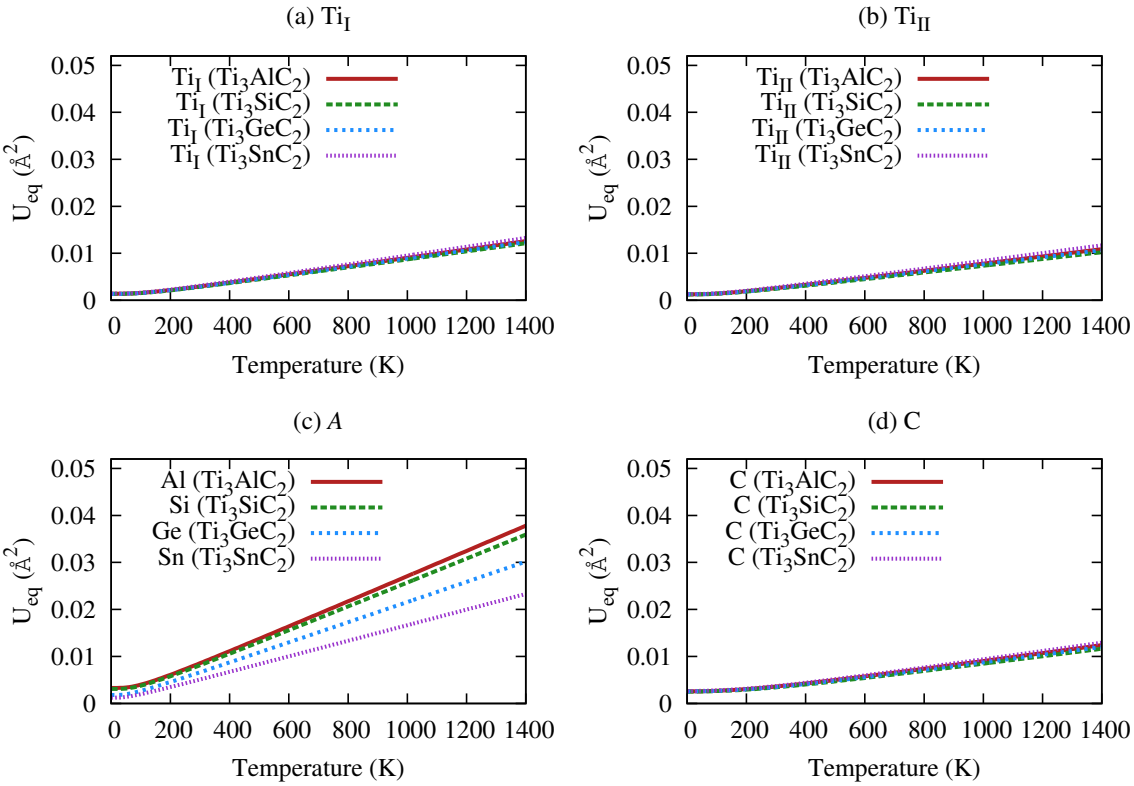

Figure 11.2: Temperature dependence of the equivalent isotropic atomic displacement parameters determined by first-principles phonon calculations for the 312 phases Ti_3AlC_2, Ti_3SiC_2, Ti_3GeC_2, and Ti_3SnC_2 showing U_{eq} for (a) Ti_I, (b) Ti_{II}, (c) *A*, and (d) C .

surprising. However, this robustness of the ADPs with variations in chemistry of neighboring atoms is not at all a rule, and it will be later shown that this is not true of all MAX phases atoms. As we have seen in the previous chapters, the motion of an atom does not only depend on the atom itself; if that were the case, lattice dynamics could be described by a bunch of independent harmonic oscillators. It is the potential between interacting bodies that controls the bonding and is one of the major components of the Hamiltonian that governs dynamical behavior in solids. Therefore, the fact that the mean-squared atomic displacement of the Ti and C do not vary significantly with variations in the *A* element is telling of the bonding in Ti and C and shows that they are more or less rigid units that are the last to compromise in terms of ADPs. Further, the

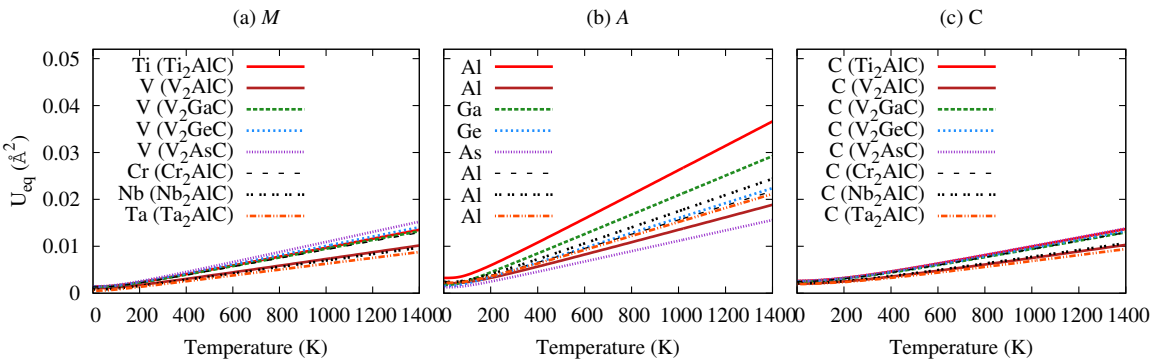

Figure 11.3: Temperature-dependence of the equivalent isotropic atomic displacement parameters determined by first-principles phonon calculations for select M_2AC phases showing U_{eq} for (a) the M atoms, (b) the A atoms, and (c) C .

ADPs for the Ti and C sites are considerably lower than those of the A elements [Fig. 11.2(c)]. This shows that the bonding between the A and Ti elements is weaker than the Ti-C bonds. Considering the Ti-C octahedra as rigid tightly-bound blocks relative to the A elements, whose bonding to the Ti atoms is analogous to a flexible spring, any changes in the spring constant (interatomic potential) as the A element changes will be more severely felt by the A element since the Ti-C units are so sturdy.

Turning to the ADPs of the A atoms, it is readily apparent that, in all cases, their amplitudes of vibration are the highest of all the atoms in all cases, and by a significant factor ($\simeq 3$ times) [Fig. 11.2 (c)]. As mentioned, the phenomenon is due to the weak bonding in the A atom (at least relative to that between Ti and C) that makes its motion less constrained. This has been observed before in the MAX phases, where previous reports have shown that the A elements "rattle" within the structure [1]. It is this rattling effect that is believed to be responsible for the low phonon conductivities of the MAX phases comprised of elements heavier than Al, despite their high specific stiffness values and high Debye temperatures [1, 58, 59]. The experimental work in this thesis also supports this, as will be discussed in the next chapter.

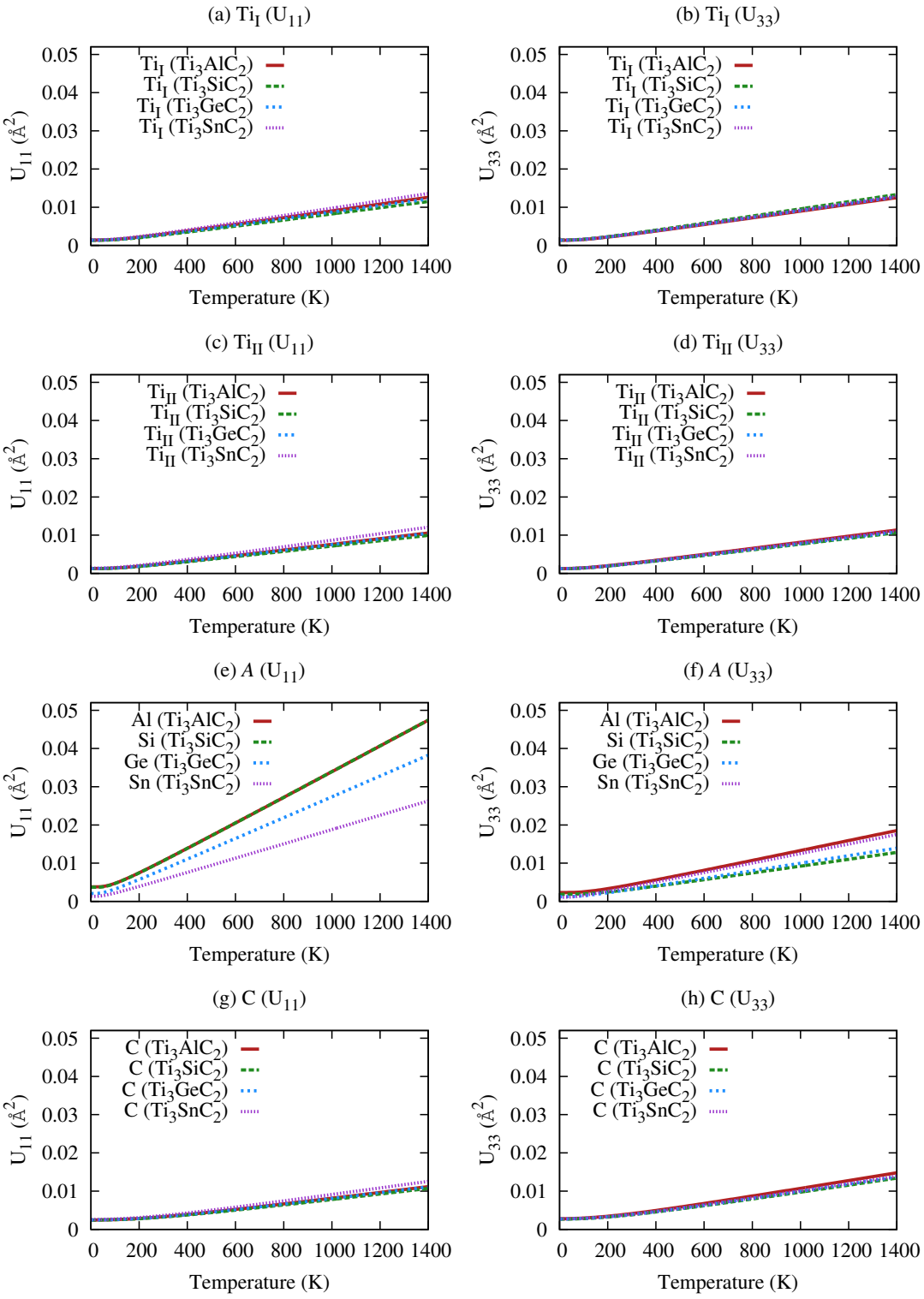

Figure 11.4: Temperature-dependence of the anisotropic atomic displacement parameters, U_{ij}, determined by first-principles phonon calculations for the 312 phases Ti_3AlC_2, Ti_3SiC_2, Ti_3GeC_2, and Ti_3SnC_2, showing U_{11} and U_{33} for Ti_I [(a) and (b)], Ti_{II} [(c) and (d)], the *A* elements [(e) and (f)], and C [(g) and (h)].

In addition to the four 312 phases, eight 211 phases were studied as well. The equivalent isotropic ADPs for these phases shown in Fig. 11.3. Here we observe the same overall trend as with the 312 phases, where the displacement amplitudes of the A elements [Fig. 11.3(b)] are higher than those of the other atoms. Since there is a more diverse set of chemistries among the 211 phases studied, the spread of the M ADPs [Figs. 11.3(a)] is greater than for the ADPs of the Ti atoms in the 312 phases, which are nearly equivalent [Figs 11.2(a) and(b)]; however, the ADPs of the M and C atoms in the 211 phases are similar to one another and their variations with respect to chemistry are less drastic than the differences in U_{eq} among the different chemistries for the A atom. Furthermore, the fact that U_{eq} for the C atom varies despite the common X element chemistry – where, on the other hand, the 312 phases share common Ti atoms in the M site – shows that the motion of X is coupled to that of M.

Another important consideration in the MAX phase crystal structure is that it is highly anisotropic. In contrast to, say, a cubic crystal structure, the environment for a given atom can be quite different in one direction than another. In terms of the crystal structure, the symmetry in the x and y direction differs drastically from that in the z direction. Therefore the overall atomic displacements within the basal planes – which is expressed as U_{11} – should be distinguished from that along the c direction, U_{33}. These U_{ij} parameters are the **anisotropic** mean-squared atomic displacement parameters, which are plotted in Figs. 11.4 and 11.5 for all the atoms in the 312 and 211 phases, respectively, under study. Here, we find that the thermal motion behaviors of the M and C atoms are more or less the same in the a and c direction. The A elements all show a highly anisotropic atomic motion behavior with $U_{11} > U_{33}$, indicating higher amplitudes of vibration within the basal planes than perpendicular to them. This suggests that the bonding of the A elements to one another is weaker than their interactions with the M atoms, which is what could lead to less constrained motion in the direction of the other A atoms than in the direction

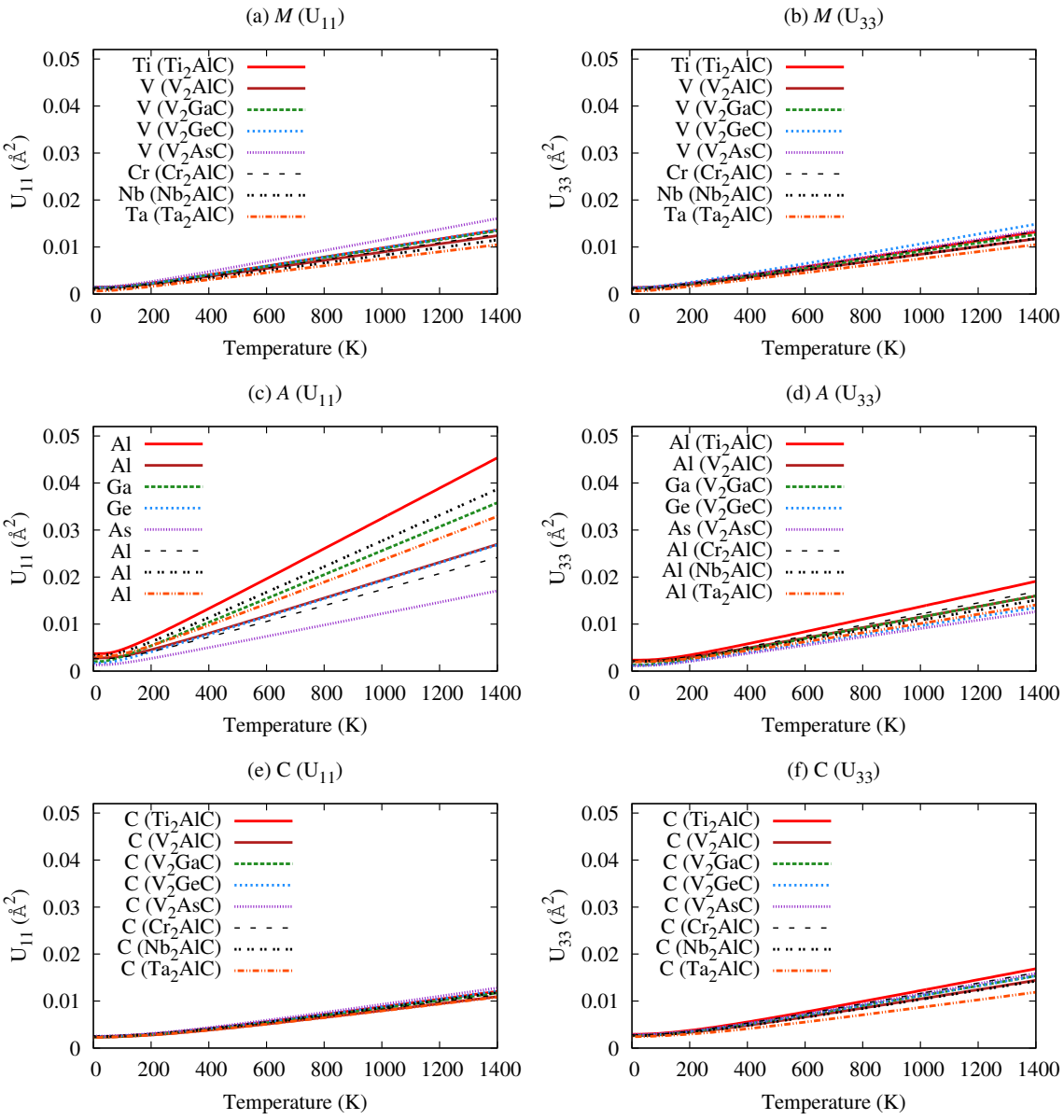

Figure 11.5: Temperature-dependence of the anisotropic atomic displacement parameters, U_{ij}, determined by first-principles phonon calculations for select 211 phases showing U_{11} and U_{33} for the M elements [(a) and (b)], the A elements, [(c) and (d)], and C [(e) and (f)].

of the M-C octahedra. In fact, in the z direction, the mean-squared displacements of the A atoms are comparable to the displacements of the M atoms. In effect, the dynamical behaviors of the A and M atoms occupy equal portions of the distances between them. Interestingly, the Si and Al atoms in the 312 phases have the same mean-squared displacement in the x-y direction [Fig. 11.4(e)] but the Al atom exhibits a higher amplitude of displacement than along z than Si and thus has the highest isotropic ADP [Fig. 11.2(c)]. Moreover, the amplitude in the z direction apparently increases with decreasing mass, at least when comparing those in the same periodic table group (it is the higher for Sn than for Ge and Si), which implies that it is more related to the constraints from the Ti than the interactions of the A atoms with one another. This is also supported by the environment in either direction dictated by the atomic arrangement.

Because of the extensive sample of phases studied, it is difficult to compare the ADPs between different phases from the temperature-dependent graphs in Figs. 11.2-11.5. The next section therefore focuses on just a single ADP at 1000°C for each phase studied to assess variations with chemistry.

11.3 TRENDS WITH MASS AND ELECTRON CONFIGURATIONS OF THE M AND A ATOMS

To better understand how the theoretical atomic motion plays into the structure, chemistry, and bonding of these materials, it is useful to consider the relationship between the ADPs to other properties and phenomena in the studied phases. This can first be accomplished by exploring the trends in the ADPs with variations in chemistry for the M sites and the A sites independently, focusing on only carbides to reduce the number of free variables by keeping X constant. Table 11.1 presents the M and A elements that make up the $M_{n+1}AX_n$ phases. They are grouped into columns according to their group in the periodic table (and also their electron configuration), and they are arranged by row according to their period in the periodic table (wherein there is a

Table 11.1: Elements that can exist as M and A atoms in the $M_{n+1}AX_n$ phases, arranged by valence electron configuration and row, or period, in the periodic table.

M atoms

period	valence *e* configuration			
	d^1s^2	d^2s^2	d^3s^2	d^5s^1
3*d*	Sc	Ti	V	Cr
4*d*		Zr	Nb	Mo
5*d*		Hf	Ta	

A atoms

period	valence *e* configuration				
	s^2	s^2p^1	s^2p^2	s^2p^3	s^2p^4
3*s*		Al	Si	P	S
4*s*		Ga	Ge	As	
5*s*	Cd	In	Sn		
6*s*		Tl	Pb		

significant increase in mass from top to bottom). This serves as a guide for assessing the ADPs in relation to the chemistry of the phases.

Comparing the mean-squared isotropic displacement of the A atoms in Fig. 11.2 with one another, they increase in order of mass: $U_{\mathrm{Al}} < U_{\mathrm{Si}} < U_{\mathrm{Ge}} < U_{\mathrm{Sn}}$. This is because the mean-squared displacement is inversely proportional to the mass of the atom and proportional to the phonon frequencies of the normal modes. Fig. 11.6 shows U_{11} and U_{33} plotted against the s period of the A atoms for the three 312 phases in group 14. Indeed, the ADPs of the A elements decrease with increasing s period, which corresponds to increasing atomic mass, but the decrease in amplitude is only within the basal planes (U_{11}); the displacement along the z direction shows a slight increase with mass. While the increase in U_{33} with A atom period is slight, this does suggest that the mass effects play a different role in the A-A interaction, which is within the basal plane, than the M-A interaction along the z direction.

Despite the clear trends in mass for the predicted ADPs, it is worth noting that the way that temperature is accounted for in this model is through an assumed distribution of the phonon population as a function of the phonon frequency for each band. The mass effects are incorporated within the harmonic model – that is, through the kinetic energy term and its effect on the frequency in the harmonic potential. Under these restrictions, the calculations predict

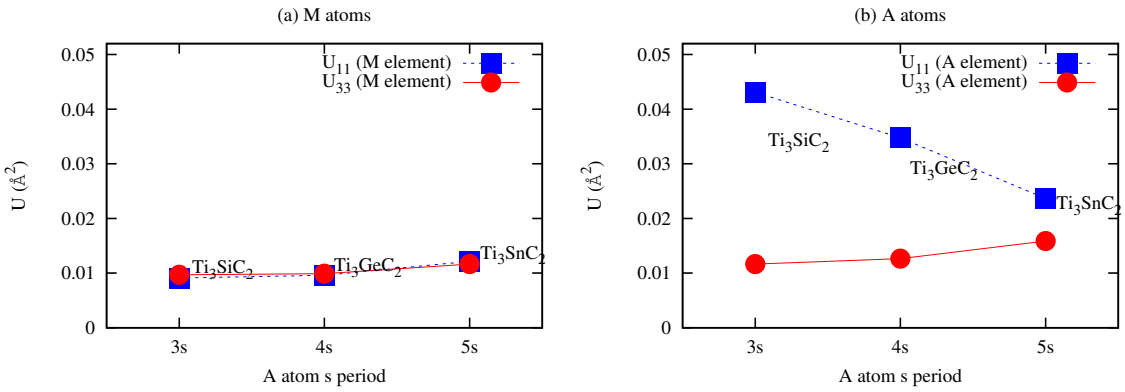

Figure 11.6: Dependence of atomic displacement parameters at 1273 K on *A* atom period (row) for 312 phases with common *M* atoms and *A* atoms with the same valence electron configuration. U_{11} (blue squares) and U_{33} (red circles) are shown for (a) the Ti_I atoms and (b) the *A* atoms.

the mass to be inversely proportional to displacement but there are inevitably anharmonic interactions between atoms that are neglected in approximating the interatomic potential in this model. If the interatomic potential plays a considerably larger role than mass – especially if it has major contributions from higher-order terms – then this may not be the true state of affairs in real systems, which will be discussed in more detail in the next chapter. For now, it is fair to say that the predictions of decreased vibrational amplitudes for heavier atoms is based on a primitive model that cannot truly describe systems with anharmonic interactions.

In addition to the strong trend predicted for the U_{eq} dependence on mass, the Al atom apparently rattles more than Si [Fig. 11.2(c)], which is not a mass effect since Al and Si are similar in that respect. Given that Al is the only atom with a different valence electron configuration from the other three, this could be related to the coupling between electronic structure and dynamical behavior of the ion cores; however, given the small extent of the difference tween U_{Al} and U_{Si}, more MAX phase stoichiometries should be included in comparisons before making any conclusions.

Fig. 11.7 plots the ADPs of the *M* and *A* atoms against *A* atom valence electron configuration

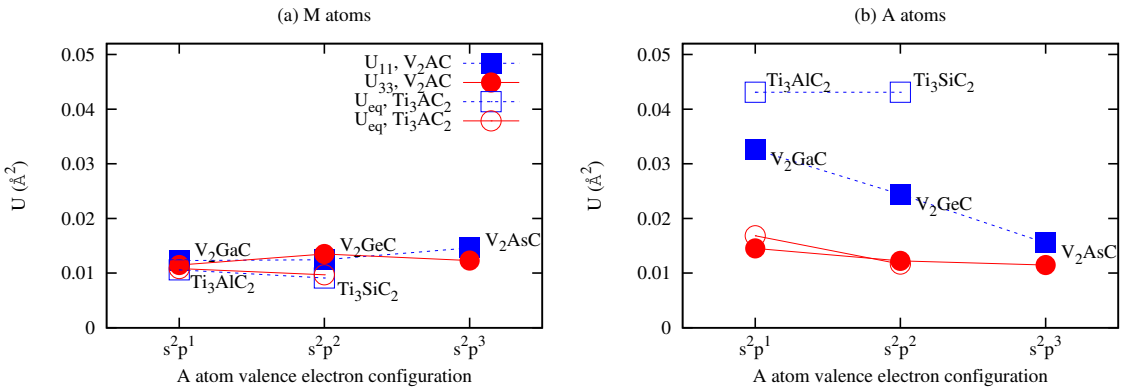

Figure 11.7: Dependence of equivalent isotropic atomic displacement parameters at 1273 K on *A* atom valence electron configuration for phases with common *M* atoms and with *A* atoms in the same row in the periodic table. The values for the V_2AC phases are represented by solid symbols; the ADPs of the Ti_3AC_2 phases are open symbols. The anisotropic ADPs U_{11} (blue squares) and U_{33} (red circles) are plotted for (a) the *M* atoms and (b) the *A* atoms.

for the two Ti-containing 312 phases with *A* elements in the 3*s* row (Al and Si) along with three V-containing 211 phases with *A* elements in in the 4*s* row (Ga, Ge, and As). Note that the two sets of phases – the 211 V_2AC phases and the 312 Ti_3AC_2 phases – do not have any common elements (except carbon), but the valence electron configurations for the *A* elements are the same for common *x* axis values and only the general trends are being compared for the sake of determining the role of the valence electron configuration.

As discussed, the decrease in U from Al to Si in the 312 phases [open squares in Fig. 11.7(b)] is slight, and only within the basal planes (*i.e.* only for U_{33}). However, the decrease in U_{33} for the *A* elements in the V-containing 211 phases [filled blue squares in Fig. 11.7(b)] is more pronounced, suggesting that, in these phases, the addition of *p* electrons leads to a decrease in the amplitudes of the *A* atom displacements. Since the ADPs generally are not largely affected by *n* (that is, there should be little difference between the U values for atoms in a 312 and 211 phase with the same chemistry), reasons for the differences likely stem from mass or valence electron configuration of the *M* atom, and the correlation of these factors with the valence

electrons of the *A* atoms. Interestingly, the *a* lattice parameters in the V-containing 211 phases increase with *p* electrons, while the *c* parameter decreases – that is, V_2GaC has the lowest *a* parameter and highest *c* parameter.

Figures 11.6 and 11.7 demonstrate that the anisotropic ADPs vary with *A* atom valence electron configuration and mass. It has been shown that increases in mass and valence electrons both lead to more isotropic displacements with lower amplitudes. Now we move onto the effect of variations in *M* atom, keeping *A* occupied with Al since it is one of the most common *A* elements.

Figure 11.8 plots U_{11} and U_{33} as a function of the valence electron configuration of the *M* atoms in the 3*d* row (Ti, V, and Cr) for Al-containing 211 phases. Despite the *M* atom being the site to vary in chemistry, the *M* vibrations are not affected by the *M* atom electron configuration; however, it does affect the *A* atom thermal motion, as more valence electrons lead to more isotropic thermal motion behavior and smaller amplitudes. The density of Cr_2AlC is significantly higher than the other two, as the lattice parameters are much smaller, so the more constrained motion is in line with the decrease in U_{11} for Al.

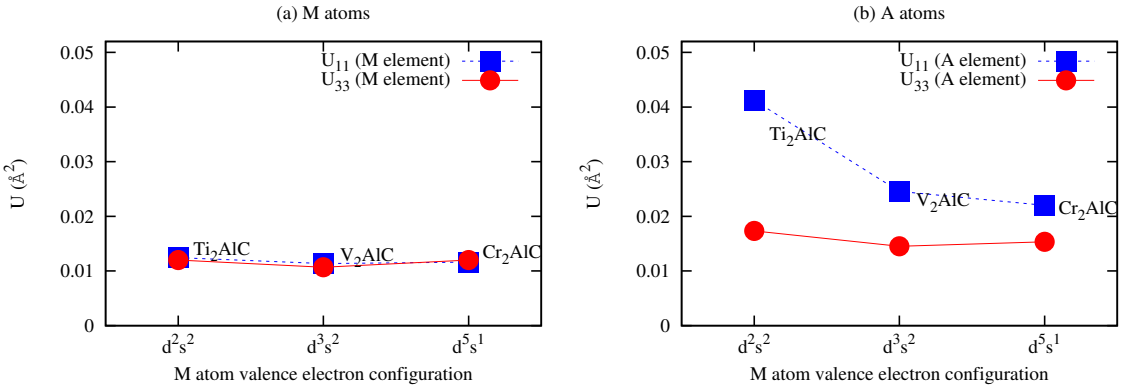

Figure 11.8: Dependence of atomic displacement parameters at 1273 K on *M* atom valence electron configuration for 211 phases with common *A* atoms and *M* atoms in the same row in the periodic table. U_{11} (blue squares) and U_{33} (red circles) are shown for (a) the *M* atoms and (b) the *A* atoms.

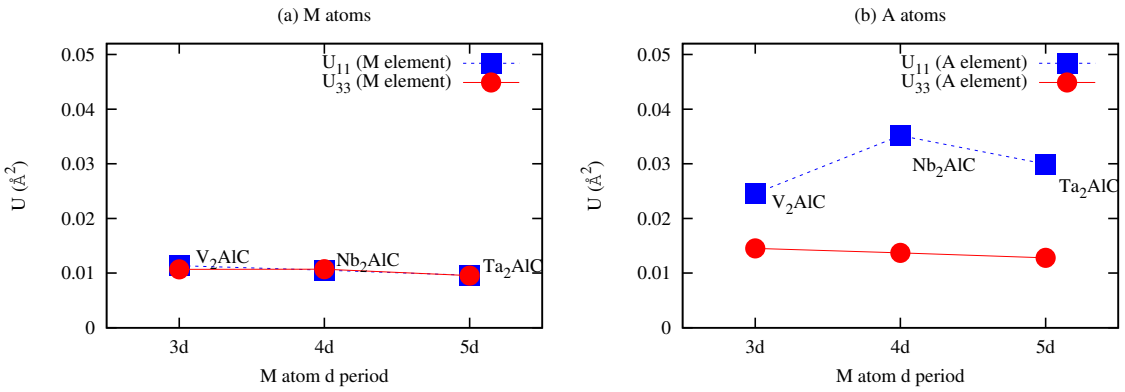

Figure 11.9: Dependence of anisotropic atomic displacement parameters at 1273 K on *M* atom period (row) for 211 phases with common *M* atoms and *A* atoms with the same valence electron configuration. U_{11} (blue squares) and U_{33} (red circles) are shown for (a) the *M* atoms and (b) the *A* atoms.

The fact that the *M* valence electron plays such a large role in the *A* atom motion shows, again, that the *M*-*A* interactions greatly influence the "rattling" effect of the *A* atom. On the other hand, variations with *M* atom mass does not play a major role, as shown in Fig. 11.9 for group 5 *M* atoms V, Nb, and Ta. Even though the *M* atoms in the three phases are drastically different in mass, the ADPs do not show any systematic variations. This further supports the notion that the role of bonding between *M* and *A* is a large factor in the movement of the *A* atom, whereas the mass of the *M* atom does not strongly influence the forces in the crystal that would factor into the *A* displacements.

All in all, the phonon calculations predict that the *A* elements, being the most weakly bonded within the crystal, should vibrate with the highest amplitude and within the basal plane. Both the mass and electron configuration of the *A* elements govern their displacements, and the ADPs are predicted to increase with decreasing mass and fewer valence electrons. The predictions also suggest that the *M* atom electron configuration influences the *A* atom motion as well, but the mass of the *M* atom does not have a large role in the vibrational character.

The next chapter will present the results for the ADPs of several of the phases studied in this

chapter, as determined from Rietveld analysis of high-temperature neutron diffraction data. The results will be compared to the predictions outlined herein to help draw general conclusions about MAX phase lattice dynamics, to validate both the theoretical and experimental procedures, and to test the behavior of the real systems against the theoretical ones of this chapter.

11.4 SUMMARY

This chapter presented results for the mean-squared atomic displacements determined from first-principles phonon calculations. First, the temperature-dependent isotropic and anisotropic ADPs were plotted for four 312 phases and a large number of 211 phases. Then, the ADPs at 1273 K were plotted against either A valence electron configuration, A-atom mass, M valence electron configuration, or M-atom mass for select sets of phases. It was shown that the ADPs of the A atoms are predicted to be higher in amplitude and more anisotropic for the phases with fewer A or M atom valence electrons or with lighter A atoms. The mass of the M atoms, on the other hand, does not play a large role in the calculated ADPs.

Chapter 12: Theory and experiment: atomic displacement parameters

It has been shown in the previous chapter that the mean-squared atomic displacements can be used to spot trends in lattice dynamics with variations in chemical bonding and atomic mass. In this chapter, ADPs are determined experimentally from high-temperature neutron diffraction (see section 8.1.2 for experimental details) and those values are then compared with the DFT results presented in Chapter 11

Along with MAX phases, titanium carbide, TiC, and tungsten carbide, WC, are also studied with first-principles calculations and HTND for benchmarking and as validation for the experimental and theoretical methodologies. TiC is chosen for its similarity in chemistry to the MAX phases studied in this work, and WC is studied to test our methodology on a hexagonal system. WC crystallizes in a hexagonal structure with space group $P\bar{6}m2$. Both TiC and WC were measured on the same neutron diffractometer as the MAX phases. The same data refinement strategy is also used. Tantalum carbide, TaC, is also studied with first-principles phonon calculations for comparison with another recent HTND paper in which its ADPs were reported in order to evaluate our results against neutron diffraction data from another diffractometer [137].

12.1 Binary carbides

I begin this study on the relatively simple systems, TiC and TaC, which have cubic NaCl-type structures (space group $Fm\bar{3}m$). For TiC, temperature dependence of the mean-squared displacements calculated from first-principles phonon calculations is compared with those obtained from HTND. For cubic structures, the thermal motion is represented as an isotropic ADP, U_{iso}, which is the mean square of the displacement of an atom in all directions. Figures

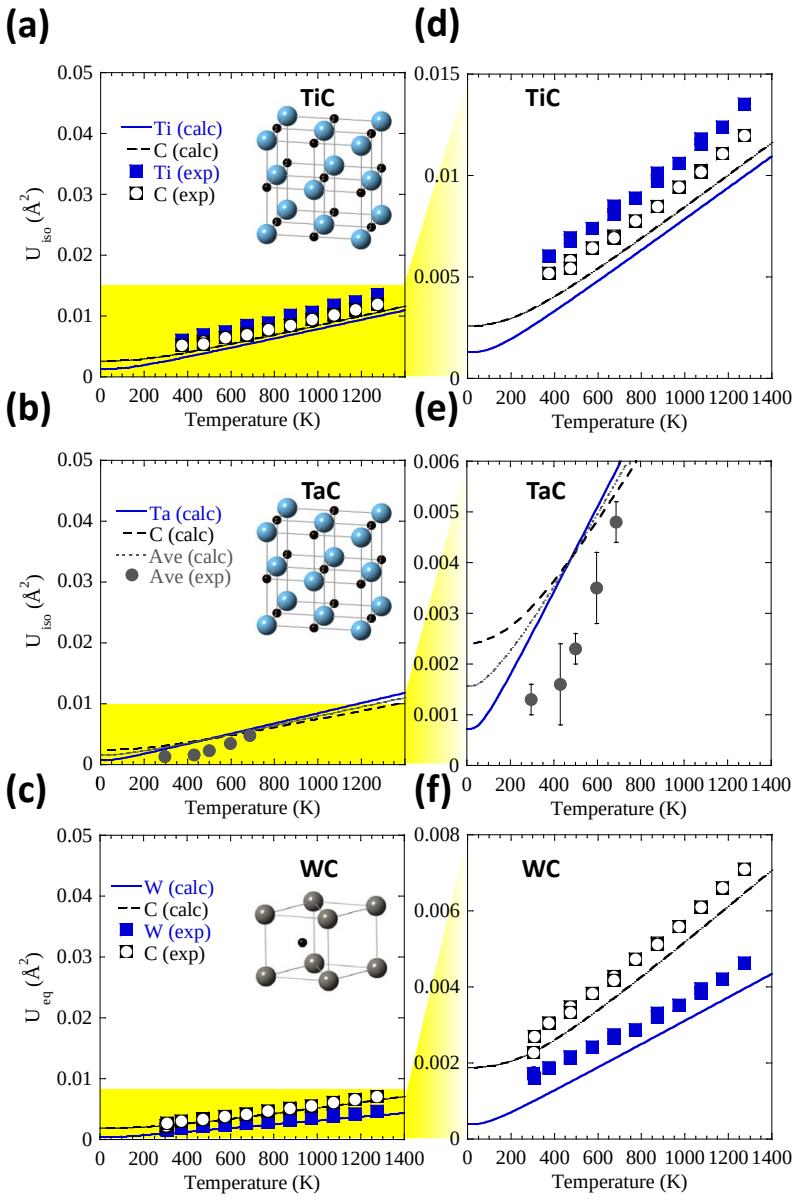

Figure 12.1: Temperature dependence of mean-squared displacement parameters in select binary carbides showing values calculated from first principles calculations (lines) and experimental values from HTND (markers): (a) U_{iso} for Ti and C atoms in TiC, (b) U_{iso} for Ta and C in TaC, where the markers show the average U_{iso} for Ta and C from Ref. [137] and, (c) U_{iso} for W and C atoms in WC. Insets show the crystal structures for each phase. (a)-(c) are plotted with a full scale to coincide with those of all other figures in this chapter. (d), (e), and (f) show the shaded regions in (a), (b), and (c), respectively. In (a) and (c), error bars are typically smaller than the symbols.

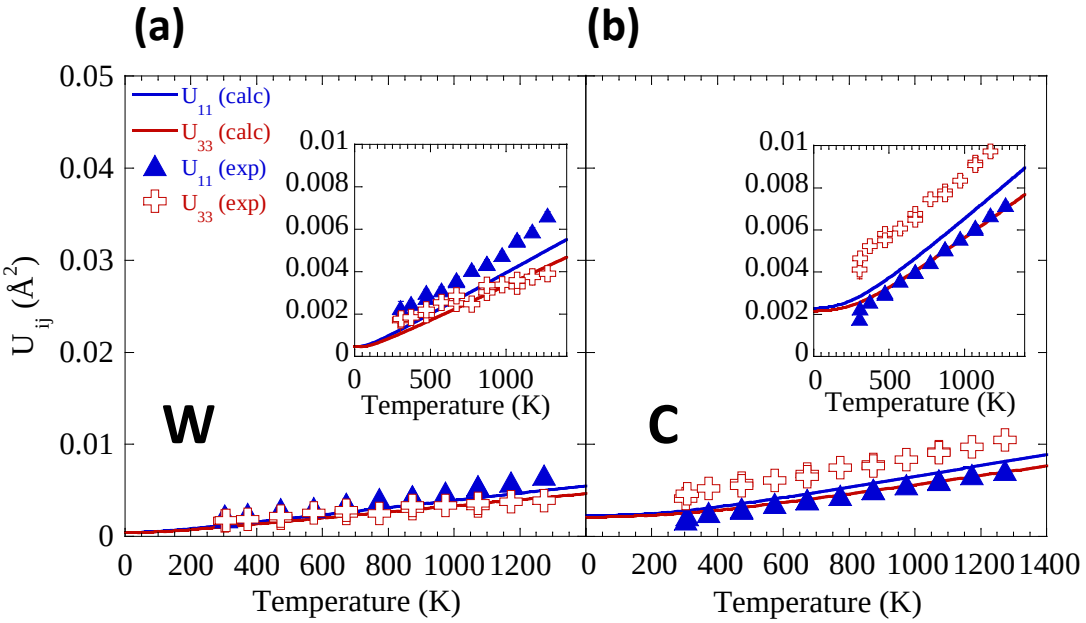

Figure 12.2: Temperature evolution of anisotropic ADPs U_{11} (blue) and U_{33} (red) of, (a) W and, (b) C in WC. Solid lines show DFT predictions; markers show experimental values determined from HTND. Insets show zoomed in regions from 0 to 0.01 Å^2. Error bars are typically smaller than the symbols.

12.1(a) and (b) show that the calculated temperature dependencies of U_{iso} (lines) are close to the experimental values determined from the HTND carried out in this work (symbols), lending credibility to the methodology for this cubic binary system. Both prediction and experiment show nearly the same ADPs for both atoms. However, the y axis limits have been chosen to be identical for the MAX phase figures, where all ADP plots are shown from 0 to 0.05 Å^2 for comparison. I also plot to their full scales [yellow shaded in regions in Figs. 12.1(a) and (b)] in Figs. 12.1(e) and (f).

Clearly, there are some discrepancies between the measured and calculated values, even for these relatively simple systems. In TiC, for instance, theory predicts that U_{iso} should be larger for C than for Ti, while the opposite is observed experimentally (see Fig. 12.1(d). Reasons for this are not clear, but may be related to the relatively weak scattering power of Ti ($\sigma_c =$

1.485b [116]) compared to C (σ_c = 5.551b [116]). It is important to note, however, that when compared to the full ADP scales we deal with for the *A* atom "rattlers" in the MAX phases, the differences between theory and experiment for these binaries are small (<3% of the full 0.05 Å^2 scale).

For TaC, the calculated mean-squared displacements are compared with a recent HTND study by Nakamura and Yashima [137], where the isotropic ADPs were estimated from Rietveld refinement of HTND data on single phase TaC. Since the error bars for U_{iso} were large in that study, the final refinement assumed $U_{\text{Ta}} = U_{\text{C}}$. Herein the atomic isotropic thermal displacement values are predicted individually for Ta and C, shown in Fig. 12.1(b) by the blue solid line and black dashed line, respectively. The predicted ADPs for Ta and C are averaged to yield average isotropic ADPs, also shown in Fig. 12.1(b) (gray dotted line), which are compared with the average U_{iso} values determined from the study in Ref. [137] (gray circles).

The predicted and experimental ADP values for TaC are in good agreement, but on this instrument (in the experimental study in Ref. [137]) the temperature dependence shows a more nonlinear behavior at lower temperatures. Note that the error bars in this study, shown in Fig. 12.1(e), are considerably higher than those for TiC measured on HIPPO [Fig. 12.1(d)], where the error bars are smaller than the symbols. The extent by which the experimental parameters deviate from the predicted values provide a reference point for the precision of the calculations and the errors involved for simple, single-phase cubic systems on the medium resolution neutron diffractometers used for these studies.

To compare the overall amplitudes of vibration of the W and C atoms, the anisotropic ADPs, U_{ij}, were converted to equivalent thermal displacement parameters, U_{eq}, assuming equation 6.29. Figure 12.1(c) plots the temperature dependence of the U_{eq} values calculated from first-principles phonon calculations for W (solid blue line) and C (dashed black line). The

experimental values are represented by blue squares and open circles for W and C, respectively. The agreement between theory and experiment is excellent, with C showing slightly higher amplitudes of vibration in both the predicted and measured results. To study the directional amplitudes of vibration, the anisotropic ADPs, U_{ij}, are plotted in Figs. 12.2(a) and 12.2(b) for W and C, respectively. Again, the main plots are to the same scale as the rest of the graphs in this chapter, but the zoomed in regions are shown in the insets. Generally, the predicted values agree well with the experimentally determined ADPs. For C [Fig. 12.2(b)], the anisotropy is reversed for theory and experiment, i.e., $U_{11} > U_{33}$ according to predictions, while the opposite is observed from the HTND experiments. However, in general, the calculated values show relatively isotropic behavior ($U_{11}/U_{33} = 1.1$), so this may be an indication of the uncertainty in the degree of anisotropy for both experimental and theoretical ADPs when the differences between U_{11} and U_{33} are small.

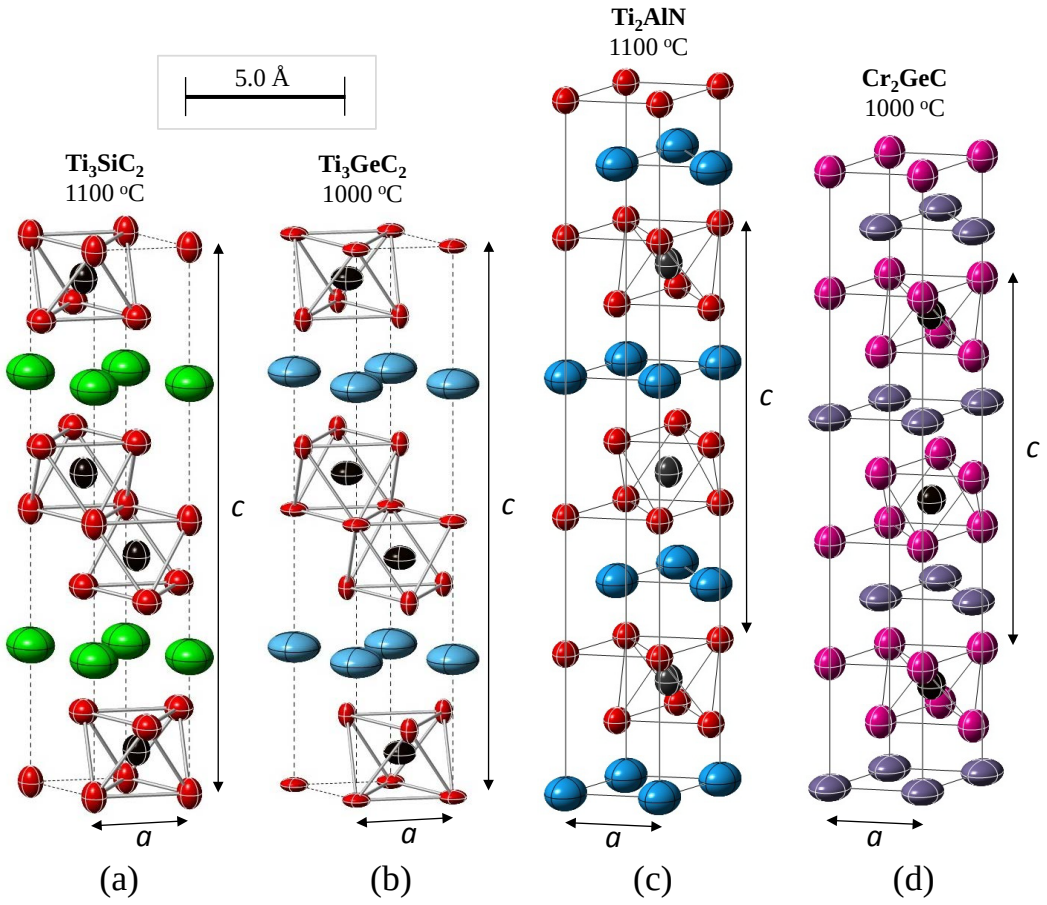

Figure 12.3: High-temperature 99% probability thermal ellipsoids for (a) Ti_3SiC_2 at 1100°C, (b) Ti_3GeC_2 at 1000°C, (c) Ti_2AlN at 1100°C, and (d) Cr_2GeC at 1000 °C [2], as determined through Rietveld analysis of the high-temperature neutron diffraction on the HIPPO diffractometer. Note that all four structures are drawn to the same scale.

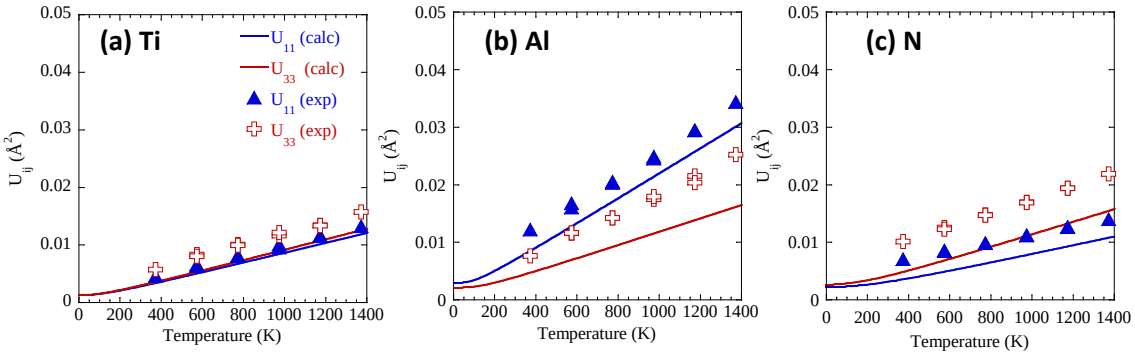

Figure 12.4: Temperature evolution of anisotropic ADPs U_{11} (blue) and U_{33} (red) of (a) Ti, (b) Al, and, (c) N atoms in Ti_2AlN. Solid lines show DFT predictions; markers show experimental values determined from HTND. Error bars are typically smaller than the symbols.

From the results shown in Figs. 12.1 and 12.2, it is evident that for the binary carbides, experimental and first-principles phonon calculations agree reasonably well. Having established a baseline for error, I now move onto the MAX phases, the real focus of this thesis.

12.2 MAX PHASES

To represent the anisotropic thermal motion obtained experimentally through HTND, the thermal ellipsoids at the highest measured temperatures for each phase are displayed in Fig. 12.3. Indeed, the anisotropic thermal motion shown by the thermal ellipsoids in Fig. 12.3 are in agreement with previous reports of the A-group elements in MAX phases acting as "rattlers" in the structure [1], and with the series of first-principles calculations in Chapter 11. It is this rattling effect that is believed to be responsible for the low phonon conductivities of the MAX phases, despite their high specific stiffness values and high Debye temperatures [1, 58, 59]. However, it should be noted that the reasons for the higher phonon conductivity of the Al-containing phases, which also exhibit this "rattler" effect, are not clear at this time.

The neutron diffraction results show that the Ge atom in Ti_3GeC_2 is even more of a "rattler"

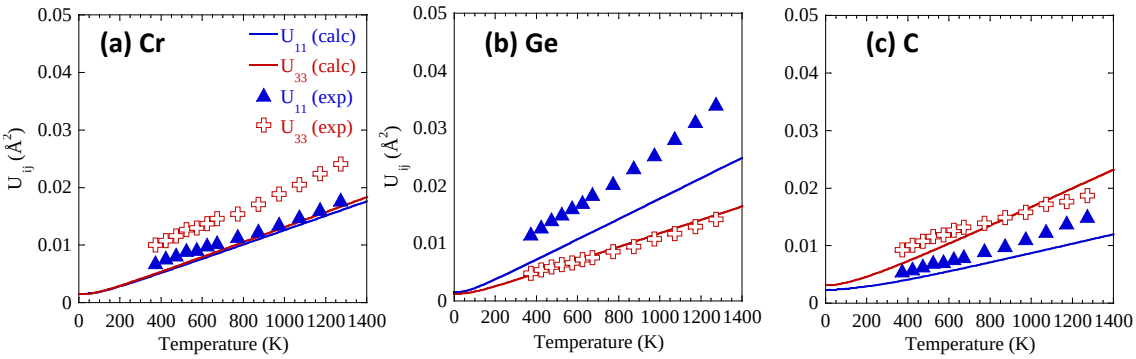

Figure 12.5: Temperature evolution of anisotropic ADPs U_{11} (blue) and U_{33} of (a) Cr, (b) Ge, and (c) C atoms in Cr_2GeC. Solid lines show DFT predictions; markers show experimental values determined from HTND. Error bars are typically smaller than the symbols.

than Si in Ti_3SiC_2. It is significant to note that the major differences between the motion in the two isostrucutral 312 phases structures (Fig. 12.3(a) and (b)) is the extent to which the Ge ellipsoids are flattened relative to those of Si. Note that the Ti_{II} atoms in Ti_3GeC_2 also flatten along the basal planes with increasing temperature. The latter conclusion is in accordance with the fact that the phonon conductivity of Ti_3GeC_2 at room temperature is negligible [1, 58] despite having a Young's modulus of over 340 GPa [52, 58]. Since the strongest bonds are between the M and X atoms in the M_2X layers, the smallest vibration amplitudes are associated with M and X atoms. The large amplitude of vibration of the Si, Al, and Ge atoms indicate that, in addition to being weakly bonded to one another within the basal plane, they are also relatively weakly bonded to their respective M atoms, in line with the "rattler" effect discussed above.

Next, the temperature-dependences of the experimentally-determined ADPs are plotted with the predicted values from first principles calculations. Figures 12.4-12.9 show the ADPs for the five select MAX phases studied through HTND, including two 211 phases (Figs. 12.4 and 12.5), three 312 phases (Figs. 12.6, 12.7, and 12.8), and one 413 phase (Fig. 12.9). Values determined

from first-principles phonon calculations (solid lines) are shown along with experimental values from Rietveld analysis of neutron time-of-flight data. The statistical uncertainties of the refined parameters result in error bars typically of the size of the symbols due to the scale used. In most cases where there is observed experimental scatter the error bars are visibly larger, as in Ti_I and Ti_{II} in Ti_3GeC_2 [Figs. 12.8(a) and (b), respectively] and Ti_I, Ti_{II}, Al, and N_I in Ti_4AlN_3 [Figs. 12.9(a)–(d)]. It should be noted that in some cases the observed scatter is greater than the error bars, indicating systematic errors such as parameter correlations, which we could not avoid in our refinement model.

Based on the totality of these results it is reasonable to conclude that for this relatively diverse set of MAX phases, qualitative agreement between the calculated and measured ADPs is achieved. In all cases, both the DFT predictions and HTND measurements show that the A atom vibrates with the highest amplitude, and vibrates more within the basal plane, i.e., $U_{11} > U_{33}$. This is in line with the notion of the A-group elements acting as "rattlers" which is consistent with the low phonon conductivity of many MAX phases [1, 58, 59].

With a few exceptions, when the experiments show that $U_{11} > U_{33}$, theory shows the same. This is especially true of the cases where there is a large difference between the U_{ij} values, i.e., large anisotropy, mostly of the *A* atoms, such as in Figs. 12.4(b) (Al in Ti_2AlN), 12.5(b) (Ge in Cr_2GeC), 12.5(c) (C in Cr_2GeC), 12.7(c) (Si in Ti_3SiC_2), 12.8(c) (Ge in Ti_3GeC_2), and 12.9(c) (Al in Ti_4AlN_3). Most of the discrepancies, on the other hand, occur for atoms with nearly isotropic thermal motion, i.e., for which the differences between the predicted U_{ij} values are small, such as in Figs. 12.5(a) (Cr in Cr_2GeC), 12.7(a) and 12.7(b) (Ti in Ti_3SiC_2), 12.8(a) and 12.8(b) (Ti in Ti_3GeC_2), and 12.9(a) (Ti in Ti_4AlN_3). It should be noted that Ti and Cr are both relatively weak neutron scatterers (for Ti, $\sigma_c = 1.485$b; for Cr, $\sigma_c = 1.66$b) [116] and, therefore, other errors could influence the refined U_{ij} values in the data analysis. A relatively

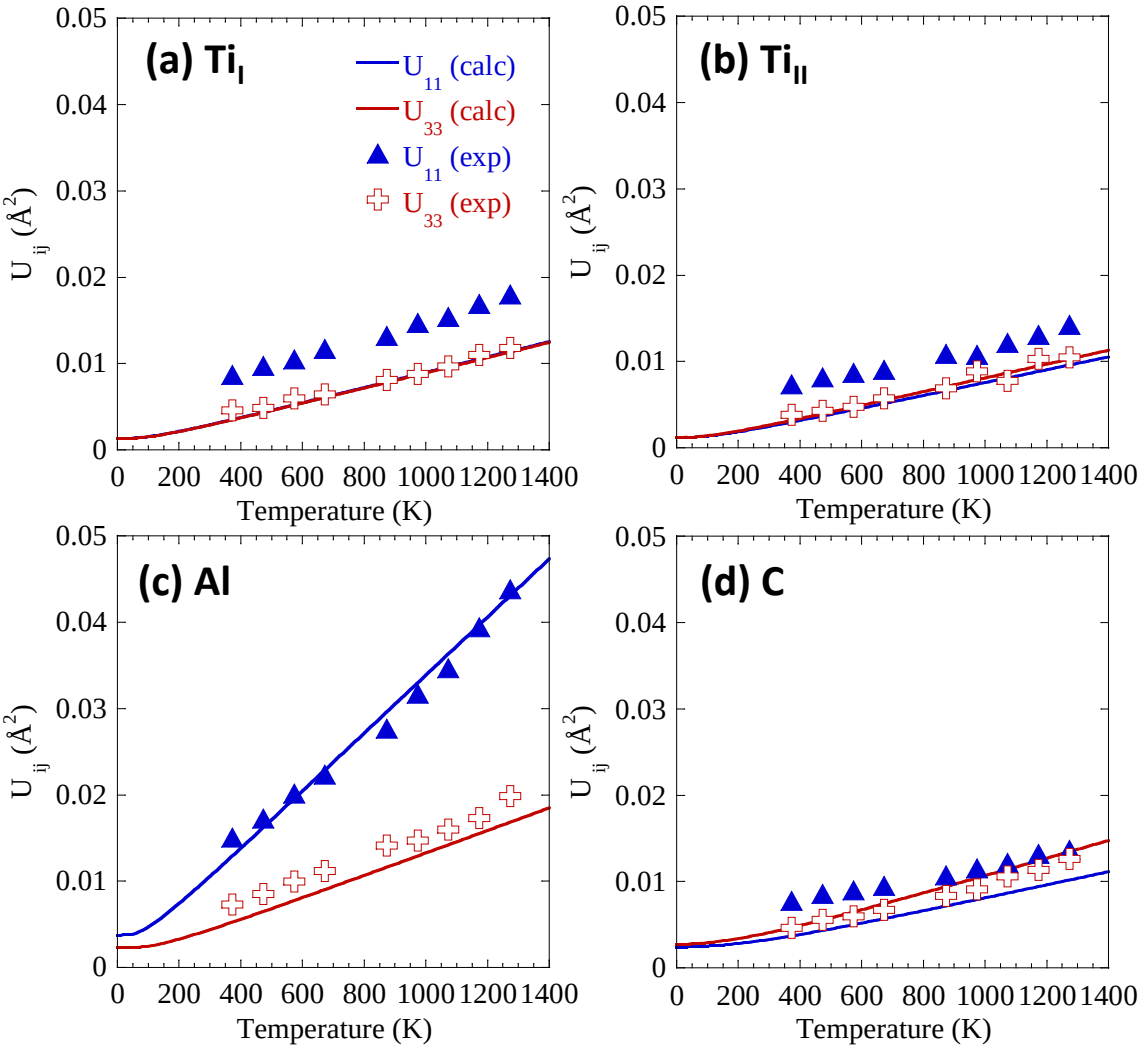

Figure 12.6: Temperature evolution of anisotropic ADPs U_{11} (blue) and U_{33} of (a) Ti_I, (b) Ti_{II}, (c) Al, and (d) C atoms in Ti_3AlC_2. Solid lines show DFT predictions; markers show experimental values determined from HTND. Error bars are typically smaller than the symbols.

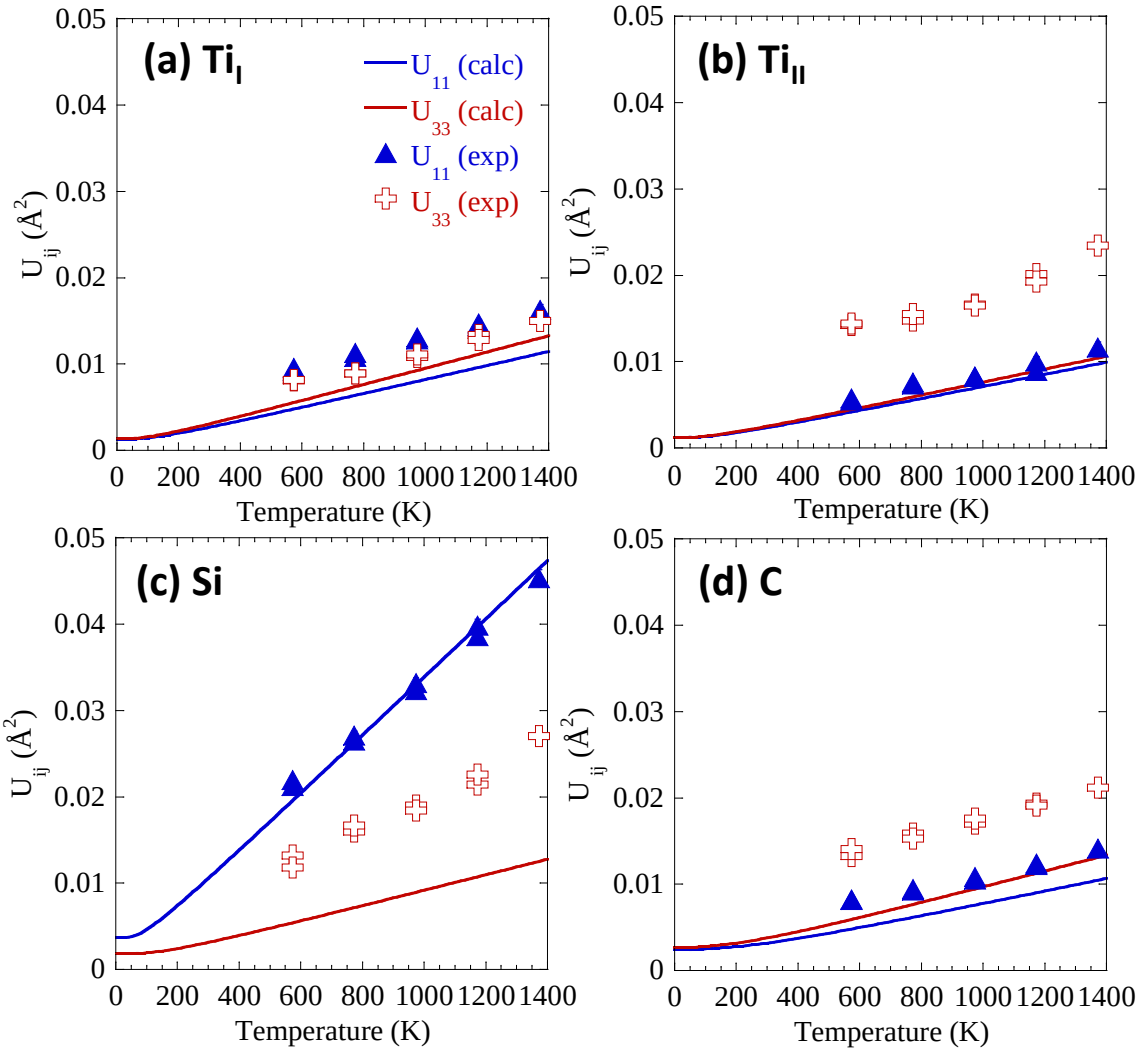

Figure 12.7: Temperature evolution of anisotropic ADPs U_{11} (blue) and U_{33} of (a) Ti_I, (b) Ti_{II}, (c) Si, and (d) C atoms in Ti_3SiC_2. Solid lines show DFT predictions; markers show experimental values determined from HTND. Error bars are typically smaller than the symbols.

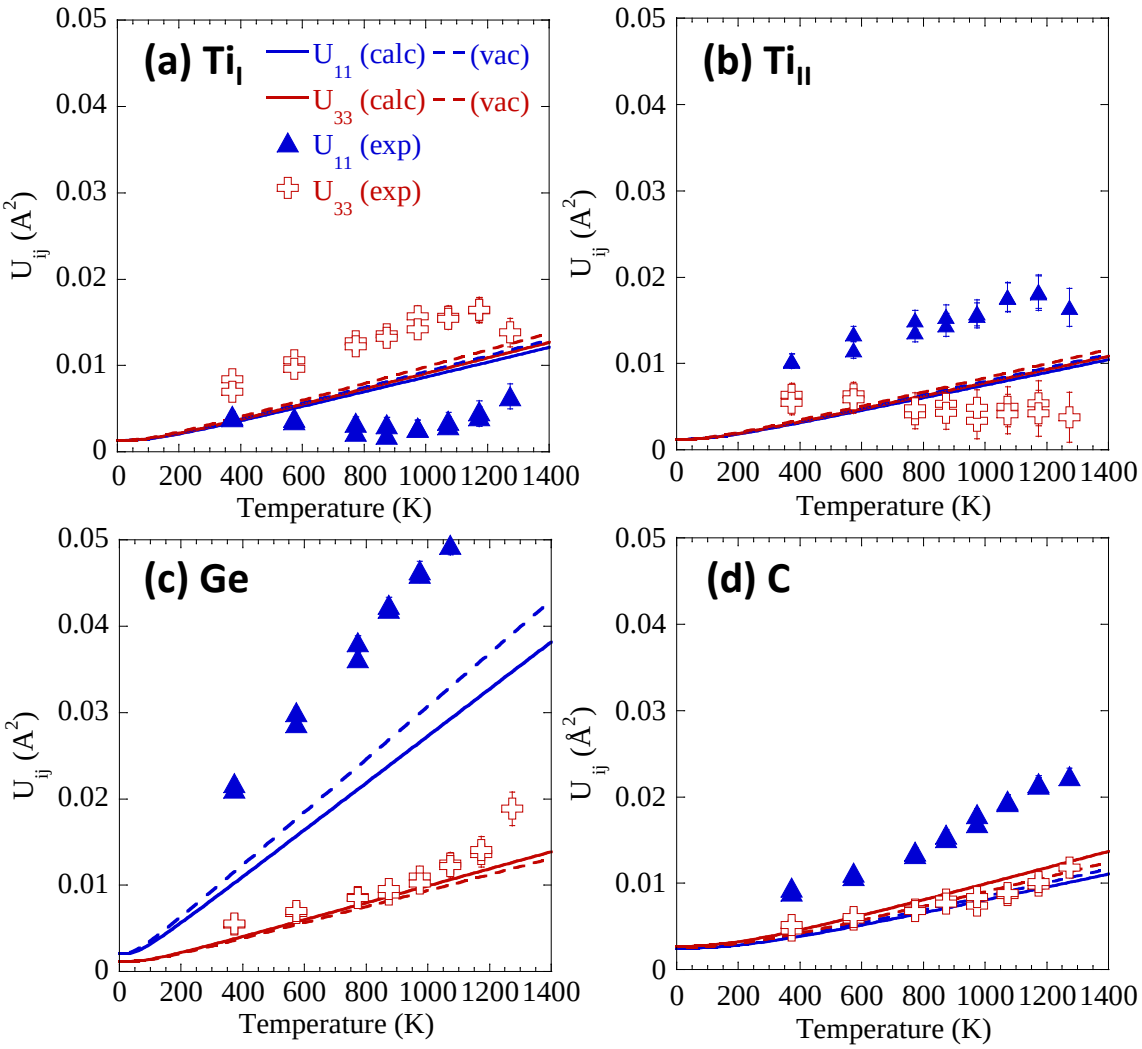

Figure 12.8: Temperature evolution of anisotropic ADPs U_{11} (blue) and U_{33} of (a) Ti_I, (b) Ti_{II}, (c) Ge, and (d) C atoms in Ti_3GeC_2. Solid lines show DFT predictions; markers show experimental values determined from HTND. Error bars are typically smaller than the symbols.

weak scattering power of an element translates to fewer constraints of the structural parameters of those atoms by the experimental diffraction data, manifesting itself as deviations such as larger error bars and more scatter of the values for thermal motion as a function of temperature. For all cases where there is qualitative agreement between predicted and calculated values, the atoms are relatively good neutron scatterers ($\sigma_c > 2$b for Si, Ge, and C).

In general, the anisotropy of the calculated average thermal motion agrees with the HTND data, at least for the *A* atoms. Beyond the agreement in the general trends, there are some slight differences hinting at phenomena that are not accounted for in the harmonic approximation of our Rietveld model and DFT calculations. Focusing on the ADPs of A-group elements, since they are the highest, it is interesting that both Al-containing phases (Ti_2AlN, Fig. 12.4; Ti_4AlN_3, Fig. 12.9) generally show good agreement between theory and experiment, where the anisotropy is well represented by our calculations, with a small offset in magnitude for Ti_2AlN. On the other hand, in both Ge-containing phases (Cr_2GeC, Fig. 12.5; Ti_3GeC_2, Fig. 12.8), U_{11} for Ge is experimentally observed to be higher than calculated, while U_{33} shows excellent agreement with first-principles calculations. The reverse is true for Si in Ti_3SiC_2 (Fig. 12.7), where U_{33} determined experimentally is higher than the calculated values, while U_{11} agrees well with first-principles calculations.

From the phonon partial density of states in Chapter 9 (Fig. 9.7), it can be seen that the phonon frequencies of the Ge states are lower than those of the Al and Si states since Ge is heavier. Furthermore, as discussed in section 9.2, the spread of the Si and Al states indicates more delocalization. The localized peak in Ti_3SiC_2 manifests itself as a higher degree of anisotropy for Si thermal vibrations than for Ge, as determined by first-principles calculations [compare Figs. 12.7(c) and 12.8(c)]. Experimentally this is not observed, which suggests either anharmonic effects that are not accounted for in this model, discrepancies in our force calculations due to

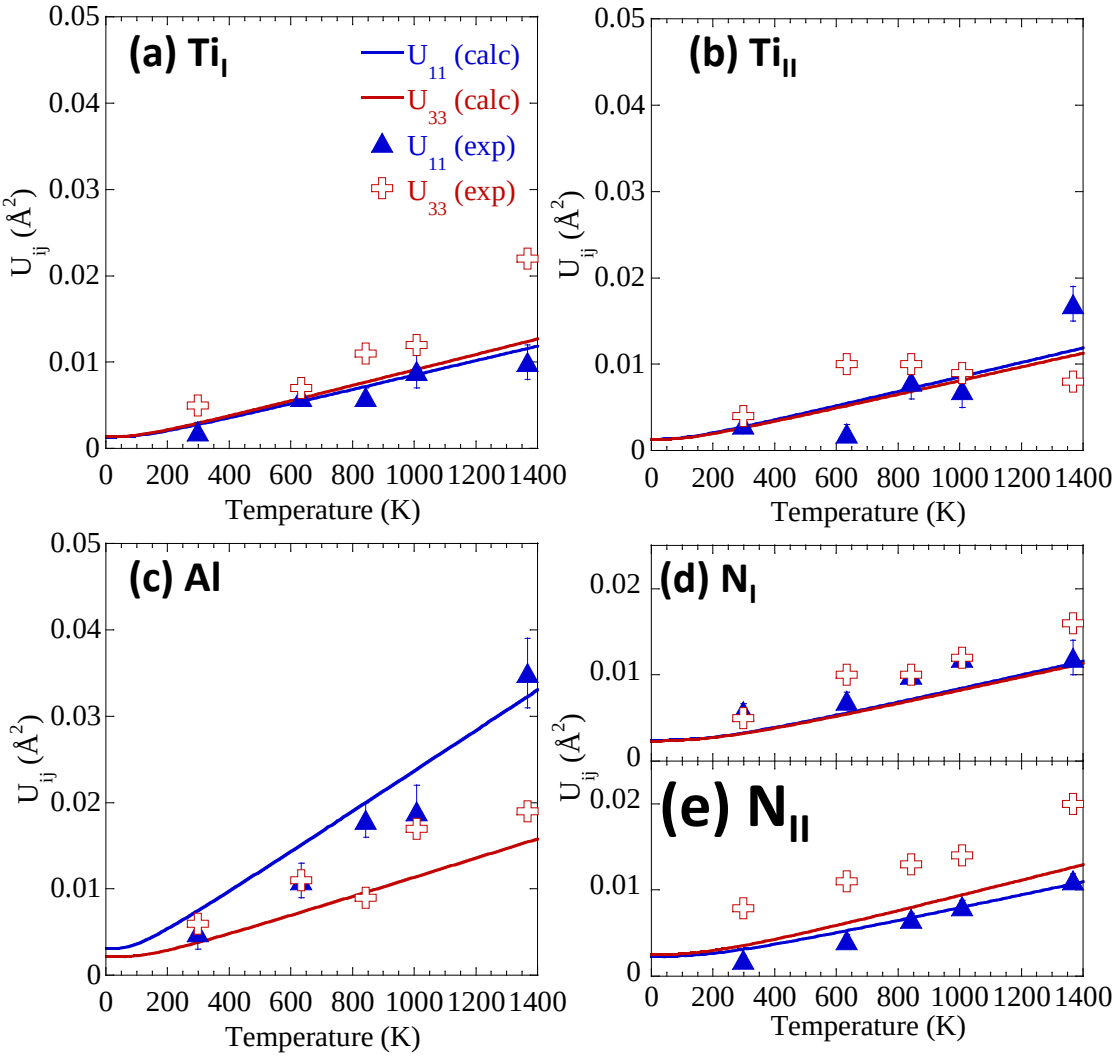

Figure 12.9: Temperature evolution of anisotropic ADPs U_{11} (blue triangles) and U_{33} (red plus signs) of (a) Ti_I, (b) Ti_{II}, (c) Al, (d) N_I, and (e) N_{II} atoms in Ti_4AlN_3. Solid lines show DFT predictions; markers show experimental values determined from HTND in Ref. [138]. Error bars are typically smaller than the symbols.

assumptions within DFT, or defects in Ti_3GeC_2 (likely Ge vacancies or stacking faults) that may cause the vibrations to shift in amplitude and direction.

Looking more closely at the two 312 phases studied (Ti_3SiC_2 in Fig. 12.7; Ti_3GeC_2 in Fig. 12.8), the phonon calculations predict that Si exhibits the highest amplitude of vibration, while this was not observed from the HTND experiments. This is apparent from the thermal ellipsoid representation of the displacements (Fig. 12.10). While the calculated displacements (right) clearly show that thermal vibrations of the Si atom (top) should be larger than the Ge (bottom), the U_{ij}s determined from HTND (left) show that the Ge ellipsoids are more "flattened" and have a higher amplitude within the basal plane. The reason for this state of affairs is unclear at this time. Sources for the discrepancies observed likely come from experimental conditions that are not taken into account in the first-principles phonon calculations herein such as defects which are most likely in the *A* layer. Recent experimental studies on Ti_3GeC_2 thin films have suggested samples to be Ge-deficient [139], which was also postulated to be responsible for the high damping measured through RUS [52]. To explore this, the estimated ADPs for Ti_3GeC_2 with 12.4% ordered Ge vacancies are shown in Fig. 12.8 as dashed lines. From these results, it is clear that vacancies on the A site could lead to a shift in the temperature-dependent ADPs, which is more in line with those observed experimentally – most notably, an increase in the U_{11} to U_{33} ratio for Ge. From the HTND experiments, U_{11}/U_{33} for Ge is 3.2, while the ratio predicted by DFT calculations is 2.7 for a perfect crystal and 3.1 for one containing 12.5% vacancies.

12.3 SUMMARY

In this chapter, the mean-squared atomic displacements determined from Rietveld analysis of HTND data are compared with values determined from first-principles phonon calculations. First, data was presented for the cubic NaCl-type binary carbides, TiN and TaC, to benchmark our

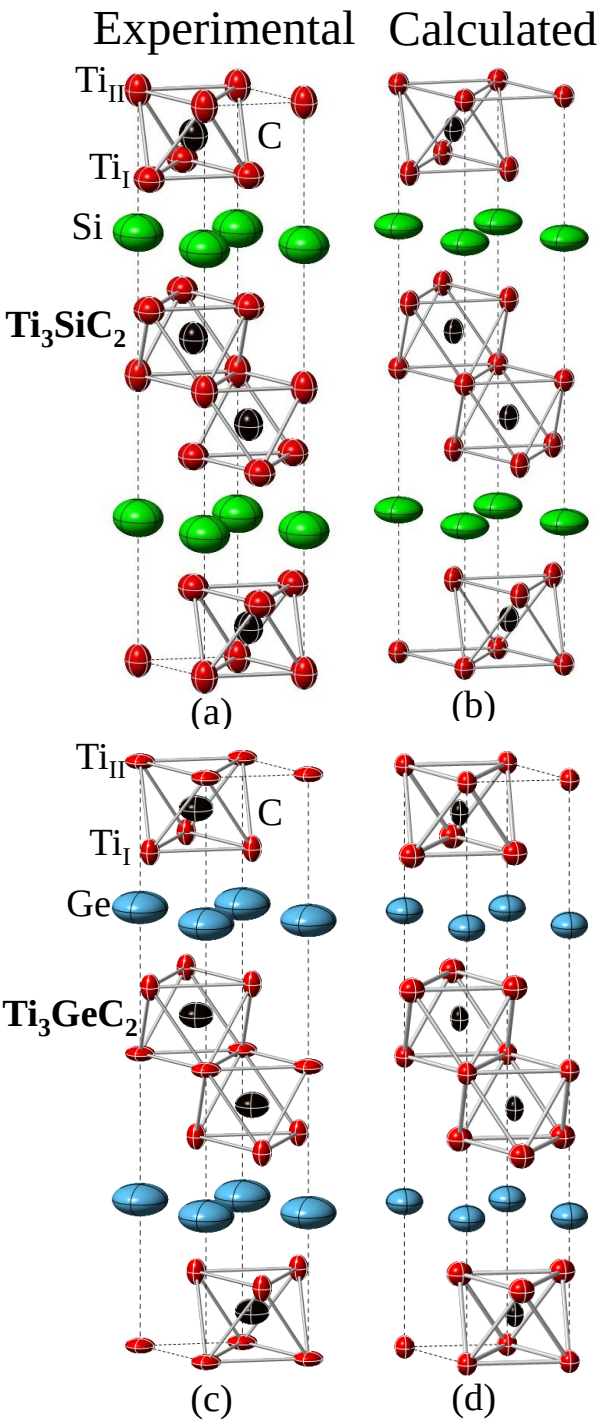

Figure 12.10: Comparison of 99% probability thermal ellipsoids of atoms in Ti_3SiC_2 at 1373 K representing (a) experimental and (b) predicted ADPs; (c) and (d) represent the experimental and predicted thermal atomic displacements, respectively, for Ti_3GeC_2 at 1273 K.

methodology and assess the error for cubic, single-phase randomly oriented powders. WC was also tested to benchmark a single-phase binary hexagonal carbide. Relatively good agreement was found for these phases, with systematic offsets in the temperature-dependent ADPs. Next, the results were presented for the anisotropic displacements of the atoms in the MAX phases. The ADPs from both theory and experiment showed that the *A* atom vibrates with the highest amplitude, anisotropically with $U_{11} > U_{33}$. Qualitatively, this trend was observed for all cases, but beyond the general trends there were discrepancies between the experimental and theoretical values that were minor in some cases and more severe in others. Generally, the Al atoms showed the best agreement while the Ge atoms showed the worst. It was proposed that Ge atoms may play a role in the unexpectedly high ADP of Ge; this idea was supported by first-principles phonon calculations on a Ge-deficient supercell of Ti_3GeC_2.

Chapter 13: Temperature-dependent crystal structures of 211 and 312 phases

Another important set of parameters that come out of the HTND experiments are the atomic positions and lattice parameters. From these, the interatomic distances, bond expansions, volume expansions, and anisotropic CTEs can be determined as well. These temperature-dependent structural parameters help shed light on bonding within the MAX phases, as they can serve as indicators of charge transfer through distortion of octahedra and differences in bond strains.

This chapter summarizes the temperature-dependent crystal structures for two 211 phases (Ti_2AlN and Cr_2GeC) and four 312 phases (Ti_3SiC_2, and Ti_3GeC_2, Ti_3SnC_2, and Ti_3AlC_2) determined from HTND. The purpose of this chapter is to introduce the general behavior of the *M-A* bonds compared to the *M-X* bonds in conventional MAX phases.

13.1 Ti_2AlN AND Cr_2GeC

The lattice parameters and unit cell volumes calculated from the HTND data are listed in Table 13.1, along with experimental room temperature values from other studies. The thermal strains, $\Delta L/L_0$, of the lattice parameters and interatomic distances are plotted as a function of temperature in Figs. 13.1(a) and (b) for Ti_2AlN and Cr_2GeC, respectively. The CTEs in the *a*- and *c*-directions, respectively, are $10.3(\pm0.2) \times 10^{-6}$ K^{-1} and $9.3(\pm0.2) \times 10^{-6}$ K^{-1} for Ti_2AlN and $12.8(\pm0.3) \times 10^{-6}$ K^{-1} and $14.6(\pm0.3) \times 10^{-6}$ K^{-1} for Cr_2GeC. The unit cell volume expansions, henceforth referred to as bulk expansions, are $10.0(\pm0.2) \times 10^{-6}$ K^{-1} for Ti_2AlN and $13.4(\pm0.2) \times 10^{-6}$ K^{-1} for Cr_2GeC. The bond lengths calculated from the structure refinement with Rietveld analysis of the HTND data are summarized in Table 13.2. The bond lengths increase linearly with temperature (Fig. **??**.

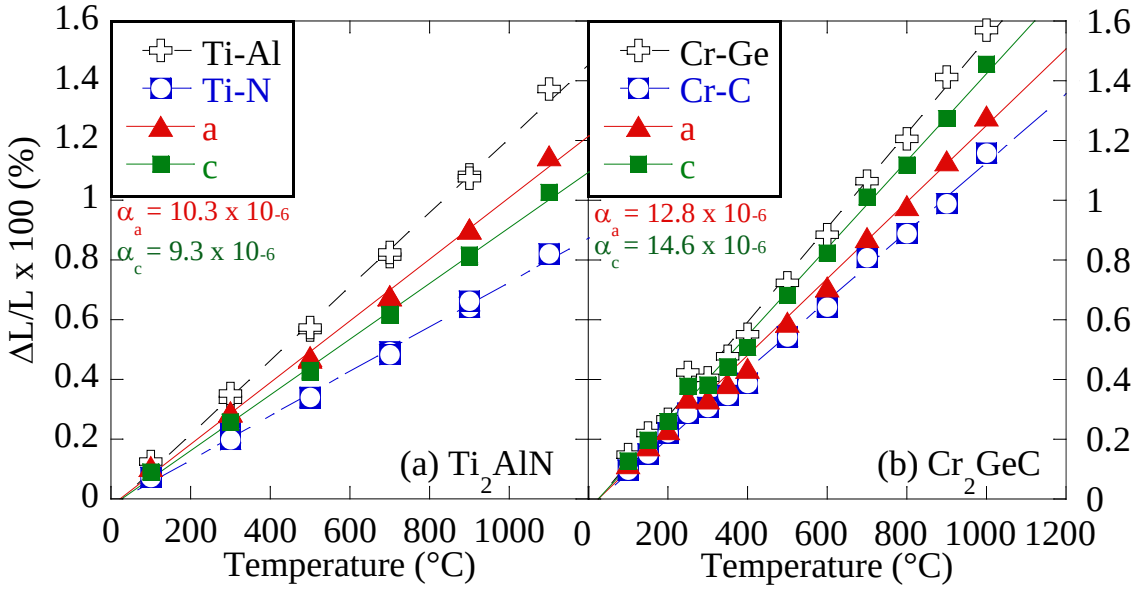

Figure 13.1: Thermal expansions of lattice parameters and selected interatomic distances in, (a) Ti_2AlN and, (b) Cr_2GeC determined from high temperature neutron diffraction. Errors are typically smaller than symbols.

In both cases the largest relative expansion is seen in the *M*–*A*, (Ti–Al or Cr–Ge) bonds, and the smallest relative expansions are observed in the *M*–*X* (Ti–N or Cr–C) bonds. For comparison, Fig. 13.2(a) plots the temperature dependence of the Ti–N bond in Ti_2AlN, along with the Ti–N bonds in TiN [140] and in Ti_4AlN_3 [138]. Figure 13.2(b) shows the structure and nomenclature of the atoms for the Ti_4AlN_3 structure. The Ti–N bonds in TiN are extrapolated from the room temperature Ti–N bond length, 2.12 Å, assuming a CTE of 9.23×10^{-6} K^{-1} [140].

The CTEs for Ti_2AlN – determined from Fig. 13.1, $10.3(\pm0.2) \times 10^{-6}$ K^{-1} and $9.3(\pm0.2) \times 10^{-6}$ K^{-1} in the *a*- and *c*-directions, respectively, with a bulk expansion of $10.0(\pm0.2) \times 10^{-6}$ K^{-1} – are larger than previously reported values determined by HTXRD, 8.6×10^{-6} K^{-1} and 7.0×10^{-6} K^{-1}, respectively [37]. They are, however, more in line with more recent HTXRD results, 10.6×10^{-6} K^{-1} and 9.7×10^{-6} K^{-1} in the *a*- and *c*-directions, respectively [38]. At 8.8×10^{-6} K^{-1}, the dilatometric CTE is lower than the bulk expansion determined herein [37].

Table 13.1: Summary of lattice parameters and unit cell volumes obtained from Rietveld refinements of HTND data for Ti_2AlN and Cr_2GeC, and room temperature values reported in Refs. [28, 33, 43, 141]. Numbers in parentheses are estimated standard deviations in the last significant figure of the refined parameter.

	Ti_2AlN			Cr_2GeC		
T (°C)	a (Å)	c(Å)	Volume Å^3)	a (Å)	c (Å)	Volume (Å^3)
RT [33], [43]	2.986(3)	13.60(2)	105.0(5)	2.952(2)	12.108(4)	91.35 (6)
RT [28],[141]	2.991	13.619	–	2.951	12.08	91.08
100	2.99029(2)†	13.6134(2)†	105.421(2)†	2.94812(3)	12.1183(2)	91.215(2)
300	2.99577(2)	13.6361(2)	105.984(2)	2.95440(3)	12.1491(2)	91.842(2)
500	3.00113(3)	13.6590(2)	106.542(2)	2.96208(3)	12.1854(2)	92.590 (2)
700	3.00733(3)	13.6848(2)	107.185(2)	2.97042(3)	12.2252(2)	93.416(2)
900	3.01400(3)	13.7115(2)	107.871(2)	2.97357(3)	12.2569(2)	94.135(2)
1000	–	–	–	2.97798(3)	12.2789(2)	94.586(2)
1100	3.02138(3)	13.7407(3)	108.631(2)	–	–	–

† Measurement taken during cooling.

Table 13.2: Summary of bond lengths, Å, in Ti_2AlN and Cr_2GeC from Rietveld refinements of HTND Data. Numbers in parentheses are estimated standard deviations in the last significant figure of the refined parameter.

	Ti_2AlN			Cr_2GeC		
T (°C)	Ti–Al	Ti–N	Ti–Ti/Al–Al	Cr–Ge	Cr–C	Cr–Cr/Ge–Ge
100	2.8201(4)†	2.08748(27)†	2.99029(2)†	2.6142(7)	1.9975(5)	2.94812(3)
300	2.8259(4)	2.09058(28)	2.99577(2)	2.6209(7)	2.0017(5)	2.95440(3)
500	2.8325(4)	2.09302(30)	3.00114(3)	2.6292(8)	2.0064(6)	2.96208(3)
700	2.8394(5)	2.09626(32)	3.00734(3)	2.6381(10)	2.0117(7)	2.97042(3)
900	2.8471 (5)	2.09938(34)	3.01401(3)	2.6472(10)	2.0153(7)	2.97357(3)
1000	–	–	–	2.6513(11)	2.0187(8)	2.97798(3)
1100	2.8552(6)	2.1031(4)	3.02139(3)	–	–	–

† Measurement taken during cooling.

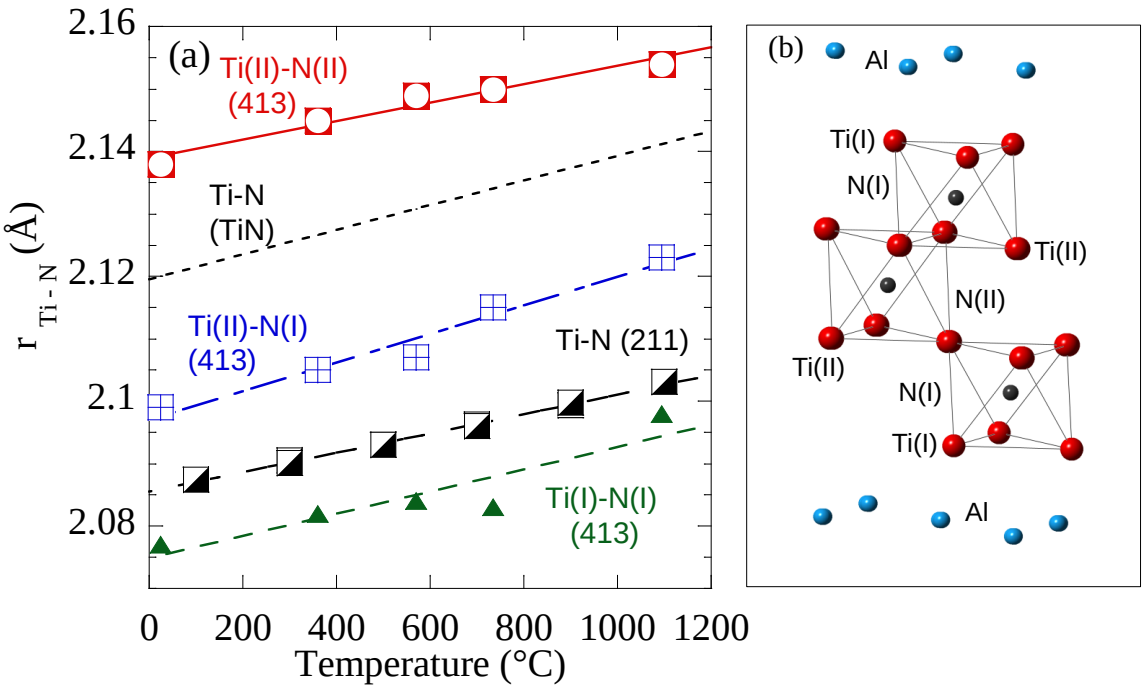

Figure 13.2: Temperature dependence of Ti–N bond lengths in Ti_2AlN (211) measured in this work compared to Ti–N in TiN, from Ref. [140], and Ti_4AlN_3 (413), from Ref. [138]. Errors are typically smaller than symbols. (b) Structure of a Ti–N octahedra in Ti_4AlN_3, labeling nomenclature adopted herein.

It should be noted that the CTE measured using dilatometry measures the expansion of the whole sample, including the secondary phases, while diffraction measures the expansion of the individual phases. A recent HTND study on the phase stability of Ti_2AlN at temperatures up to 1800°C gave a CTE of 12.7×10^{-6} K^{-1} and 11.5×10^{-6} K^{-1} in the a- and c- directions, respectively, over the 25-1800°C temperature range [142]. The differences in CTE are likely due to either secondary phases or possibly variations in the N-content. Note that in all cases, $\alpha_a > \alpha_c$. In the case of TiN, it has been shown that the CTE of N-deficient TiN_x is lower than that of stoichiometric TiN.[136, 140, 142]. Since refinement of the N site in our sample led to 97% occupancy, and neutrons interact strongly with N, which has a neutron coherent scattering length of 11.01 fm [116], it is reasonable to conclude that there is a higher N-site vacancy

concentration in our samples than those used in Refs. [142] or [38]. The XRD study in Ref. [37] included ~10-15 vol. % secondary phases, which may have affected the CTE values due to grain-grain interactions. Note that no secondary phases were detected in the Ti_2AlN sample tested herein, lending credibility to the CTE values obtained in this work. Also, in the previous dilatometric and HTXRD studies, preferred orientation may have affected the results, whereas herein the texture has been shown to be mild (see Fig. A.3) and can be ruled out as a factor. These comments notwithstanding, a systematic study in which the CTEs are measured as a function of vacancy concentration is indicated and should be carried out.

For Cr_2GeC, on the other hand, with $\alpha_a = 12.8(\pm 0.3)\times 10^{-6}$ K^{-1} and $\alpha_c = 14.6(\pm 0.3)\times 10^{-6}$ K^{-1}, the CTE is higher in the c-direction. α_c is slightly lower than the CTE previously reported from HTXRD ($\alpha_c = 17.6(\pm 0.2) \times 10^{-6}$ K^{-1} [38]), while the a lattice expansion is the same, within error bars, as that from HTXRD ($\alpha_a = 12.9(\pm 0.1) \times 10^{-6}$ K^{-1} [38]). The average CTE from HTXRD, assuming $\alpha_{ave} = \frac{2}{3}\alpha_a + \frac{1}{3}\alpha_c$, is $c = 14.5 \times 10^{-6}$ K^{-1} [38], which is slightly higher than the $13.4(\pm 0.3)\times 10^{-6}$ K^{-1} bulk expansion reported herein. Regardless of the exact values of the CTE, these results confirm, once again, that the Cr-containing MAX phases have anomalously high CTEs as compared to other MAX phases. Also, the lattice parameters of Cr_2GeC are slightly smaller than expected, which may be because of the secondary phases that constrain the unit cell, or more likely instrument alignment (since no internal standard was used for calibration).

The interatomic distances between the Ti and N atoms as a function of temperature in Ti_2AlN are compared to the same bonds in TiN and Ti_4AlN_3 in Fig. 13.2. The Ti–N bond length in Ti_2AlN (2.085 Å, extrapolated to room temperature from the HTND data) is significantly shorter than that in stoichiometric TiN (2.12Å), and is slightly higher than the Ti–N bond of the Ti layers nearest to the Al-layer in Ti_4AlN_3, determined from a HTND experiment [138]. Taken together, the thermal expansions of the various Ti–N bonds are comparable. However, a more detailed

look shows that the expansions of the Ti–N bonds in Ti_2AlN were the lowest and comparable to those in the binary.

Overall, a comparison of these two phases demonstrates how the different chemistries play into the changes of the crystal structures with temperature. While both are 211 MAX phases with the same crystal structure, they share no common elements and therefore have completely different interatomic interactions throughout the material. One significant difference between the two phases is their relative thermal expansions – that is, the anisotropy is reversed between the two. However, it is important to note here that despite the differences in the overall lattice expansion in different directions, the expansion of the *M*–*A* bonds relative to the *M*–*X* bonds is qualitatively similar, with the *M*–*A* bonds exhibiting the highest rate of expansion of all the bonds in the material in both cases. This, again, is an indication of the weaker *M*–*A* bond relative to the *M*–*X* bond and is generally observed in the MAX phases as a class. It will later be shown that situations where there are deviations from this trend may indicate disorder or other bonding intricacies. Such cases will be discussed in Chapters 14 and 15 on the higher-order MAX phase and correlated motion in Ti_3GeC_2, respectively.

13.2 Ti_3AlC_2, Ti_3SiC_2, Ti_3GeC_2, AND Ti_3SnC_2

The 312 phases have more atoms in a unit cell than the 211 phases and therefore have more symmetry-equivalent sites and more bonds of different lengths throughout the crystal structure. This section will give a brief overview of the general trends in crystal expansions and temperature-dependent bond lengths in the 312 phases. A more in-depth study of Ti_3SiC_2 and Ti_3GeC_2 will be presented in Chapter 15, where more information on the temperature-dependent bond lengths may be found.

Unlike the 211 phases, the 312 phases have two distinct Ti sites – Ti_I, which is adjacent to the

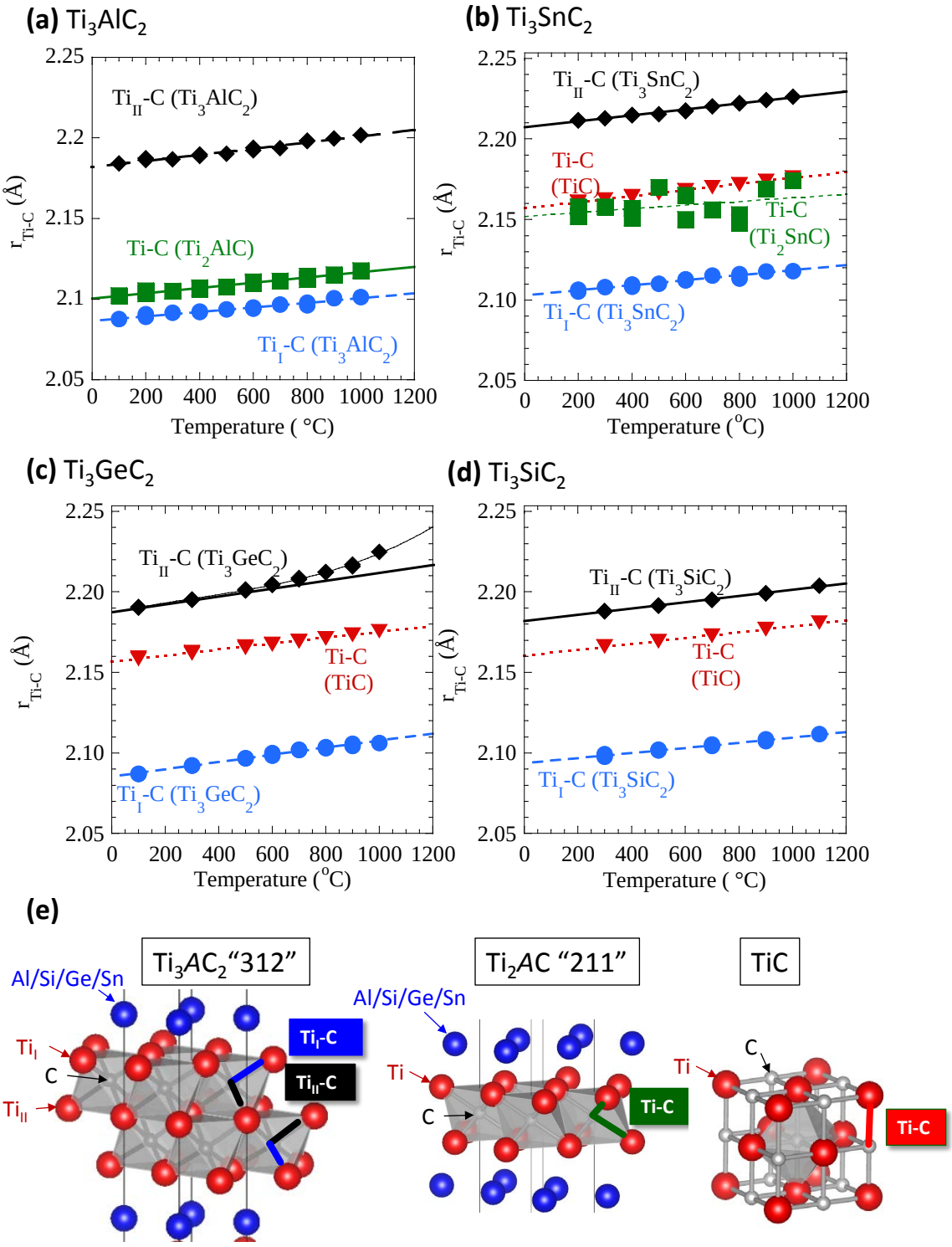

Figure 13.3: Temperature dependencies of Ti-C bond lengths for primary Ti_3AC_2 and secondary phases (TiC and/or Ti_2AC) in (a) Ti_3AlC_2, (b) Ti_3SnC_2, (c) Ti_3GeC_2, and (d) Ti_3SiC_2 samples. Note that all phases in each figure are from the same sample. Errors are typically smaller than symbols. (e) Schematics of the 312, 211, and binary TiC structures highlighting Ti-C bonds.

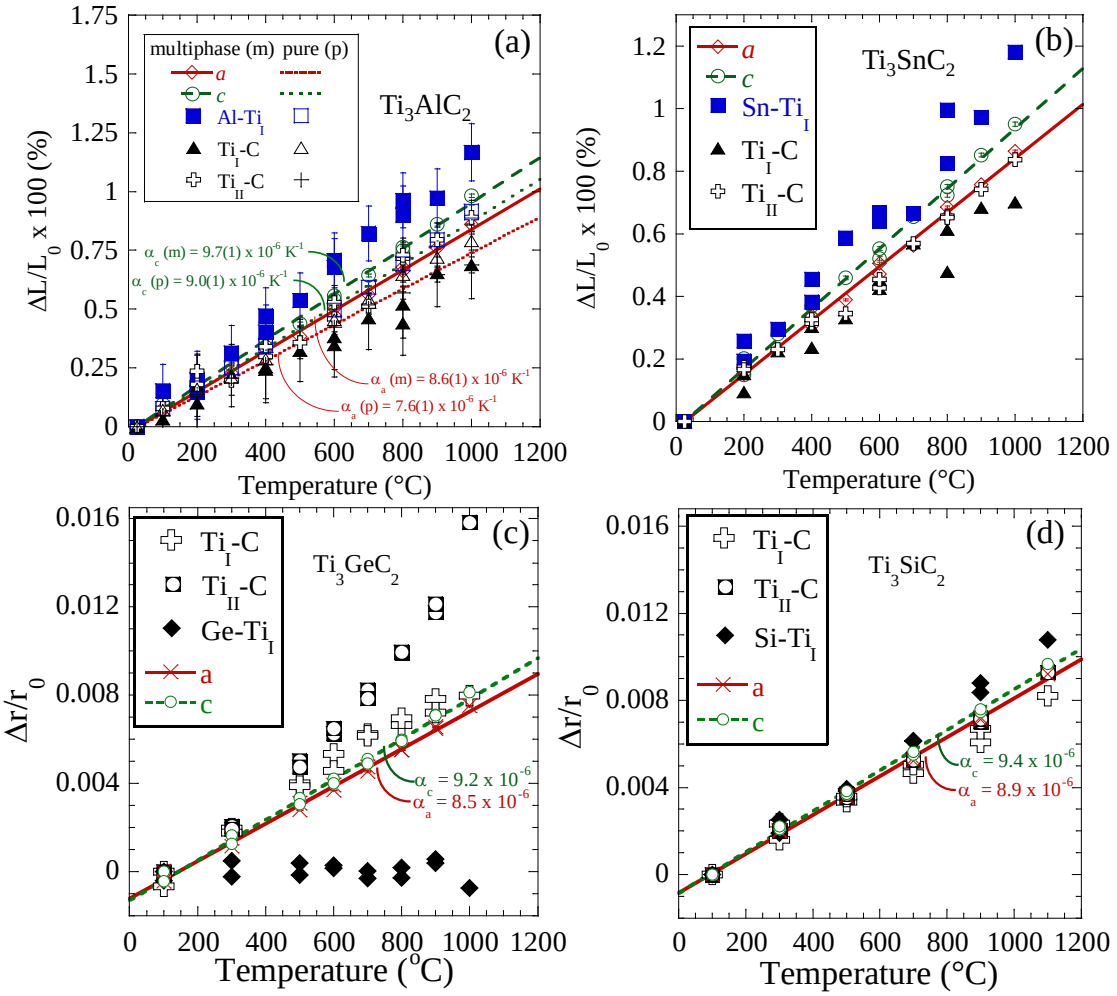

Figure 13.4: Temperature dependencies of the thermal strains of the lattice parameters and interatomic distances in (a) Ti_3AlC_2, (b) Ti_3SnC_2, (c) Ti_3GeC_2, and (d) Ti_3SiC_2. The room temperature values were extrapolated from slightly higher temperatures starting at 100°C for comparison sake. Errors are typically smaller than symbols.

A layers, and Ti_{II}, which is sandwiched between the Ti–C octahedra above and below [see Fig. 13.3(e)]. The temperature-dependent Ti–C bond lengths are shown in Figs. 13.3(a)–(d). For all the 312 structures, the Ti_I-C bonds are shorter than, while the Ti_{II}-C bonds are longer than, the Ti-C distance in TiC. This has been confirmed by first-principles calculations and other diffraction studies and is related to the charge transfer involved in the bonding intricacies, where the Ti_I atom tends to relax toward the *A*-atom plane. Also plotted for comparison in Figs. 13.3(b), (c), and (d) are the Ti-C distances in the TiC secondary phases present in the samples (red triangles). In Figs. 13.3(a) and (b), the Ti-C bond lengths for the 211 secondary phase is also plotted (green squares). Generally, the Ti–C bond lengths in the 211 phases and in TiC fall between the Ti_I and Ti_{II} bond lengths in the 312 phases.

From the results shown in Figs. 13.3(c) and (d) for the Ti_3GeC_2 and Ti_3SiC_2 HTND experiments, the CTE of the impurity TiC phase, in both Ti_3GeC_2 and Ti_3SiC_2, is estimated to be $8.5(\pm0.1) \times 10^{-6}$ K^{-1}. These values are higher than the 7.0×10^{-6} K^{-1} (Ref. [143]) or 7.4×10^{-6} K^{-1} (Ref. [140]) reported for near-stoichiometric TiC in previous studies. The reason for this state of affairs is not totally clear at this time, but could be due to either the fact that the TiC in the ternaries is nonstoichiometric and/or the result of thermal residual stresses. The measured TiC lattice parameters suggest it was stoichiometric.

Turning to all the bonds in the 312 phases [Figs. 13.4(a)-(d)], the Ti–*A* bonds in Ti_3AlC_2 [Fig. 13.4(a)], Ti_3SnC_2 [Fig. 13.4(b)], Ti_3SiC_2 [Fig. 13.4(d)] expand at a higher rate than the Ti–C bonds in the material, where the lattice expansion rates are in between the expansions of the Ti–C and Ti–*A* bonds. In Ti_3GeC_2, however, there is a strikingly different behavior. The highest expansion is for the Ti_{II}–C bond, which typically is more rigid than the Ti–*A* bonds. Further, the Ti_I–Ge bond apparently stays constant with temperature [black diamonds in Fig. 13.4(c)]. I will come back to this unexpected behavior in Chapter 15, where I will argue that this has to do

with the atomic motion behavior of the Ge atoms in the structure that may also have to do with anharmonic terms in the Ti–Ge interactions. For now, it is assumed that the bond expansion behavior in the other three 312 phases [Figs. 13.4(a), (b), and (d)] represent "normal" MAX phase behavior.

13.3 SUMMARY

In this chapter, the temperature-dependent crystal structures of Ti_2AlN, Cr_2GeC, Ti_3SiC_2, Ti_3GeC_2, Ti_3SnC_2, and Ti_3AlC_2 were presented, as determined form Rietveld analysis of high-temperature neutron diffraction data. In the 211 phases, Ti_2AlN and Cr_2GeC, the *M*-*A* bonds showed the highest expansion. In all the 312 phases, the Ti_I bonds, which involve the Ti atom adjacent to the Al layer, were shorter than the Ti_{II} bonds. In Ti_3GeC_2, the Ti_{II} exhibited a nonlinear increase in length, in conjunction with a Ti–Ge bond that was apparently constant with temperature.

Chapter 14: Temperature-dependent crystal structure of $Ti_5Al_2C_3$

In the previous chapter, I summarized the temperature dependencies of the bond lengths and lattice parameters of some 211 and 312 phases. Now, I turn to a slightly more complex structure. The focus of this chapter is on an interesting case of a "higher-order" MAX phase, $Ti_5Al_2C_3$, with a stacking sequence that alternates between 211 and 312 (see Fig. 14.1). This investigation involves the use of first-principles calculations to model the atomic displacements of the atoms in the structures as well as high-temperature neutron diffraction to measure their temperature-dependent crystal structures. The main purpose of this case study is to assess the effect of stacking sequence on the dynamical behavior of atoms and the expansions of the bonds in the structure. The results presented in this chapter also suggest that the Ti–Al bonds serve to compensate for other disorder in the system, which is demonstrated through the behavior of the Ti–Al bonds compared to the Ti–C bond behavior. Further, this work shows that the agreement between theory and experiment for the Ti–Al–C system is very good, even in such a complex multiphase system.

For the study presented in this chapter, a sample containing $Ti_5Al_2C_3$ [38(±1) wt.%], Ti_2AlC [32(±1) wt. %], Ti_3AlC_2 [18(±1) wt. %], and $(Ti_{0.5}Al_{0.5})Al$ [12(±1) wt.% was used. Only the results on the crystal structure of the phases are presented here; further information on the diffraction statistics, texture, and composition can be found in Appendix A.1.3. Most of the work presented in this chapter was published in Ref. [6]. In addition to this paper, I have written two additional papers on the Ti_5AlC_2 phase that are included in Appendix B.2.

14.1 TEMPERATURE-DEPENDENT CRYSTAL STRUCTURES OF Ti_3AlC_2, Ti_2AlC, AND $Ti_5Al_2C_3$

The temperature-dependent expansions of the lattice parameters and interatomic distances in $Ti_5Al_2C_3$, Ti_3AlC_2, and Ti_2AlC are shown in Figs. 14.3(a), (b), and (c), respectively. In Fig. 14.3(b), the parameters for the predominantly single-phase Ti_3AlC_2 sample are also plotted as open symbols, where the a and c expansions are both lower than in the multiphase sample. The anisotropic TEC values are listed in Table 14.1, along with those from previous studies for Ti_2AlC [37] and Ti_3AlC_2 [38, 144, 145].

To further compare the thermal expansions of the 3 phases, the temperature dependencies of $(\Delta V/V_o)^{1/3}$ – where ΔV is the change in unit cell at temperature T as compared to that at the reference temperature, 25°C (extrapolated), V_0 – are plotted in Fig 14.3(d), where the slope yields α_{av}. Also plotted are the results for $(Ti_{0.5}Al_{0.5})Al$, an impurity phase in the sample (see Appendix A.1.3). For Ti_2AlC, $\alpha_{av} = 9.2(\pm0.1) \times 10^{-6}$ K^{-1}; for Ti_3AlC_2, $\alpha_{av} = 9.0(\pm0.1) \times 10^{-6}$ K^{-1}; for $Ti_5Al_2C_3$ $\alpha_{av} = 9.3(\pm0.1) \times 10^{-6}$ K^{-1}. It is thus clear from Fig. 14.3(d) that the TECs of the three MAX phases are almost identical within the error bars.

The absolute values of the c and a lattice parameters [Figs. 14.4(a) and (b), Table 14.2] are also comparable, but it is apparent that Ti_3AlC_2 has the highest a lattice parameter and Ti_2AlC has the lowest, with that of $Ti_5Al_2C_3$ falling in between. The same is true of the c lattice parameters, after normalizing it by three to account for the three formula units in $Ti_5Al_2C_3$ [Fig. 14.4(b)].

The temperature dependences of the absolute values of the Ti–C and Al–Ti bonds are shown in Figs. 14.4(c) and (d), respectively. The bonds in Ti_2AlC, Ti_3AlC_2 and $Ti_5Al_2C_3$ are shown in black, red, and blue, respectively. Note that the absolute range for the scale is the same for the three graphs shown in Figs. 14.4(a), 14.4(c) and 14.4(d). The extrapolated room temperature

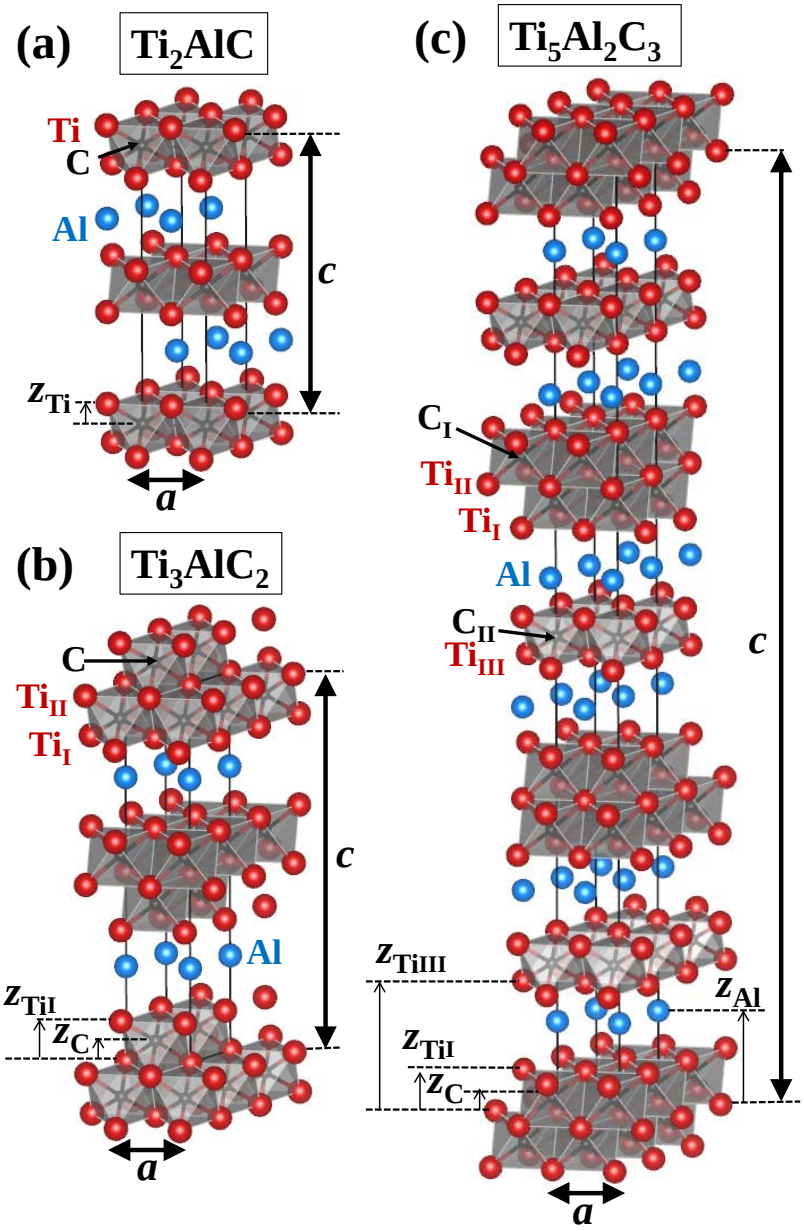

Figure 14.1: Structure of (a) Ti_2AlC, (b) Ti_3AlC_2, and (c) $Ti_5Al_2C_3$ showing lattice parameters a and c and the unique Ti, Al, and C lattice sites as constrained by symmetry, along with the refined atomic position z parameters.

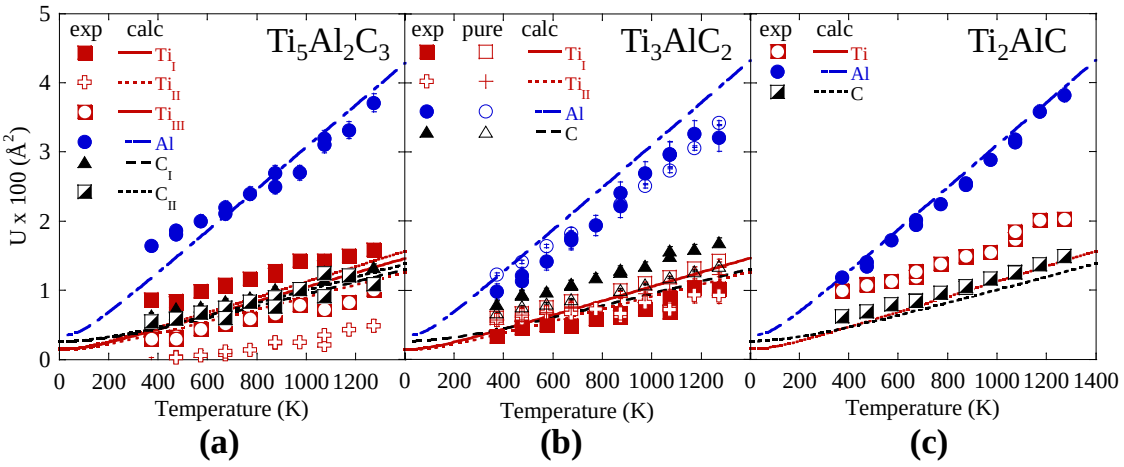

Figure 14.2: Temperature dependence of isotropic thermal displacement parameter U_{iso} during heating and cooling for atoms in (a) $Ti_5Al_2C_3$, (b) Ti_3AlC_2, and (c) Ti_2AlC. Errors are typically smaller than symbols size.

values for all bonds are also listed in Table 14.3, along with their expansion rates.

Due to the overlap of peaks in our data set we were unable to determine the anisotropic displacements as was done in our previous HTND studies [2–4, 53, 138]. Instead, we examine the isotropic ADPs, U_{iso}, which represent the mean-squared displacements of the atoms from their equilibrium positions. Figures 14.2(a), (b), and (c) show the temperature dependence of U_{iso} for the unique Ti (red), Al (blue), and C (black) atoms in $Ti_5Al_2C_3$, Ti_3AlC_2, and Ti_2AlC, respectively. In Fig. 14.2(b) the values for predominantly single-phase Ti_3AlC_2 are shown for comparison's sake.

The values calculated with first-principles phonon calculations are shown as lines. In both experimental and calculated results, the Al atom shows the highest amplitude. Figure 14.5 compares the experimental and calculated values of U_{iso} for the Al atoms in all three phases $Ti_5Al_2C_3$, Ti_3AlC_2 and Ti_2AlC in the multiphase sample, along with U_{iso} for pure Ti_3AlC_2. Also shown are the experimental U_{eq} values for the Al-containing phases Ti_2AlN and Ti_4AlN_3, determined from in previous HTND studies [2, 138], along with calculated values for those

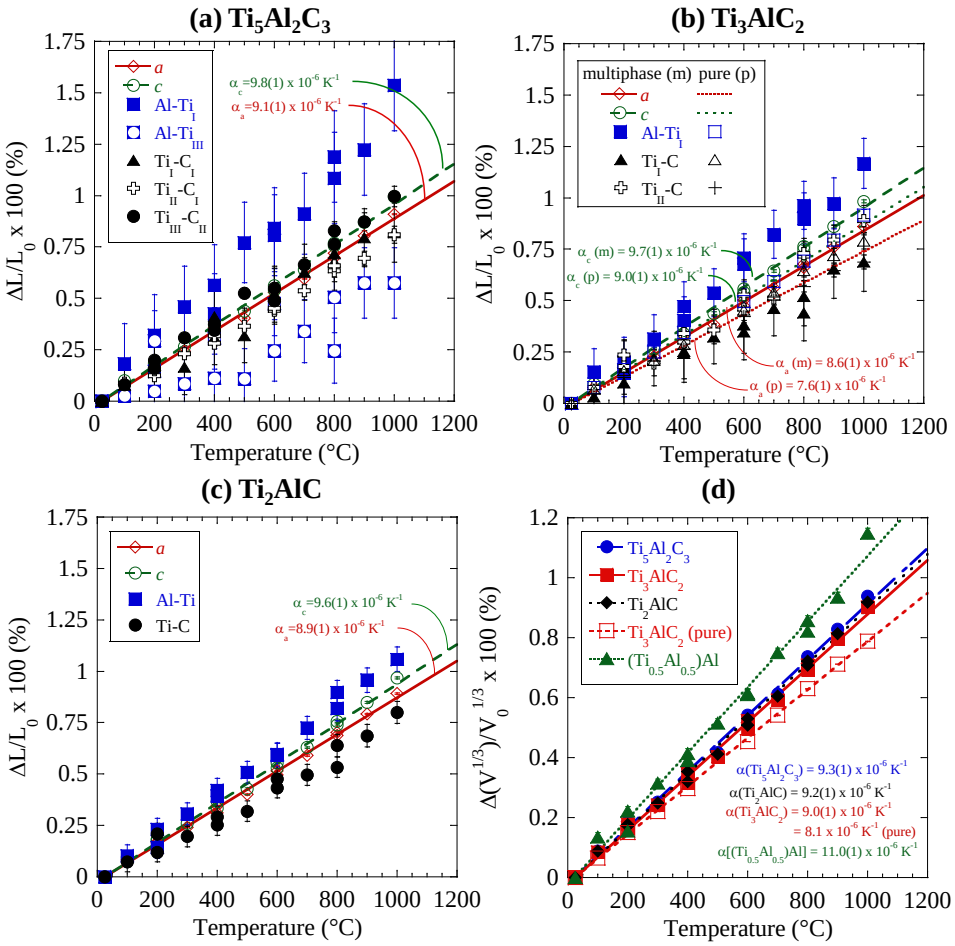

Figure 14.3: Temperature dependences of the thermal strains of the lattice parameters and interatomic distances in (a) $Ti_5Al_2C_3$, (b) Ti_3AlC_2, and (c) Ti_2AlC for the multiphase sample. In (b), the results for predominantly single-phase Ti_3AlC_2 are also shown. (d) Volume expansion of $Ti_5Al_2C_3$ (blue circles), Ti_3AlC_2 (red solid squares), and Ti_2AlC (black diamonds) in the multiphase sample, and pure Ti_3AlC_2 (open red squares). Room temperature (25°C) values were extrapolated to use for L_0 and V_0. Errors for volume expansions in (d) are typically smaller than symbols size.

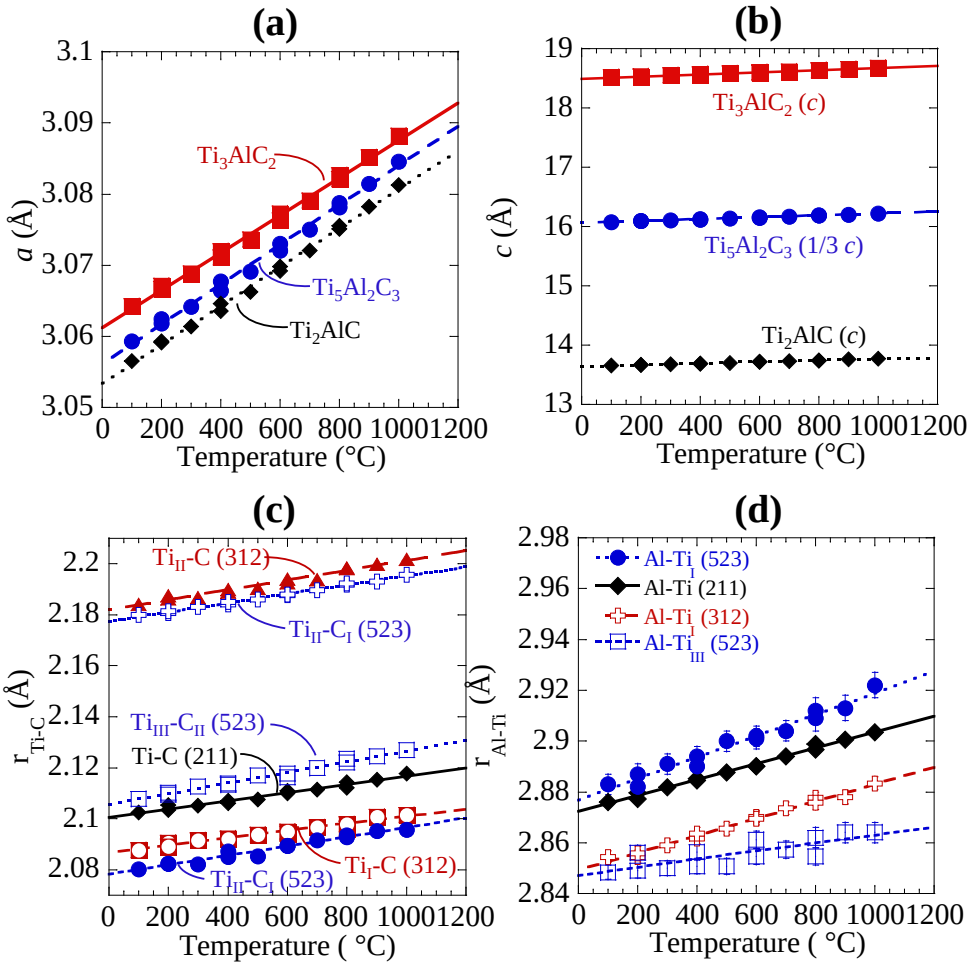

Figure 14.4: Temperature dependence of (a) *a* and (b) *c* lattice parameters, and (c) Ti–C and (d) Ti–Al interatomic distances in $Ti_5Al_2C_3$ (blue), Ti_3AlC_2 (red) and Ti_2AlC (black). Refer to Fig. 14.1 for notations of Ti and C atoms. Errors are typically smaller than symbols size.

Table 14.1: Thermal expansions from HTND for Ti–Al–C phases in the multiphase sample, along with those from other studies [37, 38, 144–147] determined through HTXRD and dilatometry. Numbers in parentheses are estimated standard deviations in the last significant digit of the refined parameters.

Phase	α_a (10^{-6} K^{-1})	α_c (10^{-6} K^{-1})	α_{av} (10^{-6} K^{-1})	Anisotropy (α_c/α_a)	Ref.
$Ti_5Al_2C_3$	9.1(1)†	9.8(1)†	9.3(1)†	1.08(3)†	This work
Ti_2AlC	9.0(1)†	9.6(1)†	9.2(1)†	1.07(3)†	This work
	7.1(3)^{a}	10.0(5)^{a}	8.1(5)^{a,b}; 8.2(2)^{c}	1.41(4)	Ref. [37]
Ti_3AlC_2	8.6(1)†	9.7(1)†	9.0(1)†	1.13(3)†	This work
	7.6(1)	9.0(1)	8.1(1)	1.18(3)	This work
	8.3(1)^{a}	11.1(1)^{a}	9.2(1)^{a,b}; 7.9(5)^{c}	1.33(1)^{a}	Ref. [38]
	-	-	9.0(2)^{c}	-	Ref. [145]
	8.5	10.2	9.2^{b}	1.2	Ref. [144]
$(Ti_{0.5}Al_{0.5})Al$	10.7(1)†	11.5(1)†	11.0(1) †	1.074(3)†	This work
γ-TiAl	-	-	10.0	-	Ref. [146]
	9.77	9.26	-	-	Ref. [147]

† Multi-phase sample.
^{a} High-temperature XRD.
^{b} Assuming $\alpha_{av} = (2/3\alpha_a + 1/3\alpha_c) = V_0^{-1/3} dV^{1/3}/dT$
^{c} Dilatometry

phases from Ref. [4]. The U_{iso} values for Al in the three Ti–Al–C phases are similar to each other, and slightly higher than U_{eq} of for Al in the Ti–Al–N phases, which is consistent with the values determined from first-principles calculations. Note that the calculated U_{iso} curves for Al in $Ti_5Al_2C_3$, Ti_2AlC, and Ti_3AlC_2 in Fig. 14.2 lie essentially on top of one another, and those for Al in Ti_2AlN and Ti_4AlN_3 are similar as well, but smaller than those of the carbide phases.

14.2 DISCUSSION

14.2.1 Lattice parameters, expansions, and anisotropies

Not surprising, the measured a- and scaled c-parameters of the 523 phase are in between those of the 211 and 312 phases [Fig. 14.4(b)]. This is also consistent with the values from our first-principles calculations (Table 14.2). Our lattice parameters are in good agreement

with literature values for Ti_2AlC [8, 33, 37], $Ti_5Al_2C_3$ [8], and Ti_3AlC_2 [8, 31]. Their order of increase is likely due to intricacies in charge transfer involved in bonding. The fact that the a lattice parameter scales with the number of Ti–C bonds is consistent with first principles calculations [8].

The overall expansions of the three MAX phases in the multiphase sample are, within their error bars, nearly equivalent (Table 14.1). The a and c lattice expansions are qualitatively comparable, with the a lattice parameters and their thermal expansions all within 1% of each other [Fig. 14.4(a)]. Consistent with previous studies, the expansion in the c direction is greater than along the a. However, for reasons discussed below, in the present study the degree of anisotropy is significantly lower than in Refs. [37, 38, 145] (Table 14.1). We now consider each of the phases separately.

Ti_2AlC: The TECs along the a- and c-direction for the Ti_2AlC sample measured herein – 8.9($\pm$0.1) $\times$ 10^{-6} $K^{-1}$and 9.6($\pm$0.1) $\times$ 10^{-6} K^{-1}respectively [Fig. 14.3(c)] – fall in between those reported previously for Ti_2AlC (Ref. [37]). The reason(s) for the discrepancy is unknown at this time but could very well reflect differences in chemistry. Recent work in the literature suggests that Ti_2AlC exists over a range of stoichiometries. For example, Bai *et al.* recently reported the existence of a Ti_2AlC_x phase where x was as low as 0.69 [148, 149]. Herein, it is more likely than not that the Ti_2AlC is Al-deficient since it is believed that the loss of Al is what triggers the transformation to the 523 and possibly the 312 phase.

Ti_3AlC_2: The TEC values measured herein for the 312 phase depended on sample. The predominantly single-phase Ti_3AlC_2 sample has a lower expansion in both directions, resulting in a statistically significant lower α_{av} of 8.1($\pm$0.1) $\times$ 10^{-6} K^{-1}(Fig. 14.3). At 9.0($\pm$0.1) $\times$ 10^{-6}

Table 14.2: Temperature-dependent *a* and *c* lattice parameters from Rietveld refinement of neutron diffraction data collected during heating and cooling. Numbers in parentheses are estimated standard deviations in the last significant figure of the refined parameters. Room temperature values are extrapolated to 25°C from linear interpolation.

	$Ti_5Al_2C_3$		Ti_2AlC		Ti_3AlC_2	
Temp. (°C)	*a* (Å)	*c* (Å)	*a* (Å)	*c* (Å)	*a* (Å)	*c* (Å)
RT (Ref.[31])	-	-	-	-	3.0753	18.578
RT (Ref. [33])	-	-	3.065(4)	13.71(3)	-	-
RT (Ref. [37])	-	-	3.051	13.637	-	-
RT (Ref. [8])	3.064(2)	48.23(2)	3.063	13.645	3.060	18.66
RT (Ref. [8])[a]	3.068	48.186	3.067	13.75	3.083	18.661
RT[b]	3.05678(6)	48.189(1)	3.05405(7)	13.6422(5)	3.06186(8)	18.4994(8)
100	3.05926(6)	48.237(1)	3.05656(7)	13.6551(5)	3.06424(8)	18.5172(8)
200	3.06184(6)	48.280(1)	3.05912(7)	13.6669(4)	3.06667(8)	18.5331(8)
300	3.06419(6)	48.317(1)	3.06141(7)	13.6777(5)	3.06887(8)	18.5483(8)
400	3.06642(6)	48.354(1)	3.06353(7)	13.6879(4)	3.07108(8)	18.5617(8)
500	3.06911(6)	48.400(1)	3.06627(7)	13.7006(4)	3.07359(8)	18.5803(8)
600	3.07208(6)	48.449(1)	3.06920(7)	13.7145(4)	3.07635(8)	18.5991(8)
700	3.07501(6)	48.497(1)	3.07206(7)	13.7280(4)	3.07908(8)	18.6184(8)
800	3.07814(6)	48.554(1)	3.07510(7)	13.7431(5)	3.08213(8)	18.6380(8)
900	3.08141(6)	48.608(2)	3.07825(7)	13.7581(5)	3.08519(8)	18.6587(9)
1000	3.08460(6)	48.667(2)	3.08126(7)	13.7743(5)	3.08818(8)	18.6811(9)
800[c]	3.07876(6)	48.559(2)	3.07552(7)	13.7453(5)	3.08264(9)	18.6404(9)
600[c]	3.07301(6)	48.459(2)	3.06978(7)	13.7180(5)	3.07730(9)	18.6025(9)
400[c]	3.06770(6)	48.368(2)	3.06460(7)	13.6922(5)	3.07200(9)	18.5684(9)
200[c]	3.06239(6)	48.279(2)	3.05928(7)	13.6672(5)	3.06712(9)	18.5337(9)

[a] Calculated from first principles.
[b] Extrapolated value
[c] Data collected during cooling

K^{-1}, α_{av} for the 312 phase in the multiphase sample is about 10% higher than in the single phase one.

$Ti_5Al_2C_3$: Since this is the first report on the effect of temperature on the lattice parameters of the 523 phase, there are no previous results to compare them with. However, the fact that α_{av} of this phase is very comparable to the 211 and 312 phases is not surprising and is consistent with the fact that the former is comprised of the same building blocks as the latter.

Lastly, a few remarks on the expansions. The ability to measure phase sensitive TECs is

an advantage of HTND, as compared to other methods such as dilatometry, that require pure phases to measure their volume TEC. However, it is important to appreciate that the TEC values measured herein per force are less anisotropic than those one would measure in loose powders. In the latter case, the solid is free to expand, whereas when the measurement is made on bulk solids, residual stresses can accrue and reduce the values of the thermal expansions in various directions. The effect is best appreciated when the TECs in the *a* and *c* directions are compared with those measured on powder Ti_2AlC samples [38].

14.2.2 Bond lengths

While the overall expansions and anisotropies in the three MAX-like phases are comparable, the most interesting aspect of this work is the relationship between bond length evolution and the stacking of the octahedra among the three phases. In the literature, it is fairly well established, both experimentally and theoretically, that the *M*–C bonds adjacent to the *A* layers (*i.e.* Ti_I-C in Fig. 14.1) are shorter than those in the stoichiometric binary *MX*, while the ones that are not, (*viz.* Ti_{II}–C, in Fig. 14.1) are longer. Figure 14.4(c) and the Ti–C lengths in Table 14.3 are fully consistent with this general conclusion. Not surprisingly, the Ti–C bond lengths in the 211 slab in the 523 phase are almost identical to those of the 211 phase [Fig. 14.4(c)]. Similarly, the Ti–C bond lengths in the 312 phase are very similar to those of the 312 slabs in the 523 phase [Fig. 14.4(c)]. This applies not only to the absolute Ti–C bond lengths values but also their thermal expansions, which are also quite comparable [Fig. 14.1(c)]. It should be noted that the longest bonds in the 312-stacked octahedra in $Ti_5Al_2C_3$ are slightly shorter than $r_{Ti_{II}-C}$ in Ti_3AlC_2, while the Ti–C bonds in the 211-stacked octahedra in $Ti_5Al_2C_3$ are slightly longer than those in Ti_2AlC [Fig. 14.4(c)]. This suggests that the structure is slightly more uniform than the individual 211- and 312-stacked phases due to the interleaved nature of the stacking sequences. These

Table 14.3: Interatomic distances in Ti_5AlC_2, Ti_2AlC, and Ti_3AlC_2 in the multiphase sample from Rietveld refinement of neutron diffraction data collected during heating and cooling, along with their expansions. All values are extrapolated to 25°C from linear interpolation.

Phase	Bond	Bond length (Å)	Bond expansion† (10^{-6} K^{-1})
$Ti_5Al_2C_3$	Al–Ti_I	2.878(2)	14.6(1)
	Al–Ti_{III}	2.848(4)	5.5(4)
	Ti_I–C_I	2.079(2)	8.8(1)
	Ti_{II}–C_I	2.1779(8)	8.1(1)
	Ti_{III}–C_{III}	2.106(1)	10.0(1)
Ti_2AlC	Al–Ti	2.873(1)	10.8(1)
	Ti–C	2.1008(7)	7.7(1)
Ti_3AlC_2	Al–Ti_I	2.854(2)	11.8(1)
	Ti_I–C	2.087(2)	6.8(1)
	Ti_{II}–C	2.182(1)	8.8(1)

† Bond expansion: $L^{-1} \cdot dL/dT$ from least-squares fit of $\Delta L/L_0$ vs. T.

comments notwithstanding, it is clear from Fig. 14.4(c) that the same structural units behave similarly. These results are gratifying because they indirectly validate our Rietveld analysis.

The situation for the Ti-Al bonds is not as clear. Since the difference between the 211 and 312 phases is the number of Ti–C octahedra between Al layers, it is expected that the only the Ti–C bonds would be significantly affected by the change in Ti–C stacking while the Al–Ti bonds should be similar among the three phases. However, we find that the Al–Ti bonds are clearly affected by stoichiometry [Fig. 14.4(d)]: r_{Ti-Al} is significantly longer in the 211 phase [black diamonds in Fig. 14.4(d)] than in the 312 phase [red crosses in Fig. 14.4(d)], while the opposite is true of those bonds in the 523 phase; *i.e.*, $r_{Al-Ti_I} > r_{Al-Ti_{III}}$ in $Ti_5Al_2C_3$ [compare blue circles and blue squares in 14.4(d)]. The reasons for this state of affairs are not fully understood, but are likely related to the following observations:

1. The Ti–C bonds are relatively stiff building blocks of the individual 312 and 211 units, as evidenced by the fact that they stay relatively the same size as in the original Ti_3AlC_2

and Ti_2AlC phases when the stacking sequences are interleaved. The dimension within the crystal that thus has the most flexibility to change is the Al–Ti bond, which connects the relatively rigid Ti–C octahedra. Therefore, it is likely that the Al–Ti bond plays a role as an effective "compensating spring" in the structure to minimize the crystal energy. Furthermore, this role would be different – and most probably more dominant – in the more complex $Ti_5Al_2C_3$ higher-order phase.

2. Among the possible factors that could be compensated for in the flexible Al–Ti bond discussed above are those related to constraints on the lattice parameters – especially on the *c*-lattice parameter, which essentially determines the Al–Ti bond length, given that the Ti–C octahedra are rigid blocks. In a sample with multiple competing phases, it is likely that these effects are prominent and manifest themselves in the Al–Ti bond.

3. The Al atoms in Ti_2AlC and Ti_3AlC_2 lie in a mirror plane within the structures, while Al is not constrained to mirror symmetry between the Ti–C atoms in the Ti_5AlC_2 phase (see FIg. 14.1). Therefore, the changes in Al–Ti distances in the 211-stacked and 312-stacked structures that occur when they are interleaved to form 523 may be a consequence of the symmetry break.

These comments notwithstanding, it is important to note that the average Ti–Al bond length in 523 (2.863 Å) is equal the average of the Ti–Al bond lengths in 312 and 211 (also 2.863 Å). The average bond expansion in 523 (10.5×10^{-6} K^{-1}) is also similar to the 211 and 312 average (11.3×10^{-6} K^{-1}). While more work is needed to fully understand the Al–Ti bond length behavior, it can be reasonably concluded that the dimensions of the Ti–C units are consistent for a given stacking, regardless of whether they are interleaved in a higher-order phase or in a conventional MAX phase. Based on this fact and the inconsistency of the Al–Ti bonds, it is

further speculated that the Al–Ti bonds serve to compensate other energy minimization factors for the crystal, especially those related to symmetry and lattice constraints.

14.2.3 Bond expansions

In Ti_2AlC and Ti_3AlC_2, the Al–Ti bonds show the highest expansion [see Table 14.1 and Figs. 14.3(b) and 14.3(c)]. To our knowledge, there are no previous reports of temperature-dependent bond lengths in any of the Ti–Al–C MAX phases to which to compare our results. However, in a previous HTND study of the nitride Ti_2AlN, the Al–Ti bond also showed a higher expansion rate than the Ti–N bond [2]. Similarly, a higher expansion rate was observed for the *A*–*M* bonds than the *M*–C bonds in Ti_3SiC_2 [3] and Cr_2GeC [2]. This result is also consistent with a high-pressure XRD study of Ti_3AlC_2, where the Al–Ti_I bond was the most compressible, while the Ti_I–C and Ti_{II}–C bonds were more rigid [150].

In Ti_5AlC_2, the expansion rate of the Al–Ti_I bond – 14.6×10^{-6} K^{-1}– is the highest of all the bonds in the sample, but the Al–Ti_{III} bond expansion is unexpectedly low, at 5.5×10^{-6} K^{-1} (Table 14.3). Note that the error bars for the Al–Ti bond expansions in $Ti_5Al_2C_3$ are the highest of those for the bonds in all phases (see Fig. 14.3). This uncertainty further suggests that the Al–Ti bond behavior is flexible within the structure and indicates other crystal imperfections and/or symmetry and lattice dimension effects, as discussed above.

14.2.4 Atomic displacement parameters

The results in Fig. 14.2 show that, like all other MAX phases studied to date, the *A* atom – Al in this case - is a rattler in that it vibrates with a significantly higher amplitude than the other atoms in the structures. The high atomic displacement parameters of Al, both calculated and experimental relative to the Ti, and C atomic displacement values [Figs. 14.2(a)-(c)] are also consistent with the relatively weaker Al bonding evidenced by the higher Al–Ti expansion rates,

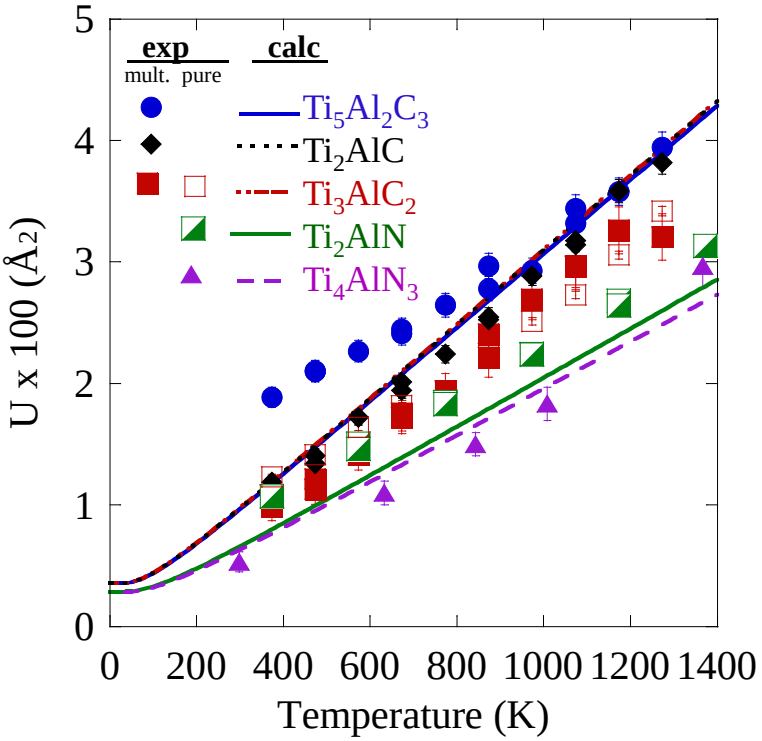

Figure 14.5: Temperature dependence of isotropic thermal motion U_{iso} of Al in $Ti_5Al_2C_3$ (blue circles), Ti_2AlC (black diamonds), and Ti_3AlC_2 (red solid squares) in the multiphase (mult.) sample, and in pure in Ti_3AlC_2 (red open squares) determined from HTND. U_{eq} of Al in predominantly single-phase Ti_2AlN (green half-filled squares) and Ti_4AlN_3 (purple triangles) are also shown, determined from HTND in Refs. [2] and [138], respectively. The lines refer to values calculated from first-principles phonon calculations, where the calculated values for Ti_2AlN and Ti_4AlN_3 are from Ref. [4]. Errors are typically smaller than symbols size.

at least in Ti_2AlC and Ti_3AlC_2 (Table 14.3) and the flexibility of the Al-Ti interaction, as discussed above.

Previous HTND studies of Ti_3SiC_2 [3, 53], Ti_3GeC_2 [3], Ti_2AlN [2], Cr_2GeC [2], and Ti_4AlN_3 [138] have shown the same rattling phenomenon for the A-group element. A comparison of the vibrational behavior of Al with two other HTND studies of the Al-containing nitrides Ti_2AlN and Ti_4AlN_3 (Fig. 14.5) further suggests that this "rattling" effect is independent of n.

The results shown in Figs. 14.2 and 14.5 also clearly indicate that from a theoretical point of view, the ADPs of the three MAX phases should be very comparable. Given that the Al atoms in Ti–Al–N nitrides are also predicted to behave similarly to one another – but different from the carbides – in their vibrational amplitudes (see lines for Ti_2AlN and Ti_4AlN_3 in Fig. 14.5), the DFT calculations indicate that the atomic displacement parameters of Al should not be greatly influenced by stoichiometry. Interestingly, the agreement between theoretical and experimental isotropic ADPs for the Al atoms is quite good in all five compounds plotted in 14.5. The agreement for the other atoms is less good for reasons that are not well understood, but are typical of the MAX phases [4].

14.3 SUMMARY

In this chapter, the temperature-dependent crystal structures of phases in a multiphase sample containing $Ti_5Al_2C_3$ [38(±1) wt.%], Ti_2AlC [32(±1) wt. %], Ti_3AlC_2 [18(±1) wt. %], and $(Ti_{0.5}Al_{0.5})Al$ [12(±1) wt.%] were presented based on Rietveld analysis of HTND data. It was shown that $Ti_5Al_2C_3$ exhibits similar thermal expansion and thermal motion parameters as Ti_2AlC and Ti_3AlC_2. In all MAX three phases, the average expansion rates of all the Al–Ti bonds are higher than the average Ti–C bond expansions. $Ti_5Al_2C_3$ consists of alternating layers of

312- and 211-like stacking, where the 312 layers are similar to Ti_3AlC_2 and the 211 layers are similar to Ti_2AlC in dimensions and bond expansions. The Al atoms in all three phases vibrate with higher amplitudes than the Ti and C atoms. This work shows that $Ti_5Al_2C_3$ exhibits similar properties to Ti_3AlC_2 and Ti_2AlC, two of the most promising MAX phases, which indicates that phase purity can be more relaxed in processing when considering applications.

Chapter 15: Correlated motion and anharmonic effects in Ti_3SiC_2 and Ti_3GeC_2

In Chapters 13 and 14, a survey of the temperature-dependent bond lengths in 211, 312, and 523 phases showed that, in general, the *M*-*A* bonds should have the highest expansions while the *M*–*X* bonds should expand at the lowest rate with temperature. Therefore, one of the most surprising results presented so far is the nonlinear increase of the Ti–C bond in Ti_3GeC_2 and the apparent lack of expansion for the Ti–Ge bond in that phase. In this chapter, this phenomenon will be addressed through a detailed study of Ti_3GeC_2 compared to Ti_3SiC_2. I will propose a correlated motion model to explain these unexpected results using the experimental HTND results for the Ti_3SiC_2 and Ti_3GeC_2 phases. It is proposed that the striking temperature-dependent bond length behavior in Ti_3GeC_2 is directly related to the behavior of the thermal vibrations. Further, an analysis of the mode-dependent Grüneisen parameter for the two phases show that the Ti-*A* interactions may have higher-order terms that have been theoretically neglected to date.

15.1 Bond lengths and angles in Ti_3SiC_2 and Ti_3GeC_2

I will begin with a discussion of the interatomic distances and lattice expansions in the two phases in light of what is already known about the crystal structure of the phases from previous studies. The thermal strains of the bonds and lattice parameters are re-plotted in Figs. 15.1(a) and (b) for Ti_3GeC_2 and Ti_3SiC_2, respectively, for convenient referencing. Note that Figs. 15.1(a) and (b) are the same as Figs. 13.4(c) and (d), respectively.

The strains along the *a* and *c* axes in Fig. 15.1 are also listed in Table 15.1, along with the unit cell volumes. Least-squares fits of the lattice parameters and unit cell volumes yield

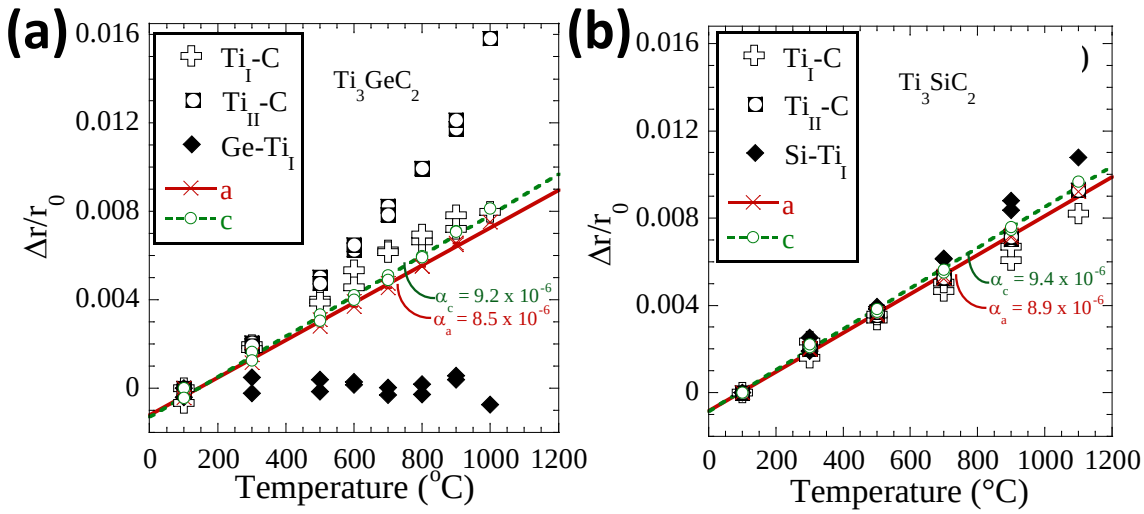

Figure 15.1: Temperature dependencies of the thermal strains of the lattice parameters and interatomic distances in (a) Ti_3GeC_2, and (b) Ti_3SiC_2. The room temperature values were extrapolated from slightly higher temperatures starting at 100°C for comparison sake. Error bars are typically smaller than symbols.

thermal-expansion coefficients of $8.9(\pm0.1)\times10^{-6}$, $9.4(\pm0.1)\times10^{-6}$, and $9.0(\pm0.1)\times10^{-6}K^{-1}$ for Ti_3SiC_2 in the *a* direction, *c* direction, and the volume expansion, respectively. For Ti_3GeC_2, the respective CTE values are $8.5(\pm0.1)\times10^{-6}$, $9.2(\pm0.1)\times10^{-6}$, and $8.7(\pm0.1)\times10^{-6}K^{1}$. The Ti_3GeC_2 expansions along the *a* and *c* directions measured in this work are in good agreement with those measured by high-temperature XRD, $8.1(\pm0.2)\times10^{-6}$ K^{-1} and $9.7(\pm0.2)\times10^{-6}$ K^{-1}, respectively [38].

The bulk CTE of composites – as measured with a dilatometer – follow, to a good approximation, the rule for mixtures whereas the phase specific CTEs measured by diffraction techniques adapt to the constraints imposed by the the pure phases. In this case, the higher CTE values observed for TiC compared to reported values for pure TiC are consistent with the constraint imposed by the more rapid shrinkage of the MAX phases from high temperatures. Similarly, the CTE values reported for the MAX phases are to be considered lower bounds, since their values for phase pure samples would be higher. (Ge also has a lower CTE than Ti_3GeC_2). The fact that

Table 15.1: Summary of lattice parameters and unit cell volumes obtained from Rietveld refinements of HTND data for Ti_3SiC_2 and Ti_3GeC_2, and room temperature values reported in Refs. [53, 56, 151]. Numbers in parentheses are estimated standard deviations in the last significant figure of the refined parameter.

	Ti_3SiC_2			Ti_3GeC_2		
T (°C)	a (Å)	c(Å)	Volume (Å^3)	a (Å)	c (Å)	Volume (Å^3)
RT (Ref. [56])	3.0665	17.671	143.906	3.0874	17.806	146.990
RT (Ref. [53])	3.06557(6)	17.6300(5)	143.485(9)	-	-	-
RT (Ref. [151])[a]	3.0705	17.670	144.273	3.0823	17.711	145.721
100	-	-	-	3.08793(5)	17.8193(5)	147.149(4)
300	3.07468(3)	17.7190(3)	145.067(2)	3.09259(5)	17.8484(5)	147.833(4)
500	3.07947(3)	17.7477(3)	145.756(2)	3.09752(6)	17.8786(5)	148.557(5)
600	-	-	-	3.10003(6)	17.8943(6)	148.928(6)
700	3.08465(3)	17.7798(3)	146.510(2)	3.10259(7)	17.9103(7)	149.308(6)
800	-	-	-	3.10497(7)	17.9258(7)	149.666(6)
900	3.09045(3)	17.8144(3)	147.348(3)	3.10822(8)	17.9456(7)	150.145(7)
1000	-	-	-	3.11111(9)	17.9644(8)	150.582(8)
1100	3.09687(3)	17.8532(3)	148.284(3)	-	-	-
900[†]	3.09078(3)	17.8166(3)	147.398(3)	3.10800(8)	17.9453(8)	150.121(7)
800[†]	-	-	-	3.10491(7)	17.9246(7)	149.650(6)
700[†]	3.08507(3)	17.7822(3)	146.570(3)	3.10196(7)	17.9065(6)	149.215(6)
600[†]	-	-	-	3.09928(6)	17.8902(6)	148.822(5)
500[†]	3.07972(3)	17.7500(3)	145.797(2)	3.09654(6)	17.8735(6)	148.420(5)
300[†]	3.07484(3)	17.7212(3)	145.101(2)	3.09149(5)	17.8416(5)	147.672(5)
100[†]	-	-	-	3.08655(5)	17.8115(5)	146.953(4)

[a] Based on first-principles calculations.
[†] Measurement taken during cooling.

the CTEs of TiC_x are identical, within error bars, in both compounds [$8.5(\pm0.1) \times 10^{-6}$K^{-1}], despite the fact that the TiC_x content in the Ti_3GeC_2 sample was ≈4 times that in Ti_3SiC_2 (see Appendix A.1), is taken as strong evidence that any stresses caused by differences in CTE do not play a significant role. This comment notwithstanding, it is hereby acknowledged that why the CTE of the TiC phase is as high as it is, especially if it is stoichiometric, is not clear. It should also be noted that the Ge and TiC_x phase fractions remain constant during heating (with the exception of the melting of Ge between 900 and 1000°C, implying that no reactions take place as a result of heating.

The only atom positions that are unconstrained by the P_{63}/mmc (No. 194) space group are the z coordinates of the Ti_I and C atoms, which are listed in Table 15.2 for Ti_3SiC_2 and

Table 15.2: z coordinates of Ti_I and C atoms in Ti_3SiC_2 and Ti_3GeC_2 obtained from Rietveld refinements of HTND data. Numbers in parentheses are estimated standard deviations in the last significant figure of the refined parameter.

	Ti_3SiC_2		Ti_3GeC_2	
T (°C)	z_{TiI}	z_C	z_{TiI}	z_C
100	-	-	0.13245(9)	0.57148(4)
300	0.13529(5)	0.57218(3)	0.1327(1)	0.57161(5)
500	0.13532(5)	0.57218(3)	0.1330(1)	0.57187(6)
600	-	-	0.1332(1)	0.57196(7)
700	0.13523(5)	0.57218(3)	0.1334(1)	0.57219(8)
800	-	-	0.1335(1)	0.57238(8)
900	0.13509(6)	0.57214(3)	0.1337(1)	0.5725(1)
1000	-	-	0.1342(1)	0.5732(1)
1100	0.13512(7)	0.57217(4)	-	-

Ti_3GeC_2. The interatomic distances at each temperature during heating and cooling, as well as room temperature values determined in previous work [51, 53, 56, 151], are listed for Ti_3SiC_2 and Ti_3GeC_2 in Tables 15.3 and 15.4, respectively. The bond lengths of Ti_3SiC_2 and Ti_3GeC_2 compounds are generally consistent with those estimated at room temperature from XRD results by Gamarnik and Barsoum [56]. Based on these results, the order of the Ti-C bonds lengths, in decreasing order, is Ti_{II}-C(Ti_3GeC_2) ≈ Ti_{II}-C(Ti_3SiC_2) > Ti_I-C(Ti_3SiC_2) >Ti_I-C(Ti_3GeC_2) (see Tables 15.3 and 15.4). As noted in Chapter 13, the Ti_{II}–C bonds are longer than the Ti–C distance in TiC while the Ti_I bonds are shorter than the distance. However, the Ti_{II}–C distance in Ti_3GeC_2 is not only longer than that in all the other 312 phases, but shows the only clearly nonlinear increase with temperature of all bonds [Fig. 15.1(a)]. This nonlinear increase is indicated by an increase in the C-atom z coordinate, z_C (Table 15.2). The z coordinate for C in Ti_3SiC_2, on the other hand, stays constant with temperature, as expected for a structure whose bond lengths expand at the same rate as the lattice parameters. As we saw from Chatper 13, all other Ti-C bonds in Ti_3AlC_2, Ti_3SiC_2, and Ti_3SnC_2 increase at a rate similar to that in TiC [see Figs. 13.3(a), (b), and (d)].

The temperature dependencies of the bond angles in Ti_3SiC_2 and Ti_3GeC_2 are shown in Fig. 15.2. The Ti_I-Si/Ge-Ti_I bond angles [Fig 15.2(a)] represent the displacement of the Ti_I layers either in the direction of, or away from, the Si/Ge layers. The Ti_I-C-Ti_{II} angles [Fig. 15.2(b)] represent the distortion of the Ti-C layers. The C-Ti_{II}-C angles [Fig. 15.2(c)] represent the compression, or expansion, around the Ti_{II} atoms shared by CTi_6 octahedra above and below the Ti mirror plane. From these results it is obvious that for Ti_3GeC_2, the Ti_I-Ge-Ti_I bond angles decrease with increasing temperature; the corresponding Ti_I-Si-Ti_I angles for Ti_3SiC_2 increase slightly. Conversely, the Ti_I-C-Ti_{II} and C-Ti_{II}-C bond angles for Ti_3GeC_2 increase slightly with increasing temperatures; those for Ti_3SiC_2 are more or less independent of temperature as in cubic TiC.

The most surprising result here is the apparent lack of expansion of the Ti_I-Ge bonds compared to the more normal response of the Ti_I-Si bonds discussed above [Figs. 15.1(a) and (b)]. We move onto a possible explanation of the bond length behavior in relation to the vibrational behavior of the *M* and *A* atoms in the 312 phases.

15.2 CORRELATED MOTION MODEL FOR Ti_3SiC_2 AND Ti_3GeC_2

To begin the analysis, illustrations of the experimentally-determined 99% probability ellipsoids at three different temperatures are shown for Ti_3SiC_2 and Ti_3GeC_2 in Figs 15.3 and 15.4.

The most likely explanation for the discrepancies can be related to the pronounced anisotropic motion of the Ge atoms [see Fig. 12.8(c)], together with the resulting correlated motions of the Ti_I and Ge atoms. More specifically, the orbiting motion of the *A* atoms around their average position in the $a-b$ plane was proposed by Togo *et al.* [132], who showed, using first-principles phonon calculations, that essentially the Ti_I and Ge atoms avoid each other as much as possible. Our argument (and evidence) is as follows:

Table 15.3: Selected interatomic distances in Ti_3SiC_2 (Å) deduced from Rietveld refinements of HTND data, and room temperature values reported in Refs. [48, 51, 53, 56, 151]. Interatomic distances in secondary phase TiC in the same sample is also included for comparison. Numbers in parentheses are estimated standard deviations in the last significant figure of the refined parameter.

	Ti_3SiC_2				TiC
T (°C)	Si-Ti_I	Ti_I-Ti_I^*	Ti_I-C	Ti_{II}-C	
RT (Ref. [48])	2.696	3.068	2.135*		-
RT (Ref. [51])	2.681	3.0575	2.088	2.176	-
RT (Ref. [53]	2.693(2)	3.06557(6)	2.085(2)	2.1814(8)	-
RT (Ref. [56])	2.6263	3.0665	2.1609*		-
RT (Ref. [151])[a]	2.6697	3.0705	2.0931	2.2033	-
300	2.6987(7)	3.07468(3)	2.0978(6)	2.1880(3)	2.16623(7)
500	2.7025(7)	3.07947(3)	2.1015(6)	2.1914(3)	2.16943(7)
700	2.7084(7)	3.08465(3)	2.1043(6)	2.1952(3)	2.17293(7)
900	2.7156(8)	3.09045(3)	2.1073(7)	2.19893(34)	2.17679(7)
1100	2.7209(10)	3.09687(3)	2.1118(8)	2.2039(4)	2.18105(8)
900 [†]	2.7144(8)	3.09078(3)	2.1086(7)	2.1992(4)	2.17693(8)
700[†]	2.7085(7)	3.08507(3)	2.1052(6)	2.1951(3)	2.17300(7)
500[†]	2.7023(7)	3.07972(3)	2.1020(6)	2.19170(29)	2.16937(7)
300[†]	2.6971(6)	3.07484(3)	2.0994(5)	2.18804(26)	2.16611(7)

[a] Based on first-principles calculations.

[*] Due to symmetry, $r_{Si-Si} = r_{TiI-TiI} = r_{TiII-TiII} = a$.

[⋆] $r_{TiI-C-TiII}/2$.

[†] Measurement taken during cooling.

Table 15.4: Selected interatomic distances in Ti_3GeC_2(Å) deduced from Rietveld refinements of HTND data, and room temperature values reported in Refs. [56, 151]. Interatomic distances in secondary phase TiC in the same sample is also included for comparison. Numbers in parentheses are estimated standard deviations in the last significant figure of the refined parameter.

	Ti_3GeC_2				TiC
T (°C)	Ge-Ti_I	Ti_I-Ti_I^*	Ti_I-C	Ti_{II}-C	
RT (Ref. [56])	2.6754	3.0874	2.1646*		-
RT (Ref. [151])[a]	2.6898	3.0823	2.0943	2.2078	-
100	2.7521(14)	3.08793(5)	2.0871(11)	2.1907(5)	2.15939(3)
300	2.7516(15)	3.09259(5)	2.0924(12)	2.1954(5)	2.16267(3)
500	2.7512(17)	3.09752(6)	2.0968(14)	2.2016(6)	2.16612(4)
600	2.7506(19)	3.10003(6)	2.0999(16)	2.2043(7)	2.16788(4)
700	2.7493(21)	3.10259(7)	2.1020(18)	2.2086(8)	2.16968(5)
800	2.7503(22)	3.10497(7)	2.1030(19)	2.2121(9)	2.17136(5)
900	2.7507(25)	3.10822(8)	2.1057(21)	2.2159(10)	2.17359(5)
1000	2.7470(29)	3.11111(9)	2.1062(25)	2.2248(12)	2.17566(6)
900†	2.7507(26)	3.10800(8)	2.1044(22)	2.2170(11)	2.17347(6)
800†	2.7485(22)	3.10491(7)	2.1037(19)	2.2124(9)	2.17126(5)
700†	2.7490(20)	3.10196(7)	2.1018(17)	2.2077(8)	2.16914(5)
600†	2.7502(19)	3.09928(6)	2.0984(16)	2.2047(7)	2.16729(4)
500†	2.7495(18)	3.09654(6)	2.0968(14)	2.2009(7)	2.16537(4)
300†	2.7492(16)	3.09149(5)	2.0922(13)	2.1951(6)	2.16178(4)
100†	2.7489(14)	3.08655(5)	2.0870(11)	2.1903(5)	2.15837(3)

[a] Based on first-principles calculations.

* Due to symmetry, $r_{Ge-Ge} = r_{TiI-TiI} = r_{TiII-TiII} = a$.

* $r_{TiI-C-TiII/2}$.

† Measurement taken during cooling.

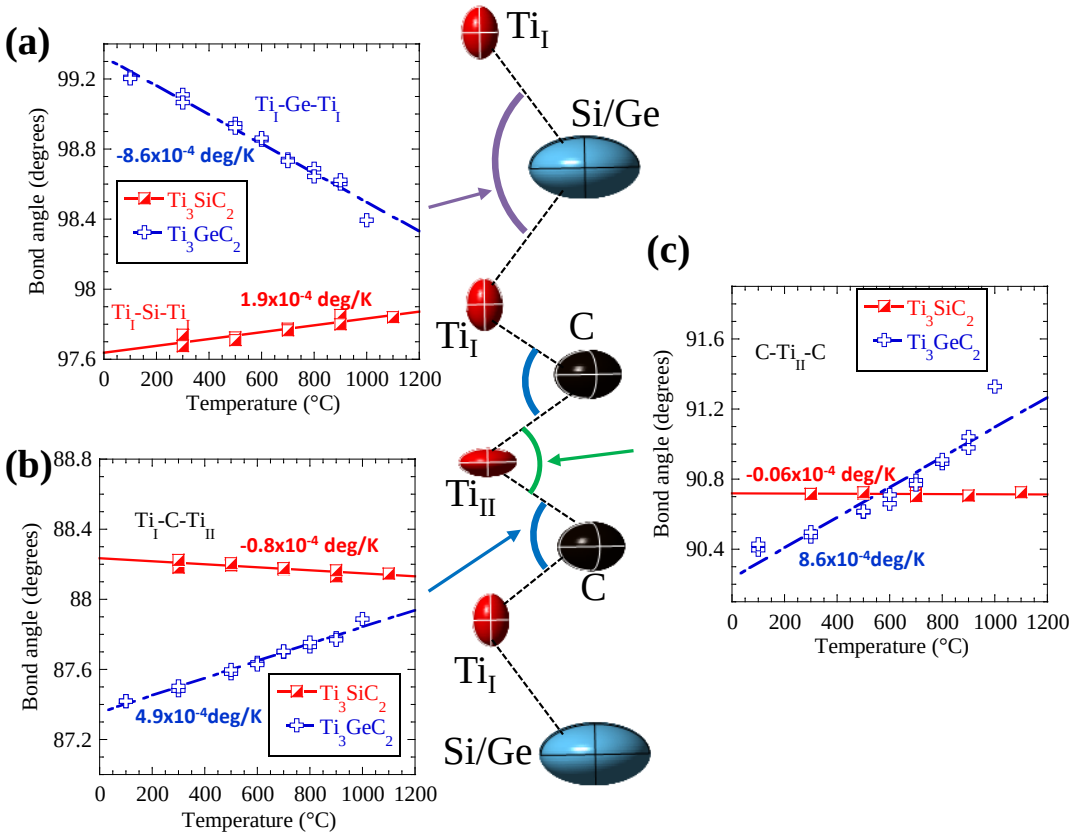

Figure 15.2: Bond angles in Ti_3SiC_2 (red squares) and Ti_3GeC_2 (blue crosses) between atoms in Ti layers with (a) the A-group (Si or Ge) layers and (b)-(c) the C layers. Inset (middle) shows a schematic of the bond angles with nomenclature adopted in the figures. The angle expansion or compression rates are listed in red and blue next to the plots in units of angle (degrees) per unit of temperature (K). Error bars are smaller than symbols.

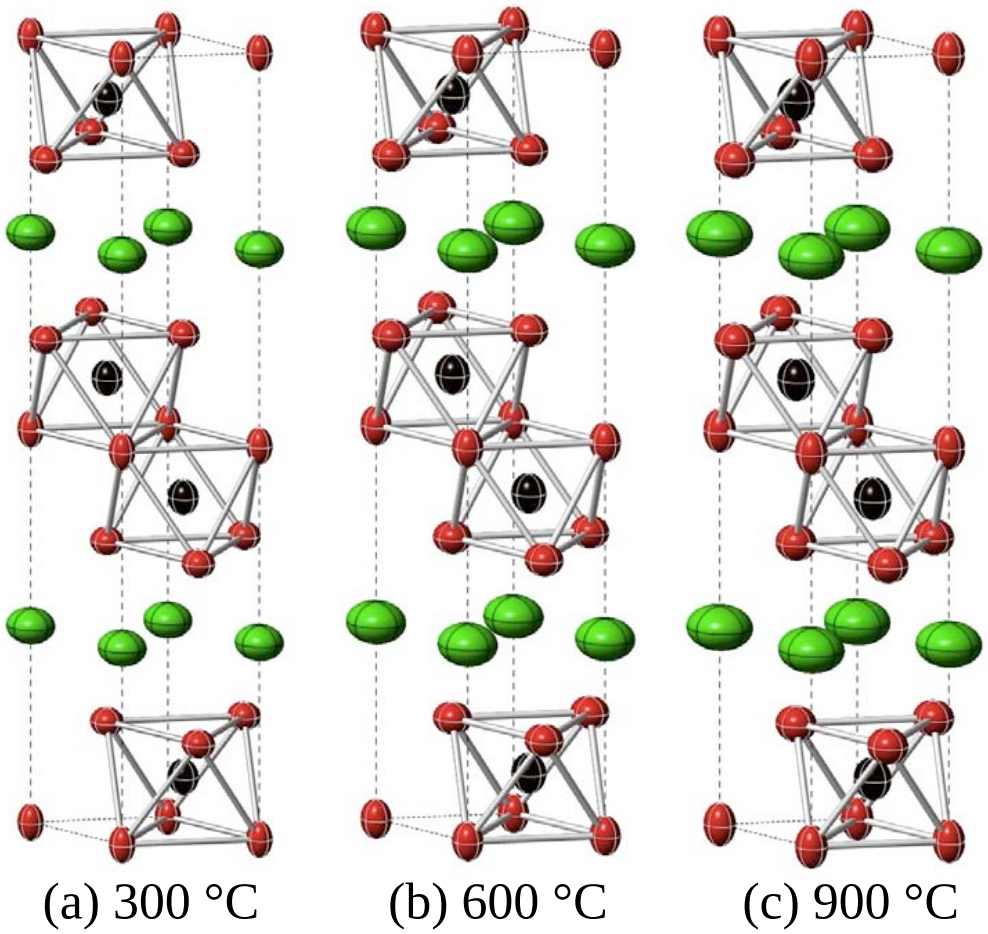

Figure 15.3: Thermal motion ellipsoids (99% probability) of Ti (red), Si (green), and C (black) in Ti_3SiC_2 at (a) 300°C, (b) 600°C, and (c) 900°C.

(i) The repulsion of the Ti_I atom is reduced temporarily when the Ge atom is displaced in the basal plane away from that Ti_I atom [see r_2 in Fig. 15.5(a)], and the Ti_I atoms can move closer to the Ge plane.

(ii) This in turn is evidenced by the fact that the Ti_I atoms vibrate more normal to the basal planes than parallel to them.

(iii) If the Ti_I and Ge atomic motions are correlated, then the instantaneous bond lengths may be approximated by the distances r_1 and r_2 [Fig. 15.5(a)] between the edges of the

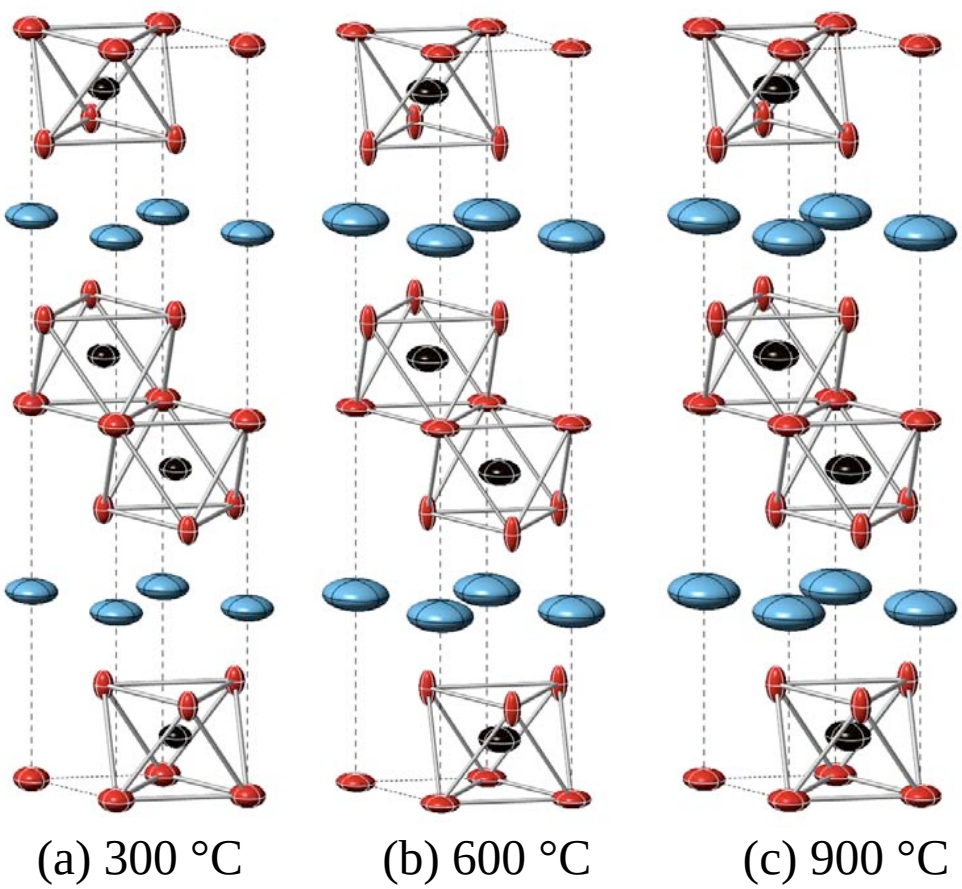

Figure 15.4: Thermal ellipsoids (99% probability) of Ti (red), Ge (blue), and C (black) in Ti_3GeC_2 at (a) 300°C, (b) 600°C, and (c) 900°C.

50% probability thermal ellipsoids. [Note that 99% probability ellipsoids are used in Fig. 15.5(a) to emphasize the effect].

In Fig. 15.5(b), r_1 and r_2 are plotted as triangles and circles, respectively. The average of these two numbers is given by the red squares [Fig. 15.5(b)]. Also shown on the same figure are the values directly obtained from Rietveld analysis, *i.e.*, distance r_3 in Fig. 15.5(a), and denoted as blue crosses in Fig. 15.5(b). In light of these calculations, the result that r_3 does not increase with temperature is but a consequence of the anisotropic and correlated motions of the Ge atoms in the basal planes. A similar effect was reported by Tucker *et al.* in quartz, explained

by the difference between the instantaneous and average positions of Si and O atoms [152].

The Si thermal ellipsoids, on the other hand, show thermal motion that is less anisotropic (Fig. 15.3) compared to Ge (Fig. 15.4). Since the Si thermal ellipsoids are not as flat as those of Ge, the Ti_I atom does not vibrate preferentially normal to the plane into the space provided, as it does in Ti_3GeC_2. Consequently, in Ti_3SiC_2, the Ti_I atoms vibrate with slight preference in the basal planes, whereas the Ti_I atoms in Ti_3GeC_2 vibrate anisotropically normal to the basal planes. A possible reason for the difference in the thermal behavior of the Si and Ge atoms is their atomic masses relative to the Ti atoms. Since Si is lighter than Ti, it is not unreasonable to conclude that their correlated motion is not as strong and thus less anisotropic. Conversely, because the Ge atom is heavier than Ti, the correlated motion effect is stronger. Consistent with these notions is the fact that the Al in Ti_4AlN_3 [138] behaves more like Si in Ti_3SiC_2.

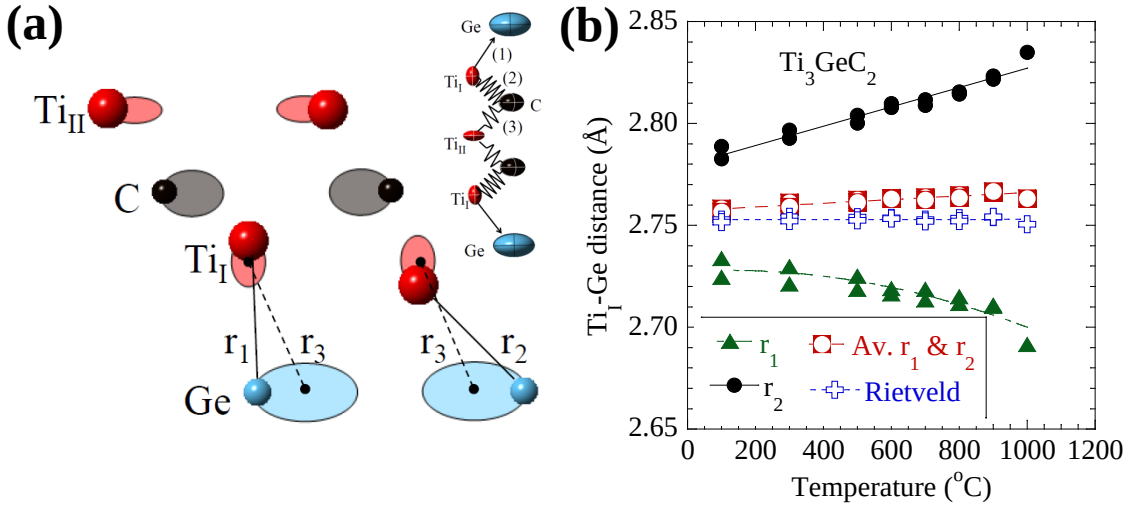

Figure 15.5: Schematic of and interatomic distances in Ti_3GeC_2: (a) 99% probability thermal ellipsoids at 1000°C showing Ti_I-Ge instantaneous positions (solid lines, r_1 and r_2) and interatomic distance between time-averaged positions (dashed lines, r_3). Inset shows sketch of the interatomic distance behavior with (1) the movement of Ti_I toward empty space provided by Ge thermal motion, (2) the more rigid bond between Ti_I and C, and (3) the weaker bond between Ti_{II} and C. (b) Temperature dependence of the Ti_I-Ge bond showing the minimum (r_1, green triangles) and maximum (r_2, black circles) interatomic distances for the 50% probability thermal ellipsoids, the average of the two (red squares), and the distances determined by the time- and space-averaged positions obtained by Rietveld analysis (blue crosses).

Based on the shape of the Ti_I thermal ellipsoids in Ti_3SiC_2, it is reasonable to assume that the correlated motion of the Ti_I – if it exists – is in the basal plane rather than normal to it. The instantaneous positions can therefore be approximated by distances r_4 and r_5 [Fig. 15.6(a)]. Here the distance determined by Rietveld analysis is given by r_6 [15.6(a)]. In this case, the average of the two "instantaneous" positions, plotted as red squares in Fig. 15.6(b), are almost identical to the values obtained from the Rietveld refinement shown as blue crosses in Fig. 15.6(b). The end result is, again, quite reasonable, but because the Si motion is less anisotropic, the increase in the Ti_I-Si bond behaves more "normally" – it expands with temperature. It is important to note that when the results shown in Figs. 15.5(b) and 15.6(b) are superimposed, at $1.71\times10^{-5}K^{-1}$, the thermal expansion of r_2 is only ≈20% smaller than that of r_5 at $2.17\times10^{-5}K^{-1}$. Said otherwise, the expansions are not as different as the ratio of the expansions, derived simply from Rietveld analysis, viz. $r_3/r_6 \simeq 0.002$, would suggest. For comparison's sake the thermal expansion of the Ti_{II}-C bond [Fig. 13.3(c)] is $\approx 1.6\times10^{-5}$ K^{-1}. Thus, in the final analysis, the expansion of the Ti_I-Si and Ti_I-Ge bonds are comparable to those of the Ti_{II}-C bonds.

The anisotropic vibrations of the Ge atoms are also manifested in the bond angles. In the case of Ti_3SiC_2, the lattice expands more or less uniformly and the angles (Fig. 15.2) are weak functions of temperature. In contrast, in Ti_3GeC_2 the expansion is accompanied by a decrease in the Ti_I-Ge-Ti_I angle with a concomitant and almost equal increase in the C-Ti_{II}-C angle. This observation is most easily explained as follows: since the Ti_I-C bond is significantly shorter than the Ti_{II}-C bond and therefore presumably stronger [Fig. 13.3(c)], the C atom follows the temporary displacement of the Ti_I atom toward the *A* plane as the Ge atoms move away as discussed above. But since the Ti_{II} atoms are located on a mirror plane, they cannot accommodate the Ti_I displacement toward the *A* plane and the Ti_{II}-C bond thus expands at

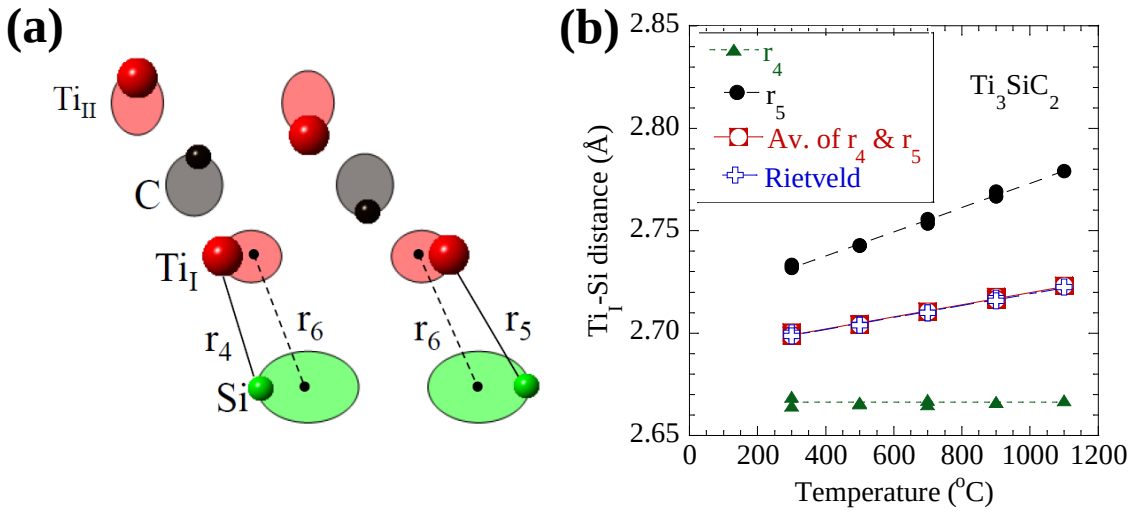

Figure 15.6: Schematic of and interatomic distances in Ti_3SiC_2: (a) 99% probability thermal ellipsoids 1100°C showing Ti_I-Si instantaneous positions (solid lines, r_4 and r_5) and interatomic distance between time-averaged positions (dashed lines, r_6). (b) Temperature dependence of the Ti_I-Si bond showing the minimum(r_4, green triangles) and maximum (r_5, black circles) interatomic distances for the 50% probability thermal ellipsoids, the average of the two (red squares), and the distances determined by the time- and space-averaged positions obtained by Rietveld analysis (blue crosses).

a higher rate than the Ti_I-C bond [see sketch in inset of Fig. 15.5(a)]. Said otherwise, the C-Ti_{II}-C and Ti_I-Ge-Ti_I bond assemblies, being the weakest, act as hinges that move in opposite directions.

In both compounds, the Ti_I-C bonds are almost identical [Figs. 13.3(b) and (c)]. And while shorter than the Ti-C bonds in TiC, their rates of expansion are very similar to the latter [Fig. 13.3 (b) and (c)]. In contradistinction, the response of the Ti_{II}-C bonds in Ti_3GeC_2 is not "normal" [Fig. 13.3(c)] for the reasons outlined above.

Lastly, I address how this unique understanding could shed light on why the internal friction in Ti_3GeC_2 increases dramatically at ≈427°C [52]. Examining the anisotropic thermal motion parameters experimentally determined through HTND, indicate that a discontinuity of sorts occurs between 300 and 500°C in Ti_3GeC_2. This is best seen in Figs. 13.3(c) and 15.1(a) where it is clear that a large increase in the Ti_{II}-C bond lengths occurs between 300 and 500°C. Another

hint, which may be more relevant, can be found by plotting the *anisotropy* of the thermal motion of all the atoms, or U_{11}/U_{33}, as a function of temperature, which is shown in Figs. 15.7(a) and (b) for Ti_3SiC_2 and Ti_3GeC_2, respectively. In Ti_3GeC_2 [Fig. 15.7(b)], below 400°C, the error bars and the scatter in the anisotropies of vibration of the Ti_{II} atoms are quite low; above that temperature, however, the noise level increases dramatically, not only at a given temperature, but between heating and cooling. Such noise is unique to the Ti_{II} atoms in Ti_3GeC_2. At this time, there is no good explanation for the discontinuity observed between 300 and 500°C in the U_{11}/U_{33} ratio for the Ti_{II} atoms [Fig. 15.7(b)] or the increase in noise level. I speculate that the dramatic increase in uncertainty is an indication that the thermal motion of Ti_{II} cannot be described by an ellipsoid at temperatures above 300-500°C. Further experimental work with high-resolution high-temperature neutron powder-diffraction data that would need to be analyzed by pair-distribution function and entropy mechanisms, of both Ti_3SiC_2 and Ti_3GeC_2, would need to be collected to experimentally verify this hypothesis.

15.3 ANHARMONICITY IN Ti_3SiC_2 AND Ti_3GeC_2 EXAMINED THROUGH THE GRÜNEISEN PARAMETER

In the previous section, a correlated motion model was proposed for both Ti_3SiC_2 and Ti_3GeC_2, and it was also postulated that the nature of the thermal vibrations is fundamentally different between Ti_3SiC_2 and Ti_3GeC_2. Furthermore, in the comparisons between experimental and theoretical mean-squared ADPs (Chapter 12), there was a disagreement between theory and experiment for U_{33} of Si in Ti_3SiC_2 [see Fig. 12.7(c)] and U_{11} in Ge in Ti_3GeC_2 [see Fig. 12.8(c)]. These aforementioned discrepancies may also originate from anharmonicity, which is not taken into account in the DFT calculations of the mean-squared displacements, U_{ij}. To explore this, I calculated the frequency dispersion of the Grüneisen parameter (see Eq. 4.57 in Chapter 4), which is shown in Figs. 15.8(a) and (b) for Ti_3SiC_2 and Ti_3GeC_2, respectively, along with their

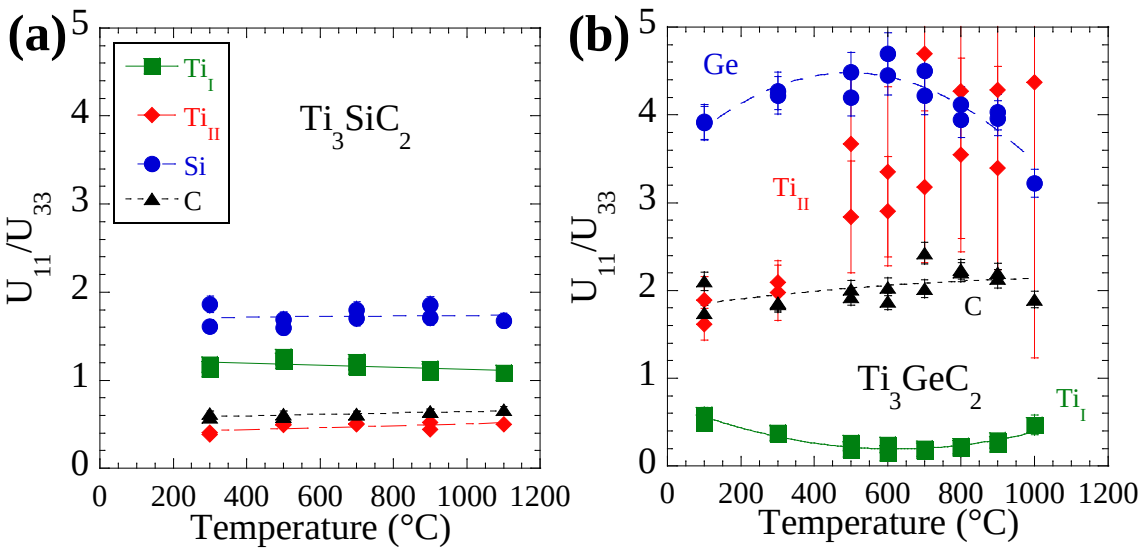

Figure 15.7: The U_{11}/U_{33} ratios for the various atoms in (a) Ti_3SiC_2 and, (b) Ti_3GeC_2 during heating and cooling.

phonon band structures. The bands and corresponding Grüneisen parameter curves are color coded to distinguish between the bands for the Grüneisen parameter dispersions. The red points in Fig. 15.8 represent the localized modes of Si and Ge, which correspond to the red PDOS curves below 5 THz [see Figs. 9.7(c) and (d)]. The localized phonon modes of C above 15 THz [see PDOS for C in Figs. 9.7(c) and 8(d)] are shown as black points in Fig. 15.8. For most of the modes in the spectrum, the Grüneisen parameter has a common value, below two. This gives an average value over the Brillouin zone (1.45 in both cases) that would lead to the conclusion that Ti_3SiC_2 and Ti_3GeC_2 are harmonic compounds to a good approximation. However for the low-frequency modes involving the A and M atoms in red (solid line) and green (dashed-dotted line) in Figs. 9.7(c) and (d), the Grüneisen parameters are larger. This in turn suggests that the interatomic potential, $\mathcal{U}(r)$, between tje A atoms and their M atom (or possibly other A atom) neighbors is anharmonic because the Grüneisen parameter is proportional to the ratio of the

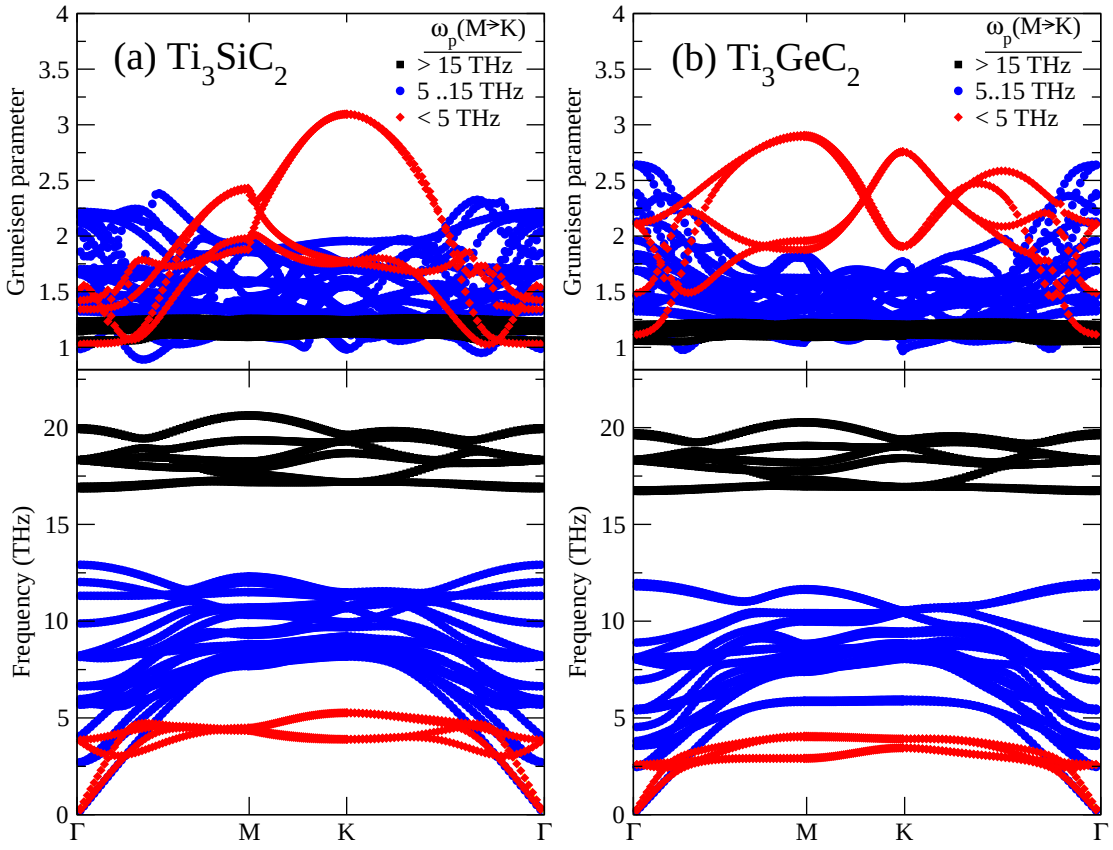

Figure 15.8: The band structure (bottom) and the mode-dependent Grüneisen parameters (top) for (a) Ti_3SiC_2 and (b) Ti_3GeC_2. The colors in the plots of the Grüneisen parameters are color coded according to $\omega_p(M \rightarrow K)$, which refers the frequency of the band between the M and K point. Red diamonds correspond to the localized phonon modes of Si and Ge below 5 THz; blue circles correspond to the frequencies between 5 and 15 THz, and black squares represent the localized phonon modes of C above 15 THz.

third- to second- derivative of u:

$$\gamma \propto \frac{u'''(r)}{u''(r)} \tag{15.1}$$

This anharmonicity could contribute to the differences observed – in fact, even if anharmonicity is usually evidenced experimentally by a quadratic dependence in the averaged squared displacement, it also modifies the coefficient of the linear term through renormalization of

the frequencies. Therefore, it has been shown that anharmonicity may play a role, and must therefore be considered, in the study of atomic motion. More work is needed, however, to understand to what extent anharmonic effects play into the ADP calculations through first principles calculations, and whether the incorporation of higher-order terms could lead to better agreement between theory and experiment. Progress can also be made on the experimental side because there are likely phenomena that cannot be described by the average structure derived from Rietveld analysis of the real-space diffraction patterns but might be accessible by maximum-entropy methods, as described by Izumi [153].

15.4 SUMMARY

In this chapter, the nonlinear expansion of the Ti_{II}–C bond in Ti_3GeC_2, along with the lack of expansion of the Ti–Ge bond, is investigated. It is shown that the temperature dependence of the bond angles coincide with the opening of the C–Ti_{II}–C during heating, which is different from the same angle in Ti_3SiC_2 that stays more constant with temperature. The unexpected behavior in the expansions of bond lengths in Ti_3GeC_2 is explained by a proposed model for correlated atomic motion that was first suggested from a theoretical phonon study [132]. It is shown that motion of the Ti and *A* (Ge or Si) atoms may be correlated in order to avoid each other as they vibrate. This type of motion would lead to a discrepancy between the instantaneous bond lengths and the distance between average atomic positions, which could explain the lack of expansion of the Ti-Ge bond that was determined from Rietveld analysis of HTND data. On the other hand, the type of correlated motion that was indicated by the thermal motion ellipsoids in Ti_3SiC_2 would lead to time- and space- average interatomic distances that happen to equal the instantaneous interatomic distances. This would explain how Rietveld analysis of HTND data could lead to physically sound bond expansions, even if atomic motion correlation was

present. Lastly, the high mode-dependent Grüneisen parameters for the low-frequency bands could indicate anharmonicity in the atomic interactions for the atoms involved in those modes – namely, Ti and Si/Ge.

Chapter 16: Summary and outlook

This thesis set out to explore the dynamical behavior in MAX phases by bringing together first-principles phonon calculations and experimental techniques, including Raman spectroscopy and neutron diffraction. DFT calculations of the phonon band structures and phonon partial density of states have been presented for ten select MAX phases, and the frequencies of Raman-activated modes were compared to Γ-point band frequencies. The relationship between the vibrational frequencies and the atoms involved was explored. High-temperature neutron diffraction was employed to investigate the temperature-dependent crystal structure of select phases, including the bond expansions and mean-squared atomic displacements. Most importantly, the first-ever DFT calculations of ADPs of MAX phases were performed and agree qualitatively with the Debye-Waller factors from diffraction techniques. As a result of these combined investigations, several new ideas have emerged from this work regarding the vibrational behavior of MAX phases:

1. The *A* elements (*e.g.* Al, Si, Ge, Sn) vibrate with the highest amplitude, and do so anisotropically within the basal planes. While *A* element "rattling" had been observed from two previous HTND experiments on Ti_3SiC_2 and Ti_4AlN_3, it had never been modeled through first-principles calculations. Through this work I have shown that this effect is universal for all MAX phases studied through HTND (8 phases) and first-principles phonon calculations (15 phases), and is related to the relatively weak bonding of the *A* element within the structure.

2. The "rattling" effect of the *A* elements has little dependence on the stacking sequence; the

isotropic atomic displacement parameters are similar among different stackings of the MX layers for the same chemistry.

3. Trends of calculated ADPs with M and A chemistry have shown that the following factors should lead to higher, more anisotropic atomic displacements for the A element:

   (i) lighter A atoms,

   (ii) fewer valence electrons for the A atom, and/or

   (iii) fewer valence electrons for the M atom.

   On the other hand, the mass of the M atom was predicted to have little effect on the vibrational character of the atoms. These concepts were further supported by the dependence of the vibrational frequency of Raman-active modes on the reduced mass of the atoms involved: the low-frequency Raman modes corresponding to M and A vibrations indicated that mass was responsible for at least some of the frequency differences, while the high-frequency modes governed by M and X atom interactions showed that the role of mass was minimal in relation to the role of chemistry in the bonding.

4. The phases that showed the best agreement between theory and experiment for the ADPs were all Al-containing, and the worst agreement was for the Ge-containing phases. The fact that the Al-containing phases are relatively good phonon conductors indicates that the relatively low phonon conductivity of most of the MAX phases is not solely because of the "rattlers" and may be related to effects that are not well-predicted by the harmonic model.

5. A model for correlated atomic motion has been provided based on the results for two of the MAX phases, Ti_3SiC_2 and Ti_3GeC_2, and high Grunëisen parameters of the low-frequency modes suggest that the phonons involving the Si and Ge atoms are localized.

The aim of this thesis was to gain a deeper understanding of the dynamical behavior of the atoms in MAX phases and understand the role they play in experimental measurements and computational materials modeling. In a general sense, these results have put the vibrational behavior of MAX phases into perspective in relation to their other properties and their trends with MAX phase chemistry. Further, they serve as a guide for future modeling of high-temperature properties by indicating which MAX phase systems are well represented by the harmonic model and which ones are driven by other higher-order bonding intricacies and/or correlation effects in atomic motion.

Now, I will walk through the main topics that have been covered and summarize the investigations that were carried out in order to accomplish the aims of this thesis. The first few chapters of Part I provided an introduction and relevant background on the materials systems studied (*i.e.* the MAX phases) and the techniques used; the final chapter of Part I summarized the details on the experimental and computational procedures for the studies in this thesis.

Part II presented and discussed the main results. First, the phonon band structures and phonon partial density of states determined from first-principles calculations were presented for a number of 211, 312, and 413 MAX phases in Chapter 9. The features of the band structures and their origins in the phonon calculations – *e.g.*, atom mass, interatomic forces – were discussed, taking into account which atoms are involved in each of the frequency ranges to explain the differences among the phases studied.

After discussing pure theory, Raman spectroscopy results were presented in Chapter 10 to investigate some of the Γ-point vibrational modes. Experimental Raman spectra for Sn-containing phases (which have a heavy *A* element) and Ta-containing phases (with a heavy *M* element) were presented and compared to related structures with lighter elements. The role of atomic mass in lattice dynamical behavior was discussed based on the frequencies of the

the Raman-active modes plotted against the reduced mass of the atom pairs involved in the vibrations. The reduced mass plots with more-or-less linear slopes indicate that mass effects must account for at least some of the differences in the vibrations and the slope of the line should be directly related to the bond stiffness.

In the next chapter (Chapter 11), the mean-squared atomic displacement calculations were introduced and discussed from a purely theoretical standpoint. The temperature-dependent ADPs were presented – first only the isotropic motion, then the anisotropic motion decomposed into Cartesian components – for four different 312 phases and fifteen different 211 phases. At this point, it was shown that in all MAX phase structures, the *A* atom vibrations should have the highest amplitudes compared to the other atoms in the material. Further, the first-principles calculations predicted highly anisotropic *A*-atom motion, where the *A* atoms vibrate more within the basal planes than perpendicular to them. Later in the chapter, the ADPs at 1273 K were considered with respect to where the atoms are situated on the periodic table. It was shown that the *A* atoms with higher masses – *i.e.*, lower in the periodic table – should vibrate more isotropically and with smaller amplitudes. Moreover, the valence electron configurations of both the *M* and the *A* atoms were predicted to affect the *A* atom vibrations, where more electrons in the outer shell should lead to smaller displacements. On the other hand, it was predicted that the *M* atom mass should not play a major role in the mean-squared atom displacements of any of the atoms in the MAX phase structures.

After introducing the "predicted" high-temperature atomic displacement behavior for a large number of MAX phases, the measured ADPs from HTND were presented for six select MAX phases: two 211 phases, three 312 phases, and a 413 phase. Here, it was shown that both the modeling and the experimental measurements capture the high displacements of the *A* atoms compared to those of the other atoms in the phases. Moreover, the results showed that both the

predicted and measured *A*-element ADPs are always anisotropic, vibrating more within the basal plane. Beyond the general trends, however, there were some discrepancies – mostly systematic offsets – between the calculated and measured values. Vacancies were suggested as a possible explanation for the Ge-containing phases, which showed the worst agreement between theory and experiment.

Next, I turned to the temperature-dependent crystal structures of 211 and 312 phases (Chapter 13) and a more complicated 523 structure (Chapter 14), which is a higher-order MAX phase. It was shown that the *M*–*A* bonds in MAX phases tend to expand at the highest rates, while the more rigid *M*–*X* bonds generally have the lowest expansion. The bond lengths in the 523 phase revealed that the *M*–*X* bonds are quite robust and are governed by the stacking of their immediate neighbors rather than the stacking sequence of the larger unit cell – that is, the 312-like octahedra maintained 312-like dimensions when interleaved between the 211 octahedra. On the other hand, the behavior of the Ti–Al bonds suggested that they compensate for other instabilities within the crystal since they are more flexible and spring-like. Interestingly, the measured isotropic atomic displacements of the Al atoms in $Ti_5Al_2C_3$ were very well-modeled with first-principles phonon calculations and did not differ much – either experimentally or theoretically – from the 211 and 312 ADPs.

Following the study on the higher-order MAX phase, the bond length behavior in Ti_3GeC_2 – first presented briefly in Chapter 13 – was discussed more in depth. To explain the nonlinear increase of one of the Ti–C bonds and the lack of expansion of the Ti–Ge bonds, a correlated motion model was proposed that would lead to different instantaneous interatomic distance compared to the time- and space-averaged distance that Rietveld analysis of HTND data measures. In addition to the correlated motion model, the mode-dependent Grüneisen parameter, γ, which takes anharmonic effects into account through the volume dependence of phonon frequencies,

was calculated as a function of phonon mode (*i.e.*, the mode-dependent Grüneisen parameter). It was shown that the high values of γ for the low-frequency bands may suggest that third-order terms in the *M*–*A* potentials may be significant in both the Ti_3GeC_2 and Ti_3SiC_2 system.

Clearly, a huge variety of new information has been provided based on the totality of the results in this thesis, but it is important to be able to distinguish the results that provide conclusions, those that provide strong evidence and directions for future work to bolster a proposed idea, and then those which cannot be fully explained and raise more questions for the time being.

I will begin by discussing the first kind of information that contributes direct conclusions and answers. There are a few points that I am able to state with a good amount of certainty that are among the findings – or related to the findings – of this research:

- The *M*–*X* bonding in the MAX phases is quite robust. Taking the four 312 phases studied, all the HTND studies showed that the distance between the C atom and the Ti atom adjacent to the *A*-atom plane is longer than the Ti–C bonds inside the octahedra. This not only shows that the *M*-*X* octahedra are sturdy blocks within the structure, but it also validates the accuracy of the HTND procedures and data analysis, at least when measuring relative atom positions.

- Based on this and other studies, the Raman frequencies in MAX phases are in fact reasonably well-modeled with first-principles calculations. The phases that were measured in this work showed good agreement with theory and in general, there are rarely major unexplainable errors in Raman studies for the MAX phases.

- The *A*-atom vibration is the highest of all the atoms and it is always anisotropic. Regardless of any quantitative errors in agreement, the qualitative atomic displacements for a large

number of phases are quite consistent – that is, there has not been a case in which either theory or experiment has not captured the anisotropic "rattler" effect of the A atom, at least where the anisotropic ADPs are accessible.

Beyond the qualitative agreement, however, the reasons for the (sometimes quite severe) disagreements between theory and experiment fall into the category of ideas that may be proposed from this work, but that would benefit from more supporting arguments and further studies.

Since perhaps the most significant contributions to MAX phase research, and materials science in general, of this thesis are the calculations of ADPs through DFT, I will now discuss this in more depth. In Tables 16.1 and 16.2 I have summarized the relative magnitudes of U_{11} and U_{33}, respectively (both experimental and theoretical) along with their errors. The thick black outlines represent the magnitudes of the calculated value and the shaded circle represents the experimental value, where the radii are proportional to $\sqrt{U_{ij}}$. The shaded regions are color-coded according to the error in U_{ij} [that is, $(U_{\text{exp}} - U_{\text{calc}})/U_{\text{calc}}$]. Red represents cases where the experimental value is greater than the predicted value, and blue indicates the opposite being true; white or neutral colors represent good agreement between theory and experiment. See legend on the bottom for interpretation of the shades.

As discussed earlier, the largest circles are for the U_{11} ADPs of the A atom, without an exception. However, from even a quick glance at Tables 16.1 and 16.2 it is readily apparent that the Ge-containing phases show the worst agreement, especially for the vibrations in the x-y direction (U_{11}, Table 16.1). On the other hand, the three Al-containing phases show relatively good agreement with theory.

Table 16.1: Overview of experimental and calculated U_{11} values at 1273 K and their errors. Thick outlines represent relative calculated ADPs; shaded regions represent experimental ADPs, where color denotes their deviations from the calculated values.

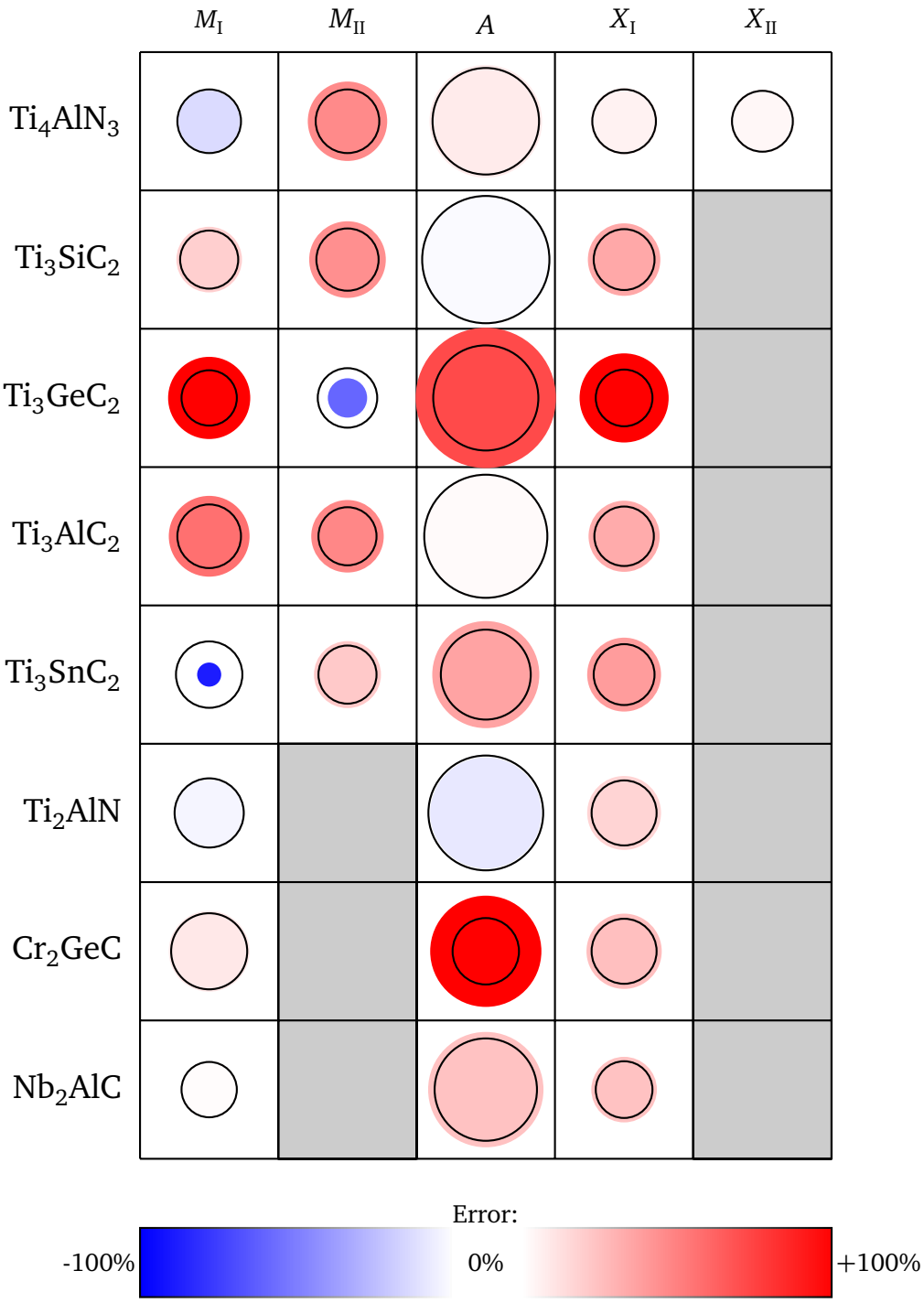

Table 16.2: Overview of experimental and calculated U_{33} values at 1273 K and their errors. Thick outlines represent relative calculated ADPs; shaded regions represent experimental ADPs, where color denotes their deviations from the calculated values.

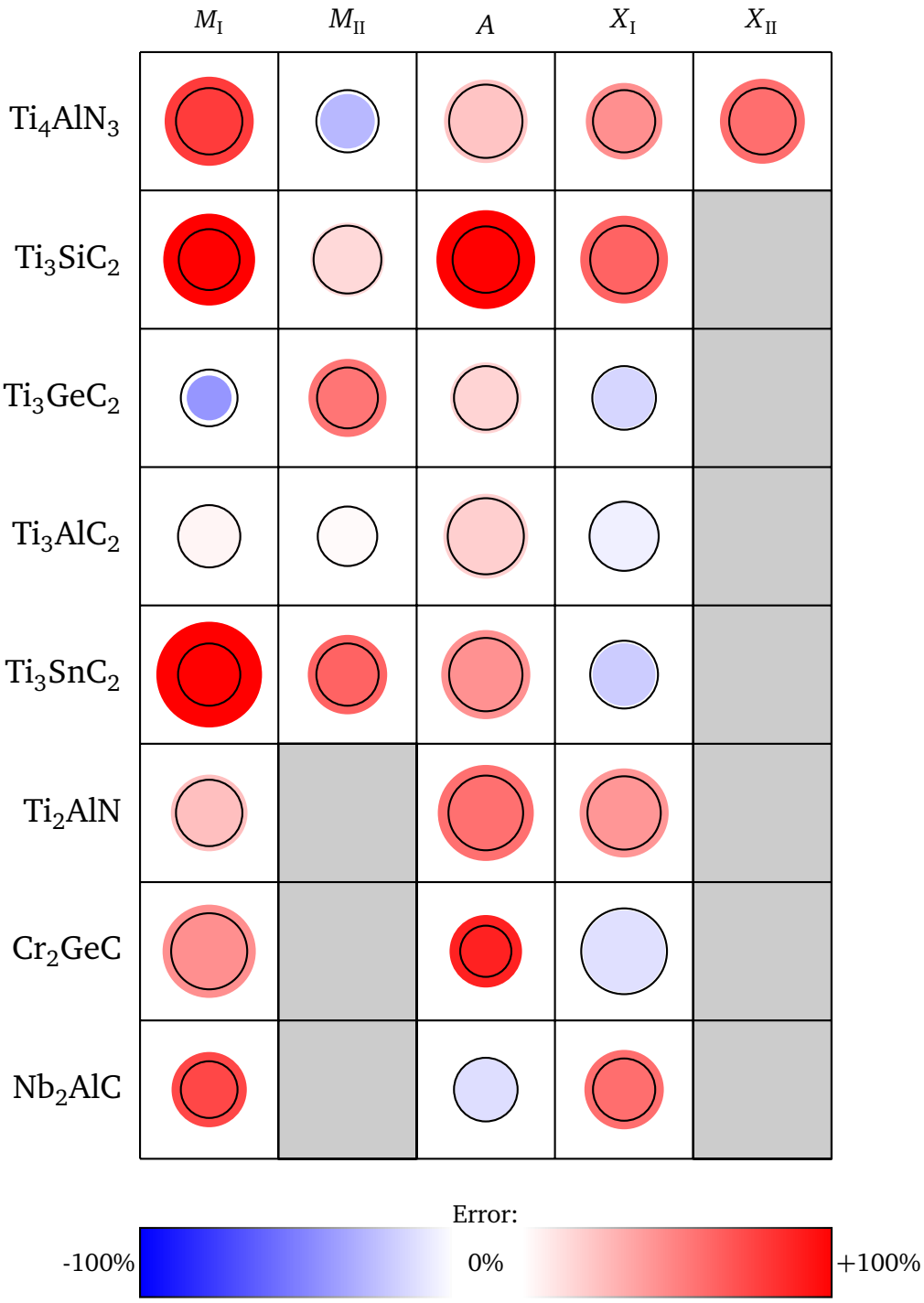

For the most part, the experimental values should not be significantly lower than the calculated values and the cases where the circles are any deep shade of blue should indicate issues with the refinement. Since Ti is not a good neutron scatterer, it is likely that all the errors in the Ti ADPs have to do with experimental issues with refinement. It should also be noted that if U_{11} for Ti is blue, then U_{33} is generally a comparable intensity of red (*e.g.* see M_I for Ti_3SnC_2 or both M atoms for Ti_4AlN_3 and Ti_3GeC_2). This suggests that the isotropic motion may show reasonable agreement, since the average of the two could be similar to the predicted value. This is an important point for future diffraction experiments with MAX phases: since the M atom vibrations are predicted to be nearly isotropic anyway, it may be wise to use U_{iso}, especially when dealing with poor scatterers.

The fact that the modeling of ADPs in Al-containing phases generally shows better agreement with HTND results than for the other phases may suggest that the behavior of Al fits the harmonic model and anharmonic effects are insignificant. Of course, more MAX phase studies would be needed to further support this. The unexpectedly high ADP of Ge in Cr_2GeC and Ti_3GeC_2, on the other hand, suggests that there are factors outside of the harmonic model that are needed to measure and/or model its vibrational behavior. The fact that Ge is such a good neutron scatterer suggests that the large amplitude of displacement may be physical to a certain extent, but that there are sources of error in the calculations such as phenomena that are not taken into account in the harmonic Hamiltonian to model the large vibrations or issues with DFT calculations of forces for Ge.

The correlated motion model proposed for Ti_3GeC_2 would explain some of the unexpected behavior in that phase, but more work is needed to fully understand its implications and to validate it. In particular, pair-distribution-function (PDF) analysis of diffraction data would help clear up some of the uncertainty in the bond lengths because the scattering from specific

atom pairs could be distinguished to measure the near-neighbor interactions. However, the main challenge with this is the synthesis of predominantly single-phase samples. The Ti_3GeC_2 sample use in this work, for instance, included around 20% TiC, which would not be suitable for PDF. Therefore, research toward making cleaner MAX phase samples is extremely important for expanding on the characterization techniques that could be employed. Similarly, making single crystal MAX phases would enable phonon dispersion measurements which could be more directly compared with the phonon band structures.

In addition to potentially useful experimental work, there are many directions for future theoretical work that would be useful for the MAX phases in general. One possible direction for future work is the use of molecular dynamics (MD) simulations for simulating the vibrational behavior of the atoms and determining the time-averaged displacement amplitude in different directions. This would not only validate the first-principles calculations of the ADPs of the MAX phases, but it could possibly provide further information about the correlation between the movement of different atoms. Additionally, other MAX-derived phases – such as MXenes (see a first-principles study in Appendix B.1) – may benefit from similar first-principles phonon calculations, which not only provide references for assessing parameters extracted from diffraction experiments but also shed light on bonding and thermal conductivity.

The theoretical work in this thesis may also be useful for diffraction experiments because the Debye-Waller factor plays into any elastic scattering experiment and is thus highly significant in getting any crystallographic information on a material. Since ADP calculations through first-principles phonon calculations are not yet used as a widespread tool for validating these parameters, further work towards calculating ADPs through phonon calculations with DFT would benefit the diffraction community as well.

Lastly, this work provides insights, tools, and even a large set of parameters that are useful in developing MAX phases for practical applications. Since most MAX phases are particularly well-suited for high-temperature applications (e.g. heating elements, nuclear reactor cladding), the ultimate aim for MAX phase modeling is to be able to predict high-temperature properties. Thermal conductivity is also a particularly useful parameter to model from a practical standpoint. The work in this thesis provides some important first steps in achieving the ultimate goal of finite-temperature modeling, and modeling of thermal transport. The calculated ADPs are temperature-dependent parameters that could be fit into multi-scale models to incorporate temperature, or even direct modeling of thermal conductivity. Furthermore, and perhaps most importantly, I have tested the accuracy of first-principles calculations (against different experimental methods) for modeling the dynamical behavior of a large sample of MAX phases – that is, $\sim$1/3 of the phases known to date. I have shown that the dynamical behavior of the Al-containing phases shows surprisingly good agreement between experiment and theory, which applies to many different stoichiometries (211, 312, 413, and even 523) and also to different experimental techniques (HTND and Raman spectroscopy). This is an especially exciting result because the Al-containing phases are also considered the most promising for practical applications. Therefore, the theoretical results on the Al-containing phases from this thesis are a starting point for developing high-temperature MAX phase modeling of methods.

Appendix A: Texture, composition, and diffraction statistics

This chapter provides additional information about samples used for HTND and Raman spectroscopy. Composition and preferred orientation for samples studied through HTND in this work are presented, as determined through Rietveld refinement of neutron time-of-flight data. Some of the fitted profiles and refinement statistics for Rietveld refinement using GSAS are also included. For the samples studied through Raman spectroscopy, basic characterization through XRD and/or HRTEM is reported.

Section A.1 includes information on the samples studied through HTND. These data are organized by phase, where the 312 phases Ti_3SiC_2 and Ti_3GeC_2 are presented together, then the 211 phases Ti_2AlN and Cr_2GeC, and finally the multi-phase sample containing the Ti-Al-C MAX-like phases Ti_2AlC, Ti_3AlC_2, and $Ti_5Al_2C_3$.

The following section, Section A.2 includes information characterization of the samples used for first-order Raman scattering, including $Ti_4Al_2C_3$, Ta_4AlC_3, Ta_2AlC, and Ti_3SnC_2.

A.1 Neutron diffraction samples

This section reports additional information for the samples used in HTND.

A.1.1 Ti_3SiC_2 and Ti_3GeC_2

The results of the Ti_3SiC_2 texture analysis [Figs. A.1(a)-(c)] show a mild (0002) fiber texture for the Ti_3SiC_2 phase; no texture change was observed during heat treatment. Texture analysis of the Ti_3GeC_2 [Figs. A.1(d)-(e)] showed very mild texture as well that did not change with heat treatment. As noted in Section 8.1.2 (which describes data refinement strategies), for both

Table A.1: Profile agreement factors for Rietveld refinements for neutron diffraction data collected during heating and cooling for Ti_3SiC_2 and Ti_3GeC_2.

T (°C)	wR_p (%)	
	Ti_3SiC_2	Ti_3GeC_2
300	1.84	1.88
500	1.60	2.00
900	1.49	2.45
900†	1.51	2.40
500†	1.63	2.23
300†	1.69	2.12

† Data collected during cooling.

samples, the parameters obtained using MAUD to incorporate preferred orientation were within error bars of those determined by the GSAS with no preferred orientation. Thus the Rietveld analysis described herein was executed in GSAS assuming random texture and full occupancy. Final bond lengths and angles were computed with GSAS.

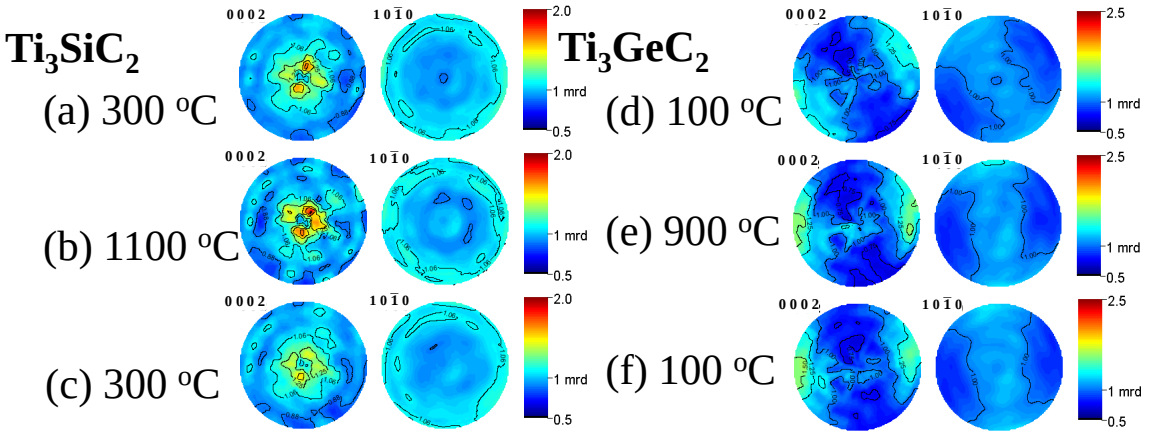

Figure A.1: Pole 0002 and 10$\bar{1}$0 figures recalculated from the orientation distribution of HIPPO data for a) Ti_3SiC_2 at 300^{o}C (before heating), b) 1100^{o}C, c) 300^{o}C (after heating) and, d) Ti_3GeC_2 at 100^o C (before heating), (e) 900 ^{o}C and, (f) 100^{o}C (after heating).

Table A.1 shows the profile agreement factors for the Rietveld analysis at 300°C, 500°C and 900 °C, giving the weighted pattern R index, wR_p [115]. Figures A.2(a) and (b) show the Rietveld fit for the neutron time-of-flight data integrated for full detector rings and the four

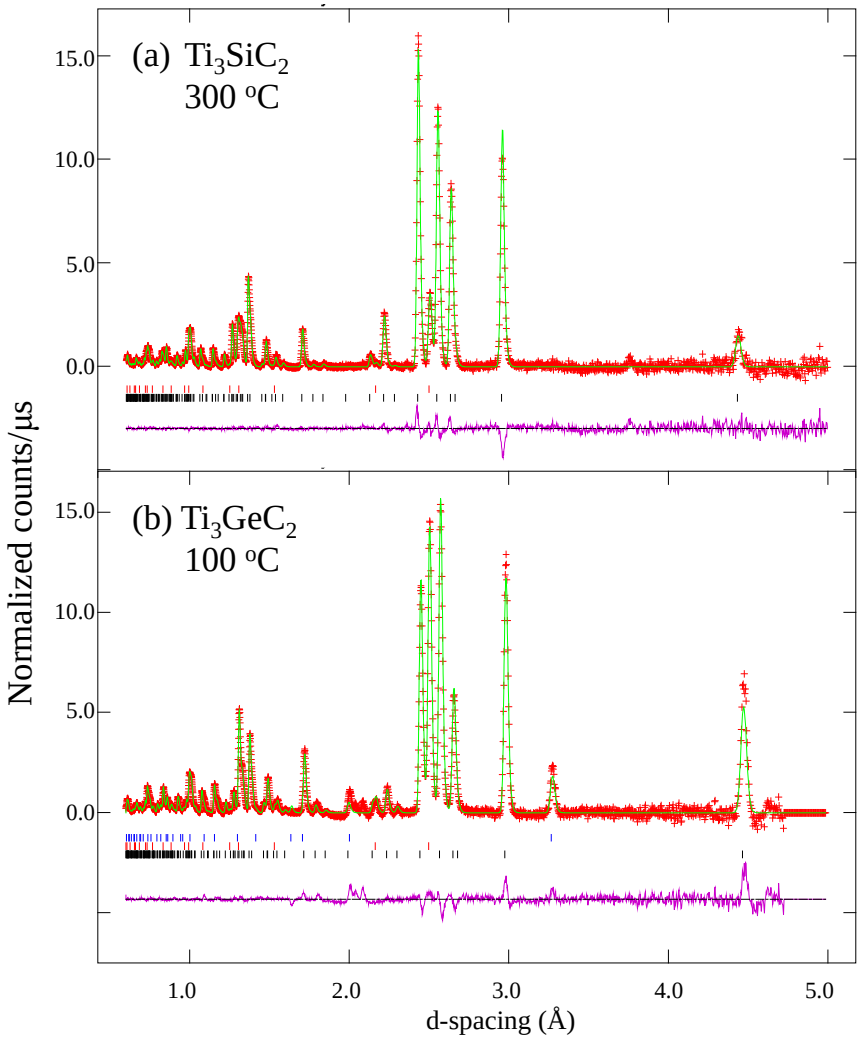

Figure A.2: Rietveld refinement of HIPPO data from 90° detector bank for (a) Ti_3SiC_2 at 300 °C and, (b) Ti_3GeC_2 at 100 °C. In both plots, the raw data points are shown as red +; calculated profile shown as solid green and, difference curve ($Y_{obs} - Y_{calc}$) is shown is solid purple line below. Reflection markers show calculated peak positions for pure Ge (blue), TiC (red), and Ti_3GeC_2/Ti_3SiC_2 (black).

measured orientations for the 90 degree detector bank at the lowest temperatures for each sample, 300°C for Ti_3SiC_2 [Fig. A.2(a)] and 100°C for Ti_3GeC_2 [Fig. A.2(b)]. The calculated (solid lines) and observed (+ signs) data are compared. The markers showing peak positions for the included phases and the difference curves, $y_{obs} - y_{calc}$, are plotted, in purple, below each figure.

In both phases, TiC, with a rock-salt structure (space group $Fm\bar{3}m$) [143] was an impurity phase. The TiC content was 5.8(±0.2) wt.% in Ti_3SiC_2 and 19.1(±0.3) wt.% in Ti_3GeC_2. These fractions remained constant with thermal cycling. Peaks corresponding to 3.0(±0.3) wt.% Ge – with a cubic structure (space group $Fm\bar{3}m$) – was also found in the Ti_3GeC_2 sample. At temperatures above 900°C, the Ge peaks disappeared, in agreement with its melting point at 917°C [154]. The fraction of Ge also remained constant upon thermal cycling. No other reactions or phase changes were observed during the thermal cycling. In the Ti_3GeC_2 sample, another minor impurity phase – with diffraction peaks near 1.8 Å and 2.1 Å – could not be identified. Peaks above ∼2.12 Å from this phase were not observed, and based on the relative peak intensities and their positions we assume it is a cubic, trigonal, or hexagonal, structure with a relatively small unit cell. Since the inclusion, or exclusion, of less than 4 wt. % Ge in the refinements had very little, if any, effect on the refined Ti_3GeC_2 structural parameters, we assume that the refined parameters for Ti_3GeC_2 are also not affected by this unaccounted impurity phase.

A.1.2 Ti_2AlN and Cr_2GeC

Texture analysis showed a very mild (0002) fiber texture that did not change during heating in both Ti_2AlN [Figs. A.3(a) and (b)] and Cr_2GeC [Figs. A.3(c) and (d)]. By averaging the four measured sample orientations and refining against the 90° and 140° detector banks

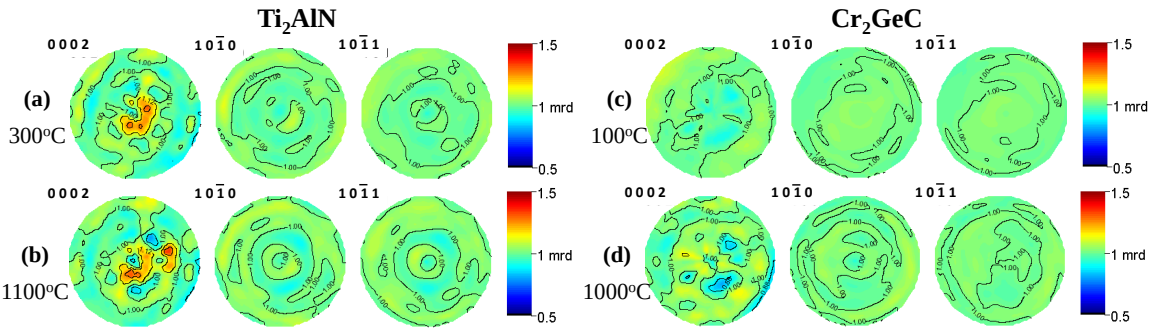

Figure A.3: Pole 0002, 10$\bar{1}$0, and 10$\bar{1}$1 figures calculated from the orientation distribution of HIPPO neutron time-of-flight data collected during heating for Ti_2AlN at (a) 300°C and (b) 1100°C, and Cr_2GeC at (c) 100°C and (d) 1000°C.

simultaneously, the existing mild preferred orientation was randomized and a random powder is therefore a valid approximation for all practical purposes

The profile agreement factors for the Rietveld analysis of HTND data for both the Ti_2AlN and Cr_2GeC samples at 100°, 300°, 500°, and 900°C are shown in Table A.2, giving the weighted pattern R index, wR_p, and goodness of fit, χ^2, which is the ratio of the weighted pattern R to the expected R index [115]. It should be noted that the HIPPO instrument repeats measurements for different detector panels with the same diffraction angle due to its detector arrangement, which is not taken into account in the expected R index and can lead to $\chi^2 < 1$ (as with Ti_2AlN). Figures A.4(a) and (b) show the Rietveld fit of the neutron time-of-flight data from the 90° 2θ

Table A.2: Profile agreement factors for Rietveld refinements for neutron diffraction data collected during heating and cooling for Ti_2AlN and Cr_2GeC.

	Ti_2AlN		Cr_2GeC	
T (°C)	wR_p (%)	χ^2	wR_p (%)	χ^2
100	1.76†	0.9131†	2.00	4.008
300	1.65	0.7589	1.97	3.781
500	1.57	0.6349	1.99	3.917
900	1.43	0.4441	1.92	3.670

† Data collected during cooling.

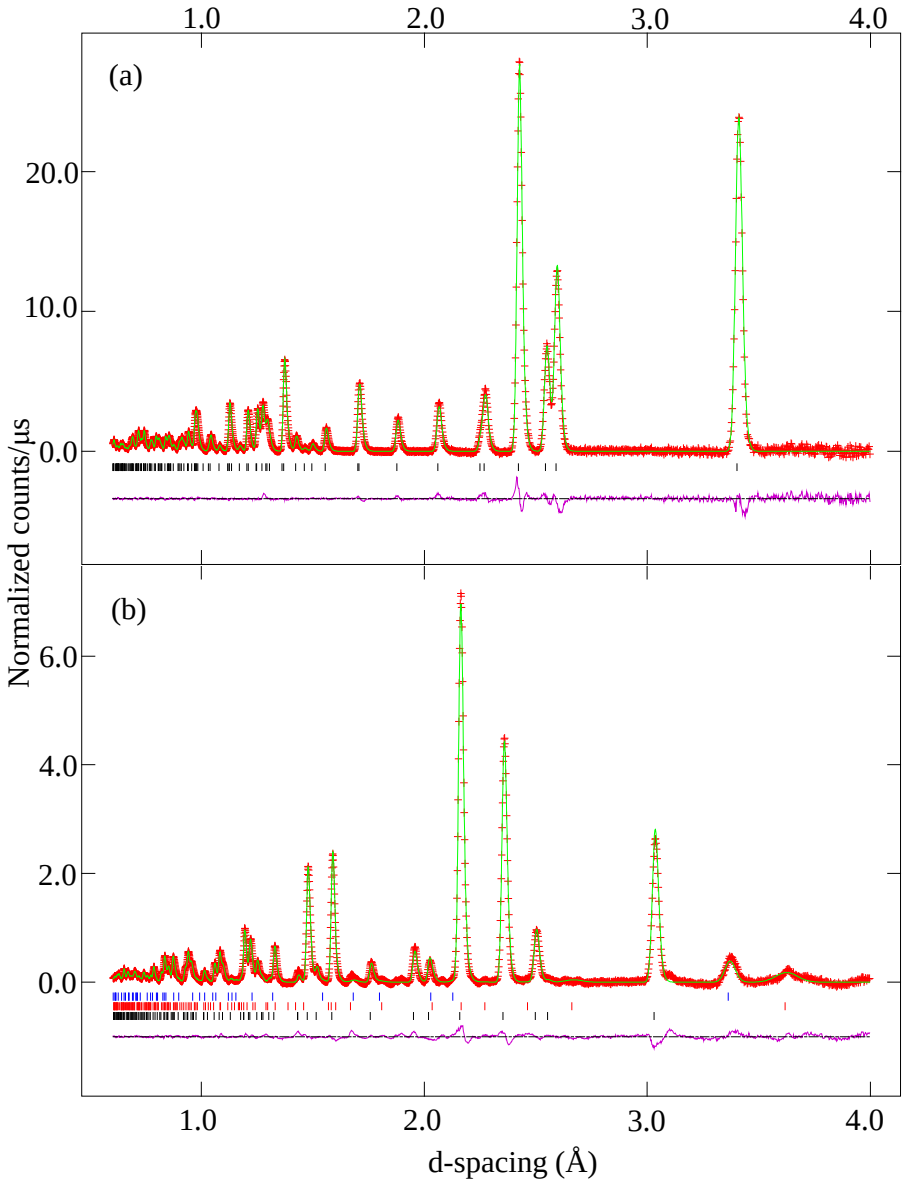

Figure A.4: Rietveld refinement of HIPPO data from the 90° 2θ detector bank for (a) Ti_2AlN at 100°C and, (b) Cr_2GeC at 100°C. Data in (a) for Ti_2AlN was collected during cooling. In both plots, the raw data points are shown as red + signs; calculated profile is shown as a solid green line. Below these, reflection markers show calculated peak positions. In (a), only markers for Ti_2AlN are shown (black). In (b), the markers correspond to Cr_2GeC (black, bottom) and secondary phases Cr_2O_3 (red, middle) and graphite (blue, top). Difference curve ($Y_{obs} - Y_{calc}$) is shown in bottom of each panel as solid purple line.

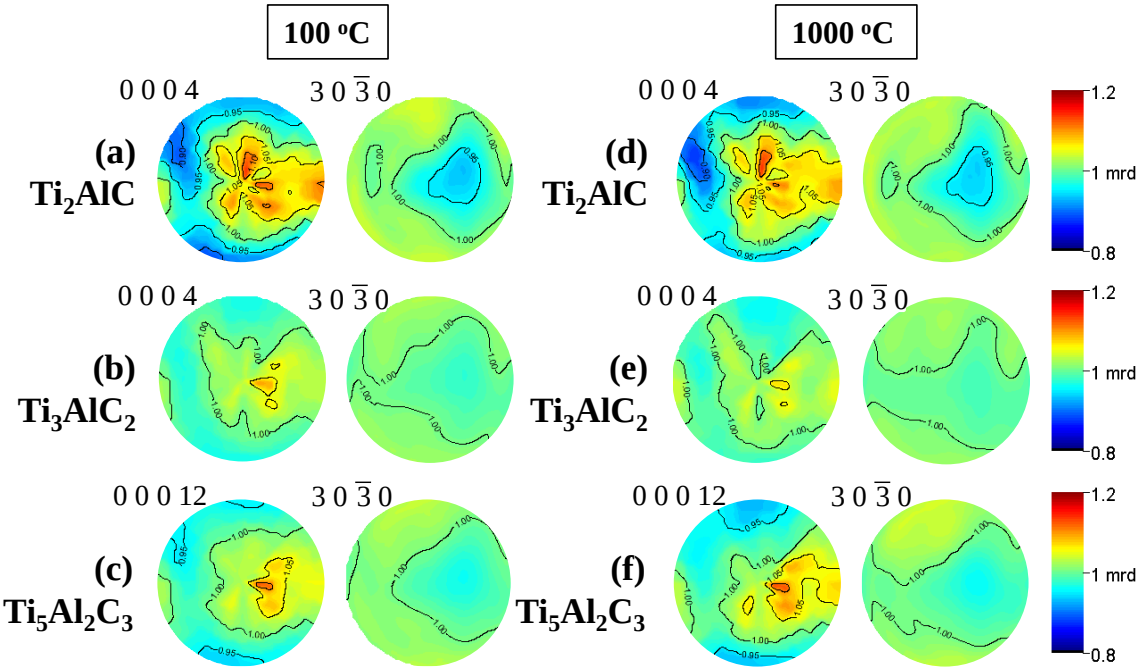

Figure A.5: Pole figures for 0 0 0 l and 3 0 $\bar{3}$ 0 recalculated from the orientation distribution of HIPPO data for (a) Ti_2AlC, (b) Ti_3AlC_2, and (c) $Ti_5Al_2C_3$ at 100°C, and (d) Ti_2AlC, (e) Ti_3AlC_2, and (f) $Ti_5Al_2C_3$ at 1000°C. Sample cylinder axis is in the center of pole figures.

detecter bank at 100°C for Ti_2AlN and Cr_2GeC, respectively, showing the observed (red + signs) and calculated (green solid line) data. The difference curve and peak markers for all phases are shown in the bottom of each figure.

No additional phases were found in the Ti_2AlN sample. Refinement of the Al and N site occupancies gave a crystal chemistry of $Ti_2AlN_{0.97}$, which remained constant with heating and cooling. In Cr_2GeC, additional phases of $\sim 4.9(\pm 0.3)$ wt. % eskolaite, Cr_2O_3, and <1 wt. % graphite 2H (hexagonal) were found and refined [see peak markers in Fig. A.4(b)]. The volume fraction of both additional phases in Cr_2GeC remained constant, within error bars, during heating and cooling.

Table A.3: Profile agreement factors for Rietveld refinements of neutron diffraction data collected during heating and cooling for a multi-phase Ti-Al-C sample.

T (°C)	wR_p (%)	χ^2	R_{exp}
100	1.34	3.959	0.67
200	1.31	4.042	0.65
600	1.23	3.599	0.65
1000	1.17	3.331	0.64
600†	1.29	3.998	0.65
200†	1.4	4.697	0.65

† Data collected during cooling.

A.1.3 Multi-phase sample containing Ti_2AlC, Ti_3AlC_2, and $Ti_5Al_2C_3$

Texture analysis (Fig. A.5) showed a mild (000l) fiber texture for all three phases. The texture did not change during heating or cooling. The MAUD refinements incorporating preferred orientation gave parameters that were within error bars of those determined without including texture by Rietveld refinement with GSAS. Therefore, all results reported in this work for phases in this sample are from the GSAS refinements assuming random texture.

The Rietveld fits for the neutron time-of-flight data – integrated for the full detector rings and the three measured orientations – are shown for the lowest temperature run at 100°C for the 90° [Fig. A.6(a)] and the 144° detector banks [Fig. A.6(a)]. The calculated fit (solid green lines) and measured data (red plus signs) are compared, with the difference curve plotted at the bottom (solid purple line). The markers above the difference curve show the peak positions for the phases: from top to bottom, $(Ti_{0.5}Al_{0.5})Al$ (green), $Ti_5Al_2C_3$ (blue), Ti_3AlC_2 (red), and Ti_2AlC (black). The higher-d-spacing peaks resulting from diffraction by the basal planes are labeled for the (0 0 0 6) peak of Ti_3AlC_2, the (0 0 0 4) peak of Ti_2AlC, and the (0 0 0 15) and (0 0 0 12) peaks of $Ti_5Al_2C_3$. The latter two peaks unambiguously identify $Ti_5Al_2C_3$ as the dominant phase in the sample, as they cannot be accounted for by any other known phase in

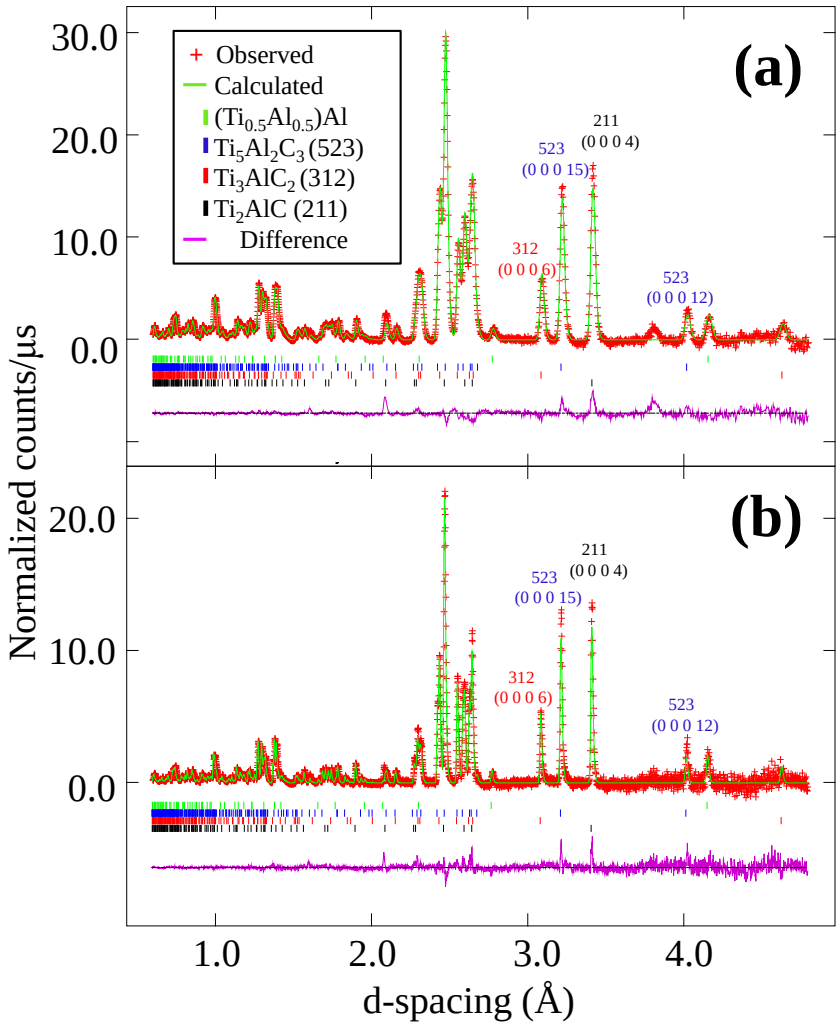

Figure A.6: Rietveld analysis of neutron diffraction data measured on HIPPO at 100°C for sample containing 38(±1) wt. % $Ti_5Al_2C_3$, 32(±1) wt.% Ti_2AlC, 18(±1) wt. % Ti_3AlC_2, and 12(±1) wt. % $(Ti_{0.5}Al_{0.5})Al$ from (a) 90° detector bank and (b) 144° detector bank. Raw data points are shown as red + symbols and the calculated profile is shown as a solid green line. Underneath, markers show calculated peak positions of each phase. From top to bottom: $(Ti_{0.5}Al_{0.5})Al$ (green), $Ti_5Al_2C_3$ (blue), Ti_3AlC_2 (red), and Ti_2AlC (black). Difference curve ($Y_{obs} - Y_{calc}$) is shown in bottom of each panel as solid purple line.

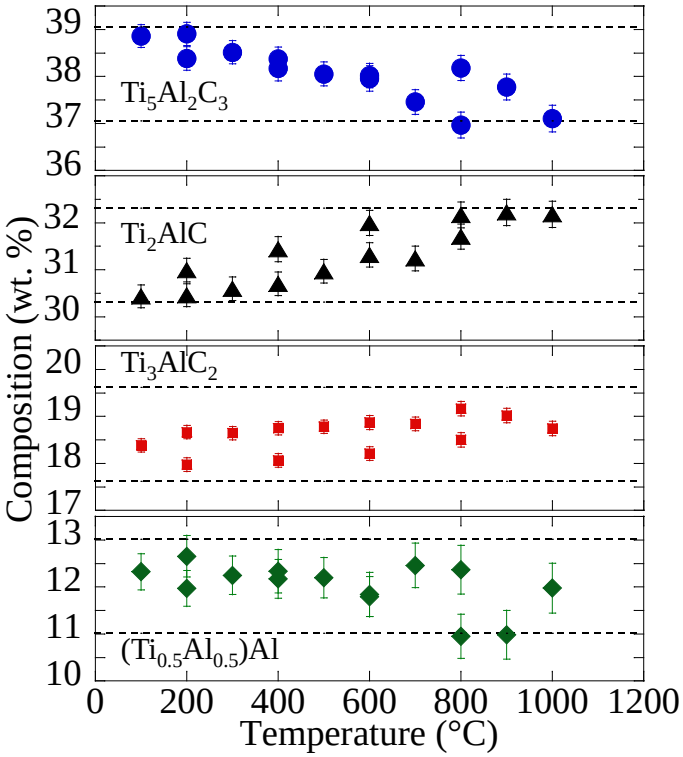

Figure A.7: Compositions (wt.%) of each phase in the Ti-Al-C sample as a function of temperature upon heating and cooling. Dashed lines indicate limits for ±1% range.

the Ti-Al-C system. The profile agreement factors for the Rietveld fits are listed in Table A.3 at select temperatures, giving the weighted profile R index, wR_p, the goodness of fit, χ^2, and the expected R factor, R_{exp} [115]. Good agreement is observed between the calculated and observed profiles, with one unidentified peak at 2.09 Å whose origin remains unclear. A broad peak at 3.80 Å is present only in the 90° bank [Fig. A.6(a)], which is likely due to background interference.

The composition determined from Rietveld analysis is 38(±1) wt. % $Ti_5Al_2C_3$, 32(±1) wt.% Ti_2AlC, 18(±1) wt. % Ti_3AlC_2, and 12(±1) wt.% $(Ti_{0.5}Al_{0.5})Al$. The temperature dependencies of the fractions of each phase are plotted in Fig. A.7, where the dashed lines indicate the ±1 wt.% limits. The compositions generally stay within 1 wt.% of the average value during heating and cooling, lending credibility to our data analysis and the resulting uncertainties for the composition.

A.2 RAMAN SPECTROSCOPY SAMPLES

This section reports additional information for the samples used for Raman spectroscopy.

A.2.1 Ta_4AlC_3, Ti_4AlN_3, and Ta_2AlC_3

The XRD pattern of the Ta_4AlC_3 sample [Fig. A.8(a)] shows that the sample is mainly Ta_4AlC_3, with a small amount of TaC. Rietveld refinement of the XRD data with the MAUD software program [122, 155, 156] showed approximately 5 wt.% TaC. The Ta_4AlC_3 a and c lattice parameters were measured to be 3.112(±0.001) Å and 24.100(±0.002) Å, respectively. This is in good agreement with Etzkorn *et al.* [68], who found a and c lattice parameters to be 3.113 (±0.0003) Å and 24.122 (±0.003) Å, respectively, and Eklund *et al.* [67] who reported a=3.109 (±0.001) Å and c=24.078 (±0.001) Å.

Figure A.8(b) shows the powder diffractogram of Ti_4AlN_3 with lattice parameters a=2.992(±0.001)

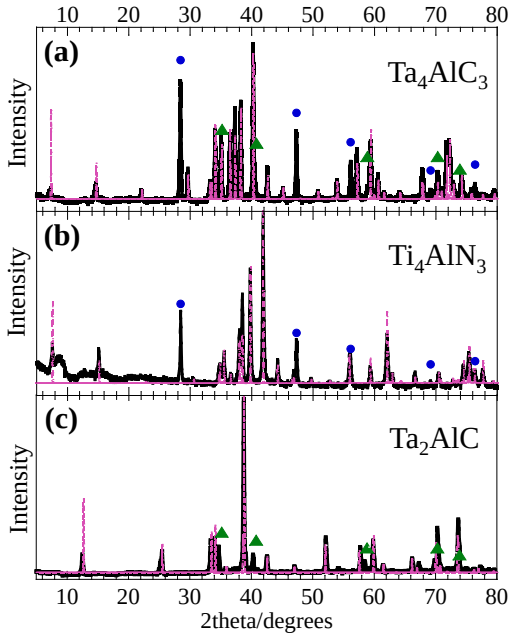

Figure A.8: XRD patterns for (a) Ta_4AlC_3, (b) Ta_4AlN_3, and (c) Ta_2AlC. Markers show peak positions for Si (blue circles) and TaC (green triangles) The dotted purple lines are the calculated XRD patterns of the majority phases.

Å and c=23.40(±0.01) Å, as determined by Rietveld refinement using MAUD. These values are also in good agreement with previous results [157] that showed a=2.988(±0.001) Å and c=23.40(±0.01) Å. The XRD pattern of the Ta_2AlC sample [Fig. A.8(c)] shows Ta_2AlC (a=3.0805(±0.0002) Å, c = 13.874(±0.001) Å) as the main phase with 14 wt.% TaC. The lattice parameters agree well with those previously reported [158], *viz.* a=3.086(±0.006) Å and c=13.85(±0.04) Å.

A.2.2 Ti_3SnC_2

As shown in Fig. A.9(a), the XRD pattern for Ti_3SnC_2 after heating to 1600°C for 4 h and cooling to room temperature shows mainly Ti_3SnC_2 in addition to Ti_2SnC, TiC, and Sn. After treatment with HCl, the Sn dissolved and the volume fractions of the different phases were

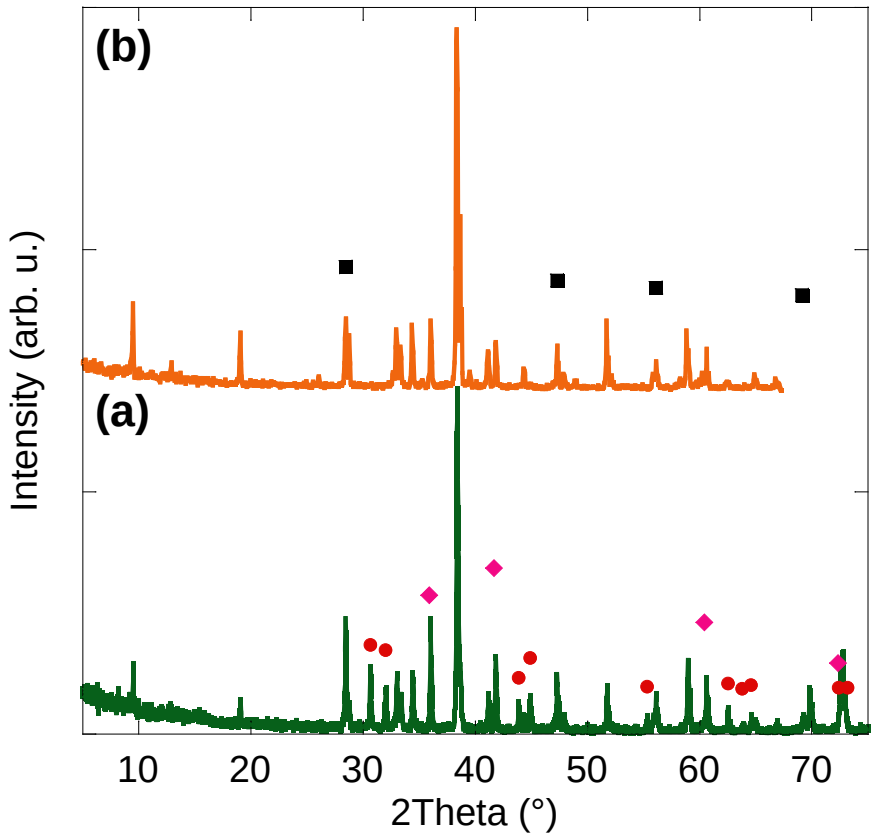

Figure A.9: XRD patterns for (a) Ti_3SnC_2 as produced after heating to 1600°C for 4h and cooling to room temperature, and (b) the same as (a) but after HCl treatment. Circles are for Sn, Diamond for TiC, and squares for Si.

estimated at 70 wt.% Ti_3SnC_2, 9 wt.% Ti_2SnC, and 21 wt.% TiC using Rietveld analysis. The lattice parameters of Ti_3SnC_2 (a = 3.137 Å, c =18.613 Å) matches very well with what was reported before [60, 61, 63].

A bright field image for a Ti_3SnC_2 particle is shown in Fig. A.10(a), and its EDS is shown in Figure A.10(b). The EDS showed Ti:Sn at.% to be around 3:1 at.%, which is evidence of the successful synthesis of the Ti_3SnC_2 phase.

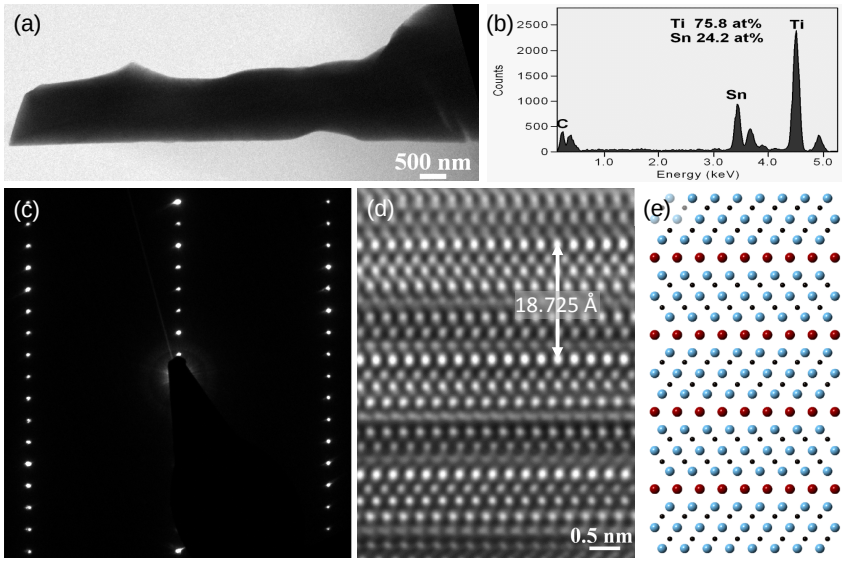

Figure A.10: (a) Bright field image for Ti_3SnC_2 particle, (b) EDS pattern for the Ti_3SnC_2 particle, (c) SAED of Ti_3SnC_2 along $[11\bar{2}0]$, (d) HRTEM images along the same direction, and (e) schematic for the crystal along $[11\bar{2}0]$ direction for Ti_3SnC_2.

Appendix B: Other works

This section includes the full text of five other interesting first-author papers I have worked on during my PhD studies, but that are outside of the scope of this thesis topic. These papers include:

- B.1: Two-dimensionsal Ta-containing transition metal carbides, $Ta_{n+1}C_n$ (where $n = 1$, 2, or 3) (*Eur. Phys. Lett.*, 2013).
- B.2: $Ti_5Al_2C_3$, a higher-order MAX phase:
  - ◇ B.2.1: A first principles, XRD, and TEM study on $Ti_5Al_2C_3$ (*J. Eur. Cer. Soc.*, 2012).
  - ◇ B.2.2: Comment on the stacking sequence of $Ti_5Al_2C_3$ (*J. Am. Cer. Soc.*, 2012).
- B.3: A study of mobile dislocations uing the $(11\bar{2}1)$ twin for MAX phases and HCP metals to represent a wall of dislocations (*Phys. Rev. B.*, 2011).
- B.4: A study on the stability of α-Ta_4AlC_3 and observations about its polymorphism (*Mat. Res. Bull.*, 2011).

B.1 FIRST-PRINCIPLES CALCULATIONS ON 2D MXENES

Published in: N.J. Lane, M.W. Barsoum, J.M. Rondinelli, "Correlation effects and spin-orbit interactions in two-dimensional hexagonal 5d transition metal carbides $Ta_{n+1}C_n$ ($n = 1, 2, 3$)" *Europhysics Letters* **101**, 57005 (2013).

Abstract

Density functional calculations are used to investigate the electronic structure of two-dimensional 5d tantalum carbides with honeycomb-like lattice structures. We focus on changes in the low-energy bands near the Fermi level with dimensionality. We find that the Ta 5d states dominate, and the extended nature of the wavefunctions makes them weakly correlated. The carbide sheets are prone to long range magnetic order and we evaluate their stability to enhanced electron–electron interactions through a Hubbard U correction. Lastly, we find that the splitting of the bands near the Fermi level caused by spin-orbit interaction decreases with increasing dimensionality. In the lowest dimensionality ($n = 1$) case, the band splitting pushes a conduction band above the Fermi level and leads to a semi-metallic band structure.

Two-dimensional (2D) free-standing crystals exhibit a range of functional properties, mainly derived from the topology of their underlying lattice and enhanced electronic and magnetic effects due to reduced dimensionality. Spin-polarized edge states,[159] for example, have been predicted for the well-studied 2D carbon material graphene,[160] owing to the topological origin of its transport properties. A large external magnetic field, however, is required to realize the quantum Hall effect, and its spin degeneracy makes it difficult to manipulate. To overcome these challenges, experimental approaches have been developed to induce magnetism by introducing transition metal adatoms [161] and point defects [162] on the surfaces.

2D binary metal oxides and dichalcogenides, e.g. ZnO, BN, MoS_2 also find widespread interest. New functionalities originate from the presence of more diverse chemistries. [163, 164] However, in most existing pristine 2D free standing materials, magnetic ordering is absent and the tunability of the electronic structure is limited to electrostatic doping. A more promising avenue includes directly incorporating transition metals with multiple orbital degrees of freedom and highly-correlated electrons into to the lattice. Magnetism, for example, was recently predicted for VX_2 (X=S, Se) monolayers.[165] Alternatively, heavier 5d transition metals with strong spin-orbit coupling can be either deposited on the surface or directly integrated into the lattice of the 2D materials. Recent first principles calculations show that graphene decorated with 5d transition metals can exhibit remarkable magnetic and topological transport properties [166]. The magnetic coupling induced by such treatments on nonmagnetic 2D materials, however, is difficult to control in actual applications due to unintentional impurities and defects.

In this Letter, we focus on low-dimensional hexagonal materials, consisting of alternating layers of carbon and tantalum. These Ta-containing transition metal carbides are part of a recently discovered group of 2D materials called "MXenes" synthesized by chemical exfoliation.[167] Similar to the previously studied Ta-decorated graphene structures, [166] these materials contain sheets of carbon in the inner layers and Ta atoms on the surface. In this case, however, the Ta layers are ordered, rendering them less susceptible to defects and more favorable for deliberate surface functionalization. Furthermore, these materials are derived from MAX phases, which are a large fam-

ily of layered carbides and nitrides with the general formula $M_{n+1}AX_n$, where $n = 1 \cdots 3$, M is an early transition metal, A is an A-group element (mostly from groups 13 and 14), and X is carbon and/or nitrogen. [1] Since the stacking sequence of the $X\mathrm{M}_6$ octahedra in the hexagonal MAX phases depends on the stoichiometry, the MXene sheets have the advantage that dimensionality controls both the system size and the symmetry between the two surfaces [Fig. B.1(a)].

The 2D MXenes have the general formula $M_{n+1}X_n$, and they crystallize in sheets containing 1, 2, or 3 layers of $X\mathrm{M}_6$ octahedra depending on n. Their recent synthesis [167] has spawned interest for uses in energy applications, including anodes in Li ion batteries [168, 169] and electrodes for supercapacitors. There are a number of recent theoretical studies, [170–172] mainly focusing on the Ti-containing phases. However, modeling work on MXenes in the Ta-C system have not yet been reported, despite their recent synthesis [173]. Motivated by the structural flexibility, possible enhanced electron–electron interactions, and the strong spin-orbit coupling parameter for Ta ($\zeta_d = 1970$ cm^{-1})[174], we use *ab initio* electronic structure calculations to investigate the effect of dimensionality (n) and electron correlations on the band structure and magnetic ordering in $\mathrm{Ta}_{n+1}\mathrm{C}_n$, $n = 1 \cdots 3$.

First-principles density functional calculations are performed using the Vienna *Ab initio* Simulation Package (VASP) [129], with a plane wave cutoff of 500 eV and the projector-augmented wave method (PAW)[126] to treat the interaction between the core and valence electrons; we treat the Ta 5p electrons as valence electrons. For the site-decomposed density of states, partial occupations are set using the tetrahedron method with Blöchl corrections. In the band structure calculations, Gaussian smearing with a smearing width of 0.10 eV was used. Reciprocal space integrations are performed using a $15 \times 15 \times 2$ k-point mesh. We investigate the effects of electron–electron interactions by using both the local (spin) density approximation [L(S)DA)] and the improved generalized gradient approximation (GGA) of Perdew-Burke-Eruzerhof (PBEsol) for solids[175] with the rotationally invariant Hubbard U correction ($+U$) of Liechtenstein *et al* [176]. For the on-site exchange interaction, we test values of J from 0.2 to 1.5 eV and determine J does not have a strong effect on the stability of the magnetic configurations with U. J is therefore kept constant at 0.5 eV throughout. The high measured conductivity of $\mathrm{Ta}_4\mathrm{C}_3$[173], and the robustly metallic electronic structures of bulk TaC[177] and the MAX phases [1], suggest that electron correlation effects should be weak. We, therefore, anticipate the LDA and PBEsol functionals to provide an adequate description of the electronic and magnetic properties of these materials.

The $\mathrm{Ta}_{n+1}\mathrm{C}_n$ unit cells used in our calculations contain two symmetry equivalent free-standing sheets that are separated by 11-13 Å of vacuum. We obtain the equilibrium structures at the LDA and PBEsol level by minimization of the total energy computed for a range of a lattice parameters, performing a full relaxation of the atomic positions along the c-direction until the forces are converged below a tolerance of 5 meV Å^{-1}.

Table B.1 contains the ground state atomic structure descriptors obtained with the LDA and PBEsol functionals. These ground state atomic structures are used for all subsequent band structure and energy calculations according to the corresponding dimensionality and functional. The LDA functional, for all values of n, predicts equilibrium lattice parameters that are smaller than those obtained with PBEsol; nonetheless, both functionals are in good agreement, within $< 1\%$ of each other and the available experimental data[173] for $\mathrm{Ta}_4\mathrm{C}_3$. We also summarize the interatomic distances between the different Ta and C atoms corresponding to the sites labeled in Fig. B.1(a). For all 2D sheets explored, the Ta atoms at the surface layer have shorter Ta–C bonds than those in the center of the sheet, i.e. $d(\mathrm{Ta_I}\text{–C}) < d(\mathrm{Ta_{II}}\text{–C})$, which is also consistent with the bond lengths in MAX phases [1].

While there are slight differences in the

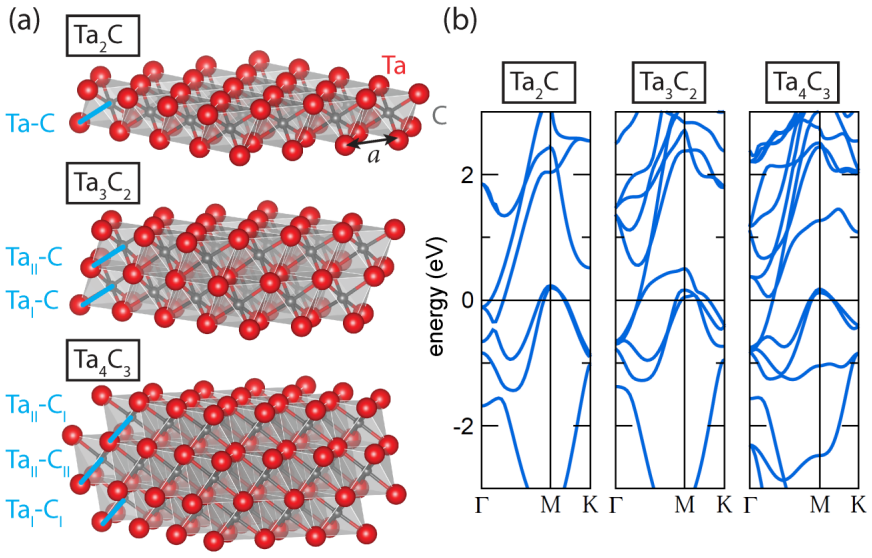

Figure B.1: The two-dimensional $Ta_{n+1}C_n$ ($n = 1, 2, 3$) sheets (a) all possess hexagonal symmetry. The lattice constants, a, and select interatomic Ta–C distances are highlighted (cf. Table B.1). (b) LDA electronic band structures for each compound along the path $\Gamma(0,0,0) \rightarrow M(\frac{1}{2},0,0) \rightarrow K(\frac{1}{2},\frac{1}{2},0)$.

lattice dimensions and atomic positions, the average interatomic distances and lattice parameters are similar between the three stoichiometries. This suggests that any differences in electronic structure should originate from either the stacking of the octahedra or the number of occupied Ta d bands available, which depends on the ratio of Ta to C atoms. To explore these possible differences, we begin by computing the electronic band structures with the LDA functional. For $n = 1$, we find two dispersive Ta d-bands crossing the Fermi level (E_F) along $\Gamma - M$ [Fig. B.1(b), left]. The two free-electron pockets centered at Γ are similar to those found in 3D metals despite the 2D nature of the MXene sheet. Further, the hole pockets at M make this a semi-metal with possible p-type conductor features that may be highly temperature dependent.

In contrast, in Ta_3C_2 ($n = 2$) we find multiple bands crossings at the Fermi level, with metallic-like partial occupancy centered around M. The band structure for Ta_4C_3 ($n = 3$) shows similar features as Ta_2C, with nearly fully occupied Ta d states at M. However, in this case a single Ta band, with nearly linear dispersion, crosses the Fermi level along $\Gamma - M$. Indeed the site-decomposed partial densities-of-states (DOS) confirm that the region near E_F is largely controlled by the Ta d states [Figs. B.2(a–c)].

Figs. B.2(d–f) show the spatial distribution of the electrons within 0.2 eV of E_F. We find a strong dependence on dimensionality for the charge distribution. Intriguingly, this spatial distribution about the Ta site in $n = 1$, *viz* Ta_2C [Fig. B.2(d)], and the inner Ta atom in $n = 3$, *viz* Ta_4C_3 [Fig. B.2(f)], share similar features—the charge around the atom is distributed into six lobes, three above and three below the Ta atom. The inner Ta atom in $n = 2$ (Ta_3C_2) [Fig. B.2(d)] shows strikingly different behavior, with a small distribution of charge collected above and below the Ta atom, aligned parallel to the c-axis.

To understand the atomic-scale origin of these features, we examine more closely the crystal structures of each sheet. Ta_2C ($n = 1$) consists of a single Ta–C octahedron with stack-

Table B.1: Summary of lattice parameters, a, and Ta–C bond lengths, d, in Å with respect to dimensionality, n, obtained with LDA and PBEsol functionals. Embolden values correspond to experimental data taken from Ref. [173].

	n	length	LDA	PBEsol	
Ta_2C	1	a	3.041	3.058	
		d(Ta–C)	2.127	2.139	
Ta_3C_2	2	a	3.086	3.112	
		d(Ta_I–C)	2.110	2.127	
		d(Ta_{II}–C)	2.220	2.236	
Ta_4C_3	3	a	3.077	3.094	(**3.1**)
		d(Ta_I–C)	2.119	2.131	
		d(Ta_{II}–C_I)	2.201	2.210	
		d(Ta_{II}–C_{II})	2.215	2.226	

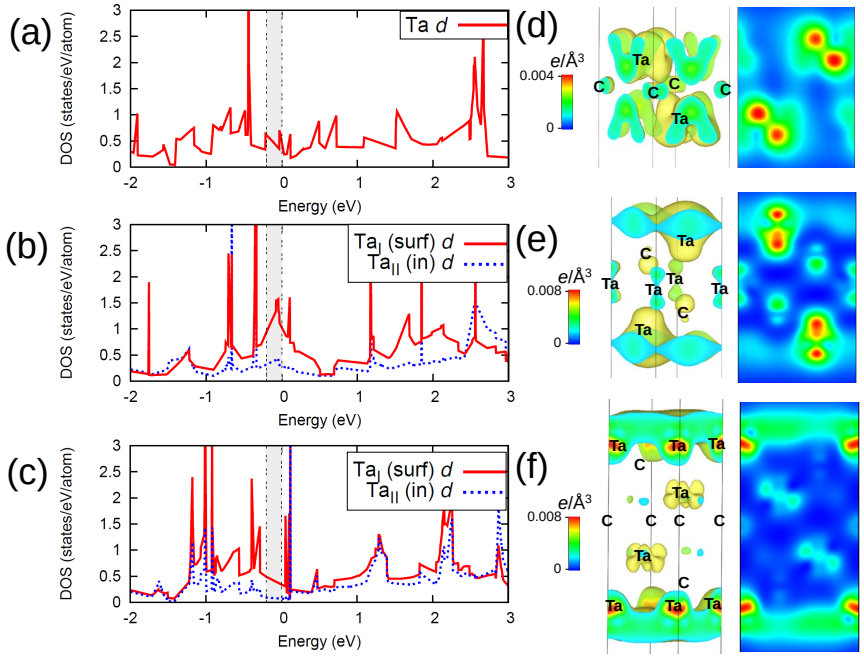

Figure B.2: Site-decomposed partial DOS computed within the LDA for the surface (surf) and inner (in) layer Ta sites in (a) Ta_2C, (b) Ta_3C_2, and (c) Ta_4C_3. Note that the contribution from the C atoms to the DOS within this energy window is small and therefore not shown. The spatial distribution of the partial charge density from 0.2 eV up to the Fermi level (shaded region) is also shown in (d), (e), and (f) for Ta_2C, Ta_3C_2, and Ta_4C_3, respectively. The 2D contours are projections on the $(11\bar{2}0)$ plane.

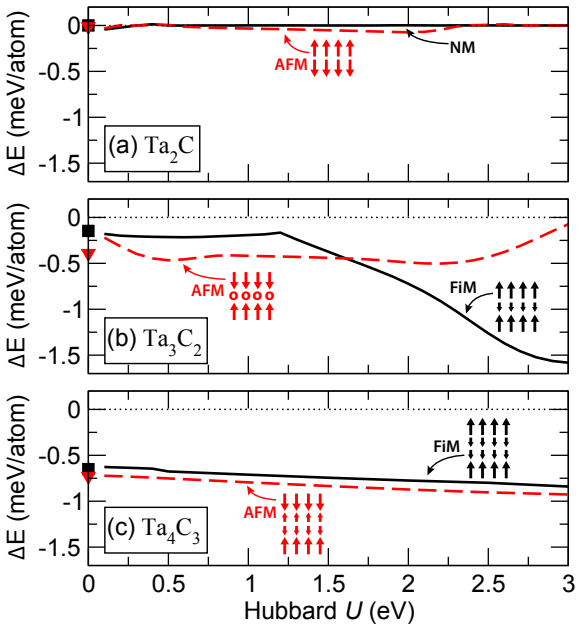

Figure B.3: The L(S)DA+U energy differences, ΔE, between the magnetic and non-magnetic (NM) states with U for (a) Ta_2C, (b) Ta_3C_2, and (c) Ta_4C_2. Energies given per Ta atom. The points at $U = 0$ eV are obtained without the Hubbard U method. Schematics (inset) illustrate the spin ordering of the Ta atoms with ferrimagnetic (FiM) or antiferromagnetic (AFM) order, where the arrows represent the relative magnitudes and directions of spin, and the open circles indicate Ta atoms with no magnetic moment.

ing sequence AcB, where uppercase letters denote the Ta atom and lower case letters represent the stacking of carbon atoms. Ta_4C_3 ($n = 3$), therefore, is obtained as a Ta_2C layer, AcB, with an extra Ta atom on each surface – that is, Cb[AcB]aC. Note that this is the only structure in which two Ta atoms on either surface have the same stacking. On the other hand, Ta_3C_2 ($n = 2$) has a stacking sequence of AcBaC, so the symmetry of the AcB layer is broken due to the odd number of layers. This suggests that the differences in the charge distribution we find in Figs. B.2(d–f) are largely governed by the stacking sequence of the CTa_6 units—a degree of freedom unique to the MXene phases. Such differences in the electron distribution near E_F due to the asymmetric stacking are also visible in the shape of the DOS [shaded region in Fig. B.2(b)]. The charge is concentrated at the surface for Ta_3C_2 and Ta_4C_3, consistent with the higher partial density of states for the Ta surface atoms [Figs. B.2(b–c)].

The large number of Ta d-states at E_F and the sensitivity of the electronic structure to the sheet dimensionality suggest the possibility of stable long range magnetic spin configurations. We therefore performed a series of spin-polarized calculations with two different starting configurations, corresponding to ferromagnetic (FM), ferrimagnetic (FiM), and antiferromagnetic (AFM) spin order on the Ta sites to systematically explore the possible magnetic orders with respect to n. We carried out unconstrained-spin density calculations to find the stable magnetic ordering (Fig. B.3) and compared the total energy of those states to that of the non-spin-polarized case. Given the limited ability of DFT to fully capture correlation effects, including transition metal ions with partially filled d shells, we now add the Hubbard U correction to the standard PBEsol

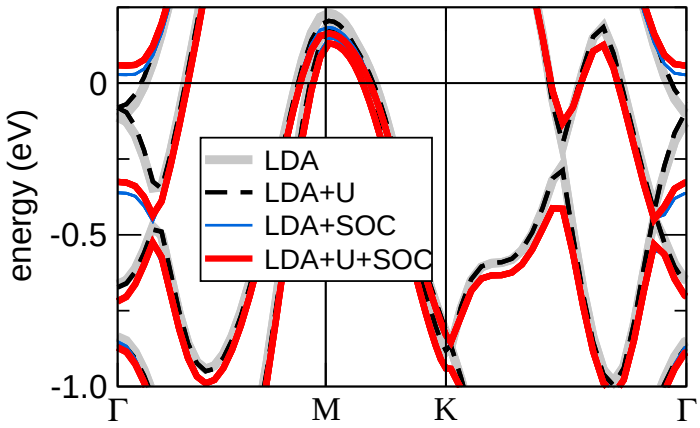

Figure B.4: LDA band structure for Ta_2C without spin or correlation (gray, thick lines), using LDA+U with U=1eV (black, broken lines), with spin-orbit coupling (SOC) (blue, solid lines), and with SOC using LDA+U with U=1 eV (red, thick lines).

(PBEsol+U) and LSDA (LSDA+U) functionals [178]. Since it was recently suggested that Ta-containing MAX phases are weakly correlated [179], we explored $U < 3.0$ eV.

Figure B.3 shows the change in total energy of the spin-polarized states computed with the LSDA+U functional compared to the non-magnetic (NM) case. The change in energy is calculated as a function of U by $\Delta E(U) = [E_M(U) - E_{NM}(U)]/N$, where $E_M(U)$ and $E_{NM}(U)$ are the total energies of the magnetic and non-magnetic states, respectively, for a given U value. N is the number of atoms per unit cell.

In most cases, the magnetically ordered configurations are lower in energy than the NM state. For $n = 1$, the FM state could not be stabilized with LDA calculations, and weak magnetic ordering is observed in the metastable AFM state [Fig. B.3(a)]. As the dimensionality increases, the AFM case becomes more stable. Our main results are summarized in Table B.2, where the values in parentheses specify the U values above which the specific magnetic ordering becomes stable. For Ta_3C_2, both LSDA+U and PBEsol+U calculations predict a FiM configuration, whereas an AFM ordering is predicted for Ta_4C_3, but only with the LSDA+U exchange-correlation functional (Table B.2). Note that in Ta_4C_3 no ordered magnetic phase was found to be stable with either PBEsol and PBEsol+U.

Table B.2: Summary of the stable spin polarized ground states for the $Ta_{n+1}C_n$ MXene phases using different exchange-correlation functionals with and without a Hubbard U correction. Notations (schematics) for the magnetic states are given in the caption (insets) to Fig. B.3.

	Ta_2C	Ta_3C_2	Ta_4C_3
LDA	NM	AFM	AFM
LDA+U	AFM ($U > 0.5$)	FiM ($U > 1.6$)	AFM
PBEsol	AFM	AFM	NM
PBEsol+U	FM ($U > 0.1$)	FiM ($U > 0.9$)	NM

In all cases, the surface Ta atoms are spin polarized in the same direction for FiM order and in opposite directions for AFM. The Ta atoms in the inner layers are weakly spin-polarized in the direction opposite to the surface Ta atoms in both the FiM and AFM configurations, with the exception of the AFM configuration of Ta_3C_2, which is constrained by symmetry. The addition of U generally has a small effect on the electronic structure, leading to a slight shift of the Ta d-bands uniformly to higher energies.

We now evaluate the effect of spin-orbit coupling (SOC) on the band structure with respect to n. Here we find that SOC splits the bands near the Fermi level, manifesting as a shift in energy, especially for the highest occupied Ta d-bands. It has the strongest effect on Ta_2C (Fig. B.4), where the band splitting is prominent and pushes one of the formerly occupied degenerate bands below ≈ -0.11 eV to above E_F, driving a transition from a band structure with two band crossings to one with Fermi surface with small electron and hole pockets. Including electron correlation (+U) within LDA and LDA+SOC causes only a small energy shift to those states (Fig. B.4). For Ta_2C, the spin-orbit splitting at the top of the valence band at Γ (Δ_{SO}=269 meV) is comparable to that observed in GaAs (Δ_{SO}=342 meV)[180], and more than 3 orders of magnitude larger than graphene ($\Delta_{SO} =\sim 0.05$ meV)[181]. The result is that this double band crossing near Γ shifts to a single linear band crossing as one band splits off and is pushed above the Fermi level. This shift toward a more semi-metallic electronic state should be experimentally observed in its transport properties, which are predicted to be fundamentally different from the $n = 2$ and $n = 3$ MXenes.

In summary, we have shown that the Ta-based 5d electronic structure is sensitive to dimensionality. All explored phases exhibit correlation stabilized magnetic order that is not found in the bulk MAX phase structures. The LSDA+U method stabilizes the ferromagnetic ordering in the case of $n = 2$, and for $n = 1$ spin-orbit coupling shifts the electronic band structure with a transition from a two-band to a nearly filled single band. In these 2D MXenes, the electronic structure is controlled by the stacking of the CTa_6 octahedra and the states derived from the surface Ta atoms. Tailoring the electronic structure could therefore be achieved through end group functionalization of the surfaces of the MXene sheets. This opens up possibilities for engineering a class of tunable functional 2D materials. We conjecture that one could maintain a band structure with linear graphene-like crossings where the Fermi surface is nearly completely controlled by a single band – like that observed in Ta_2C – through epitaxial strain engineering. Overall, the Ta-containing graphene-like carbides show great promise as functional 2D materials that can be synthesized in different dimensionalities, leading to a range of stacking sequences and stoichiometries that offer a variety of electronic and magnetic behaviors.

B.2 $Ti_5Al_2C_3$, A HIGHER-ORDER MAX PHASE

This section consists of two papers, one on the synthesis and characterization of bulk $Ti_5Al_2C_3$, and another comment on the correct stacking sequence for this phase.

B.2.1 A first principles, XRD, and TEM study on $Ti_5Al_2C_3$

Published in: N.J. Lane, M. Naguib, J. Lu, L. Hultman, M.W. Barsoum, "Structure of a new bulk $Ti_5AlC_2C_3$ MAX phase produced by the topotactic trasformation of Ti_2AlC" *Journal of the European Ceramic Society* **32** [12] 3485-3491 (2012).

Abstract

Upon annealing cold-pressed Ti_2AlC, -325 mesh powders, at 1500 °C for 8 h in argon, the resulting partially sintered sample contained 43(%±2) wt.% of the layered ternary carbide $Ti_5Al_2C_3$. Herein, the X-ray powder diffraction pattern of $Ti_5Al_2C_3$ is reported for the first time. Its structure and stoichiometry are confirmed through high-resolution transmission electron microscopy. This phase has a trigonal structure (space group P3) with a unit cell consisting of 3 formula units and cell parameters of a=3.064 Å, c=48.23 Å. The lattice parameters determined through first principles calculations agree reasonably well with the experimentally determined values. At 147.1 GPa, the calculated bulk modulus falls between the bulk moduli of the MAX phases Ti_2AlC and Ti_3AlC2. The transformation from Ti_2AlC to $Ti_5Al_2C_3$ is topotactic.

Introduction

Binary, early transition metal carbides possess a number of desirable properties including high-temperature stability, high melting point, high hardness, and low compressibility relative to metals; however, their applications are limited because they are brittle, difficult to machine, and highly susceptible to thermal shock. The Ti–Al–C system includes ternary phases that possess ceramic-like properties of their binary relative, TiC, while overcoming many shortcomings of the latter by acquiring some of the more favorable properties of metals. Most notably, two of the ternaries in the system are part of a family of nanolaminated compounds known as MAX phases, which have the general formula $M_{n+1}AX_n$ ($n = 1 - 3$) where M is an early transition metal, A is an element from groups IIIA or IVA, and X is C or N. They can be further characterized according to their value of n: "2 1 1" for $n = 1$, "3 1 2" for $n = 2$, and "4 1 3" for $n = 3$.

The synthesis of Ti_2AlC was first reported in the 1960s [28], along with some 3 1 2 phases, including Ti_3SiC_2 [48]. Several decades later in 1994, Pietzka and Schuster synthesized Ti_3AlC_2 for the first time and found that it was isostructural with Ti_3SiC_2 [31]. It was later discovered that, as a class, the MAX phases have unusual yet attractive and sometimes unique combinations of properties, and these phases have since attracted a great deal of interest [16–18, 182]. They are excellent electric and thermal conductors with exceptional thermal shock resistance. While they are elastically quite stiff, they are also relatively soft and readily machinable, with exceptional damage tolerance [16, 17, 20]. Some are creep and fatigue resistant [23–25]. Of the > 60 MAX phases known to date, Ti_2AlC and Ti_3AlC_2 are particularly significant when considering the transition of MAX phases from the laboratory to practical applications. They have perhaps the greatest potential for commercialization due to their excellent oxidation resistance and the accessibility of their starting materials, which are relatively inexpensive and readily available [26, 55].

In the Ti–Al–C system, three ternary compounds have been reported to date. Two of them, Ti_3AlC_2 and Ti_2AlC, are MAX phases, which crystallize in a hexagonal lattice (space group $P6_3/mmc$) composed of M-X octahedra stacked between layers of the A element. Another ternary carbide, Ti_3AlC, has a structure similar to oxide perovskites, with Ti and Al forming an FCC-like structure and C in the body-centered octahedral hole [183, 184].

Since Ti_2AlC and Ti_3AlC_2 are two of the more promising MAX phases for industrial and commercial uses, the ability to fine-tune their stoichiometry and crystal structure (for example, by altering their stacking sequences) would open more opportunities for engineering their properties. In the present study, we report on the synthesis of a new MAXphase, $Ti_5Al_2C_3$. Its stacking sequence can be considered as alternate layers of Ti_2AlC and Ti_3AlC_2. This phase has previously been reported by Lin *et al.* as an "intergrown structure" in Ti_2AlC bulk samples [185] and by Wilhelmsson *et al.* in Ti_2AlC thin films [81]. In both cases, however, it was only observed in small domains through transmission electron microscope, TEM, analysis. Consequently, its X-ray diffraction, XRD, patterns are unknown.

Herein, we show that $Ti_5Al_2C_3$ can be synthesized in bulk. We determine its long-range crystal structure, stacking, and stoichiometry through XRD and TEM analysis. We also perform first principles calculations to determine its ground state parameters and its electronic structure.

Experimental details

The sample was made by heating Ti_2AlC powders that were commercially obtained (3-ONE-2,Voorhees, NJ, >92 wt.% purity; particle size $< 44\mu$m, *i.e.*,-325 mesh) in an alumina tube furnace under flowing argon, Ar, at 10°C/min to 1500°C. The powders were then held at temperature for 8 h. After cooling to room temperature, powders were obtained from the resultant partially sintered bulk piece (relative density of ≈80%) using a titanium nitride coated milling bit.

XRD patterns were obtained with a powder diffractometer (Rigaku Smartlab, Japan) using Cu Kα radiation and a step scan of 0.02°, with 1 s per step. Si powderwas added to some samples as an internal standard to calibrate the diffraction angles and the instrumental peak broadening. Rietveld analysis was performed using Material Analysis by Diffraction/Reflectivity (MAUD) software [155, 156] assuming the presence of Ti_2AlC, Ti_3AlC_2, Si and a proposed phase $Ti_5Al_2C_3$ [Fig. B.7(a)]. The phase fractions, background, lattice parameters (except for Si), thermal factors, and symmetry-constrained atomic positions of Ti_2AlC and Ti_3AlC_2 were refined using the least-squares refinement implemented in MAUD.

Samples for TEM observation were collected by a holey carbon grid after suspending the powder in ethanol. The TEM used (FEI Tecnai G2 TF 20 UT) had a 0.19 nm point resolution and 200 kV working voltage. The crystal structure of the new phase was investigated by selected area electron diffraction (SAED) and high resolution TEM (HRTEM), together with image simulation.

Ab initio calculations, based on density functional theory (DFT), were performed using the Perdew-Burke-Eruzerhof (PBE) generalized gradient approximation (GGA) [98] with a plane wave cutoff of 400 eV. The total energy was converged to <0.02 meV/atom with a 13 × 13 × 2 Γ-centered k-point grid, as implemented in the VASP software. For Ti, the semi-core 3p states were treated as valence electrons. Computations of the electronic properties and structural parameters were carried with calculations of the total density of states (DOS) and energy minimization through the relaxation of atomic positions and c/a ratio for a range of fixed volumes. The equilibrium volume and bulk moduli were obtained with the modified Morse equation of state fit of the total energy as a function of volume [186].

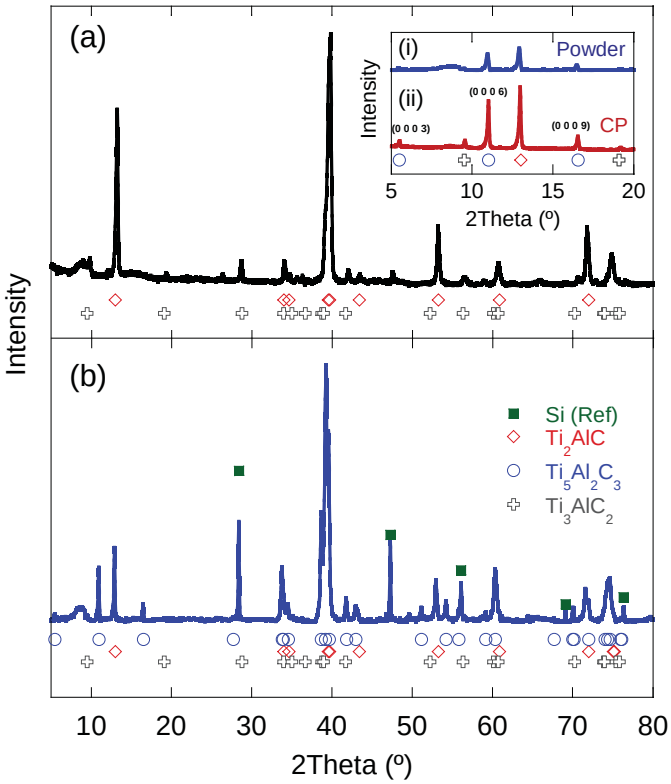

Figure B.5: XRD patterns of Ti_2AlC powder sample, (a) as received and (b) after heat treatment. Inset shows region between $2\theta = 5°$ and 20° for the sample after heat treatment, indexing the (0003), (0006) and (0009) peaks for $Ti_5Al_2C_3$: (i) sample in powder form, and (ii) cold-pressed pellet (CP), where both patterns are normalized to the Si peak at $2\theta = 28.5°$ (not shown). Markers show peak positions for Si (green squares), Ti_2AlC (red diamonds), $Ti_5Al_2C_3$ (blue circles), and Ti_3AlC_2 (gray crosses). XRD patterns are shifted to accommodate markers.

Results and discussion

The XRD patterns of the Ti_2AlC powder sample before and after heat treatment is shown in Figs. B.5(a) and (b), respectively. Before heat treatment [Fig. B.5(a)], the sample was predominantly single phase Ti_2AlC (red diamond markers), with a small amount (∼9 wt.%) of Ti_3AlC_2 (gray crosses). After heat treatment [Fig. B.5(b)], additional peaks appeared corresponding to the additional phase we identified as $Ti_5Al_2C_3$ (blue circles). The peaks at $2\theta = 5.6°$, 11.0° and 16.5° correspond to the (0 0 0 3), (0 0 0 6) and (0 0 0 9) peaks for $Ti_5Al_2C_3$, respectively. From these distinct peaks that cannot be accounted for by Ti_2AlC or Ti_3AlC_2, it is readily apparent that the sample contains a substantial amount of this new phase.

To emphasize and confirm the assignment of the (0 0 0 l) peaks, we collected patterns from discs produced by cold pressing, CPing, the heat-treated powders at loads corresponding to a stress of ≈1GPa. The inset of Fig. B.5 shows the $2\theta = 5 - 20°$ region of the XRD pattern from (i) the powder sample, and (ii) the cold-pressed sample. The two patterns are normalized to the (1 1 1) peak for Si at $2\theta = 28.5°$ (not shown). The (0 0 0 3), (0 0 0 6), and (0 0 0 9) peaks of $Ti_5Al_2C_3$ are labeled, and their

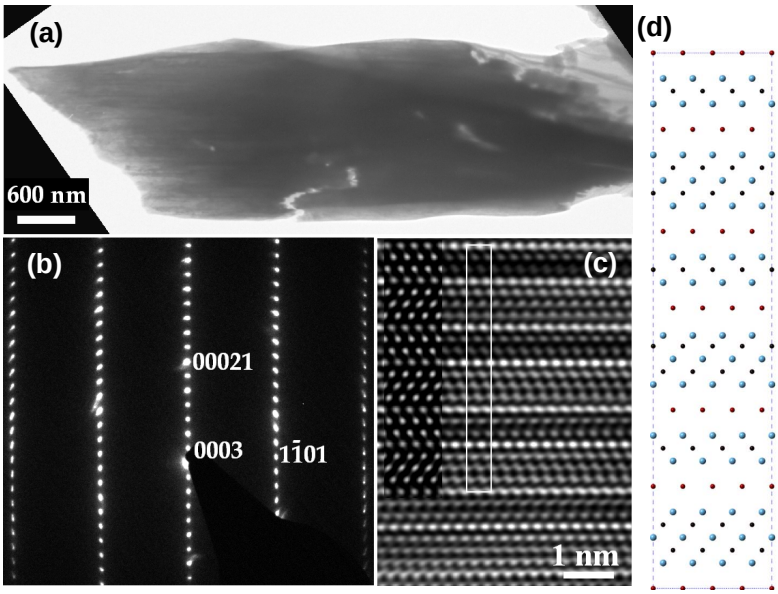

Figure B.6: High-resolution TEM (HRTEM) image of a heat-treated $Ti_5Al_2C_3$ sample: (a) large grain of $Ti_5Al_2C_3$, (b) selected area electron diffraction (SAED) pattern shown parallel to the [11$\bar{2}$0] direction, (c) HRTEM image of the [11$\bar{2}$0] axis projection showing $Ti_5Al_2C_3$ stacking, and (d) illustration of the [11$\bar{2}$0] plane for comparison with highlighted region in (c).

positions are marked by blue circles. A clear increase in the intensity of these peaks, and not others, with CPing confirms assigning these peaks to the 0 0 0 l planes. The MAX phases are layered and cold pressing orients the basal planes parallel to the loading direction. Note that the peak at 13.0° is the (0 0 0 2) peak of Ti_2AlC, which also increases with CPing.

Rietveld refinement with MAUD gave 43(±2) wt.% $Ti_5Al_2C_3$ for the sample after heat treatment, with 49(±2) wt.% Ti_2AlC, and 7(±2) wt.% Ti_3AlC_2. The lattice parameters of $Ti_5Al_2C_3$ are $a = 3.064(2)$ Å, $c = 48.23(2)$ Å and its space group is P3m1 (156) *

The structure was confirmed by HRTEM (Fig. B.6), where there are alternate layers containing 2 and 3 Ti layers, sandwiched between Al layers, with C filling the octahedral sites in between Ti layers, in agreement with the simulated image of the [11$\bar{2}$0] zone axis projection. The space group of this phase is different from that of Ti_3AlC_2 and Ti_2AlC due to the break in symmetry caused by the alternating stacking sequence. This structure has the same stacking sequence observed in the TEM in Ref. [81].

The HRTEM image is also consistent with the equilibrium structure from first principles calculations. The full structure is shown in Fig. B.7(a), compared to the structures of Ti_3AlC_2 [Fig. B.7(b)] and Ti_2AlC [Fig. B.7(c)]. The stacking sequence for the Ti and Al atoms are shown next to the structures. A unit cell of $Ti_5Al_2C_3$ consists of three formula units with a total of 6 Al layers, where every other region between the Al layers is filled with one Ti–C octahedra, as seen in Ti_2AlC, and rest contain two Ti–C octahedra, as in Ti_3AlC_2. In order to accommodate this structure, the stacking

*Note: it has since been discovered that a higher-symmetry space group, $R3m$, can be used to represent the same stacking.

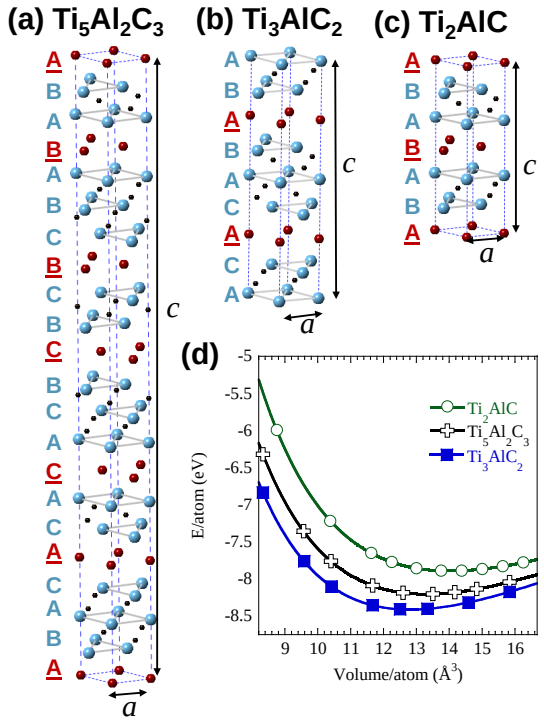

Figure B.7: Crystal structure and stacking sequence of (a) $Ti_5Al_2C_3$, (b) Ti_2AlC, and (c) Ti_3AlC_2. (d) Volume vs. energy plot for the three structures in (a)-(c), showing values determined from first principles calculations (solid data points) and the MO88 equation of state fit (lines).

sequence of the Al layer must shift every two layers. Fig. Fig. B.7(d) shows the volume vs. energy plot determined by first principle calculations, as well as the equation of state fits. The bulk modulus, B, determined through the fit is highest for Ti_3AlC_2, which is apparent in Fig. B.7(d) from its higher curvature. The bulk moduli for Ti_2AlC, Ti_3AlC_2, and $Ti_5Al_2C_3$ are listed in Table 1, where B varies in the order Ti_2AlC<$Ti_5Al_2C_3$ <Ti_3AlC_2. The lattice parameters determined by first principles calculations agree well with the experimental values from XRD (Table B.3).

The calculated electronic density of states is shown in Fig. B.8, where 0 corresponds to the Fermi level. All DOS units are per number of atoms in the unit cell in Fig. B.7(a). The density of states is quite similar to that of Ti_2AlC and Ti_3AlC_2 [187, 189, 190], where its conductivity is predominantly due to the Ti d orbitals. Since the stoichiometry is 2.5:1:1.5 (effectively that of a MAX phase with $n = 1.5$), it should be expected to have electronic properties that fall somewhere between Ti_2AlC and Ti_3AlC_2.

Since both Ti_2AlC and Ti_3AlC_2 are generally synthesized at temperatures between 800 and 1500°C [37, 55, 82, 145, 191], the phase produced through heat treatment is highly dependent on the elemental ratios of the starting powders. In the sample investigated in this study, we found regions where $Ti_5Al_2C_3$ was present in the same grain as Ti_3AlC_2 (Fig. B.9). It is therefore reasonable to assume that the formation of $Ti_5Al_2C_3$ is topotactic, most likely occurring through outward diffusion of Al and the re-ordering of TiC octahedra in Ti_2AlC. A phe-

Table B.3: Lattice parameters of $Ti_5Al_2C_3$, Ti_2AlC, and Ti_3AlC_2 phases in powder sample determined from XRD and calculated lattice parameters (a and c, bulk moduli (B), and density determined from first principles calculations.

	$Ti_5Al_2C_3$		Ti_2AlC		Ti_3AlC_2	
	Exp.	Calc.	Exp.	Calc.	Exp.	Calc.
a (Å)	3.064	3.068	3.063 (3.051[a])	3.067	3.060 (3.0753[d])	3.083
c (Å)	48.23	48.45	13.645 (13.637[a])	13.75	18.661 (18.578[d])	18.66
B (GPa)	-	147.1	(186e)	136, (166[b])	226[f]	156, (190[c])
Density (g/cm^3)	-	4.13	-	3.99	-	4.21

[a] Ref. [37].
[b] Ref. [187].
[c] Ref. [151].
[d] Ref. [31].
[e] Ref. [33].
[f] Ref. [188].

nomenon that could help explain the formation of $Ti_5Al_2C_3$ is a so-called gradient structure, reported in a hot-pressing study of the Ti-Al-C system by Mei *et al* [192]. In that study, various compositions of Ti, Al, and C powders were hot pressed at 1500°C for 60 min under 30MPa. Although they did not report any $Ti_5Al_2C_3$ phase, they found that the samples contained an inhomogeneous structure throughout their volumes where most of the phases were Al-deficient. Moreover, the Ti content was constant along the axial direction, whereas the Al distribution increased continuously from the hot pressed surface to the center of the sample. As a result, the relative volumes of TiC, Ti_3AlC_2, and Ti_2AlC varied gradually. The evaporation of Al was considered a fundamental reason for such a formation, since Al has a higher vapor pressure than Ti at 1500°C [193].

Here, we postulate that the evaporation of Al from Ti_2AlC results in a higher Ti:Al ratio, causing $Ti_5Al_2C_3$ to be more thermodynamically favorable. It is reasonable to assume that further heating would convert $Ti_5Al_2C_3$ to Ti_3AlC_2 and ultimately to TiC_x.

The results presented herein provide evidence for a new bulk MAX phase, $Ti_5Al_2C_3$ – with a stacking sequence combining that of Ti_3AlC_2 and Ti_2AlC and properties similar to the two phases – that exists in bulk,

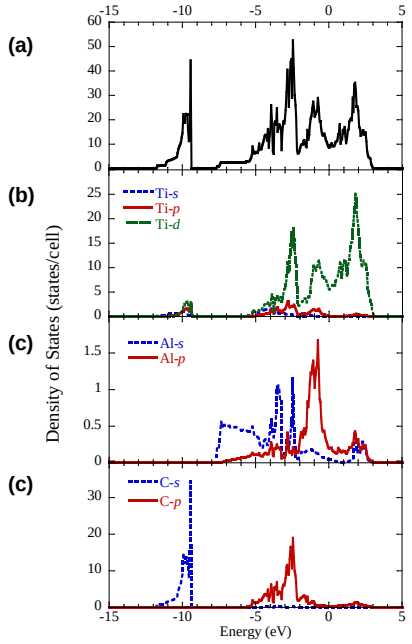

Figure B.8: Electronic density of states as determined by first principles calculations, showing (a) total density of states, and partial density of states for (b) Ti, (c) Al, and (d) C. The Fermi level is located at 0 eV.

formed when Ti_2AlC powders are heated to 1500°C for 8 h. Work to explore the effect of annealing times and temperatures on the microstructure and atomic ordering of ternary phases in the Ti–Al–C system would be needed

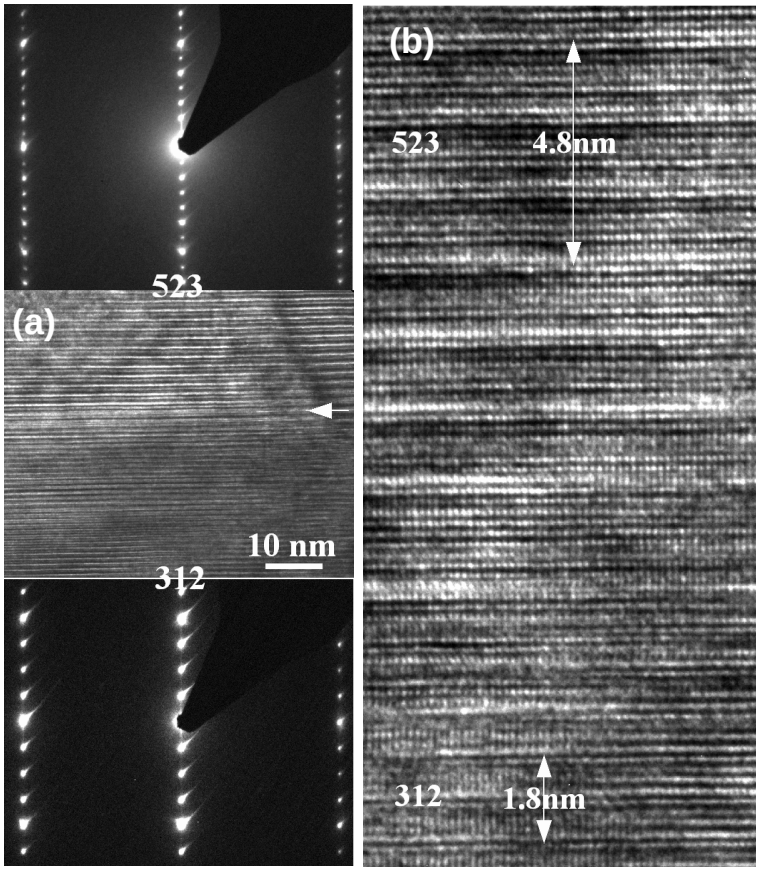

Figure B.9: HRTEM image of a grain containing both $Ti_5Al_2C_3$ and Ti_3AlC_2 showing (a) lower-resolution and (b) higher-resolution TEM micrographs with respective unit cells indicated [the interface between the two phases is indicated by an arrow in (a)] with corresponding SAED patterns from the $Ti_5Al_2C_3$ ("523") and Ti_3AlC_2 ("312") regions shown above and below figure (a), respectively.

to understand the kinetics and mechanisms for the formation of the $Ti_5Al_2C_3$ phase.

Conclusions

A new bulk ternary MAX phase, $Ti_5Al_2C_3$, was synthesized in bulk form for the first time by heating Ti_2AlC under Ar for 8 h at 1500°C. The transition from Ti_2AlC to $Ti_5Al_2C_3$ is topotactic. The crystal structure of $Ti_5Al_2C_3$ was found to be trigonal (P3m1) [†], with *a* and *c* parameters of 3.067Å, 48.16Å, respectively. The stacking of atomic layers in $Ti_5Al_2C_3$ can be considered as a combination of that in Ti_2AlC and Ti_3AlC_2.

Note added in proof

This paper was submitted on Jan 16, 2012. As our paper was being reviewed, we discovered a paper by Wang *et al*. [83] that was submitted

[†]Note: it has since been discovered that a higher-symmetry space group, *R*3*m*, can be used to represent the same stacking.

to *J AmCer Soc* on Feb. 7, 2012, accepted a week later and available online shortly thereafter. We note that our paper takes precedence as the original report because it was submitted first. More importantly, the paper by Wang *et al*. suggests a structure that is different from that reported herein.We explored the differences between the two possible structures and made the following observations:

(i) First principles calculations on the total energies of the unit cells show that the configuration reported herein has a lower equilibrium energy (higher relative stability) compared to that reported in Ref. [83], with an energy difference of ∼0.06 eV/atom.

(ii) In all other known $M_{n+1}AX_n$ phases with $n > 1$, the M–X layers have a stacking sequence corresponding to $BcAbC$, where the upper case is for the M atoms and the lower case is for the X atom. In the proposed structure (Fig. 3) in Ref. [83], the Ti-C layers have a $BaCaB$ stacking. This has never been observed in any structure in the MAX phase family. Furthermore, the XRD and (not atomically resolved) HRTEM data in Ref. [83] cannot verify the $BaCaB$ stacking, and contain insufficient information to permit a structure determination.

(iii) It has been previously noted [66] (see also the review in Ref. [82]) that in order to preserve the correct stacking in theMAX phases with 5:2:3 stoichiometry, the $P6_3/mmc$ symmetry must be broken and the crystal structure must be indexed with a hexagonal lattice with 3 formula units. The (0 0 0 n) peaks are then indexed by (0 0 0 3n), where n is the l index for a cell containing one formula unit. In the suggested structure in Ref. [83], they are incorrectly indexed by (0 0 0 2n).

There are other reasons why the structure given by Wang *et al*. is most probably incorrect. For the sake of brevity, these are not discussed here, but in a separate paper to be published elsewhere

B.2.2 A comment on the stacking sequence in Ti_5AlC_2

Published in: N.J. Lane, M. Naguib, J. Lu, P. Eklund, L. Hultman, M.W. Barsoum, "Comment on '$Ti_5Al_2C_3$: A new ternary carbide belonging to MAX phases in the Ti-Al-C system' " *Journal of the American Ceramic Society* **95** [10] 3352-3354 (2012).

The $M_{n+1}AX_n$ phases ($n = 1$, 2 or 3, M = transition metal, A = A-group element, X = carbon or nitrogen) are usually classified into three groups based on their n values, i.e., "211" for $n = 1$, "312" for $n = 2$, etc. In addition, there is also a category of "intergrown phases" such as the "523" and "725" phases, with alternating half-unit-cell layers of "211" and "312" (="523") or "312" and "413" (="725"). These phases were first reported in 2004 in the Ti–Si–C system by Palmquist *et al* [66]. Since then others were discovered as minority phases in bulk samples [**?**] and thin films [65, 81, 194**?**]. Palmquist *et al* [66] noted that the alternating stacking of even and odd M layers induces a lateral translation of the A position, breaking the $P6_3/mmc$ symmetry of the regular MAX phases. Said otherwise, the A atoms are not positioned above each other until after three repetitions. It follows that the c axis of a $M_5A_2X_3$ phase has to be three times the average of the M_2AX and M_3AX_2 c-axes. This description has been echoed in several other papers. [79, 82]. A complete structure description was, however, not available until we very recently synthesized bulk samples with a high fraction of $Ti_5Al_2C_3$ which, in turn, permitted a complete structure determination [8]. We concluded that the space group was $P3m1$ and the crystal structure indeed consists of three formula units, with a c lattice parameter of 48.23 Å.

Very recently, Wang *et al*. [83] reported on $Ti_5Al_2C_3$ prepared by hot pressing Ti, Al, and C powders, and suggested a structure with $P6_3/mmc$ space group symmetry. It is important to note at the outset, that neither the X-ray diffraction (XRD) nor transmission electron microscopy (TEM) results presented by Wang *et al*. are sufficient to verify their proposed stacking sequence. Their hypothetical structure [see Fig. 1(c)] has Ti_1 and Ti_2 at Wyckoff position $4f$, Ti_3 at $2d$, Al at $4e$, C1 at $2a$, and C_2 at $4e$ with lattice parameters $a = 3.038$ Å and $c = 32.261$ Å. The purpose of this comment is to make the case that this structure is most probably incorrect.

Our evidence against $P6_3/mmc$ symmetry is multifold. First, in Wang *et al*.'s suggested structure, the Ti-C layers appear with a $BaCaB$ stacking [Fig. B.10(c)], where the upper case is for the Ti and the lower case is for the C atoms. This stacking has never been observed in any $M_{n+1}AX_n$ phase with $n > 1$. In all known 312 and 413 structures, the M–X layers have a stacking sequence of $BcAbC$.

Second, Fig. B.10(a) shows an atomically resolved TEM image (beam along $[11\bar{2}0]$ zone axis) and Fig. B.10(b) shows the corresponding selected area electron diffraction pattern (SAED) reproduced from Ref. [83]. The stacking suggested by Wang *et al*. [Fig. 3, re-plotted herein as Fig. B.10(c)] does not correspond to the experimentally observed stacking, which instead matches our structural model [Fig. B.10(d)]. Third, SAED simulations demonstrate that in [0001] and $[1\bar{1}00]$ zone axes (not shown) there is not much difference between the two structures. However, in the [11 =20] zone axis, there is an obvious difference [compare Figs. B.10(e) and (f)]. In contradiction to the experimental SAED pattern [Fig. B.10(b)], in the simulated pattern for the structure suggested by Wang *et al*. [Fig. B.10(e)] there are more $(1\bar{1}0l)$ reflections and mirror symmetry. Simulation of our structure [Fig. B.10(f)], on the other hand, has fewer reflections and does not show mirror symmetry, which is consistent with our experimental SAED pattern [Fig. B.10(b)].

Fourth, simulations of XRD patterns for each of the structures show significant differences in both peak position and intensity [Fig. B.10(g)]. The experimental XRD pattern [blue

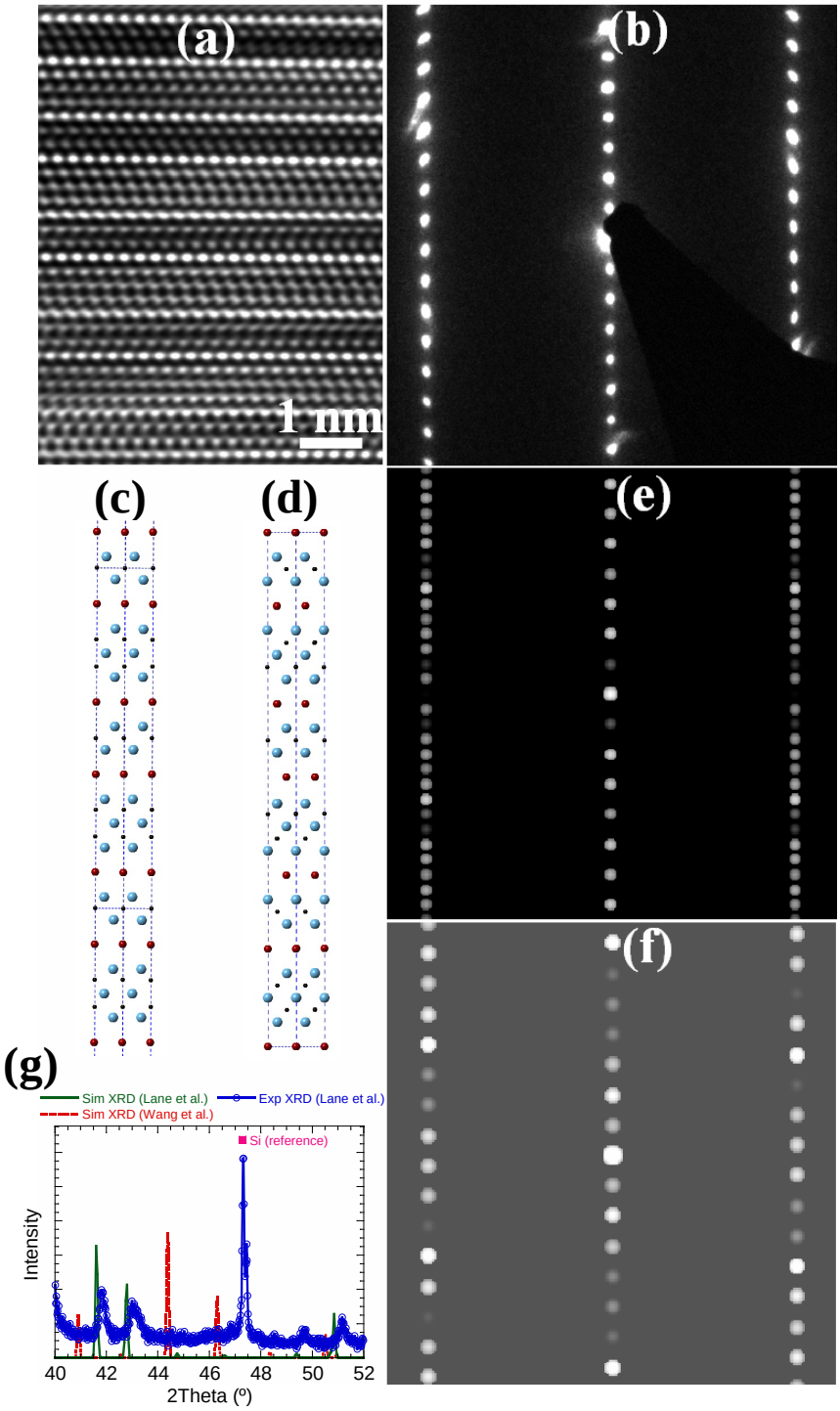

Figure B.10: (a) Experimental atomically resolved TEM image and (b) SAED pattern, both from Ref. [8]. (c) Suggested stacking of Wang *et al.*, and (d) stacking in our structural model [8]. (e) and (f) are simulations of SAED patterns corresponding to (c) and (d), respectively. All are in the $[11\bar{2}0]$ zone axis. (g) Simulated and experimental XRD patterns for Ti_5AlC_2: Simulated XRD pattern of structure from Ref. [8] (green solid), the simulated pattern of the structure suggested by Wang *et al.* [83], (red dashed), and experimental XRD pattern for sample containing 42 wt% $Ti_5Al_2C_3$ from Ref. [8] (blue lines with open circles).

lines with open circles in Fig. B.10(g)] has significant peaks that are only predicted in the simulated XRD pattern for our structure [green solid pattern in Fig. B.10(g)] but not for the simulation of Wang *et al*.âĂŹs structure [red dashed pattern in Fig. B.10(g)], such as the peaks at 41.7 and 42.8°. Even more importantly, the structure suggested by Wang *et al*. should exhibit a large peak at 44.35°, which is not observed in either experimental study [8, 83]. The XRD pattern reported by Wang *et al*. is thus incompatible with their proposed structure.

Note that the XRD pattern we published in Ref. [8], and partially reproduced in Fig. B.10(g), has multiple prominent $Ti_5Al_2C_3$ peaks, whereas the one reported by Wang *et al*. shows only one peak – at 2θ of 11° – that can be attributed to $Ti_5Al_2C_3$. It follows that the Rietveld refinement they report to have carried out must be either invalid or, at the very least, questionable.

Lastly, we performed first-principles calculations based on density functional theory to calculate the total energies of each of the unit cells. The Perdew-Burke-Eruzerhof (PBE) generalized gradient approximation (GGA) [98] functional was used, with a plane wave cutoff of 400 eV. The total energy was converged to $<$ 0.02 eV/atom with a $11 \times 11 \times 2$ Monkhorst-Pack-type Γ-centered k-point mesh, as implemented in the VASP software. The equilibrium volume and bulk moduli were obtained with the modified Morse (MO88) equation of state fit of the total energy as a function of volume [186]. The structure suggested by Wang *et al*. was found to be the less stable of the two, with an energy difference of ∼0.06 eV/ atom.

In conclusion, the evidence presented by Wang *et al*. is insufficient to confirm their structure with space group $P6_3/mmc$. Our experimental and first-principles calculations provide evidence for the $P3m1$ space group. Needless to add, if anybody can provide XRD, atomically resolved TEM and SAED results that agree with Wang *et al*.âĂŹs hypothetical structure we would gladly accept that there are two polymorphs for $Ti_5Al_2C_3$.

B.3 FIRST-PRINCIPLES CALCULATIONS ON THE $(11\bar{2}1)$ TWIN AS A DISLOCATION WALL

Published in: N.J. Lane, S.I. Simak, A. S. Mikhaylushkin, I. A. Abrikosov, L. Hultman, M.W. Barsoum, "A first principles study of dislocations in HCP metals through the investigation of the $(11\bar{2}1)$ twin boundary" *Physical Review B* **84**, 184101 (2011).

Abstract

Herein we use first principles calculations to study the energy of the $(11\bar{2}1)$ twin boundary in Zr, Zn, Mg, Ti, and Be. This boundary is important for understanding the microyielding and damping of hexagonal close packed metals. The $(11\bar{2}1)$ twin boundary is unique in that it is comprised of – and can form by the glide of – basal dislocations nucleating at every c-lattice parameter. The effect of the number of atoms between boundaries on the boundary energy, and the resulting lattice strains of the relaxed structures, are quantified. It is shown that the energies obtained converge within 32-64 atoms/supercell. The structures with higher second-order elastic constant term, c_{44}, also have higher boundary energies. We further show that the critical resolved shear stresses of the basal dislocations at 0 K, which make up the $(11\bar{2}1)$, twin are so low as to be below the threshold of the first principles calculations.

Introduction

Hexagonal metals (HM) have been studied for decades due to their technological importance. While their mechanisms for plastic deformation under high strains are widely accepted, their low-strain ($\epsilon < 1\%$) behavior has, until recently, not been very well understood. The deformation of HM under low strains is a crucial piece of the deformation puzzle for HM, especially when considering phenomena such as microyielding and damping. A breakthrough toward understanding the early deformation of HM came about recently when we showed that they are kinking nonlinear elastic (KNE) solids [195–197]. Macroscopically, KNE solids are characterized by the formation of fully, and spontaneously, reversible closed hysteresis stress-strain loops. The size of these loops, which corresponds to the energy dissipated per unit volume, scales with the maximum applied stress squared and is a strong function of grain size.

It is currently postulated that the deformation mechanism that leads to these characteristic stress-strain loops involves the nucleation, growth, and annihilation of incipient kink bands (IKBs) [198]. IKBs [Fig. B.11(a)] are concentric dislocation loops that nucleate and grow under an applied load, and they are spontaneously annihilated when the load is removed. A sufficient condition for a solid to be KNE is plastic anisotropy, where the dislocations are confined to two dimensions – usually the basal planes in hexagonal metals. Characteristics that often lead to this include a high c/a ratio and low c_{44}, where c and a are the lattice constants of the unit cell, and c_{44} is the second-order elastic shear constant. Most layered solids, graphite, the $M_{n+1}AX_n$ phases, and mica can also be classified as KNE solids, among others [195, 199–201].

Macro- and microscale models for the deformation of KNE solids have been developed and agree well with experimental results [200, 201]. However, modeling at the atomic level is still lacking. To fully describe the nucleation and growth of IKBs [Fig. B.11(a)], and their transformation to mobile dislocation walls (MDWs) [Fig. B.11(a)], and ultimately kink bands (KBs) [Fig. B.11(b)], it is essential to understand the structure of the MDWs [Fig.

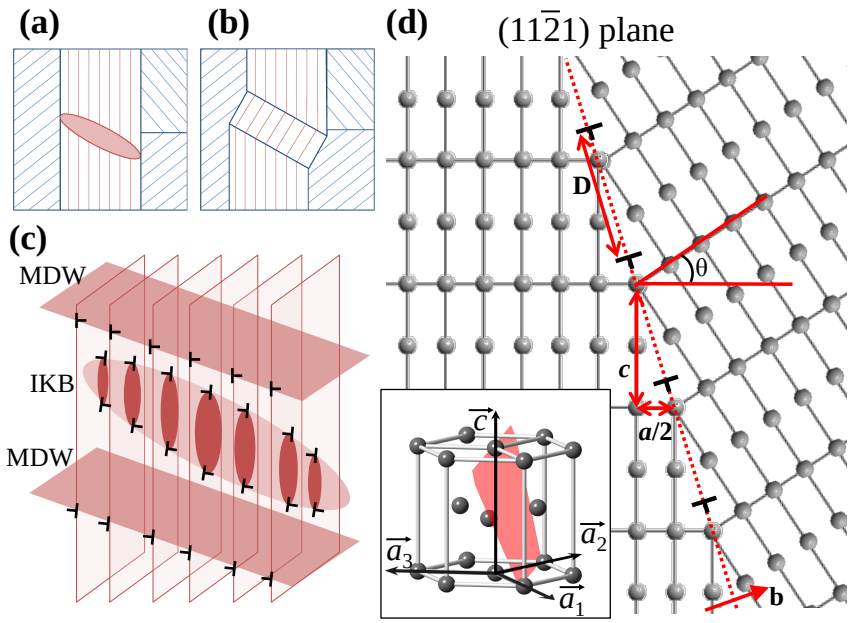

Figure B.11: Schematic of (a) an IKB, (b) KBs, and (c) the dislocation structure of the IKB and MDWs shown in (a). The (1$\bar{1}$00) plane view of the (11$\bar{2}$1) twin is shown in (d), showing the (11$\bar{2}$1) plane (dotted line), the twin angle θ, and edge dislocations every c lattice parameter. Inset (bottom left) shows the (11$\bar{2}$1) plane.

B.11(c)].

The ultimate goal of this work is to model IKBs and their nucleation from an atomistic point of view. The goal of this paper, however, is much more modest and represents a first step towards our ultimate goal, in that we chose to study the atomistics of the (11$\bar{2}$1) twin in HM. The (11$\bar{2}$1) twin is of particular interest because it is a special kink boundary in which a basal plane dislocation is nucleated every c lattice parameter [Fig. B.11(d)]. The (11$\bar{2}$1) twin stands out as the only twin in which all lattice sites are correctly sheared to their twin positions, and lattice shuffles are thus not required [202]. Said otherwise, this twin can form solely by basal dislocation glide. Study of this twin can be traced back to Palache,[203] who reported the twinning features in graphite as (11$\bar{2}$1) twins. A full description of the structure of all twinning elements of this boundary was first provided by Freise and Kelly [204], who identified the (11$\bar{2}$1) twin boundary as a wall of basal dislocations in graphite. Based on Shockley and ReadâĂŹs model for the energy of dislocations along a grain boundary [205], they proposed that the (11$\bar{2}$1) twin was composed of alternating partial dislocations along the boundary. Minonishi et al.[206] also found that the stable relaxed structure at the interface leads to a change in stacking sequence across the boundary [see Fig. B.12(a) and B.12(b)], which renders it effectively shuffleless. Similar results were obtained by Serra and Bacon [207]. Since this kink boundary is, at first approximation, a boundary of edge and screw dislocations, it follows that investigation of the energy and structure of the (11$\bar{2}$1) twin would be useful for enhancing our understanding of dislocations, KBs, and ultimately KNE solids. To our knowledge, the (11$\bar{2}$1) twin has to date not been investigated using first principles calculations in the way it is dealt with herein.

Among atomistic modeling approaches, emphasis is put on first principles, or ab initio, calculations based on full electronic structures for obtaining accurate energies. However, the study of dislocations is not a well-tested territory for ab initio calculations since the supercells needed to adequately account for the long-range elastic fields can be quite large. With a supercell approach, it is difficult to isolate the effects of the dislocations, or defects within the cell, from the surface effects caused by its periodicity. To eliminate surface effects, full periodic boundary conditions must therefore be satisfied, which is only possible if the Burgers vector of the supercell is zero. This approach has been employed for dislocation cores in cubic systems [208–210] and boundary surface energies in Mg [211], but generally the use of *ab initio* calculations to study boundaries and dislocations has still been few and far between. The main reason for this is the computational limitations for the large number of atoms required, along with the boundary conditions, which impose limitations on the special boundary structures that can be simulated.

The purpose of this study is to report on the energy and structure of the $(11\bar{2}1)$ twin in the HMs Mg, Ti, Zn, Zr, and Be, through the supercell approach using ab initio calculations. The effects of supercell size on the boundary energies, for each element, are considered. We also calculate the unit cell parameters and c_{44} and explore how these parameters relate to our results on the twin boundary energies. The critical resolved shear stresses of the dislocations are also estimated to be below the threshold of the ab initio calculations.

Calculations

Ab initio calculations based on density functional theory (DFT) were performed using the projector-augmented wave (PAW) [126, 212] method, as implemented in the VASP code [127–129]. The exchange-correlation function used was the Perdew- Burke-Ernzerhof (PBE) generalized gradient approximation (GGA) [98]. The potential for Zr included 4*s* semicore states. The boundary energy calculations involved calculating the total energy of twinned and perfect crystal structures, with the same number of atoms per unit cell. For each set of calculations, a supercell of the perfect crystal structure, with the required number of atoms, was used to converge the k-point mesh and plane wave cutoff with respect to the c/a ratio, compressibility (bulk modulus), and equilibrium volume relaxation. This led to a plane wave cutoff of 210 eV, 178 eV, 276 eV, 230 eV, and 247 eV for Mg, Ti, Zn, Zr, and Be, respectively, and Γ-centered k-point grids of $25\times25\times25$ for 2 atoms, $9\times9\times9$ for 32 atoms, and $5\times5\times5$ for 64 and 80 atoms. For each structure, the total energy was converged to 10^{-6} eV/cell at fixed volumes while relaxing the c/a ratio and atomic positions. The equilibrium structure and energy were determined by fitting the total energy as a function of volume to the modified Morse equation of state [186].

For the twin boundary calculations, supercells with two $(11\bar{2}1)$ twin boundaries consisting of 32, 64, and 80 atomswere constructed. This was accomplished by shifting the hexagonal coordinates to orthogonal axes, with the x direction normal to the $(11\bar{2}1)$ plane and the y and z directions parallel to the plane. Figure B.12(a) shows a unit cell with 32 atoms, consisting of rows of undistorted hexagonal close-packed (hcp) crystals with 7 atomic planes between the boundaries. Supercells with 64 and 80 atoms (not shown) consist of 15 and 20 atomic planes, respectively, between the boundaries. After slicing the cell along the $(11\bar{2}1)$ plane and mirroring the structure about the plane, a shift from ABAB to ACAC stacking sequence across the boundary is necessary, resulting in the structures shown in Fig. B.12(b) and (c).

The boundary interfacial energy, $E_{(11\bar{2}1)}$,was extracted from the energy of the supercell and the energy of a perfect hcp crystal, assuming:

$$E_{(11\bar{2}1)} = \frac{n\cdot(E_{\text{supercell}} - E_{\text{hcp}})}{2\cdot A} \tag{B.1}$$

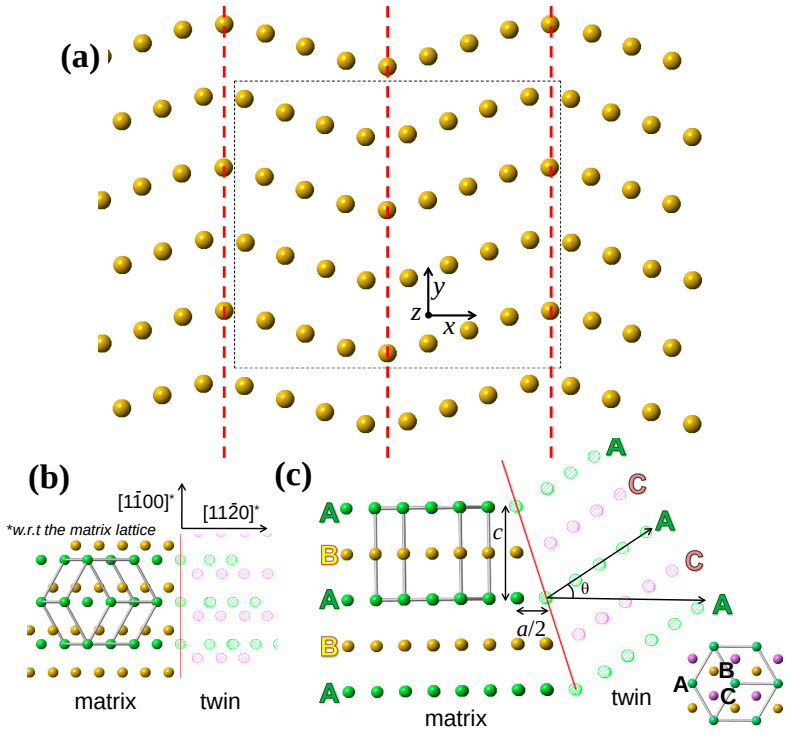

Figure B.12: (a) (1$\bar{1}$00) plane view of relaxed atom positions of repeating structure with two (11$\bar{2}$1) twin boundaries for a 32 atom, unit cell, showing (11$\bar{2}$1) planes (red lines) and the boundaries for the unit cell (dotted lines). (b) The structure of the (11$\bar{2}$1) twin in an hcp material in the ($\bar{1}$126) plane projection. (c) (1$\bar{1}$00) plane projection of the (11$\bar{2}$1) twin, illustrating stacking sequence. Red line represents the (11$\bar{2}$1) plane. For (b) and (c), green, yellow, and pink atoms correspond to A, B, and C stacking, respectively (see inset, bottom right); solid and striped atoms correspond to matrix (ABAB) and twin (ACAC) lattice, respectively.

where n is the number of atoms in the supercell, and $E_{\text{supercell}}$ and E_{hcp} are the energies per atom of the supercell with the twin boundary and the perfect hcp crystal, respectively. A is the area of the boundary given by the cross product of the axes in the x and z directions.

As noted already, and for reasons discussed later herein, our analysis also involves c_{44}. This was calculated by applying lattice distortions and deriving the elastic constants from the stress-strain relationship [215] as implemented in VASP 5.2.

Results and discussion

The results of the interfacial energy calculations on the (11$\bar{2}$1) boundary are summarized in Table B.4 along with values previously calculated using other methods [206, 213, 214] and the twin boundary angle θ. With the exception of Zn, increasing the number of atoms to 64 atoms only changes the energy of the boundary by less than 5% compared to 32 atoms. The larger differences for Zn are most likely due to the distortion from ideal packing indicated by the anomalously large c/a structure. In general, however, the fact that the bound-

Table B.4: Interfacial energies of the $(11\bar{2}1)$ twin boundary in selected hcp metals for different supercell sizes, compared to values obtained in previous work.

Metal	Supercell size	Interfacial Energy (mJ/m^2)		
		Our work	Previous work	θ (degrees)
Mg	32	122.3	147[a], 480[b]	31.7
	64	127.3		
	80	125.6		
Ti	32	238.0	150[a], 180.8[c]	32.4
	64	234.9		
	80	233.2		
Zr	32	235.1	169[a]	32.0
		228.7		
	64	230.7		
Zn	32	229.7	480[b]	27.5
	64	196.3		
Be	32	1034.4	1810[b]	32.4
	64	1073.3		

[a]From Ref. [213], Finnis-Sinclair (FS) embedded-atom potential technique
[b]From Ref.[214], based on pseudopotential theory
[c]From Ref. [206], Lennard-Jones potential fitted to Ti truncated between sixth and seventh nearest neighbors

ary energy contribution to the total cell energy does not change significantly with the number of atoms implies that there is no considerable interaction between the boundaries, and thus the dislocations along them, at these supercell sizes. Therefore, for most of the hcp metals studied herein, the small number of atoms was considered sufficient for the purposes of calculating boundary/dislocation structures.

Since there are no previous ab initio calculations on the $(11\bar{2}1)$ boundary for comparison, we can only judge the values obtained against other techniques, such as the embedded atom method (EAM) [216] and Finnis-Sinclair (FS) [217] method. Both of these are considered less accurate than ab initio calculations, especially for materials where covalent bonding is important, such as Ti, Zr, or, especially, Be. Previous work on hcp twins has shown that while structures produced by empirical models are fairly close to those obtained from ab initio calculations, the energies can be quite different [218]. Generally, EAM and FS methods lead to a wide range of energy values that vary significantly in either direction, demonstrating the need for accurate potentials. For example, in Zr, the $(10\bar{1}2)$ twin, which is morphologically similar to the $(11\bar{2}1)$ twin, yields a boundary energy of 150 mJ/m^2 [219] and 151 mJ/m^2 [220] from *ab initio* studies, while the results from FS simulations lead to 262 mJ/m^2 [218] and 123 mJ/m^2 [220]. For the same twin in Mg, *ab initio* calculations lead to a boundary energy of 114 mJ/m^2 [218, 220] and 118 mJ/m^2 [211], while the results from FS simulations lead to 188 mJ/m62 [213], and EAM results lead to 800-1010 mJ/m^2 [214].

A more useful evaluation of our results comes from an assessment of them in relation to c_{44}. It is well established in classical dislocation theory that the energy of a dislocation, its core, and the Peierls stress all scale with the shear modulus, G [205]. It is therefore reasonable to assume that the $(11\bar{2}1)$ boundary

energy should scale with c_{44}. As a benchmark for evaluating the relative values, our results – as calculated from VASP as outlined in the previous section – are listed in Table B.5.

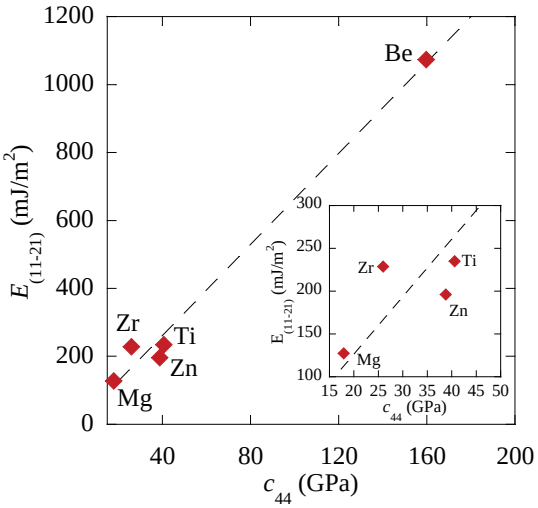

Figure B.13: Twin boundary energy vs c_{44} calculated for Ti, Zr, Zn, Mg, and Be. Inset shows plot zoomed into lower-left region. Least squares fit of the results yields a correlation coefficient, R^2, of 0.99.

Values also listed in Table B.5 are the ground state parameters for the crystal structures of all HM studied herein, compared with experimental values. All values for the lattice parameters are within 2% of the experimental values, and the bulk moduli are within 6% of the experimental values, lending credibility to the potentials used.

Figure B.13 shows that a correlation between the boundary energy and c_{44} indeed exists, with a linear fit having $R^2 = 0.99$. This result is taken as indirect evidence for the validity of our methodology. It is significant to note that the twin boundary energy of Be is approximately an order of magnitude higher than the other metals studied. Its bulk modulus and total energies, however, are comparable to Ti, and thus the higher boundary energy of Be cannot be related to its compressibility or be an artifact of the energy relaxations. The fact that c_{44} of Be is also about an order of magnitude higher than the other metals studied is thus significant and consistent with the notion that the boundary energy is related to the energy of the dislocations.

The way dislocations move is contingent on the energetics of bonding related to the dislocation core.

As a loose definition, one can define the core as the region of crystal lattice around the dislocation line in which the relative displacement of the neighboring atoms exceeds the elastic limit (for example, 2% in terms of local shear strain) [221]. Because core structure, under zero stress, has been given importance for its connection to mechanisms of dislocation motion [218, 222**?** , 223], the equilibrium structure of the bonding in and around the boundary should be considered as well. Figure B.14 shows the variations of interatomic distances within the basal planes in the 80 atom $(11\bar{2}1)$ supercell of Mg, as compared to the equilibrium structure obtained herein (Table B.5). All atomistic configurations are visualized using Atomeye software [224]. Consistent with the limited effect of the number of atoms on the boundary energies, the size of the distorted regions is similar for all supercell sizes studied.

Figure B.15 shows the von Mises shear strain invariant, which is a way of representing the strain fields of each atomic environment compared to the system average, or the overall local distortion as compared to the perfect crystal, as implemented in Atomeye [225]. Here again, the von Mises strains on the atoms away from the boundary are close to zero. Along the basal planes, the absolute effective "strain" falls below 1.5% at a distance of approximately $1.5a$ from the boundary. Similar results (not shown) were obtained for the other elements explored herein, regardless of their boundary energies. Because the relative displacements of the atoms outside of the strained regions, or effective core, do not contribute much to the energy of dislocation translation, the small deviation in the core size implies that for solids with higher boundary energies, such as Be, the bond stretching and bending involved are much more energetically expensive.

Table B.5: Calculated lattice parameters, bulk moduli, B, and c_{44} values for HM

Metal		a (Å)	c (Å)	c/a	B (GPa)	c_{44} (GPa)
Mg	Calc.	3.198	5.174	1.618	37	17.9
	Calc.[a]	3.138	5.107	1.627	37	17.7
	Exp.[b]	3.209	5.211	1.624	36	16.4
Ti	Calc.	2.926	4.612	1.576	116	40.6
	Calc.[a] 2	.900	4.671	1.611	123	50.4
	Exp.[b]	2.951	4.684	1.587	110	46.7
Zr	Calc.	3.236	5.171	1.598	96	26.0
	Calc.[a]	3.229	5.166	1.600	101	43.0
	Exp.[b]	3.232	5.148	1.593	97	32.1
Zn	Calc.	2.643	5.087	1.925	58	38.8
	Calc.[d,e]	2.648	5.085	1.921	60	23.2
	Exp.[b]	2.665	4.947	1.856	60	39.6
Be	Calc.	2.264	3.573	1.578	122	159.7
	Calc.[c]	2.294	3.608	1.573	122	160.2
	Exp.[b]	2.287	3.583	1.567	114	162.5

[a] [a] From Reference 60.
[b] From Reference 61.
[c] From Reference 62.
[d] From Reference 63.
[e] From Reference 64 for c_{44}.

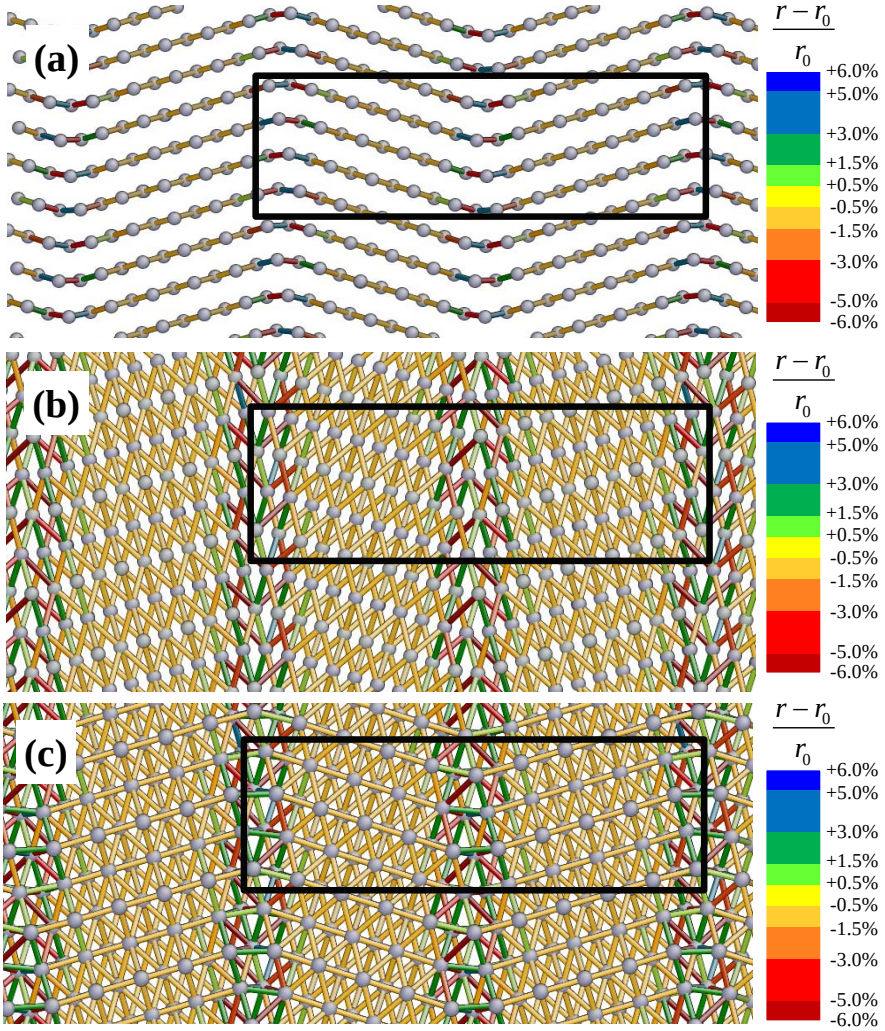

Figure B.14: Relative interatomic distances of structure obtained from the ab initio energy relaxations of the $(11\bar{2}1)$ twin supercell for Mg with 80 atoms. Deviations of interatomic distances are represented as strains compared to r0, the interatomic distances in the unit cell from ab initio calculations. For clarity, (a) shows only strains along the *a* direction, (b) shows only strains in the *c* direction, and (c) shows interatomic distances between all nearest neighbors. Boundary of repeating supercell is shown as dark rectangle.

We can go further in our assessment of the mobility of this boundary by not only identifying the regions where atom distances deviate from equilibrium, but also by assessing the dislocation structure within this region. As noted already, not only is the structure of the $(11\bar{2}1)$ twin composed of dislocations, but the latter are glissile. Freise and Kelly [204] and Minonishi et al. [206] found that the stable relaxed structure at the interface leads to a change in stacking sequence across the boundary [see Figs. B.12(a) and B.12(b)], which enables the boundary to move, within the basal planes, with effectively no atomic rearrangements. We note in passing that the work of Serra and Bacon [207], on the same boundary, is so different from our approach that no meaningful comparisons can be made. For example, they identified the twin dislocations as being mixed with edge and screw components in the $(11\bar{2}6)$ direction and pointed out that despite the small magnitude of the Burgers vector, $\sim a/7$, the core registry is spread over a region 50–100 times this in width, suggesting that the step may be very mobile [226]. Herein, we treat the boundary as a low-angle grain boundary with a Burgers vector equal to a.

Experimentally, the mechanical damping effect due to reversible $(11\bar{2}1)$ twin boundary movement was found in Zr [227–229] as well as Co [230], which is also consistent with the fact that dislocations along the $(11\bar{2}1)$ twin are mobile and result in reversible crystal slipping on a single glide. To investigate this further, we explored the atomic shifts and energies involved in shifting the boundary by a Burgers vector along the basal planes in 32 atom supercells [Fig. B.16]. The structures with the original [Fig. B.16(a)] and shifted [Fig. B.16(b)] boundaries were first relaxed as described in the previous section, and a chain of seven images was generated by linear interpolation between the two end structures. We used the nudged elastic band method [231, 232], as implemented by VASP, to simultaneously optimize the intermediate images and calculate the energy barrier to move the atoms into the atomic positions of the shifted boundary. For both Mg and Be, the energy is extremely small; at < 0.1 mJ/m^2, the difference in boundary energy as a barrier is below the resolution of the ab initio calculations, indicating that factors beyond detection of modeling at the atomic scale must be dominant for dislocation glide. As far as we are aware, this is the first time such a conclusion has been reached using ab initio calculations for basal plane dislocations in HM. This conclusion is in agreement with the fact that Tinder and Washburn [233] were unable to measure a threshold stress for the motion of dislocations in pure Cu. They also clearly showed that plastic deformation commences from almost zero stress in copper and zinc [234]. These findings are also in line with the results reported by Roberts and Brown [235, 236] for zinc and the results of Brydges [237], who later showed that the critical resolved shear stress (CRSS) in pure Cu single crystals continuously decreased with decreasing dislocation density.

This work on Zn and Cu is also consistent with results by Roberts and Hartman [238, 239] on Mg. In 1964, they published a paper on the temperature dependence of microyielding stresses in Mg single crystals [239]. In that work, they reported that at shear stresses, ÏĎ higher than about 0.04 to 0.07 MPa, fully and spontaneously reversible, closed stress-strain loops were observed. At about 0.35 MPa, the loops were no longer closed. In Fig. 3 of their paper, they published the loops for one of their samples – tested at room temperature – that was pre-deformed to a shear strain of 0.66% prior to cycling. More importantly, they noted that initial loading of annealed samples to any stress level always resulted in permanent strain. In other words, the yield point for as-received samples was below the detectability limit of their equipment, i.e., < 0.01 MPa. Recently, we showed that damping and microyielding inMg were due to the nucleation and growth of IKBs [195, 196]. When we apply our IKB model to their results, we obtain CRSS values of the order of 0.02 MPa for the crystals that were pre-deformed to 0.66%. As noted by Agnew and Nie in a recent review of Mg [240], it is still not known what exactly

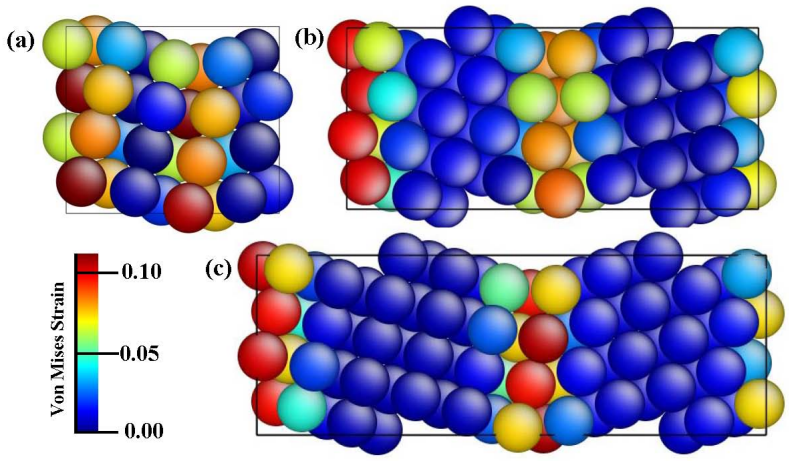

Figure B.15: Von Mises shear strain maps of atomistic configurations from relaxed $(11\bar{2}1)$ twin structures with repeating unit cells containing (a) 32 atoms, (b) 64 atoms, and (c) 80 atoms.

dictates the nucleation and growth of twins nor what dictates the CRSS. Hutchinson and Barnett [241] have also emphasized the disparate nature of the data for CRSS from tensile or compressive testing of single crystals, and the fact that the CRSS values used for polycrystal modeling have a much narrower distribution. For hcp metals, it is likely that the mobility of dislocation walls is dictated by extrinsic barriers such as other dislocations, defects, or precipitates, which would also explain the disparate nature of CRSS when grain boundaries are introduced (i.e., for polycrystalline materials). However, given the fact that dislocation glide is generally observed as the easiest system for accommodating stresses [242], and that the $(11\bar{2}1)$ twin has been observed to be mobile [204, 215, 226], as confirmed herein, these results are consistent with the IKB model when considering the ability of dislocations to move reversibly at the atomic scale. Directions for future calculations in analyzing the full reversible motion of dislocation walls lie in identifying the extrinsic factors, perhaps at other length scales, that may play a role during IKB formation and annihilation.

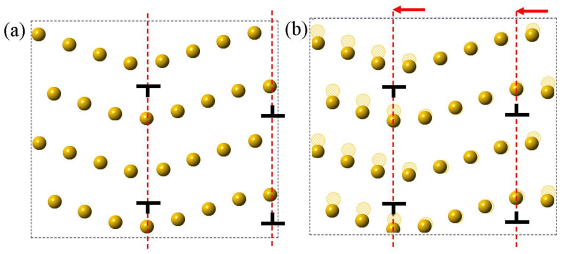

Figure B.16: Illustration of the movement of the dislocation boundaries (dashed lines) by one Burgers vector: (a) initial positions and (b) positions after the boundary has shifted one Burgers vector, shown by the red arrow. Original atom positions are also shown by the hatched circles to illustrate the movement of individual atoms.

Overall, the results on the convergence of energy with supercell size show us that the difference in total energy is indeed introduced by the boundaries and not the atoms in between them, nor the interactions between boundaries. Furthermore, the energy convergence with supercell size indicates that the smallest number of atoms (i.e., 32) is, for these materials, sufficient for investigating the energy effects of the dislocation structures. Thus, this is a sound

method for calculating the energy induced by dislocations without having to go to extremely large numbers of atoms.

Conclusions

The energy and atom arrangements of the $(11\bar{2}1)$ twin boundary in Mg, Ti, Zr, Zn, and Be were determined from ab initio calculations. The boundary energies scale linearly with c_{44}. The dislocation energy and core structure for the supercell with 32 atoms are sufficient and provide similar results as the supercell with 80 atoms. The study of the core arrangement and energetics of the $(11\bar{2}1)$ boundary through ab initio methods can shed light onto the dislocation motion through basal slip, and thus the deformation of hcp solids through kinking.

B.4 HIGH-TEMPERATURE STABILITY OF α-Ta_4AlC_3

Published in: N.J. Lane, P. Eklund, J. Lu, C.B. Spencer, L.Hultman, M.W. Barsoum, "High-temperature stability of α–Ta_4AlC_3" *Materials Research Bulletin*, **46**, 1088-1091 (2011).

Abstract

Cold-pressed α-Ta_4AlC_3 powders were annealed up to 1750 °C to test first-principles predictions of Îś-Îš phase-stability reversal at 1600 °C. Up to 1600 °C, the α-Ta_4AlC_3 samples were stable with no indications of any α-β transformation, as shown by the strong characteristic X-ray diffraction peaks of α-Ta−$4AlC_3$ and the zigzag stacking observed by transmission electron microscopy. These results show that, in this experimental situation, high temperature alone is not sufficient to cause the α-β transformation.

Graphical summary

Polymorphism in the MAX Phase Ta_4AlC_3

In this study, stability of α-Ta_4AlC_3 is investigated to test a hypothesized thermodynamically-driven α-to-β phase transformation. It is found that the α phase is stable up to 1600 C, with impurities and point defects most likely increasing the stability of the α-Ta_4AlC_3.

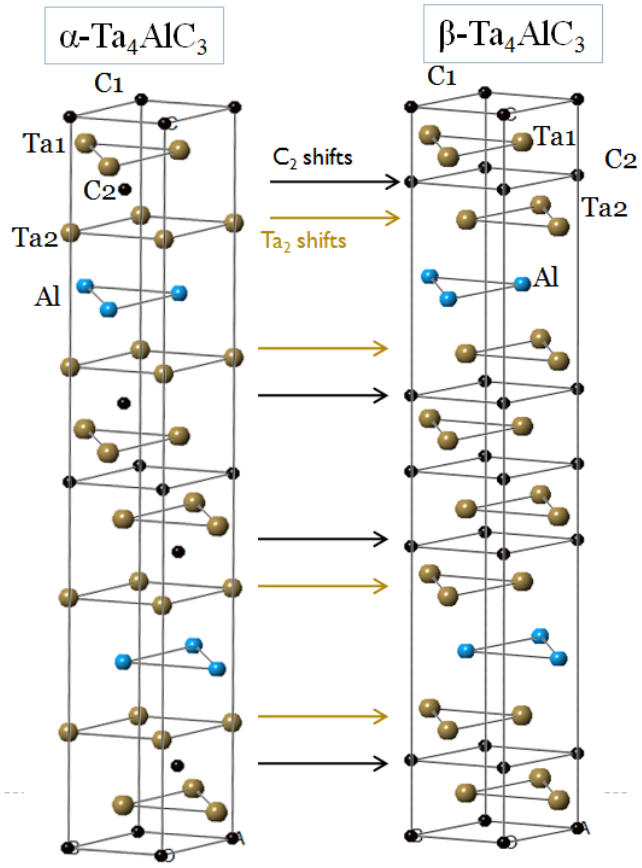

Introduction

The layered ternary $M_{n+1}AX_n$ ceramics, or "MAX" phases, where M is an early transition metal, A is an A-group element, and X is C or N, crystallize in the space group $P6_3/mmc$ and contain alternate layers that stack along the c direction consisting of octahedral M_6X building blocks that form a zigzag pattern with close-packed A-group atomic mirror planes [1, 82, 243]. The MAX phases are classified into 3 groups based on their n values, i.e., "211" for $n = 1$, "3 1 2" for $n = 2$, and "413" for $n = 3$. While the 211 and 312 MAX phases have been extensively investigated and characterized, it was long believed that Ti_4AlN_3 was the only 413 MAX phase [64]. Since 2004, however, several new 413 phases have been discovered; first with the synthesis of Ti_4SiC_3 and Ti_4GeC_3 thin films [65, 66] and then bulk synthesis of Ta_4AlC_3 in the form of polycrystals [67, 69–71] and single crystals [68]. More recently, the 413 phases V_4AlC_3 [72, 73], Nb_4AlC_3 [74], and Ti_4GaC_3 [75] were also synthesized in bulk form. Of the experimentally identified 413 phases, only Ta_4AlC_3 has shown polymorphism.

Manoun et al. [71] found large differences between experimental and calculated data in their high-pressure X-ray diffraction study of sintered Ta_4AlC_3 and tentatively attributed this to preferred orientation. Soon afterwards, however, Lin et al. showed that their hot-pressed Ta_4AlC_3 structures exhibited a different stacking sequence from the structure of Ti4AlN3 [69, 244] explaining the discrepancies observed by Manoun et al. In contrast, Etzkorn et al. synthesized Ta_4AlC_3 single crystals and found the same stacking sequence to be that of Ti_4AlN_3 [68]. Eklund et al. also observed this stacking in Ta_4AlC_3 powder and concluded that there were two Ta_4AlC_3 polymorphs. The two polymorphs are now known as α-Ta_4AlC_3, with Ti_4AlN_3-like stacking sequence, and β-Ta_4AlC_3, in which the Ta_{II} and C_{II} atom positions [‡]

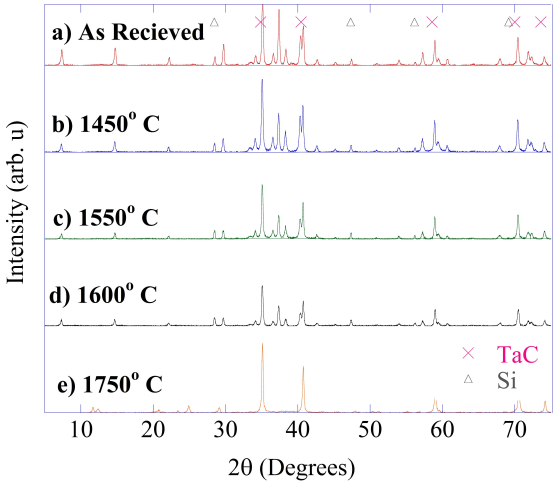

Figure B.17: Measured XRD patterns for a-Ta_4AlC_3 powder (a) as-received and after coldpressing, and successively annealing to temperatures (b) 1450 8C, (c) 1550 8C, (d) 1600 8C and (e) 1750 8C. Markers on top of the various peaks denote the phases TaC (X) and Si standard (Δ).

are shifted resulting in de-twinning and loss of the normal characteristic zigzag stacking of the TiX_6 layers.

The MAX phases have also shown another type of polymorphism that has been demonstrated in the 312 and 211 phases and involves shearing of the A layers. This type of polymorphism appears to be driven by shear strain under high-pressure conditions and/or TEM sample preparation [82, 134, 245–248]. In Ta_4AlC_3, on the other hand, the polymorphism is most likely thermodynamically driven with structural differences confined to the Ta_4C_3 slabs [67, 69, 82]. A number of recent papers have been published on the polymorphs of Ta_4AlC_3 [243, 249, 250]. Since this polymorphism would also be expected in V_4AlC_3 and Nb_4AlC_3, as V and Nb have the same number of valence electrons as Ta, Wang et al. [76] performed first principles studies to investigate reasons for this discrepancy. They predicted that a polymorphic phase transformation from

[‡]In the Ta_4AlC_3 structures, there are two different Ta sites, those adjacent to Al sites, and those not. These sites are referred to herein as Ta_I and Ta_{II}, respectively. Similarly, the two nonequivalent C sites are referred to as C_I and C_{II}.

α- to β- Ta_4AlC_3 is thermodynamically favorable at 1600°C, unlike in V_4AlC_3 and Nb_4AlC_3 [76]. The main origin of the predicted decrease in relative free energy from α- to β-Ta_4AlC_3 is the relative strength of the Ta_{II}–C_{II} bond, which is shorter in β-Ta_4AlC_3. In the present study, we experimentally test this prediction by heating coldpressed α-Ta_4AlC_3 powders to temperatures as high as 1750°C.

Experimental details

Experimental details for the synthesis of the a-Ta_4AlC_3 powder can be found elsewhere [67]. Approximately 3 g of the as-received powder was cold pressed into a pellet, with a radius of 6.5 mm at 700 MPa. The pellet was embedded in approximately 5.9 g of un-compacted Ta_4AlC_3 powder in a 100 mm diameter alumina crucible. The crucible was placed in an alumina tube furnace with a flowing Ar atmosphere in three successive heat treatments. The first annealing was at 1450°C for 1 h, followed by a second at annealing at 1550°C also for one hour, followed by one 1600°C for 2 h. The heating rate in all cases was constant at 5°Cmin^{-1}. Finally the sample was heated in a vacuum, graphite furnace at 8°Cmin^{-1} to 1750°C for 4 h. The latter furnace was used since the Ar furnace used for the first three runs was limited to 1600°C. In all cases, the sample was furnace cooled.

X-ray diffraction (XRD) was performed on the as-prepared powder and after each heat treatment in a powder diffractometer using Cu Kα radiation. Approximately 10 wt.% Si was mixed by mortar and pestle with the powder samples to normalize peak intensities for comparison. The data was normalized to the Si peak intensities. The simulations of the XRD patterns of Ta_4AlC_3 accounting for defects (vacancies and antisites) were performed using the CaRIne software [251]. The microstructures of the as-prepared and annealed at 1550°C powder samples were characterized by using a FEI Tecnai G2 TF 20 UT transmission electron microscope (TEM) operated at 200 kV with a 0.19 nm point resolution. The TEM specimens were made by suspending the powder in ethanol and collecting grains on holey carbon grids.

Results

Fig. B.17(a)–(e) shows the XRD patterns of the as-received and coldpressed Ta_4AlC_3 powder and after annealing at 1450°C, 1550°C, 1600°C, and 1750°C, respectively. All annealed samples up to 1600°C retain the α-Ta_4AlC_3 structure. This is obvious from the intensities of the peaks indexed in Fig. B.18, as (10$\bar{1}$2), (10$\bar{1}$4), (10 $\bar{1}$6) and (10$\bar{1}$7) peaks. In β-Ta_4AlC_3 the intensities of these peaks are negligible and would have been strongly reduced in intensity had an α-β transformation occurred [7,26]. Furthermore, the (10$\bar{1}$5) peak intensity would have significantly increased in intensity had β-Ta_4AlC_3 formed. After the heat treatment at 1750°C, only TaC is observed [Fig. B.17(e)]. While there are no indications of any a–b phase transformations, the following systematic observation can be made: the basal reflections decrease in intensity in relation to non-basal ones. This is clear from the

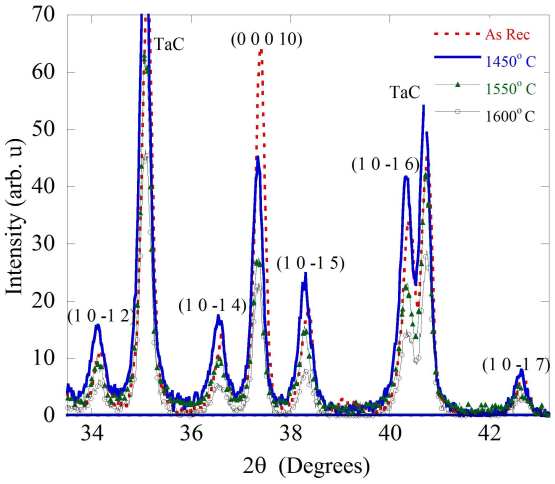

Figure B.18: Detail of the 2θ range 33–44° of the measured XRD patters for the as-received a-Ta_4AlC_3 (red dashed line) and after annealing of 1450°C (blue solid line), 1550°C (green triangles), and 1600°C (black circles).

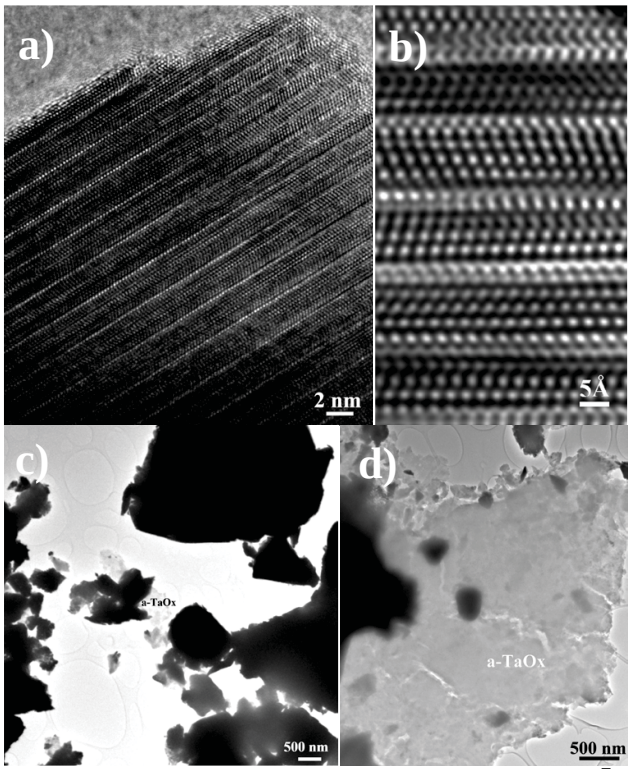

Figure B.19: HRTEM of the lattice of α-Ti_4AlC_3 annealed at 1550°C in the $[11\bar{2}0]$ zone axis projection, showing zig-zag pattern stacking sequence typical of α-Ti_4AlC_3: (a) low magnification overview image and, (b) image of three unit cells. (b) and (c) are TEM images showing amorphous TaOx phase found in as-received Ta_4AlC_3 powder and after annealing at 1550°C, respectively. After the high temperature anneal the volume fraction of TaO_x increases noticeably.

(0 0 0 2), (0 0 0 4), (0 0 0 6) and (0 0 0 8) peaks shown in Fig. 1 at approximately $2\theta =$ 7°, 15°, 22°, and 29°, respectively, as well as the (0 0 0 10) peak indexed in Fig. B.18, which all decrease in intensity relative to the (1 0 $\bar{1}$ l) peaks compared to room temperature.

The as-received powder and the sample annealed at 1550°C were characterized by high resolution TEM. In agreement with the XRD results, these samples were found to contain only the α-Ta_4AlC_3 phase. Fig. B.19(a) is a HRTEM image along $[11\bar{2}0]$ zone axis of α-Ta_4AlC_3 from the annealed sample. A magnified image presenting three unit cells is shown in Fig. B.19(b). Fig. B.19(c) and (d) show areas of the Ta_4AlC_3 samples where an amorphous tantalum oxide phase was found in the as-received material and that annealed at 1550°C, respectively. The amorphous material consists only of Ta and O, as confirmed by qualitative EDS. The annealed sample contained significantly more amorphous tantalum oxide than the as-received powder.

Discussion

Based on the above results, it is clear that cold-pressed α-Ta_4AlC_3 powder does not transform to β-Ta_4AlC_3 by heat treatment alone as predicted by the *ab initio* calculations of Wang et al. [76]. Therefore, there must be other factors that drive the α–β phase transformation.

First, heating the α-Ta_4AlC_3 samples in the Ar furnace leads to experimental conditions that deviate from the ideal stoichiometry and purity assumed in the *ab initio* calculations. For instance, the presence of secondary phases (*e.g.* TaC), the possibility of oxidation in the furnace, and the creation of defects such as vacancies are not accounted for in the theoretical predictions. Second, there are significantly more TaO_x impurities in the heat-treated sample [Fig. B.19(d)] compared to the as-received powder [Fig. B.19(c)]. Oxidation may thus affect the predicted phase transformation. Third, experimental studies of the β-Ta_4AlC_3 polymorph involve synthesis through hot pressing in addition to higher temperatures [69–71] and the synthesis pressure may also affect the relative phase stability. To test this hypothesis we hot-pressed a stoichiometric mixture of TaC, Al, and graphite powders in a graphite-heated vacuum hot-press at 1500°C for 2 h under a pressure of 70 MPa. Again, the resulting phase was α-Ta_4AlC_3 with unreacted TaC, as confirmed by XRD (not shown).

In support of these arguments, our results show a decrease in basal peak intensity relative to the non-basal peaks. From simulations of the XRD patterns (Fig. B.20), we conclude that these shifts in relative intensities of basal vs. non-basal peaks can be caused by vacancies on the Ta_I sites or Ta antisite defects on the Al positions. Excess Al (*i.e.*, occupancy greater than 1) would also explain the effect, but the excess would have to be large (30-40%) and is therefore less likely than the other effects. Fig. B.20 shows that all three types of defects have roughly the same effect on the diffraction pattern, with the intensities of the basal plane peaks decreasing relative to the non-basal peak intensities. Vacancies on Al sites or Ta_{II} sites would have the opposite effect on the XRD patterns. This is interesting because vacancies on the Al sites would be expected since extended heating at high temperatures results in TaC_x, which may suggest a degree of preferred orientation. These results combined with the experimental XRD patterns (Fig. B.17) show the possible changes in stoichiometry caused by annealing α-Ta_4AlC_3 and can also be connected to the relative phase stability. While there is no phase transformation, there are indeed systematic changes in the XRD patterns that can be attributed to these possible defects, which may increase the relative stability of the α-Ta_4AlC_3 polymorph.

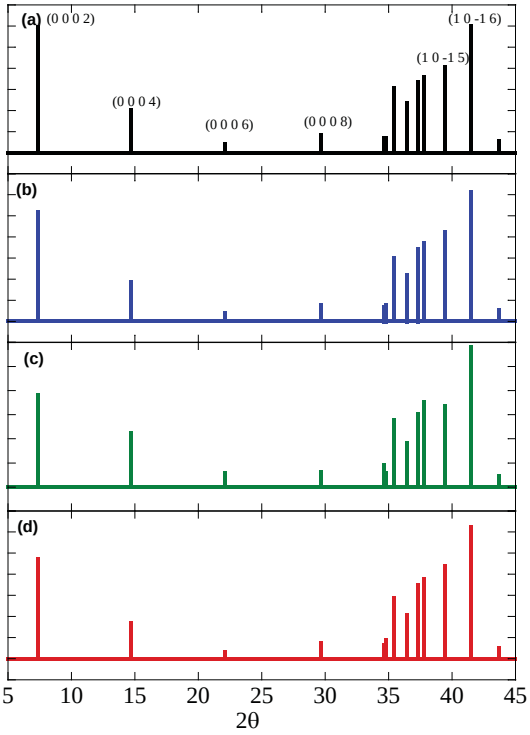

Figure B.20: Simulations of XRD patterns for α-Ta_4AlC_3, (a) perfect crystal, (b) with 30% excess Al, (c) 10% vacancies on the Ta_I sites, and, (d) 10% antisite defects on both Al positions.

Summary and conclusions

No evidence of an α–β phase transformation during the annealing of α-Ta_4AlC_3 at temperatures up to 1600°C was found, contradicting ab initio calculations that predict a transformation around 1600°C. Heating to 1750°C converts the α-Ta_4AlC_3 to TaC_x. The reason for this apparent discrepancy may be the differences between the idealized conditions for the *ab initio* calculations and non-ideal experimental conditions, including the presence of defects.

Heating the powders, however, resulted in a diminution of the relative intensities of the (0 0 0 l) peaks, which is likely due to the formation of vacancies or antisites. These results indicate the need for more calculations to study the effects of vacancies, antisite defects, impurities such as oxygen, and pressure on the relative phase stabilities.

Appendix C: Acronyms

ADP atomic displacement parameter

CTE coefficient of thermal expansion

DFT density functional theory

DOS density of states

E-WIMV entropy [algorithm of] Williams, Imhof, Matthies, Vinel

GGA generalized gradient approximation

hcp hexagonal close-packed

HIPPO High Pressure Preferred Orientation [diffractometer]

HTND high-temperature neutron diffraction

HTXRD high-temperature X-ray diffraction

IKB incipient kink band

KNE kinking nonlinear elastic

LDA local density approximation

ND neutron diffraction

PAW projector augmented wave

PDOS partial density of states

PBE [functional of] Perdew, Burke, and Eruzerhof

TEM transmission electron microscopy

TOF time-of-flight

VASP Vienna *Ab intio* Simulation Package

XRD X-ray diffraction

Appendix D: Notations

MAX PHASE NOTATIONS

MAX	$M_{n+1}AX_n$
211	M_2AX $(n = 1)$
312	M_3AX_2 $(n = 2)$
413	M_4AX_3 $(n = 3)$
M	metal element in MAX phase
A	A-group element in MAX phase
X	carbon or nitrogen in MAX phase

OTHER NOTATIONS

V	volume
a,c	lattice parameters
x, y, z	internal coordinates in unit cell
ω	frequency
α	coefficient of thermal expansion
$\mathcal{H}$	Hamiltonian operator
$\mathcal{V}$	potential energy
$\mathcal{T}$	kinetic energy
$\mathcal{U}(x)$	elastic potential energy between atoms separated by x
$\boldsymbol{D}$	dynamical matrix
$u(R)$	atomic displacement of atom on site R
Φ	force constant matrix
U_{ij}	anisotropic mean-squared displacement
U_{eq}	equivalent isotropic mean-squared displacement
$\mathrm{U}_{\mathrm{iso}}$	isotropic mean-squared displacement

Bibliography

[1] M.W. Barsoum. $M_{N+1}AX_N$ phases: A new class of solids: Thermodynamically stable nanolaminates. *Progress in Solid State Chemistry*, 28(1-4):201–281, 2000.

[2] N. J. Lane, S. C. Vogel, and M. W. Barsoum. Temperature-dependent crystal structures of Ti_2AlN and Cr_2GeC as determined from high temperature neutron diffraction. *Journal of the American Ceramic Society*, 94(10):3473–3479, 2011.

[3] N. J. Lane, S. C. Vogel, and M. W. Barsoum. High-temperature neutron diffraction and the temperature-dependent crystal structures of the MAX phases Ti_3SiC_2 and Ti_3GeC_2. *Physical Review B*, 82:174109, 2010.

[4] N. J. Lane, S. C. Vogel, G. Hug, A. Togo, L. Chaput, L. Hultman, and M. W. Barsoum. Neutron diffraction measurements and first-principles study of thermal motion of atoms in select $M_{n+1}AX_n$ and binary MX transition-metal carbide phases. *Physical Review B*, 86: 214301, 2012.

[5] N. J. Lane, M. Naguib, V. Presser, G. Hug, L. Hultman, and M. W. Barsoum. First-order Raman scattering of the MAX phases Ta_4AlC_3, Nb_4AlC_3, Ti_4AlN_3, and Ta_2AlC. *Journal of Raman Spectroscopy*, 43(7):954–958, 2012.

[6] N. J. Lane, S. C. Vogel, E. N Caspi, and M. W. Barsoum. High-temperature neutron diffraction and first-principles study of temperature-dependent crystal structures and atomic vibrations in Ti_3AlC_2, Ti_2AlC, and $Ti_5Al_2C_3$. *Journal of Applied Physics*, 113(18): 183519–183519, 2013.

[7] N. J. Lane, M. W. Barsoum, and J. M. Rondinelli. Correlation effects and spin-orbit interactions in two-dimensional hexagonal 5d transition metal carbides, $Ta_{n+1}C_n$ (n = 1,2,3). *Europhysics Letters*, (101):57003, 2013.

[8] N. J. Lane, M. Naguib, J. Lu, L. Hultman, and M. W. Barsoum. Structure of a new bulk $Ti_5Al_2C_3$ MAX phase produced by the topotactic transformation of Ti_2AlC. *Journal of the European Ceramic Society*, 32(12):3485–3491, 2012.

[9] N. J. Lane, M. Naguib, J. Lu, P. Eklund, L. Hultman, and M. W. Barsoum. Comment on '$Ti_5Al_2C_3$: A new ternary carbide belonging to max phases in the Ti–Al–C system'. *Journal of the American Ceramic Society*, 95(10):3352–3354, 2012.

[10] N. J. Lane, S. I. Simak, A. S. Mikhaylushkin, I. A. Abrikosov, L. Hultman, and M.W. Barsoum. A first principles study of dislocations in HCP metals through the investigation of the $(11\bar{2}1)$ twin boundary. *Physical Review B*, 84:184101, 2011.

[11] N. J. Lane, P. Eklund, J. Lu, C.B. Spencer, L. Hultman, and M. W. Barsoum. High-temperature stability of α-Ta_4AlC_3. *Materials Research Bulletin*, 46:1088–1091, 2011.

[12] T. Hahn and P. Paufler. International tables for crystallography A: space-group symmetry. *Crystal Research and Technology*, 19(10):1306–1306, 1984.

[13] M. T. Dove. *Structure and Dynamics: An atomic view of materials*. Oxford Master Series in Condensed Matter Physics. Oxford University Press, Oxford, UK, 2003.

[14] N. W. Ashcroft and N. D. Mermin. *Solid state physics*. Holt, Rinehart, and Winston, New York, NY, 1976.

[15] C. Kittel. *Introduction to solid state physics*. Wiley, Chichester, NY, 1996.

[16] M. W. Barsoum and T. El-Raghy. Synthesis and characterization of a remarkable ceramic: Ti_3SiC_2. *Journal of the American Ceramic Society*, 79(7):1953–1956, 1996.

[17] T. El-Raghy, A. Zavaliangos, M. W. Barsoum, and S. R. Kalidindi. Damage mechanisms around hardness indentations in Ti_3SiC_2. *Journal of the American Ceramic Society*, 80(2): 513–516, 1997.

[18] M. W. Barsoum, T. El-Raghy, and L. U. J. T. Ogbuji. Oxidation of Ti_3SiC_2 in air. *Journal of the Electrochemical Society*, 144(7):2508–2516, 1997.

[19] M.W. Barsoum and T. El-Raghy. A progress report on Ti_3SiC_2, Ti_3GeC_2, and the H-phases, M_2B_X. *Journal of Materials Synthesis and Processing*, 5(3):197–216, 1997.

[20] A. Ganguly, T. Zhen, and M. W. Barsoum. Synthesis and mechanical properties of Ti_3GeC_2 and $Ti_3(Si_xGe_{1-x})C_2$ (x=0.5, 0.75) solid solutions. *Journal of Alloys and Compounds*, 376(1-2):287–295, 2004.

[21] M. W. Barsoum and T. El-Raghy. The MAX phases: Unique new carbide and nitride materials. *American Scientist*, 89(4):334–343, 2001.

[22] D. J. Tallman, M. Naguib, B. Anasori, and M. W. Barsoum. Tensile creep of Ti_2AlC in air in the temperature range 1000°-1150°C. *Scripta Materialia*, 66(10):805 – 808, 2012.

[23] M. Radovic, M. W. Barsoum, T. El-Raghy, and S. Wiederhorn. Tensile creep of fine grained (3-5 μm) Ti_3SiC_2 in the 1000-1200°C temperature range. *Acta Materialia*, 49 (19):4103–4112, 2001.

[24] M. Radovic, M. W. Barsoum, T. El-Raghy, and S. M. Wiederhorn. Tensile creep of coarse-grained Ti_3SiC_2 in the 1000-1200 degrees C temperature range. *Journal of Alloys and Compounds*, 361(1–2):299–312, 2003.

[25] T. Zhen, M. W. Barsoum, S. R. Kalidindi, M. Radovic, Z. M. Sun, and T. El-Raghy. Compressive creep of fine and coarse-grained T_3SiC_2 in air in the 1100-1300°c temperature range. *Acta Materialia*, 53(19):4963–4973, 2005.

[26] M. Sundberg, G. Malmqvist, A. Magnusson, and T. El-Raghy. Alumina forming high temperature silicides and carbides. *Ceramics International*, 30(7):1899 – 1904, 2004.

[27] S. Li, G. Song, K. Kwakernaak, S. van der Zwaag, and W. G. Sloof. Multiple crack healing of a Ti_2AlC ceramic. *Journal of the European Ceramic Society*, 32(8):1813 – 1820, 2012.

[28] W. Jeitschko, H. Nowotny, and F. Benesovsky. Kohlenstoffhaltige ternare verbindungen (V-Ge-C, Nb-Ga-C, Ta-Ga-C, Ta-Ge-C, Cr-Ga-C und Cr-Ge-C). *Monatshefte für Chemie*, 94: 844, 1963.

[29] W. Jeitschko, H. Nowotny, and F. Benesovsky. Ti_2AlN, eine stickstoffhaltige h-phase. *Monatshefte für Chemie*, 94:1198, 1963.

[30] J. C. Schuster and J. Bauer. The ternary-system titanium aluminum nitrogen. *Journal of Solid State Chemistry*, 53(2):260–265, 1984.

[31] M. A. Pietzka and J. C. Schuster. Phase equilibria in the quaternary system Ti–Al–C–N. *Journal of the American Ceramic Society*, 79(9):2321–2330, 1996.

[32] M. W. Barsoum, D. Brodkin, and T. El Raghy. Layered machinable ceramics for high temperature applications. *Scripta Materialia*, 36(5):535–541, 1997.

[33] B. Manoun, F. X. Zhang, S. K. Saxena, T. El-Raghy, and M. W. Barsoum. X-ray high-pressure study of Ti_2AlN and Ti_2AlC. *Journal of Physics and Chemistry of Solids*, 67(9–10): 2091–2094, 2006.

[34] T. Scabarozi, A. Ganguly, J. D. Hettinger, S. E. Lofland, S. Amini, P. Finkel, T. El-Raghy, and M. W. Barsoum. Electronic and thermal properties of $Ti_3Al(C_{0.5}N_{0.5})_2$, $Ti_2Al(C_{0.5}N_{0.5})$ and Ti_2AlN. *Journal of Applied Physics*, 104(7):073713, 2008.

[35] M. Bugnet, T. Cabioc'h, V. Mauchamp, P. Guerin, M. Marteau, and M. Jaouen. Stability of the nitrogen-deficient Ti_2AlN_x MAX phase in Ar^{2+}-irradiated (Ti,Al)N/Ti_2AlN_x multilayers. *Journal of Materials Science*, 45(20):5547–5552, 2010.

[36] M. Radovic, A. Ganguly, and M. W. Barsoum. Elastic properties and phonon conductivities of $Ti_3Al(C_{0.5},N_{0.5})$ and $Ti_2Al(C_{0.5},N_{0.5})$ solid solutions. *Journal of Materials Research*, 23 (6):1517–1521, 2008.

[37] M. W. Barsoum, M. Ali, and T. El-Raghy. Processing and characterization of Ti_2AlC, Ti_2AlN, and $Ti_2AlC_{0.5}N0_{0.5}$. *Metallurgical and Materials Transactions A*, 31(7):1857–1865, 2000.

[38] T. H. Scabarozi, S. Amini, O. Leaffer, A. Ganguly, S. Gupta, W. Tambussi, S. Clipper, J. E. Spanier, M. W. Barsoum, J. D. Hettinger, and S. E. Lofland. Thermal expansion of select $M_{n+1}AX_n$ (M=early transition metal, A=A group element, X=C or N) phases measured by high temperature x-ray diffraction and dilatometry. *Journal of Applied Physics*, 105(1): 013543, 2009.

[39] M. Magnuson, M. Mattesini, S. Li, C. Hoglund, M. Beckers, L. Hultman, and O. Eriksson. Bonding mechanism in the nitrides Ti_2AlN and TiN: an experimental and theoretical investigation. *Physical Review B*, 76(19):195127, 2007.

[40] M. Magnuson, O. Wilhelmsson, J. P. Palmquist, U. Jansson, M. Mattesini, S. Li, R. Ahuja, and O. Eriksson. Electronic structure and chemical bonding in Ti_2AlC investigated by soft x-ray emission spectroscopy. *Physical Review B*, 74(19):195108, 2006.

[41] O. D. Leaffer, S. Gupta, M. W. Barsoum, and J. E. Spanier. On the raman scattering from selected M_2AC compounds. *Journal of Materials Research*, 22(10):2651–2654, 2007.

[42] B. Manoun, S. Amini, S. Gupta, S. K. Saxena, and M. W. Barsoum. On the compression behavior of Cr_2GeC and V_2GeC up to quasi-hydrostatic pressures of 50 GPa. *Journal of Physics-Condensed Matter*, 19(45):456218, 2007.

[43] S. Amini, A. Zhou, S. Gupta, A. Devillier, P. Finkel, and M. W. Barsoum. Synthesis and elastic and mechanical properties of Cr_2GeC. *Journal of Materials Research*, 23: 2157–2165, 2008.

[44] Y. J. Kang, T. Fey, and P. Greil. Synthesis of Ti_2SnC MAX phase by mechanical activation and melt infiltration. *Advanced Engineering Materials*, 14(1-2):85–91, 2012.

[45] J.Y. Wu and K. Chai. Strengthening of Cu-Ti_2SnC composites due to microstructural changes in the material. *Key Engineering Materials*, 353:429–432, 2007.

[46] J. Y. Wu, Y. C. Zhou, and J. Y. Wang. Tribological behavior of Ti_2SnC particulate reinforced copper matrix composites. *Materials Science and Engineering: A*, 422(1–2):266–271, 2006.

[47] L. Jaworska. Diamond composite with Ti_2SnC and Zr_2SnC phases. *Journal of Achievements in Materials and Manufacturing Engineering*, 55(1):33–38, 2012.

[48] W. Jeitschko and H. Nowotny. Die kristallstruktur von Ti_3SiC_2 - ein neuer komplexcarbid-typ. *Monatshefte für Chemie*, 98(2):329–337, 1967.

[49] Wolfsgruber H., Nowotny H., and Benesovsky F. Die krystallstruktur von Ti_3GeC_2. *Monatshefte für Chemie*, 98(6):2403–2405, 1967.

[50] S. Arunajatesan and A. H. Carim. Symmetry and crystal-structure of Ti_3SiC_2. *Materials Letters*, 20(5-6):319–324, 1994.

[51] E. H. Kisi, J. A. A. Crossley, S. Myhra, and M. W. Barsoum. Structure and crystal chemistry of Ti_3SiC_2. *Journal of Physics and Chemistry of Solids*, 59(9):1437–1443, 1998.

[52] M. Radovic, M. W. Barsoum, A. Ganguly, T. Zhen, P. Finkel, S. R. Kalidindi, and E. Lara-Curzio. On the elastic properties and mechanical damping of Ti_3SiC_2, Ti_3GeC_2, $Ti_3Si_{0.5}Al_{0.5}C_2$ and Ti_2AlC in the 300–1573 k temperature range. *Acta Materialia*, 54(10): 2757–2767, 2006.

[53] M. W. Barsoum, T. El-Raghy, C. J. Rawn, W. D. Porter, H. Wang, E. A. Payzant, and C. R. Hubbard. Thermal properties of Ti_3SiC_2. *Journal of Physics and Chemistry of Solids*, 60 (4):429–439, 1999.

[54] X. H. Wang and Y. C. Zhou. Oxidation behavior of Ti_3AlC_2 at 1000-1400 degrees c in air. *Corrosion Science*, 45(5):891–907, 2003.

[55] X.H. Wang and Y.C. Zhou. High-temperature oxidation behavior of Ti_2AlC in air. *Oxidation of Metals*, 59:303–320, 2003.

[56] M. Y. Gamarnik and M. W. Barsoum. Bond lengths in the ternary compounds Ti_3SiC_2, Ti_3GeC_2 and Ti_2GeC. *Journal of Materials Science*, 34(1):169–174, 1999.

[57] Y. C. Zhou and Z. M. Sun. Electronic structure of the layered compound Ti_3GeC_2. *Journal of Applied Physics*, 86(3):1430–1432, 1999.

[58] P. Finkel, B. Seaman, K. Harrell, J. Palma, J. D. Hettinger, S. E. Lofland, A. Ganguly, M. W. Barsoum, Z. Sun, S. Li, and R. Ahuja. Electronic, thermal, and elastic properties of $Ti_3Si_{1-x}Ge_xC_2$ solid solutions. *Physical Review B*, 70(8):085104, 2004.

[59] M. K. Drulis, A. Czopnik, H. Drulis, J. E. Spanier, A. Ganguly, and M. W. Barsoum. On the heat capacity of Ti_3GeC_2. *Materials Science and Engineering B-Solid State Materials for Advanced Technology*, 119(2):159–163, 2005.

[60] H. Högberg, J. Emmerlich, P. Eklund, O. Wilhelmsson, J. P. Palmquist, U. Jansson, and L. Hultman. Growth and property characterization of epitaxial MAX-phase thin films from the Ti_{n+1}(Si,Ge,Sn)C_n systems. *Advances in Science and Technology*, 45, 2006.

[61] S. Dubois, T. Cabioc'h, P. Chartier, V. Gauthier, and M. Jaouen. A new ternary nanolaminate carbide: Ti_3SnC_2. *Journal of the American Ceramic Society*, 90(8):2642–2644, 2007.

[62] C. Tromas, N. Ouabadi, V. Gauthier-Brunet, M. Jaouen, and S. Dubois. Mechanical properties of nanolaminate Ti_3SnC_2 carbide determined by nanohardness cartography. *Journal of the American Ceramic Society*, 93(2):330–333, 2010.

[63] S. Dubois, G. P. Bei, C. Tromas, V. Gauthier-Brunet, and P. Gadaud. Synthesis, microstructure, and mechanical properties of $Ti_3(Sn_{1-x}Al_x)C_2$ MAX phase solid solutions. *International Journal of Applied Ceramic Technology*, 7(6):719–729, 2010.

[64] M. W. Barsoum, L. Farber, I. Levin, A. Procopio, T. El-Raghy, and A. Berner. High-resolution transmission electron microscopy of Ti_4AlN_3, or $Ti_3Al_2N_2$ revisited. *Journal of the American Ceramic Society*, 82(9):2545–2547, 1999.

[65] H. Högberg, P. Eklund, J. Emmerlich, J. Birch, and L. Hultman. Epitaxial Ti_2GeC, Ti_3GeC_2, and Ti_4GeC_3 MAX-phase thin films grown by magnetron sputtering. *Journal of Materials Research*, 20(4):779–782, 2005.

[66] J. P. Palmquist, S. Li, P. O. ÅPersson, J. Emmerlich, O. Wilhelmsson, H. Högberg, M. I. Katsnelson, B. Johansson, R. Ahuja, O. Eriksson, L. Hultman, and U. Jansson. $M_{n+1}AX_n$ phases in the Ti–Si–C system studied by thin-film synthesis and ab initio calculations. *Physical Review B*, 70(16):165401, 2004.

[67] P. Eklund, J. P. Palmquist, J. Howing, D. H. Trinh, T. El-Raghy, H. Högberg, and L. Hultman. Ta_4AlC_3: Phase determination, polymorphism and deformation. *Acta Materialia*, 55(14): 4723–4729, 2007.

[68] J. Etzkorn, M. Ade, and H. Hillebrecht. Ta_3AlC_2 and Ta_4AlC_3 – single-crystal investigations of two new ternary carbides of tantalum synthesized by the molten metal technique. *Inorganic Chemistry*, 46(4):1410–1418, 2007.

[69] Z. J. Lin, M. J. Zhuo, Y. C. Zhou, M. S. Li, and J. Y. Wang. Structural characterization of a new layered-ternary Ta_4AlC_3 ceramic. *Journal of Materials Research*, 21(10):2587–2592, 2006.

[70] Z. J. Lin, M. J. Zhuo, Y. C. Zhou, M. S. Li, and J. Y. Wang. Microstructures and theoretical bulk modulus of layered ternary tantalum aluminum carbides. *Journal of the American Ceramic Society*, 89(12):3765–3769, 2006.

[71] B. Manoun, S. K. Saxena, T. El-Raghy, and M. W. Barsoum. High-pressure x-ray diffraction study of Ta_4AlC_3. *Applied Physics Letters*, 88(20):201902, 2006.

[72] J. Etzkorn, M. Ade, and H. Hillebrecht. V_2AlC, V_4AlC_3-x (x approximate to 0.31), and $V_{12}Al_3C_8$: Synthesis, crystal growth, structure, and superstructure. *Inorganic Chemistry*, 46(18):7646–7653, 2007.

[73] C. F. Hu, J. Zhang, J. M. Wang, F. Z. Li, J. Y. Wang, and Y. C. Zhou. Crystal structure of V_4AlC_3: A new layered ternary carbide. *Journal of the American Ceramic Society*, 91(2): 636–639, 2008.

[74] C. F. Hu, F. Z. Li, J. Zhang, J. M. Wang, J. Y. Wang, and Y. C. Zhou. Nb_4AlC_3: A new compound belonging to the max phases. *Scripta Materialia*, 57(10):893–896, 2007.

[75] J. Etzkorn, M. Ade, D. Kotzott, M. Kleczek, and H. Hillebrecht. Ti_2GaC, Ti_4GaC_3 and Cr_2GaC – synthesis, crystal growth and structure analysis of Ga-containing MAX-phases $M_{n+1}GaC_n$ with M = Ti, Cr and n=1, 3. *Journal of Solid State Chemistry*, 182(5): 995–1002, 2009.

[76] J. Y. Wang, J. M. Wang, Y. C. Zhou, Z. J. Lin, and C. F. Hu. Ab initio study of polymorphism in layered ternary carbide M_4AlC_3 (M = V, Nb and Ta). *Scripta Materialia*, 58(12):1043–1046, 2008.

[77] J. E. Spanier, S. Gupta, M. Amer, and M. W. Barsoum. First-order Raman scattering from the $M_{n+1}AX_n$ phases. *Physical Review B*, 71:12103, 2005.

[78] P. Eklund, M. Beckers, J. Frodelius, H. Högberg, and L. Hultman. Magnetron sputtering of Ti_3SiC_2 thin films from a compound target. *Journal of Vacuum Science & Technology A*, 25(5):1381–1388, 2007.

[79] Epitaxial growth and electrical-transport properties of $Ti_7Si_2C_5$ thin films synthesized by reactive sputter-deposition. *Scripta Materialia*, (9):811–814, 2011.

[80] S. Kerdsongpanya, K. Buchholt, O. Tengstrand, J. Lu, J. Jensen, L. Hultman, and P. Eklund. Phase-stabilization and substrate effects on nucleation and growth of $(Ti,V)_{n+1}GeC_n$ thin films. *Journal of Applied Physics*, 110(5), 2011.

[81] O. Wilhelmsson, J. P. Palmquist, E. Lewin, J. Emmerlich, P. Eklund, P. O. Å . Persson, H. Högberg, S. Li, R. Ahuja, O. Eriksson, L. Hultman, and U. Jansson. Deposition and characterization of ternary thin films within the Ti–Al–C system by DC magnetron sputtering. *Journal of Crystal Growth*, 291(1):290–300, 2006.

[82] P. Eklund, M. Beckers, U. Jansson, H. Högberg, and L. Hultman. The $M_{n+1}AX_n$ phases: Materials science and thin-film processing. *Thin Solid Films*, 518(8):1851–1878, 2010.

[83] X. Wang, H. Zhang, L. Zheng, Y. Ma, X. Lu, Y. Sun, and Y. Zhou. $Ti_5Al_2C_3$: A new ternary carbide belonging to MAX phases in the Ti–Al–C system. *Journal of the American Ceramic Society*, 95(5):1508–1510, 2012.

[84] H. Zhang, X. Wang, Y. Ma, L. Sun, L. Zheng, and Y. Zhou. Crystal structure determination of nanolaminated $Ti_5Al_2C_3$ by combined techniques of XRPD, TEM and ab initio calculations. *Journal of Advanced Ceramics*, 1:268–273, 2012.

[85] A.K. Gathak and L.S. Kothari. *An introduction to lattice dynamics*. Addison-wesley publishing company, Philippines, 1972.

[86] B. T. M. Willis and A. W. Pryor. *Thermal vibrations in crystallography*. Cambridge University Press, London, United Kingdom, 1975.

[87] D. C. Wallace. *Thermodynamics of Crystals*. John Wiley & Sons, Chemung, NY, U.S.A., 1972.

[88] A. van de Walle and G. Ceder. The effect of lattice vibrations on substitutional alloy thermodynamics. *Reviews in Modern Physics*, 74(1):11–45, 2002.

[89] E. Schrödinger. Quantization as an eigenvalue problem. *Annalen der Physik*, 79:489–527, 1926.

[90] M. Born and R. Oppenheimer. The quantum theory of molecules. *Annalen der Physik*, 84: 457–484, 1927.

[91] P. Hohenberg and W. Kohn. Inhomogeneous electron gas. *Physical Review*, 136:B864–B871, 1964.

[92] W. Kohn and L. J. Sham. Self-consistent equations including exchange and correlation effects. *Physical Review*, 140:A1133–A1138, 1965.

[93] P. A. M. Dirac. Note on exchange phenomena in the thomas atom. *Mathematical Proceedings of the Cambridge Philosophical Society*, 26:376–385, 6 1930.

[94] J. P. Perdew and Y. Wang. Accurate and simple analytic representation of the electron-gas correlation energy. *Physical Review B*, 45:13244–13249, 1992.

[95] J. P. Perdew and A. Zunger. Self-interaction correction to density-functional approximations for many-electron systems. *Phyical Review B*, 23:5048, 1981.

[96] S. H. Vosko, L. Wilk, and M. Nusair. Accurate spin-dependent electron liquid correlation energies for local spin density calculations: a critical analysis. *Canadian Journal of Physics*, 58(8):1200–1211, 1980.

[97] D. M. Ceperley and B. J. Alder. Ground state of the electron gas by a stochastic method. *Physical Review Letters*, 45:566–569, 1980.

[98] J. P. Perdew, K. Burke, and M. Ernzerhof. Generalized gradient approximation made simple. *Physical Review Letters*, 77(18):3865, 1996.

[99] A. Zoroddu, F. Bernardini, P. Ruggerone, and V. Fiorentini. First-principles prediction of structure, energetics, formation enthalpy, elastic constants, polarization, and piezoelectric constants of AlN, GaN, and InN: Comparison of local and gradient-corrected density-functional theory. *Physical Review B*, 64(4):045208, 2001.

[100] M. Cococcioni, A. Dal Corso, and S. de Gironcoli. Structural, electronic, and magnetic properties of Fe_2 SiO_4 fayalite: Comparison of LDA and GGA results. *Physical Review B*, 67(9):094106, 2003.

[101] J. E. Jaffe, J. A. Snyder, Z. Lin, and A. C. Hess. LDA and GGA calculations for high-pressure phase transitions in ZnO and MgO. *Physical Review B*, 62(3):1660, 2000.

[102] D. Music, Z. Sun, R. Ahuja, and J. M. Schneider. Coupling in nanolaminated ternary carbides studied by theoretical means: The influence of electronic potential approximations. *Physical Review B*, 73(13):134117, 2006.

[103] G Kresse, J Furthmüller, and J Hafner. Ab initio force constant approach to phonon dispersion relations of diamond and graphite. *Europhysics Letters*, 32(9):729, 1995.

[104] S. Baroni, S. de Gironcoli, and Paolo Dal Corso, A.and Giannozzi. Phonons and related crystal properties from density-functional perturbation theory. *Reviews of Modern Physics*, 73(2):515–562, 2001.

[105] X. Gonze and J.-P. Vigneron. Density-functional approach to nonlinear-response coefficients of solids. *Physical Review B*, 39:13120–13128, 1989.

[106] S. W. Lovesey. *Theory of neutron scattering from condensed matter, Volume 1*. International series of monographs on physics. Clarendon Press, Oxford, 1986.

[107] S. W. Lovesey. *Theory of neutron scattering from condensed matter, Volume 2*. International series of monographs on physics. Clarendon Press, Oxford, 1986.

[108] G.E. Bacon. *Neutron scattering in chemistry*. Butterworth & Co., London, UK, 1977.

[109] G.E. Bacon. *Neutron diffraction*. Clarendon Press, Oxford, 1955.

[110] A.C. Larson and R.B. Von Dreele. GSAS General Structure Analysis System. LAUR 86-748, Los Alamos, NM, 2004.

[111] R. X. Fischer and E. Tillmanns. The equivalent isotropic displacement factor. *Acta Crystallographica*, C44, 1988.

[112] B. Buras and J. Leciejewicz. A new method for neutron diffraction crystal structure investigations. *Physica Status Solidi B*, 4(2):349–355, 1964.

[113] H. R. Wenk, L. Lutterotti, and S. Vogel. Texture analysis with the new HIPPO TOF diffractometer. *Nuclear Instruments & Methods in Physics Research Section A*, 515(3): 575–588, 2003.

[114] H. Rietveld. A profile refinement method for nuclear and magnetic structures. *Journal of Applied Crystallography*, 2(2):65–71, 1969.

[115] B. H. Toby. R factors in rietveld analysis: How good is good enough? *Powder Diffraction*, 21(1):67–70, 2006.

[116] V. F. Sears. Neutron scattering lengths and cross sections. *Neutron News*, 3(3):26–37, 1992.

[117] A new radiation. *Indian Journal of Physics*, 1928.

[118] T. El-Raghy and M. W. Barsoum. Processing and mechanical properties of Ti_3SiC_2: I, reaction path and microstructure evolution. *Journal of the American Ceramic Society*, 82 (10):2849–2854, 1999.

[119] M.W. Barsoum, T. El-Raghy, and A. Procopio. Characterization of Ti_4AlN_3. *Metallurgical and Materials Transactions A*, 31:333–337, 2000. ISSN 1073-5623.

[120] S. C. Vogel, C. Hartig, L. Lutterotti, R. B. Von Dreele, H. R. Wenk, and D. J. Williams. Texture measurements using the new neutron diffractometer HIPPO and their analysis using the Rietveld method. *Powder Diffraction*, 19(1):65–68, 2004.

[121] A study of the vibrational behavior of Ti_3SnC_2 in the 25–1000°C temperature range through high-temperature neutron diffraction, Raman spectroscopy, and first-principles calculations. *In preparation*, 2013.

[122] L. Lutterotti, S. Matthies, H. R. Wenk, A. S. Schultz, and J. W. Richardson. Combined texture and structure analysis of deformed limestone from time-of-flight neutron diffraction spectra. *Journal of Applied Physics*, 81(2):594–600, 1997.

[123] Y. Wang and J. C. Huang. Texture analysis in hexagonal materials. *Materials Chemistry and Physics*, 81(1):11–26, 2003.

[124] S. Matthies, J. Pehl, H. R. Wenk, L. Lutterotti, and S. C. Vogel. Quantitative texture analysis with the HIPPO neutron TOF diffractometer. *Journal of Applied Crystallography*, 38:462–475, 2005.

[125] S. C. Vogel. gsaslanguage: a GSAS script language for automated rietveld refinements of diffraction data. *Journal of Applied Crystallography*, 44(4):873–877, 2011.

[126] P. E. Blöchl. Projector augmented-wave method. *Physical Review B*, 50(24):17953–17979, 1994.

[127] G. Kresse and J. Hafner. Ab initio molecular dynamics for liquid metals. *Physical Review B*, 47(1):558–561, 1993.

[128] G. Kresse and J. Hafner. Ab-initio molecular-dynamics simulation of the liquid-metal amorphous-semiconductor transition in germanium. *Physical Review B*, 49:14251–14269, 1994.

[129] G. Kresse and J. Furthmüller. Efficient iterative schemes for ab initio total-energy calculations using a plane-wave basis set. *Physical Review B*, 54(16):11169–11186, 1996.

[130] A. Togo, F. Oba, and I. Tanaka. First-principles calculations of the ferroelastic transition between rutile-type and $CaCl_2$-type SiO_2 at high pressures. *Physical Review B*, 78:134106, 2008.

[131] A. Togo. Program download, phonopy. 2009. URL http://phonopy.sourceforge.net/.

[132] A. Togo, L. Chaput, I. Tanaka, and G. Hug. First-principles phonon calculations of thermal expansion in Ti_3SiC_2, Ti_3AlC_2, and Ti_3GeC_2. *Physical Review B*, 81:174301, 2010.

[133] J. Wang, Y. Zhou, Z. Lin, F. Meng, and F Li. Raman active modes and heat capacities of Ti_2AlC and Cr_2AlC ceramics: first principles and experimental investigations. *Applied Physics Letters*, 86, 2005.

[134] Jing-Yang Wang and Yan-Chun Zhou. Polymorphism of Ti_3SiC_2 ceramic: First-principles investigations. *Physical Review B*, 69:144108, 2004.

[135] V. Presser, M. Naguib, L. Chaput, A. Togo, G. Hug, and M. W. Barsoum. First-order Raman scattering of the MAX phases: Ti_2AlN, $Ti_2Al(C_{0.5}N_{0.5})$, Ti_2AlC, $(Ti_{0.5}V_{0.5})_2AlC$, V_2AlC, Ti_3AlC_2, and Ti_3GeC_2. *Journal of Raman Spectroscopy*, 43(1):168–172, 2012.

[136] L.E. Toth. *Transition Metal Carbides and Nitrides*. Academic Press, New York, NY, 1971.

[137] M. Yashima and K. Nakamura. Crystal structure of NaCl-type transition metal monocarbides MC (M = V, Ti, Nb, Ta, Hf, Zr), a neutron powder diffraction study. *Materials Science and Engineering B*, 148(1–3):69–72, 2008.

[138] M. W. Barsoum, C. J. Rawn, T. El-Raghy, A. T. Procopio, W. D. Porter, H. Wang, and C. R. Hubbard. Thermal properties of Ti_4AlN_3. *Journal of Applied Physics*, 87(12):8407–8414, 2000.

[139] K. Buchholt, P. Eklund, J. Jensen, J. Lu, R. Ghandi, M. Domeij, C. M. Zetterling, G. Behan, H. Zhang, A. Lloyd Spetz, and L. Hultman. Growth and characterization of epitaxial Ti_3GeC_2 thin films on 4H-SiC(0001). *Journal of Crystal Growth*, 343(1):133–137, 2012.

[140] H.O. Pierson. *Handbook of Refractory Carbides and Nitrides*. Noyes, Westwood, NJ, 1996.

[141] G. Hug, M. Jaouen, and M. W. Barsoum. X-ray absorption spectroscopy, EELS, and full-potential augmented plane wave study of the electronic structure of Ti_2AlC, Ti_2AlN, Nb_2AlC, and $(Ti_{0.5}Nb_{0.5})_2AlC$. *Physical Review B*, 71(2):24105, 2005.

[142] I. M. Low, W. K. Pang, S. J. Kennedy, and R. I. Smith. High-temperature thermal stability of Ti_2AlN and Ti_4AlN_3: A comparative diffraction study. *Journal of the European Ceramic Society*, 31(1-2):159–166, 2011.

[143] C.R. Houska. Thermal expansion and atomic vibration amplitudes for TiC, TiN, ZrC, ZrN and pure tungsten. *Journal of Physical Chemistry Solids*, 25:359–366, 1964.

[144] W. K. Pang, I. M. Low, and Z. M. Sun. In situ high-temperature diffraction study of the thermal dissociation of Ti_3AlC_2 in vacuum. *Journal of the American Ceramic Society*, 93 (9):2871–2876, 2010.

[145] N. V. Tzenov and M. W. Barsoum. Synthesis and characterization of Ti_3AlC_2. *Journal of the American Ceramic Society*, 83(4):825–832, 2000.

[146] T. A. Hahn. Thermal-expansion of TiAl+TiB_2 alloys and model-calculations of stresses and expansion of continuous fiber composites. *International Journal of Thermophysics*, 12 (4):711–722, 1991.

[147] Y. He, R. B. Schwarz, T. Darling, M. Hundley, S. H. Whang, and Z. M. Wang. Elastic constants and thermal expansion of single crystal γ-TiAl from 300 to 750 k. *Materials Science and Engineering A*, 239–240(0):157–163, 1997.

[148] Y. Bai, XD He, YB Li, CC Zhu, and Sam Zhang. Rapid synthesis of bulk Ti_2AlC by self-propagating high temperature combustion synthesis with a pseudo-hot isostatic pressing process. *Journal of Materials Research*, 24(8):2528–35, 2009.

[149] Y. Bai, X. He, C. Zhu, and G. Chen. Microstructures, electrical, thermal, and mechanical properties of bulk Ti_2AlC synthesized by self-propagating high-temperature combustion synthesis with pseudo hot isostatic pressing. *Journal of the American Ceramic Society*, 2012.

[150] H. Zhang, X. Wu, K. G. Nickel, J. Chen, and V. Presser. High-pressure powder x-ray diffraction experiments and ab initio calculation of Ti_3AlC_2. *Journal of Applied Physics*, 106(1):013519, 2009.

[151] Y. C. Zhou, Z. M. Sun, X. H. Wang, and S. Q. Chen. Ab initio geometry optimization and ground state properties of layered ternary carbides Ti_3MC_2 (M = Al, Si and Ge). *Journal of Physics-Condensed Matter*, 13(44):10001–10010, 2001.

[152] M. G. Tucker, M. T. Dove, and D. A. Keen. Direct measurement of the thermal expansion of the Si-O bond by neutron total scattering. *Journal of Physics Condensed Matter*, 12(26): L425–L430, 2000.

[153] F. Izumi. Beyond the ability of Rietveld analysis: MEM-based pattern fitting. *Solid State Ionics*, 172:1–6, 2004.

[154] C.J. Glassbrenner and G. A. Slack. Thermal conductivity of silicon and germanium from 3K to the melting point. *Physical Review*, 134(4A):1058–1069, 1964.

[155] L. Lutterotti. Program download, maud: Material analysis using diffraction, 1997–2009. URL http://www.ing.unitn.it/~maud/.

[156] L. Lutterotti, S. Matthies, and H.-R. Wenk. MAUD: a friendly Java program for Material Analysis Using Diffraction luca lutterotti. *IUCr: CPD Newsletters*, 21:14, 1999.

[157] C. J Rawn, M. W Barsoum, T. El-Raghy, A. Procopio, C. M. Hoffmann, and C. R. Hubbard. Structure of Ti_4AlN_3 – a layered $M_{n-1}AX_n$ nitride. *Materials Research Bulletin*, 35:1785, 2000.

[158] B. Manoun, R. P. Gulve, S. K. Saxena, S. Gupta, M. W. Barsoum, and C. S. Zha. Compression behavior of M_2AlC (M = Ti, V, Cr, Nb, and Ta) phases to above 50 GPa. *Physical Review B*, 73(2):024110, 2006.

[159] C. L. Kane and E. J. Mele. Quantum spin hall effect in graphene. *Physical Review Letters*, 95:226801, 2005.

[160] K. S. Novoselov, A. K. Geim, S. V. Morozov, D. Jiang, D. Zhang, S. V. Dubonos, I. V. Grigorieva, and A. A. Firsov. *Science*, 306:666, 2004.

[161] A. V. Krasheninnikov, P. O. Lehtinen, A. S. Foster, P. Pyykko, and R. M Nieminen. Embedding transition-metal atoms in graphene: Structure, bonding, and magnetism. *Physical Review Letters*, 102:126807, 2009.

[162] J. S. Crvenka, M. I. Katsnelson, and C. F. J Flipse. Room-temperature ferromagnetism in graphite driven by two-dimensional networks of point defects. *Nature Physics*, 5:840, 2009.

[163] A. M. Seayad and D. M. Antonelli. Recent advances in hydrogen storage in metal-containing inorganic nanostructures and related materials. *Advanced Materials*, 16:765, 2004.

[164] Y. D. Ma, Y. Dai, W. Wei, C. N. Niu, L. Yu, and B. B. Huang. First-principles study of the graphene $MoSe_2$ heterobilayers. *Journal of Physical Chemistry C*, 115:20237, 2011.

[165] Y. Ma, Y. Dai, M. Guo, C. Niu, Y. Zhu, and B. Huang. Evidence of the existence of magnetism in pristine VX_2 Monolayers (X = S, Se) and their strain-induced tunable magnetic properties. *ACS Nano*, 6(2):1695–1701, 2012.

[166] H. Zhang, C. Lazo, S. Blügel, S. Heinze, and Y. Mokrousov. Electrically tunable quantum anomalous hall effect in graphene decorated by 5*d* transition-metal adatoms. *Physical Review Letters*, 108:056802, 2012.

[167] M. Naguib, M. Kurtoglu, V. Presser, J. Lu, J. Niu, M. Heon, L. Hultman, Y. Gogotsi, and M. W. Barsoum. Two-dimensional nanocrystals: Two-dimensional nanocrystals produced by exfoliation of ti_3alc_2. *Advanced Materials*, 23(37):4207–4207, 2011.

[168] M. Naguib, J. Come, B. Dyatkin, V. Presser, P-L Taberna, P. Simon, M. W. Barsoum, and Y. Gogotsi. MXene: a promising transition metal carbide anode for lithium-ion batteries. *Electrochem. Comm.*, 16(1):61–64, 2012.

[169] J. Come, M. Naguib, P. Rozier, M. W. Barsoumc, Y. Gogotsi, P.-L. Tabernaa, M. Morcrette, and P. Simon. A non-aqueous asymmetric cell with a Ti_2C-based two-dimensional negative electrode. *J. Electrochem. Soc.*, 159:A1368, 2012.

[170] Q. Tang, Z. Zhou, and P. Shen. Are mxenes promising anode materials for Li ion batteries? computational studies on electronic properties and Li storage capability of Ti_3C_2 and $Ti_3C_2X_2$ (X = F, OH) monolayer. *J. Am. Chem. Soc.*, 134:16909, 2012.

[171] I. R. Shein and A. L. Ivanovskii. Planar nano-block structures $Ti_{n+1}Al_{0.5}C_n$ and $Ti_{n+1}C_n$ ($n = 1$, and 2) from MAX phases: structural, electronic properties and relative stability from first principles calculations. *Superlattices and Microstructures*, 52:147–157, 2012.

[172] M. Kurtoglu, M. Naguib, Y. Gogotsi, and M. W. Barsoum. First principles study of two-dimensional early transition metal carbides. *MRS Comm.*, 2:133, 2012.

[173] M. Naguib, O. Mashtalir, J. Carle, V. Presser, J. Lu, L. Hultman, Y. Gogotsi, and M. W. Barsoum. Two-dimensional transition metal carbides. *ACS Nano*, 6(2):1322–1331, 2012.

[174] M. Montalti, A. Credi, L. Prodi, and M. T. Gandolfi. *Handbook of Photochemistry*. CRC Press, 2006.

[175] J. P. Perdew, A. Ruzsinszky, G. I. Csonka, O. A. Vydrov, G. E. Scuseria, L. A. Constantin, X. Zhou, and K. Burke. Restoring the density-gradient expansion for exchange in solids and surfaces. *Physical Review Letters*, 100:136406, 2008.

[176] A. I. Liechtenstein, V. I. Anisimov, and J. Zaanen. Density-functional theory and strong interactions: Orbital ordering in Mott-Hubbard insulators. *Physical Review B*, 52:R5467–R5470, 1995.

[177] H. Li, L. Zhang, Q. Zeng, K. Guan, K. Li, H. Ren, S. Liu, and L. Cheng. Structural, elastic and electronic properties of transition metal carbides TMC (TM=Ti, Zr, Hf and Ta) from first-principles calculations. *Solid State Communications*, 151(8):602 – 606, 2011.

[178] V. I. Anisimov, A. I. Poteryaev, M. A. Korotin, A. O. Anokhin, and G. Kotliar. First-principles calculations of the electronic structure and spectra of strongly correlated systems: dynamical mean-field theory. *Journal of Physics: Condensed Matter*, 9(35):7359, 1997.

[179] W. Sun, W. Luo, and R. Ahuja. Role of correlation and relativistic effects in MAX phases. *Journal of Materials Science*, 47:7615–7620, 2012.

[180] P. Carrier and S. H. Wei. Calculated spin-orbit splitting of all diamondlike and zinc-blende semiconductors: Effects of $p_{1/2}$ local orbitals and chemical trends. *Physical Review B*, 70: 035212, 2004.

[181] J. C. Boettger and S. B. Trickey. First-principles calculation of the spin-orbit splitting in graphene. *Physical Review B*, 75:121402, 2007.

[182] Michel W. Barsoum and Miladin Radovic. Elastic and mechanical properties of the max phases. *Annual Review of Materials Research*, 41(1):195–227, 2011.

[183] S. Riaz, H. M. Flower, and D. R. F. West. Phase relationships involving TiC and Ti_3AlC (P phase) in Ti–Al–C system. *Materials Science and Technology*, 16(9):984–992, 2000.

[184] S. F. Matar, Y. Le Petitcorps, and J. Etourneau. Ab initio study of the chemical role of carbon within TiAl alloy system: Application to composite materials. *Computational Materials Science*, 10(1-4):314–318, 1998.

[185] Z. J. Lin, M. J. Zhuo, Y. C. Zhou, M. S. Li, and J. Y. Wang. Microstructural characterization of layered ternary Ti_2AlC. *Acta Materialia*, 54(4):1009–1015, 2006.

[186] P.M. Morse. Diatomic molecules according to the wave mechanics. ii. vibrational levels. *Physical Review*, 34:57–64, 1929.

[187] Z. M. Sun, R. Ahuja, S. Li, and J. M. Schneider. Structure and bulk modulus of M_2AlC (M=Ti, V, and Cr). *Applied Physics Letters*, 83(5):899–901, 2003.

[188] B. Manoun, S. K. Saxena, G. Hug, A. Ganguly, E. N. Hoffman, and M. W. Barsoum. Synthesis and compressibility of $Ti_3(Al,Sn_{0.2})C_2$ and $Ti_3Al(C_{0.5},N_{0.5})_2$. *Journal of Applied Physics*, 101(11):113523, 2007.

[189] Z. M. Sun, D. Music, R. Ahuja, and J. M. Schneider. Electronic origin of shearing in m_2ac (m = ti, v, cr, a = al, ga). *Journal of Physics-Condensed Matter*, 17(46):7169–7176, 2005.

[190] Z. M. Sun, D. Music, R. Ahuja, S. Li, and J. M. Schneider. Bonding and classification of nanolayered ternary carbides. *Physical Review B*, 70(9), 2004.

[191] X. H. Wang and Y. C. Zhou. Stability and selective oxidation of aluminum in nano-laminate Ti_3AlC_2 upon heating in argon. *Chemistry of Materials*, 15(19):3716–3720, 2003.

[192] B. C. Mei, X. L. Hong, J. Q. Zhu, and W. B. Zhou. Gradient structure of ti–al–c ternary carbide prepared by hot-pressing sintering. *Journal of Wuhan University of Technology-Materials Science Edition*, 20(2):5–7, 2005.

[193] N. S. Jacobson, M. P. Brady, and G. M. Mehrotra. Thermodynamics of selected Ti–Al and Ti–Al–Cr alloys. *Oxidation of Metals*, 52(5-6):537–556, 1999.

[194] H. Högberg, L. Hultman, J. Emmerlich, T. Joelsson, P. Eklund, J. M. Molina-Aldareguia, J. P. Palmquist, O. Wilhelmsson, and U. Jansson. Growth and characterization of MAX-phase thin films. *Surface Coating Technology*, (1–3):6–10, 2005.

[195] A. G. Zhou, S. Basu, and M. W. Barsoum. Kinking nonlinear elasticity, damping and microyielding of hexagonal close-packed metals. *Acta Materialia*, 56(1):60–67, 2008.

[196] A. Zhou and M. Barsoum. Kinking nonlinear elasticity and the deformation of magnesium. *Metallurgical and Materials Transactions A*, 40(7):1741–1756, 2009.

[197] A. G. Zhou, D. Brown, S. Vogel, O. Yeheskel, and M. W. Barsoum. On the kinking nonlinear elastic deformation of cobalt. *Materials Science and Engineering A*, 527(18–19): 4664–4673, 2010.

[198] M.W. Barsoum and S. Basu. Kinking nonlinear elastic solids. In J. Buschow, R. Cahn, M.C. Flemings, B. Ilschner, E.J. Kramer, S. Mahajan, and P. Veyssiere, editors, *Encyclopedia of Materials: Science and Technology*, pages 1–23. 2010.

[199] M. W. Barsoum, A. Murugaiah, S. R. Kalidindi, and T. Zhen. Kinking nonlinear elastic solids, nanoindentations, and geology. *Physical Review Letters*, 92(25):255508, 2004.

[200] M. W. Barsoum, T. Zhen, A. Zhou, S. Basu, and S. R. Kalidindi. Microscale modeling of kinking nonlinear elastic solids. *Physical Review B*, 71(13):134101, 2005.

[201] S. R. Kalidindi, T. Zhen, and M. W. Barsoum. Macroscale constitutive modeling of kinking nonlinear elastic solids. *Materials Science and Engineering A*, 418(1-2):95–98, 2006.

[202] J. W. Christian and S. Mahajan. Deformation twinning. *Progress in Materials Science*, 39 (1-2):1–157, 1995.

[203] C. Palache. Morphology of graphite, arsenopyrite, pyrite, and arsenic. *American Mineralogist*, 26:709, 1941.

[204] A. Kelly E.J. Freise. Twinning in graphite. *Proceedings of the Physical Society A*, 264: 269–76, 1961.

[205] W. T. Read and W. Shockley. Dislocation models of crystal grain boundaries. *Physical Review*, 78(3):275, 1950.

[206] Y. Minonishi, S. Ishioka, M. Koiwa, and S. Morozumi. The structure of $(11\bar{2}1)$ twin boundaries in hcp crystals. *Physica Status Solidi a-Applied Research*, 71(1):253–258, 1981.

[207] A. Serra and D. J. Bacon. Computer-simulation of twin boundaries in the hcp metals. *Philosophical Magazine A*, 54(6):793–804, 1986.

[208] A. Arya and Emily A. Carter. Structure, bonding, and adhesion at the tic(100)/fe(110) interface from first principles. *The Journal of Chemical Physics*, 118(19):8982, 2003.

[209] E. Clouet, L. Ventelon, and F. Willaime. Dislocation core energies and core fields from first principles. *Physical Review Letters*, 102(5), 2009.

[210] L. Ventelon and F. Willaime. Core structure and peierls potential of screw dislocations in α-fe from first principles: cluster versus dipole approaches. *Journal of Computer-Aided Materials Design*, 14(S1):85–94, 2008.

[211] Y. Wang, L. Q. Chen, Z. K. Liu, and S. N. Mathaudhu. First-principles calculations of twin-boundary and stacking-fault energies in magnesium. *Scripta Materialia*, 62(9): 646–649, 2010.

[212] G. Kresse and D. Joubert. From ultrasoft pseudopotentials to the projector augmented-wave method. *Physical Review B*, 59(3):1758–1775, 1999.

[213] A. Serra and D. J. Bacon. Computer-simulation of twinning dislocation in magnesium using a many-body potential. *Philosophical Magazine a-Physics of Condensed Matter Structure Defects and Mechanical Properties*, 63(5):1001–1012, 1991.

[214] J. P. Simon. Computer-simulation of twin boundaries in hcp normal metals - Li, Be, Mg, Zn, Cd. *Journal of Physics F-Metal Physics*, 10(3):337–345, 1980.

[215] Y. Le Page and P. Saxe. Symmetry-general least-squares extraction of elastic data for strained materials from ab initio calculations of stress. *Physical Review B*, 65:104104, 2002.

[216] M. S. Daw and M. I. Baskes. Embedded-atom method – derivation and application to impurities, surfaces, and other defects in metals. *Physical Review B*, 29(12):6443–6453, 1984.

[217] M. W. Finnis and J. E. Sinclair. A simple empirical N-body potential for transition-metals. *Philosophical Magazine A*, 50(1):45–55, 1984.

[218] M. H. Yoo, J. R. Morris, K. M. Ho, and S. R. Agnew. Nonbasal deformation modes of hcp metals and alloys: Role of dislocation source and mobility. *Metallurgical and Materials Transactions A*, 33(3):813–822, 2002.

[219] J. R. Morris, Y. Y. Ye, K. M. Ho, C. T. Chan, and M. H. Yoo. Structures and energies of compression twin boundaries in hcp Ti and Zr. *Philosophical Magazine A*, 72(3):751–763, 1995.

[220] J. R. Morris, Y. Y. Ye, and M. H. Yoo. First-principles examination of the $(10\bar{1}2)$ twin boundary in hcp metals. *Philosophical Magazine*, 85(2-3):233–238, 2005.

[221] W. Cai, V. V. Bulatov, J. Chang, J. Li, and S. Yip. Dislocation core structure and mobility. In F.R.N. Nabarro and J. P. Hirth, editors, *Dislocations in Solids*, volume 12. 2004.

[222] V. Vitek. Core structure of screw dislocations in body-centred cubic metals: relation to symmetry and interatomic bonding. *Philosophical Magazine*, 84(3-5):415–428, 2004.

[223] J. A. Yasi, T. Nogaret, D. R. Trinkle, Y. Qi, L. G. Hector, and W. A. Curtin. Basal and prism dislocation cores in magnesium: comparison of first-principles and embedded-atom-potential methods predictions. *Modelling and Simulation in Materials Science and Engineering*, 17(5):055012, 2009.

[224] Ju Li. AtomEye: an efficient atomistic configuration viewer. *Modelling and Simulation in Materials Science and Engineering*, 11(2):173, 2003.

[225] J. Li. *Modeling Microstructural Effects on Deformation Resistance and Thermal Conductivity*. PhD thesis, 2000.

[226] A. Serra, D. J. Bacon, and R. C. Pond. The crystallography and core structure of twinning dislocations in hcp metals. *Acta Metallurgica*, 36(12):3183–3203, 1988.

[227] R.E. Reed-Hill, E.P. Dahlberg, and W.A. Jr. Slippy. Some anelastic effects in zirconium at room temperature resulting from prestrain at 77 deg K. *Trans. Met. Soc.*, 233:1766–71, 1965.

[228] A. Akhtar and A. Teghtsoonian. Plastic deformation of zirconium single crystals. *Acta Metallurgica*, 19(7):655–663, 1971.

[229] J. F. Bingert, T. A. Mason, G. C. Kaschner, P. J. Maudlin, and G. T. Gray. Deformation twinning in polycrystalline zr: Insights from electron backscattered diffraction characterization. *Metallurgical and Materials Transactions a-Physical Metallurgy and Materials Science*, 33(3):955–963, 2002.

[230] S. Vaidya and S. Mahajan. Accommodation and formation of $(11\bar{2}1)$ twins in Co single-crystals. *Acta Metallurgica*, 28(8):1123–1131, 1980.

[231] G. Mills, H. Jónsson, and G. K. Schenter. Reversible work transition-state theory – application to dissociative adsorption of hydrogen. *Surface Science*, 324(2–3):305–337, 1995.

[232] H. Jónsson, G. Mills, and K. W. Jacobson. Nudged elastic band method for finding minimum energy paths of transitions. In B. J. Berne, G. Ciccotti, and D. F. Coker, editors, *Classical and Quantum Dynamics in Condensed Phase Simulations*. World Scientific, 1998.

[233] R. F. Tinder and J. Washburn. Factors affecting the initiation of plastic flow in metals. *22nd Technical Report, UC Berkeley California*, Part I, Minterals Res. Lab, 1962.

[234] R. F. Tinder and J. Washburn. The initiation of plastic flow in copper. *Acta Metallurgica*, 12(2):129–137, 1964.

[235] J. M. Roberts and N Brown. Microstrain in zinc single crystals. *Transactions of the American Institute of Mining, Metallurgical, and Petroleum Engineers*, 218:454, 1960.

[236] J. M. Roberts and N. Brown. Low frequency friction in zinc single crystals. *Acta Metallurgica*, 10:430–441, 1962.

[237] W. T. Brydges. The dependence of yield stress on forest dislocation density in copper single crystals. *Philosophical Magazine*, 15(137):1079 – 1081, 1967.

[238] J. M. Roberts and D. E. Hartman. Theory of dislocation hysteresis with application to damping measurements in magnesium single crystals. *Journal of the Physical Society of Japan*, 18:119, 1963.

[239] J. M. Roberts and D. E. Hartman. The temperature dependence of the microyield points in prestrained magnesium single crystals. *Transactions of the American Institute of Mining, Metallurgical, and Petroleum Engineers*, 230:1125–1133, 1964.

[240] S. R. Agnew and J. F. Nie. Preface to the viewpoint set on: The current state of magnesium alloy science and technology. *Scripta Materialia*, 63(7):671–673, 2010.

[241] W. B. Hutchinson and M. R. Barnett. Effective values of critical resolved shear stress for slip in polycrystalline magnesium and other hcp metals. *Scripta Materialia*, 63(7): 737–740, 2010.

[242] J. J. Jonas, T. Mu, S.and Al-Samman, G. Gottstein, L. Jiang, and T. Martin. The role of strain accommodation during the variant selection of primary twins in magnesium. *Acta Materialia*, 59(5):2046–2056, 2011.

[243] J. Y. Wang and Y. C. Zhou. Recent progress in theoretical prediction, preparation, and characterization of layered ternary transition-metal carbides. *Annual Review of Materials Research*, 39:415–443, 2009.

[244] Z. J. Lin, M. J. Zhuo, Y. C. Zhou, M. S. Li, and J. Y. Wang. Structural characterization of a new layered-ternary Ta_4AlC_3 ceramic (erratum, vol 21, pg 2587, 2006). *Journal of Materials Research*, 22(3):816–816, 2007.

[245] T. Liao, J. Wang, and Y. Zhou. Basal-plane slip systems and polymorphic phase transformation in Ti_2AlC and Ti_2AlN: a first-principles study. *Journal of Physics-Condensed Matter*, 18(27):6183–6192, 2006.

[246] Z. Sun, J. Zhou, D. Music, R. Ahuja, and J. M. Schneider. Phase stability of Ti_3SiC_2 at elevated temperatures. *Scripta Materialia*, 54(1):105–107, 2006.

[247] Z. W. Wang, C. S. Zha, and M. W. Barsoum. Compressibility and pressure-induced phase transformation of Ti_3GeC_2. *Applied Physics Letters*, 85(16):3453–3455, 2004.

[248] R. Yu, Q. Zhan, L. L. He, Y. C. Zhou, and H. Q. Ye. Polymorphism of Ti_3SiC_2. *Journal of Materials Research*, 17(5):948–950, 2002.

[249] X. H. Deng, B. B. Fan, and W. Lu. First-principles investigations on elastic properties of α- and β-Ta_4AlC_3. *Solid State Communications*, 149(11-12):441–444, 2009.

[250] Y. L. Du, Z. M. Sun, H. Hashimoto, and W. B. Tian. Bonding properties and bulk modulus of M_4AlC_3 (M = V, Nb, and Ta) studied by first-principles calculations. *Physica Status Solidi B*, 246(5):1039–1043, 2009.

[251] C. Boudias and D. Monceau. Carine crystalography, 1989 - 1998.

Vita

Education

Drexel University: Philadelphia, PA
PhD in Materials Science and Engineering **April 2009 – April 2013**

University of California, Los Angeles (UCLA): Los Angeles, CA
B.S. in Materials Science and Engineering **Sept 2004 – June 2008**

Research and Collaborative Projects

Graduate Research Assistant, Drexel University: Philadelphia, PA	**2009–2013**
Visiting Core Researcher, Materials Defects Program, IPAM, UCLA: Los Angeles, CA	**2012**
Visiting Graduate Researcher, ONERA, LEM Group: Chatîllon, France	**2011**
Visiting Graduate Researcher, Linköping University, IFM: Linköping, Sweden	**2010–2011**
Summer Research Assistant, LANL, LANSCE, Lujan Center: Los Alamos, NM	**2009**

Fellowships and Awards

Awards: Outstanding Promise Doctoral Award, Drexel (2013), Appreciation Award for leadership in IPAM-MD2012 (2012), PhD Laureate, ICAMM (2012), Lindau Nobel Laureate Meeting Drexel Nominee (2011).

Fellowships: Leroy Resser Endowed Fellowship (2012), NSF IGERT Fellowship (2010–2012), DoE GAANN Fellowship (2009–2010), FIAS Research Fellowship (2008–2009), California 90 Percentile Governor's Scholarship (2008).

Travel Awards: IPAM-UCLA travel and stipend funding (2012), ACNS travel award (2012), THERMEC travel scholarship (2011), Drexel graduate international travel award (2011), STONE funding for LANL experiments (2010), Material Advantage MS&T travel award (2010), LANSCE neutron school funding (2009).

Presentations

Invited talks:
N.J. Lane, S.C. Vogel, T. Proffen, M.W. Barsoum, *THERMEC*, Quebec City, Canada, August 2011.
N.J. Lane, S.C. Vogel, M.W. Barsoum, *MS&T* Houston, TX, October 2010.

Other presentations in:
IPAM-UCLA MD seminars (Los Angeles, CA, 2012), ACNS (Washington, DC, 2012), ICAMM (Nantes, France, 2012), ASM Chuck Burns (Philadelphia, PA, 2012), ICME (Seven Springs, PA, 2012), ICACC (Daytona Beach, FL, 2011), MS&T (Houston, TX, 2010)

Publications

11. N.J. Lane, S.C. Vogel, E.N. Caspi, M.W. Barsoum, *J. Appl. Phys.*, **113** 183519 (2013).
10. N.J. Lane, M.W. Barsoum, J.M. Rondinelli, *Eur. Phys. Lett.* **101** 57003 (2013).
9. N.J. Lane, A. Togo, L. Chaput, S. C. Vogel, G. Hug, L, Hultman, M.W. Barsoum, *Phys. Rev. B* **86** 214301 (2012).
8. N.J. Lane, M. Naguib, J. Lu, P. Eklund, L, Hultman, M.W. Barsoum, *J. Am. Cer. Soc.* **95** [10] 3352-3354 (2012).
7. N.J. Lane, M. Naguib, J. Lu, L, Hultman, M.W. Barsoum, *J. Eur. Cer. Soc.* **32** [12] 3485-3491 (2012).
6. N.J. Lane, M. Naguib, V. Presser, G. Hug, L. Hultman, M.W. Barsoum, *J. Raman Spectrosc.* **43** [10] 954-958 (2012).
5. N.J. Lane, S.I. Simak, A.S. Mikhaylushkin, I.A. Abrikosov, L. Hultman, M.W. Barsoum, *Phys. Rev. B* **84**, 184101 (2011).
4. M. Naguib, V. Presser, N.J. Lane, D. Tallman, Y. Gogotsi, J. Lu, L. Hultman, M.W. Barsoum, *RSC Advances* **1**, 1493-1499 (2011).
3. N.J. Lane, S.C. Vogel, M.W. Barsoum, *J. Am. Cer. Soc.* **94** [10] 3473-3479, (2011).
2. N.J. Lane, P. Eklund, J. Lu, C.B. Spencer, L. Hultman, M.W. Barsoum, *Mat. Res. Bull.*, **46**, 1088-1091 (2011).
1. N.J. Lane, S.C. Vogel, M.W. Barsoum, *Phys. Rev. B*, **82**, 174109 (2010).